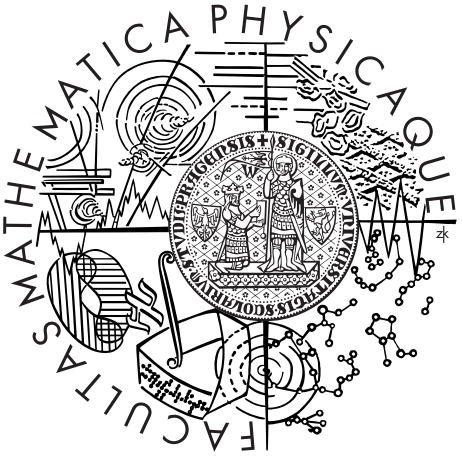
Charles University
Faculty of Mathematics and Physics

DOCTORAL THESIS



Libor Nouzák

Laboratory investigation of dust charging and impact ionization

Department of Surface and Plasma Science

Supervisor of doctoral thesis:	Doc. RNDr. Jiří Pavlů, Ph.D.
Program of study:	Physics
Study branch:	4f2 – Physics of Plasmas and Ionized medium

Prague 2018

I declare that I carried out this doctoral thesis independently, and only with the cited sources, literature and other professional sources.

I understand that my work relates to the rights and obligations under the Act No. 121/2000 Sb., the Copyright Act, as amended, in particular the fact that the Charles University has the right to conclude a license agreement on the use of this work as a school work pursuant to Section 60 paragraph 1 of the Copyright Act.

In Prague on May 17, 2018

At the first, I would like to thank my parents for their love and support in everything what I've ever done during my studies. I would like to express my deepest thanks to Dr. Jiří Pavlů for his guidance, supervision and friendly discussions which at the end resulted in completion of this thesis. I would also like to thank Professors Zdeněk Němeček and Jana Šafránková for their helpful neverending advices and encouragement and Professor Zoltan Sternovsky for a careful reading and suggestions to the text. I would also like to acknowledge the helpful discussions with my other colleagues: Dr. Marek Vyšinka, Dr. Jakub Vaverka and Dr. Ivana Richterová during my studies. I gratefully acknowledge support by the Grant Agency of the Charles University under project number 728616, by the Czech Science Foundation project under number 16-05762S. Finally, I would like to thank the K. Urbánek foundation for a support of my visits in Colorado University in Boulder.

Název práce: Laboratorní studium nabíjení prachu a jeho ionizace dopadem

Autor: Libor Nouzák

Katedra: Katedra fyziky povrchů a plazmatu

Vedoucí disertační práce: Doc. RNDr. Jiří Pavlů, Ph.D., Katedra fyziky povrchů a plazmatu

Abstrakt:

Řada kosmických misí zkoumá vlastnosti prachu jako jednoho z hlavních elementů naší sluneční soustavy. Mezi relevantní nabíjecí procesy patří interakce s elektrony a ionty slunečního větru a často dominantní fotoemise slunečním UV zářením. Práce studuje jednotlivé nabíjecí procesy odděleně v laboratorních podmínkách. Jedno prachové zrno je chyceno v elektrodynamické pasti a je vystaveno elektronovému, iontovému a UV svazku s proměnnou energií. V práci popisujeme metodu jak určit výstupní práci jednoho takového prachového zrna a její závislost na materiálu. Předmětem druhé skupiny experimentů je vzájemné působení nabitých prachových zrn s pevnými povrchy. Ty zahrnují laboratorní vyšetřování odezvy zmenšeného modelu družice Cassini na dopady železných prachových zrn urychlených na rychlosti 5–25 km/s. Práce diskutuje experimentální uspořádání, jeho omezení a prezentuje výsledky naměřené v monopólové a dipólové konfiguraci antén. Ukazuje se, že amplituda a polarita zaznamenaných signálů závisí na velikosti napětí na anténnách a družici. Závěrem stručně představujeme mechanismus vedoucí ke generování těchto signálů.

Klíčová slova: nabíjení prachu, fotoemise, zánik prachových zrn, dopad prachu, ionizace dopadem

Title: Laboratory investigation of dust charging and impact ionization

Author: Libor Nouzák

Department: Department of Surface and Plasma Science

Supervisor: Doc. RNDr. Jiří Pavlů, Ph.D., Department of Surface and Plasma Science

Abstract:

A number of spacecraft missions investigate properties of dust as one of the main elements of interest of our solar system. In this environment, the relevant charging processes are interactions with solar wind electrons and ions and photoemission by solar UV which often dominates. The present thesis studies charging processes separately in laboratory. We store a single dust grain in an electrodynamic trap and expose it to electron, ion, and UV beams with variable energies. We describe a method of the work function determination of a single dust grain and its dependence on the grain material. The interaction of the charged dust grains with solid surfaces is a subject of the second experiment. Laboratory investigations of the response of a scaled down model of the Cassini spacecraft to impacts of submicron iron grains accelerated to velocities 5–25 km/s. The thesis discusses an experimental set-up, its limitations, and presents results measured in both monopole and dipole antenna configurations. We demonstrate that the amplitude and polarity of the recorded signals depend on the antennas and the spacecraft body biases and briefly introduce the mechanism leading to the signal generation.

Keywords: dust charging, photoemission, destruction of dust, dust impact, impact ionization

„Víš, když chceš dokázat, že jsi filozof, musíš napsat knihu. Pak na to dostaneš papír a oficiální žínku filozofa.“ [1].

Filozof Didactylos (T. Pratchett: Malí bohové, TALPRESS 1997)

[1] *“Got to write a book, see, to prove you’re a philosopher. Then you get your scroll and free official philosopher’s loofah.”*
Philosopher Didactylos (T. Pratchett: Small Gods, HarperCollins Publishers Ltd., 1992)

Contents

1 Introduction **3**
- 1.1 The interplanetary medium . . . 4
- 1.2 Cometary Comae . . . 7
- 1.3 The Earth's upper atmosphere . . . 9
- 1.4 Lunar plasma environment . . . 10
  - 1.4.1 Lunar dust motion due to interaction with plasma . . . 11
- 1.5 Planetary rings . . . 13
  - 1.5.1 Jupiter's ring system . . . 13
  - 1.5.2 Saturn's ring system . . . 14

2 Charging of dust grains **19**
- 2.1 Charging of isolated dust grains . . . 20
- 2.2 Ion and electron collections . . . 20
- 2.3 Secondary electron emission . . . 21
  - 2.3.1 Electron impact . . . 21
  - 2.3.2 Ion impact . . . 22
- 2.4 Electron and ion field emissions . . . 23
- 2.5 Photoemission . . . 24
  - 2.5.1 Work function . . . 26
  - 2.5.2 Photoelectron yield . . . 26
  - 2.5.3 Photoconductivity . . . 29
- 2.6 Thermionic effect . . . 30
- 2.7 Radioactivity . . . 30
- 2.8 Contact charging . . . 31
- 2.9 Frictional charging . . . 32
- 2.10 Grain charging in the solar system . . . 33

3 Creation and destruction of dust grains **35**
- 3.1 Dust production by comets . . . 35
- 3.2 Plasma induced sputtering and alteration . . . 35
- 3.3 Electrostatic fragmentation of charged grains . . . 37
- 3.4 Coagulation of charged and neutral dust grains . . . 38
- 3.5 Melting and evaporation of grains . . . 39
- 3.6 Impact ionization process . . . 39

4 Goals of the thesis **41**

5 Photoemission study of dust in linear electrodynamic trap 43
5.1 Experimental setup . . . 44
5.1.1 Electron gun . . . 45
5.1.2 Ion gun . . . 46
5.1.3 UV source . . . 46
5.1.4 Vacuum system . . . 47
5.2 Measurement techniques . . . 50
5.2.1 Determination of the grain mass . . . 50
5.2.2 I–V charactericteristics . . . 50
5.2.3 Determination of UV photon flux . . . 51
5.3 Experimental results . . . 53
5.3.1 Photoemission of lunar dust simulant . . . 53

6 Investigation of dust impact from antenna signals 61
6.1 Experimental setup for antenna signal study . . . 62
6.2 Experimental results . . . 65

7 Conclusions 73

Appendix 75
Principle of linear electrodynamic trap . . . 75

Bibliography 78

Papers attached to the thesis 105
Nouzák et al. [2013] . . . 106
Nouzák et al. [2014] . . . 114
Nouzák et al. [2016] . . . 125
Vyšinka et al. [2017] . . . 133
Nouzák et al. [2017] . . . 142

Chapter 1

Introduction

Dusty plasmas are rather ubiquitous in space [Verheest, 2000; Mendis and Rosenberg, 1994; Northrop, 1997]. As a cosmic dust we usually mean solid objects with sizes between a few molecules to 100 μm of various materials and shapes. Dust is present and plays a significant role in a number of environments in space, such as interstellar clouds, circumstellar clouds, solar system, etc., where the presence of charged dust particles has been well established.

The space between the stars known as interstellar medium is composed of gas carrying of 99 wt% and dust (1 wt%) [Boulanger *et al.*, 1950; Shirley and Fairbridge, 1997]. The gaseous part of the interstellar medium contains 91 at% of hydrogen and 9 at% of helium, with 0.1 at% atoms of elements heavier than helium [Ferriere, 2001]. This part continually decreases with time due to the collapse of giant molecular clouds and formation of a new generations of stars. The presence of dust in interstellar or circumstellar clouds is well known for a long time from star infrared emission (Fig. 1.1 – left).

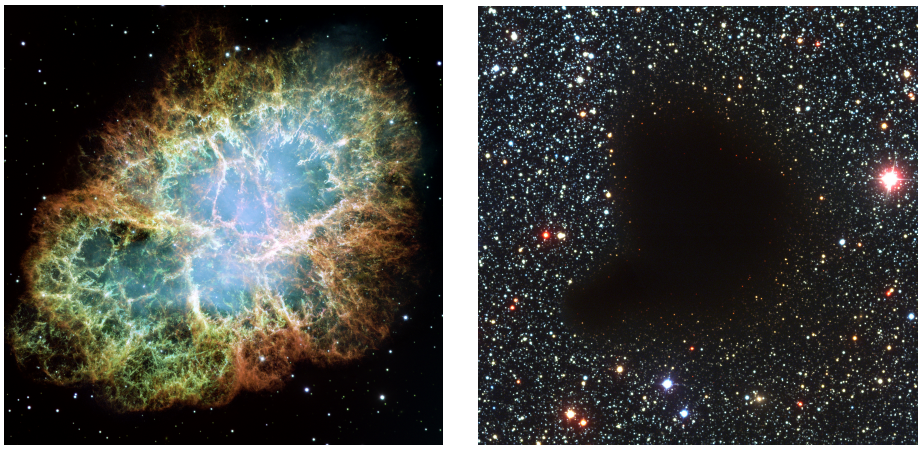


Figure 1.1: Crab nebula observed by Hubble telescope (left) and Bernard nebula observed by VLT ANTU telescope (right). Adopted from https://www.spacetelescope.org/images/ and https://cdn.eso.org/images/large/eso9924a.jpg.

Unquestionably, the most abundant gaseous part of molecular clouds – molecular hydrogen, is formed on grain surfaces. Other molecules might result from reactions on grain surfaces as well [Watson, 1976]. The grain surfaces can also be efficient for ortho–para conversion of molecular hydrogen in the interstellar

medium [Bron *et al.*, 2016]. The dust grains in interstellar or circumstellar clouds are both dielectrics (ices, silicates, etc.) and conductors (graphite, magnetite, amorphous carbon, etc) [Tielens and Allamandola, 1985; Tielens, 1996]. When the light from stars comes through the interstellar cloud, two scenarios can be expected. If the interstellar cloud is dense, the light can fully extinct and a dark nebula is created (Fig. 1.1 – right). When the cloud is tenuous, the light goes through and only part of the light spectrum extincts due to dispersion [Draine, 2003; Savage and Mathis, 1979]. The amount of extinction depends on thickness and density of the interstellar cloud and also on the wavelength of the incoming light. Because the typical sizes of dust in the interstellar cloud prefer dispersion of the blue light, the cloud seems blue colored, if we observe it from side. On the other hand, if we look on the source of light directly through the cloud, it appears red. This effect is known as interstellar reddening.

Typical parameters of dust-laden plasmas in interstellar clouds are $n_e = 10^{-3}\,\mathrm{cm}^{-3}$, $T_e \approx 12\,\mathrm{K}$, $n_d \approx 10^{-7}\,\mathrm{cm}^{-3}$, $r_d \approx 0.2\,\mu\mathrm{m}$, and $n_n \approx 10^4\,\mathrm{cm}^{-3}$, where subscript e reffers to electrons, d to dust grains, and n to neutrals [Mendis, 1996; Tsytovich, 1997]. In contrary, there are many regions in which shock-heated plasmas or hot gases propagate through regions containing grains and neutral gases [Draine *et al.*, 1983]. These plasmas can be generated by supernova remnants and their temperatures and densities can vary enormously depending in the nature of the shock [Klein *et al.*, 2002]. Typical densities and temperatures of these remnants range from $1\,\mathrm{cm}^{-3}$ and $10^5\,\mathrm{K}$ to $10^{-3}\,\mathrm{cm}^{-3}$ and $10^8\,\mathrm{K}$.

Solar system is also full of dust. The existence of dust in the early solar nebula has been advocated by the Nobel Laureate Hannes Alfvén [Alvén, 1954]. The coagulation of the dust grains in the solar nebula have led to "planetesimals" from which comets and planets have been formed [Weidenshilling, 1980]. The physical properties of dust grains that can be found in the interplanetary space (as size, mass, density, charge, etc.) depend on their origin and surroundings. The sources of the dust grains in the solar system are, for example, micrometeoroids [Genge *et al.*, 2008], space debris [Klinkrad, 2006], man-made pollution, lunar impact ejecta [Gladman *et al.*, 1995], Kuiper Belt [Liou *et al.*, 1996], asteroids [Dermott *et al.*, 2002], and comets [Liou and Zook, 1996].

In next sections we briefly explain some important characteristics of the dust grains in their natural plasma environments. We will discuss different regions of our solar system, namely interplanetary medium, Earth's atmosphere, Moon's plasma environment, planetary rings, and comets.

1.1 The interplanetary medium

The interplanetary space is not empty but it is full of dust known as "interplanetary dust". The presence of interplanetary dust particles is well known from the zodiacal light observations first noted by Joshua Childrey [1661] and first interpreted by Jean Dominique Cassini [1683]. The zodiacal light is created due to dust grains distributed throughout the inner solar system. Recent modeling initiated by infrared astronomical satellite observations indicates that the strongest contributors to interplanetary dust grains within 5 AU are comets, which contribute to a population with a broad range of inclinations [Nesvorný *et al.*, 2010]. The asteroids are the other important sources of the interplanetary

dust. They produce dust due to their mutual collisions in the asteroid belt. Dust grains smaller than 1 cm gradually spiral into the Sun on timescale ranging from thousands to millions of years through the combination of solar wind drag and the Pointing-Robertson drag [Kimura *et al.*, 2002]. It has been estimated that roughly 40 000 tons of the interplanetary dust reaches the Earth's atmosphere every year [Zook, 2001].

Interplanetary dust grains can be collected in the stratosphere, in polar ices, or in impact equipments on spacecrafts. Grains from polar ices can be larger than the stratospheric particles, but they are more heated, and may actually contain various pollutions. Grains collected in space can be complemented with velocity and trajectory information, unlike those collected in the Earth stratosphere or in ice. But generally, the collected particles are highly deformed, melted, or even completely vaporized. The stratospheric collection provides the least contaminated and heated grains. The high-altitude (18–20 km) stratospheric research aircrafts and baloons are used to collect interplanetary dust [Brownlee, 1985]. The size of most collected interplanetary grains is in the range of 5–100 μm. The interplanetary dust grains are often very fragile and fluffy (Fig. 1.2). Sometimes so fragile that they disintegrate into a large number of fragments when they impact a collector surface.

The interplanetary dust grains are sometimes very rich in carbon. But, they are usually composed of submicrometer mineral grains (hydrous or anhydrous), and some grains contain glassy modules, called interstellar silicates. There are many grains that appear to contain abundant pre-solar molecular cloud material, marked by traces of isotopic anomalies in H and N [Messenger, 2000]. Objects in interplanetary space are exposed to the continously expanding solar corona, called solar wind [e.g. Lanzerotti, 1987] which contains mostly electrons and 1 keV protons at 1 AU distance. Heavier species as helium ions are also present [Formisano and Moreno, 1971].

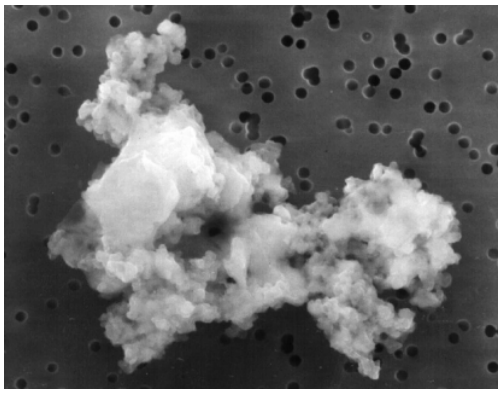


Figure 1.2: Fluffy interplanetary dust particle collected in the stratosphere of the Earth. Adopted from http://sci.esa.int/herschel/50256-a-fluffy-aggregate-of-dust-grains/.

The solar wind flux is of the order of $2 \cdot 10^{12}$ particles $\cdot \mathrm{m}^{-2}\mathrm{s}^{-1}$ at ≈ 1 AU and corresponds to a number density of ions (and electrons) of 3 to 10 cm^{-3} [Schwenn, 2001]. Positive ions and electrons of the solar wind add up to a quasineutral plasma. The solar wind flux decreases with the solar distance r from a point source as $\sim 1/r^2$. The typical plasma temperature is $\approx 10^5$ K at 1 AU and decreases with increasing distance from the Sun [Schwenn, 2001].

The solar wind flux is accompanied by high-energy particles associated with active solar regions, very energetic particles produced in solar flares, and galactic cosmic-ray particles [Vilmer, 2012]. A typical large flare event has a total fluence of protons with energies greater than 10 MeV of the order of 10^{14} particles $\cdot \mathrm{m}^{-2}$ [Goswami *et al.*, 1988]. The average flux of these energetic particles is four orders

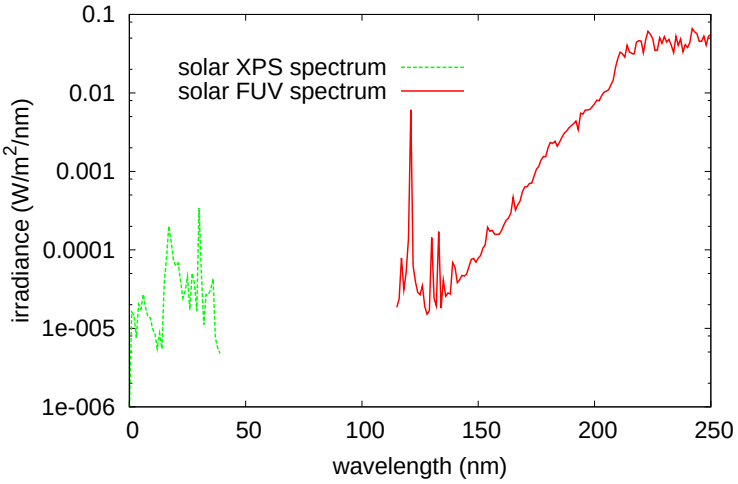


Figure 1.3: Solar spectrum measured by the SORCE spacecraft. Data dopted from SORCE spacecraft website: http://lasp.colorado.edu/home/sorce/data/.

of magnitude lower than the solar wind flux. Besides the solar wind particles, the grains are exposed to a background cosmic-ray particles in the interplanetary as well as in the interstellar medium [Simpson, 1983]. The energy of the cosmic-ray background is primarily contained in the energetic ions with smaller fractions carried by γ-rays and electrons.

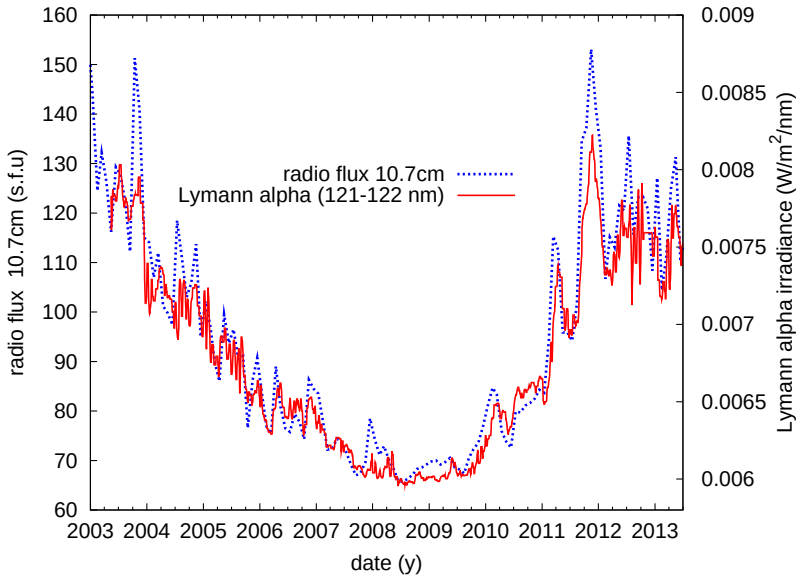


Figure 1.4: Variation of Lymann-α line irradiance with solar cycle and its comparison with radio flux 10.7 cm.

Our Sun produces both the UV and EUV radiations. The solar spectrum consists of continous radiation with a strong Lymann-α line 121.5 nm (10.2 eV) (Fig. 1.3). The instensity of the Lymann-α line varies with 11 year period of solar cycle (Fig. 1.4). These variations have strong corellation with the F10.7 index that is available from ground based measurements (Fig. 1.4). The solar Lyman-α flux is by a factor of 10^3 higher than the solar-wind flux, but the total energy flux exceeds it only by about a factor of 10.

1.2 Cometary Comae

The origin of life on the Earth is still mysterious. Some scientists believe and try to find more and more evidence that material created in the space and delivered to the Earth by comet and meteor impacts could bring or boost the start of life on the Earth. Some meteorites and comets bring molecules from far and unknown parts of the universe [Oró *et al.*, 2006; Chyba and McDonald, 1995]. These molecules can be used as building blocks for creating of certain kinds of larger molecules critical for life [Oró, 1961; Hoyle and Wickramasinghe, 1981; Anders, 1989; Huebner and Boice, 1992]. Anyway, there are still no direct evidence for these suggestions.

Comets are small, very fragile and irregularly shaped bodies composed of a mixture of non-volatile components and frozen gases. They usually have highly elliptical orbits that bring them very close to the Sun and swing them deeply into the space. The comet structures are diverse and very dynamic, but they always develop a surrounding cloud of diffuse material, called a coma, which usually grows in size and brightness as the comet approaches the Sun. As comets get close to the Sun, their tails of luminous material extend from the head for millions of kilometres in the anti-sunward direction.

When the comet is far from the Sun, the nucleus is cold and its material is frozen. When it approaches the Sun, at a few AU, the surface of the nucleus starts to warm up, and the volatiles evaporate. The evaporated molecules boil off and carry out small solid grains and forms the comet's gas and dust coma.

The force caused by radiation pressure of the Sun and the solar wind accelerate cometary material away at different velocities according to the size and mass of released objects. Thus, massive dust is accelerated slowly and its tail tends to be curved. The ion tail is lighter, and it appears as a nearly straight line extending away from the comet's head.



Figure 1.5: Hale-Bopp comet with its two distinct tails. Adopted from https://www2.jpl.nasa.gov/comet/gif/candy5.jpg.

Fig. 1.5 shows a view of the Hale-Bopp comet with two distinct tails. The thin blue plasma tail is made of gases and the broad white tail is made of macroscopic dust grains.

The Hale-Bopp comet is the unique example of the comet which has more than two distinct tails of dust and gases. A sodium tail very well separated from the dust and the ion tails was discovered [Cremonese *et al.*, 1997a; Wilson *et al.*, 1998]. An accurate analysis of the measured data revealed that the comet Hale-Bopp had two distinct sodium tails with a completely different morphologies called narrow and diffuse sodium tail [Cremonese *et al.*, 1997b; Cremonese and Fulle, 1997]. The first one is characterized by fast atoms coming directly from the comet. The second one is superimposed on the dust tail. More information about the sizes and composition of cometary dust particles provided Vega and Giotto spacecrafts. Vega 1 and Vega 2 carried the

dust impact mass analyser (PUMA) which provided the first direct mesurements of chemical and physical properties of dust originated from Halley comet. It was found that grains of mass $< 10^{-14}$g are more abundant than it was predicted by models and they are rich with light elementes such as H, C, N, and O (called as CHON material) [Sagdeev, 1989; Kissel *et al.*, 1986]. Models of comet Halley dust coma developed for the Giotto mission [Reinhard, 1997; Divine, 1981; Hellmich and Keller, 1981] have ignored grains $< 0.3\,\mu$m, despite cometary evidence and direct detection of grains $< 0.1\,\mu$m in meteor streams [Singer and Stanley, 1980]. The grain composition may be partly silicaceous [Ney, 1977], but high ratios of radiation pressure to gravitation force imply presence of conducting materials like iron, magnetite or graphite [Koutchmy and Lamy, 1978]. The presence of carbonaceous grains was confirmed by analysis of PUMA results [Fomenkova and Sherwood, 1994]. Besides CHON rich dust, the rock-forming elements Mg, Si, and Fe were the second most abundant dust type [McDonnell *et al.*, 1991; Schulze *et al.*, 1997; Jessberger, 1998]. The complex organic material have been also found [Fomenkova and Sherwood, 1994; Fomenkova, 1998]. Typical parameters of a dust-laden plasma inside and outside the ionopause (a plasma boundary which separates the region of smoothly/cold outward flowing cometary ions) of Halley's comet are shown in Tab. 1.1.

Halley's Comet	$n_e(cm^{-3})$	$T_e(K)$	$n_d(cm^{-3})$	$r_d(\mu m)$
inside ionopause	$10^3 - 10^4$	$< 10^3$	10^{-3}	$0.1 - 10$
outside ionopause	$10^2 - 10^3$	$\approx 10^4$	$5 \cdot 10^{-9} - 10^{-7}$	$0.01 - 10$

Table 1.1: Typical parameters of a dusty plasma inside and outside the Halley's Comet ionopause (data adopted from Mendis *et al.* [1985] and de Angelis *et al.* [1988]).

One of the most ambitious projects focused on collection of dust samples from the coma of comet Wild 2 was the project Stardust [Tsou *et al.*, 2003]. The primary mission was successfully completed when the collected dust samples in the capsule filled with the aerogel blocks returned onto the parachute to Earth in January 2006. In the clean area, the sealed cover was opened and investigation of the collected particles under the microscope begun. The individual optical images of particles with surroundig aerogel (Fig. 1.6) provided information about the aerogel compresion, molting and desintegration of particles during the impact as the particle propageted through. The different types of tracks were left in aerogel (Fig. 1.7), their shape and length carried information about the size, weakness, and initial energy of impacted particles [Burchell *et al.*, 2008]. The slices of a single grain placed under the transmission electron microscope (TEM) [Leroux *et al.*, 2008] with combination of electron energy loss (EELS), TOF-SIMS analysis [Stephan *et al.*, 2008a,b] and X-ray analysis [Nakamura *et al.*, 2008] provided information about the size, shape, and volume composition of the investigated particle. Isotopic analysis revealed heterogenity of grains consistent with the Cl meteorite composition [Stephan *et al.*, 2008a]. The Cu, Zn, and Ga appear to be the most aboundand elements of the Wild 2 material [Flynn *et al.*, 2006]. The organic components were also found [Sandford *et al.*, 2006].



Figure 1.6: Optical image of dust grain surrounded by aerogel. Adopted from https://stardust.jpl.nasa.gov/news/status/060512.html.

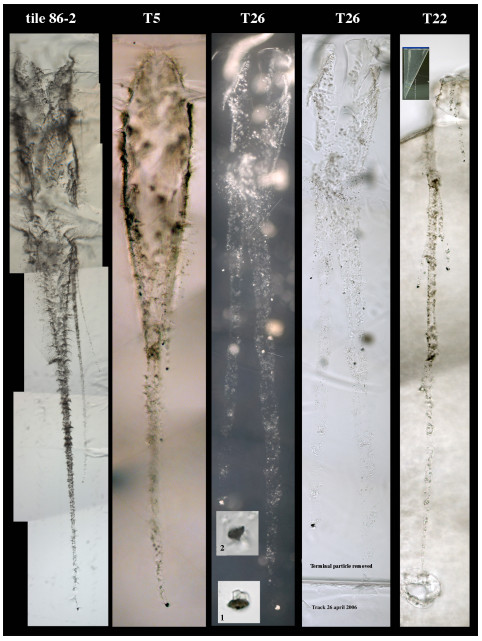


Figure 1.7: Different tracks of grains in the aerogel. Adopted from https://stardust.jpl.nasa.gov/news/status/060512.html.

1.3 The Earth's upper atmosphere

The polar summer mesopause is located between 80 and 90 km of altitude and it is the most important part of our Earth's environment from dust point of view because charged dust particles were observed there [Cho and Kelley, 1993; Havnes *et al.*, 1996a]. The most significant phenomenon is the formation of a special type of clouds known as "noctilucent clouds" (NLCs), first time reported in 1885 [Backhouse, 1885].

During the rocket launches in years 1957–1958, interesting peculiarity of the polar mesopause was revealed: it was much colder in the summer than in the winter [Stroud *et al.*, 1959]. This observation supported speculations that the NLCs were composed of ice that was formed at extremely low temperatures (even below 110 K) [von Zahn and Meyer, 1989]. Other important phenomena known as the polar mesospheric summer echoes (PMSE) and observed as strong radar backscatter at VHF frequencies [Balsley *et al.*, 1983; Hoppe *et al.*, 1988, 1990] can be also found there. The electron depletion and positive ion enhancement layers exist at the heights of the PMSE [Ulwick *et al.*, 1988; Thomas, 1991; Cho and Kelley, 1993].

Some theories explain the PMSE and the electron depletion by presence of heavy ion clusters or highly positively charged dust particles [Kelley, 1987]. The total charge density on dust surface is significant compared to the electron or ion component [Havnes *et al.*, 1990a; Reid, 1990]. The collection of plasma particles charges dust slightly negative (typically a few unit charges or less). A high charge on a dust particle can be reached only if the dust is subject of photoemission, but it can happen only occasionally for pure ice with its high photoelectric workfunction [Baron *et al.*, 1978]. On the other hand, the smallness of the dust particles and

possible surface impurities (e.g., meteoric dust) may lead to high photoelectric yields and low work functions [Gail and Sedlmayr, 1980; Schmidt-Ott *et al.*, 1980; Burtscher *et al.*, 1984]. Typical parameters of dust-laden plasmas in NLCs are $n_e \approx 10^3\,cm^{-3}$, $T_e \approx 150\,K$, $n_d \approx 10 - 10^3\,cm^{-3}$, $r_d \approx 0.1\,\mu m$, $n_n \approx 10^{14}\,cm^{-3}$ (subscript n refers to neutral gas) [Mendis, 1996].

The most significant source of dust in the Earth's atmosphere is manmade pollution (terrestrial aerosols). One of the sources are high flying aircrafts, rocket and space shuttle exhausts [Bernhardt *et al.*, 1995].

The basic properties (such as constituents, size, density, etc.) of dust grains in our Earth's surroundings provided recent balloon and aircraft collections (see Tab. 1.2). The parameters of the plasma and dust particles depend on the situation we consider. The characteristic properties of the plasma and dust in rocket exhausts and flames are shown in Tab. 1.3.

Origin	Composition	Radius(μm)	Density(cm^{-3})
Shuttle exhausts	dirty ice	$5 \cdot 10^{-3}$	$3 \cdot 10^4$
Terrestrial aerosol	Al_2O_3 spheroid	$0.1 - 10$	$10^{-10} - 10^{-6}$
Micrometeoroid	60% chondritic 30% iron-sulphur-nickel 10% silicates (olivine)	5-10	$10^{-10} - 10^{-9}$
Industrial contamination	magnetite spherules	~ 10	$\sim 10^{-5}$

Table 1.2: Typical parameters of the dust in the Earth's surroundings (adopted from [de Angelis, 1992]).

	$n_e(cm^{-3})$	$T_e(K)$	$n_d(cm^{-3})$	$r_d(\mu m)$
Rocket Exhausts	10^{13}	3500	$3 \cdot 10^8$	0.5
Flames	10^{12}	2300	10^{11}	0.01

Table 1.3: Typical parameters of the dust and plasma of rocket exhausts and flames (data adopted from Mendis [1996]).

1.4 Lunar plasma environment

The surface of the Moon is composed of rocks and lunar regolith, which has been formed during long period of meteoroid impacts. The size of the regolith grains ranges from centimeters to submicrons [Heiken *et al.*, 1991]. The finest grains covering the lunar surface are called a lunar dust or simply dust. Dust on the day side of the Moon is exposed to solar wind particles and photons from the Sun, which cause its charging (Fig. 1.8).

The photoemission is dominant charging process on the day side of the Moon and charge its surface to positive potential about +10 V [Freeman and Ibrahim, 1975; Manka, 1973]. The UV flux from the Sun is dominated by strong Lymann alpha line. On the dark side of the Moon, the solar wind electrons are collected

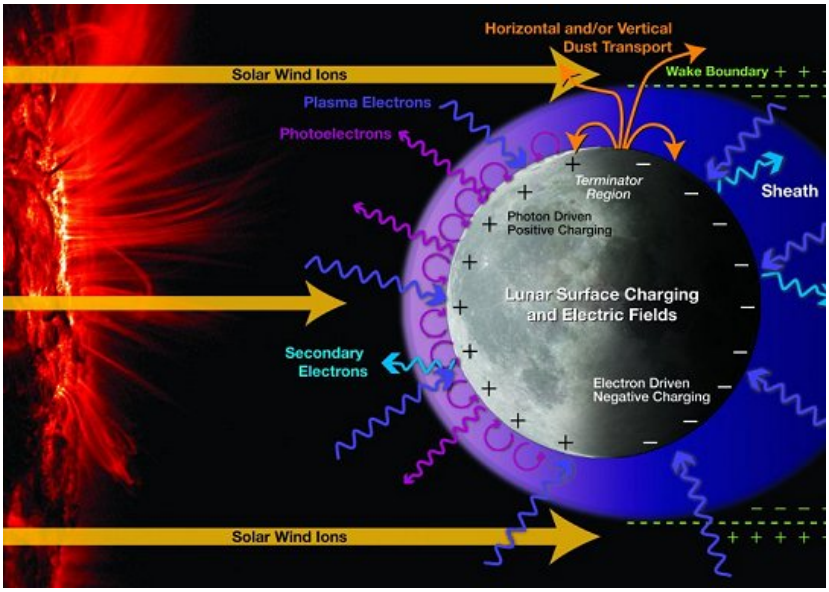


Figure 1.8: Solar wind interaction with the Moon. Credit: Jasper Halekas and Greg Delory of U.C. Berkeley, and Bill Farrell and Tim Stubbs of the Goddard Space Flight Center.

and charge the Moon surface to negative potential of the order of –100 V [Halekas *et al.*, 2005]. The Moon spends most of its trajectory in solar wind but also part of the trajectory goes through Earth magnetosphere, plasma sheet and lobes [Hapgood, 2007]. The plasma parameters can rapidly change during crossing these regions [Vaverka *et al.*, 2016]. The UV gradient across the solar terminator (the boundary between day and night sides of the Moon) or Moon crossing of different plasma regions may form clouds of electrostatically charged dust, which can be set into motion as the terminator moves.

Besides charging, the solar wind protons are implanted into the lunar regolith and form neutral atoms and molecules of hydrogen or compounds that contain hydrogen [Starukhina, 2001]. The absorbed solar wind protons can be chemically bonded to atoms of the lunar regolith, particularly with oxygen atoms and they can form hydroxyl groups [Zeller *et al.*, 1966].

1.4.1 Lunar dust motion due to interaction with plasma

Dust levitation and transport above a lunar surface was indicated on the images taken by the Surveyor landers [Rennilson and Criwsell, 1974], by the visual observations made by the Apollo 17 crew [Zook and McCoy, 1991] and by the *in-situ* measurements of the Lunar Ejecta and Meteorite Experiment (LEAM) [Berg *et al.*, 1975]. Hovewer, the recent detailed analysis of the Apollo 17 LEAM data by Grün and Horányi [2013] has shown that their interpretation is uncorrect and it is caused by degradation of the instrument due to exposion to strong variations of the lunar environment at the terminator region.

The lift-off and transport of the lunar dust can be triggered by incoming interplanetary dust. However, the available data indicates that a magnitude of dust lift-off rate is many orders higher than expected. Alternative explanation involves dust charging and electrostatic forces [Rennilson and Criwsell, 1974].

Several models have been developed to describe the mobility of dust particles in a plasma environment above a lunar surface [Singer and Walker, 1962; Criswell, 1973; Nitter and Havnes, 1992; Nitter *et al.*, 1994, 1998; Stubbs *et al.*, 2006; Borisov and Mall, 2006]. However, none of them provide a satisfactory explanation for the initial lift-off of dust grains. It has been suggested that time dependent charging at the terminator region may lead to the lift-off [Criswell and De, 1977b,a; Pelizzari and Criswell, 1978].

The fundamental problem of this suggestion is the fact that only a very small fraction of dust grains can carry even a single elementary charge. Thus, strong vertical electric fields are needed to overcome gravity, and probably even more important adhesive and cohesive forces [Hartzell *et al.*, 2013].

The calculations of Sternovsky *et al.* [2008] have shown that the solar activity can significantly change the conditions for lunar dust transport. The dust activity increases with increasing photoemission faster than linearly due to change of both the charge on the dust and the electric field. The highest dust activity is expected during solar flares. It is further expected that dust mobilization will be the stronger across terminator where positively and negatively charged surfaces are adjacent to each other which allows to create a much stronger electric field [Wang *et al.*, 2007].

Not only the photoemission can influence the dust mobilization. The properly determined photoemission parameters of the grain like photoelectron yield and work function and variations of these parameters with photon energy and properties of the grain (shape, roughnes of the surface, composition) can be also important for determination of the electric field necessary for the dust transport.

Laboratory measurements of the photoemission for satellite and lunar surface materials [Feuerbacher and Fitton, 1972; Feuerbacher *et al.*, 1972] have shown the variation of the photoelectric yield of soil samples returned by the Apollo 14 and 15 missions [Feuerbacher *et al.*, 1972; Willis *et al.*, 1973] with energy of incident photons and found its maximum as 0.07 e/ph for wavelength 90 nm (14 eV). The relatively low value of the photoelectron yield was attributed to the granulated form of the soil sample rather than to its chemical composition. Due to the roughness of the surface a large fraction of the emitted electrons can be quickly recaptured and the photoelectron yield is reduced.

However, experiments pertaining to isolated dust charging and interactions between planetary dust analogs and plasma particles or UV are rare [Horányi *et al.*, 1998; Abbas *et al.*, 2006; Sickafoose *et al.*, 2000].

The unique experimental setup with linear electrodynamic trap presented in this thesis allows studies of interaction of single dust grain with plasma particles and UV photons. The first experimental results of photoemission measurements of MLS-1 (Minnesota Lunar Simulant 1), particularly determination of its work-function, are introduced.

1.5 Planetary rings

It is well known that most of the rings of the outer giant planets (such as Jupiter, Saturn, Uranus, Neptune) are populated by dust grains from microns to meters in size. Generally, the grains of planetary rings are in general similar to their nearby moons. Saturn's rings are predominantly populated by water ice and Jupiter's rings are derived from nearby moons. Below, we provide a brief description about the investigation, behaviour, and origin of dust particles in Jupiter's and Saturn's planetary ring systems.

1.5.1 Jupiter's ring system

The faint ring system of Jupiter was discovered by Voyager 1 [Smith *et al.*, 1979b] by taking a single image (Fig. 1.9). A more complete set of images were taken by Voyager 2 [Smith *et al.*, 1979a]. Jupiter's rings have three major components, namely the main ring, the halo, and the gossamer ring. The outermost (gossamer) Jupiter's ring is actually two rings circumscribed by the orbits of the Amalthea and Thebe. The Galileo data clearly shown that the gossamer rings are generated by these two moons.



Figure 1.9: Jupiter with its great red spot observed by Voyger. Adopted from https://voyager.jpl.nasa.gov/galleries/images-voyager-took/jupiter/.

The main ring is about 7000 km wide and has an abrupt outer boundary about 129 000 km from the centre of the planet [Showalter *et al.*, 1987]. The main ring encompasses the orbits of two small moons, Adrastea and Metis, which act as the source of dust for the ring.

The narrow collimated quasi-periodic high-speed streams of fine dust grains ejected from Jupiter were observed by the dust detector on board the Ulysses spacecraft [Hamilton and Burns, 1993; Grün *et al.*, 1992]. The approximately monthly periodicity (28 $\pm$ 3 days) [Grün *et al.*, 1993] suggests that all streams are derived from a single source. Many different origins of this source were suggested like different dusty regions (main ring, halo, and the gossamer rings) [Burns *et al.*, 1980; Hamilton and Burns, 1993] or volcanoes on one of the Jovian moon Io [Johnson *et al.*, 1980; Morfill *et al.*, 1980]. Horányi *et al.* [1993b] proposed a model in which electromagnetic forces within the Jupiter's magnetosphere can accelerate and eject small dust particles. The Io moon was proposed as a source of the dust and the observed stream periodicity arised from resonance between the orbital and rotational periods of Io and Jupiter respectively [Horányi *et al.*, 1993a].

The chemical composition of Jovian dust stream grains was establish much later, when Cassini with its CDA detector (Cosmic Dust Analyser) made the swingby manoeuvre around Jupiter at the distance more than 1 AU on its way

to Saturn. Sodium, chlorine, sulphur, and potassium were identified as grain components. Sodium chloride was a main constituent of detected Jovian dust in contrary to observations of gas components in the atmosphere of Io, where the sulphur is dominant, while alkali and halogen species are minor components [Postberg *et al.*, 2006].

1.5.2 Saturn's ring system

The rings of Saturn have puzzled astronomers since they were first discovered by Galileo in 1610 using his first telescope [Whitehouse, 2009]. The puzzles have only significantly increased since Voyagers 1 [Synnott *et al.*, 1981] and 2 [Smith *et al.*, 1982] imaged the ring system extensively in 1980 and 1981.

The Voyager 1 planetary radio-astronomy (PRA) and plasma-wave subsystem (PWS) *in-situ* measurements were first in which were identified dust impacts from their characteristic electromagnetic signatures during the flyby of the spacecraft around the E ring in 1980 [Gurnett *et al.*, 1983; Meyer-Vernet *et al.*, 1996].

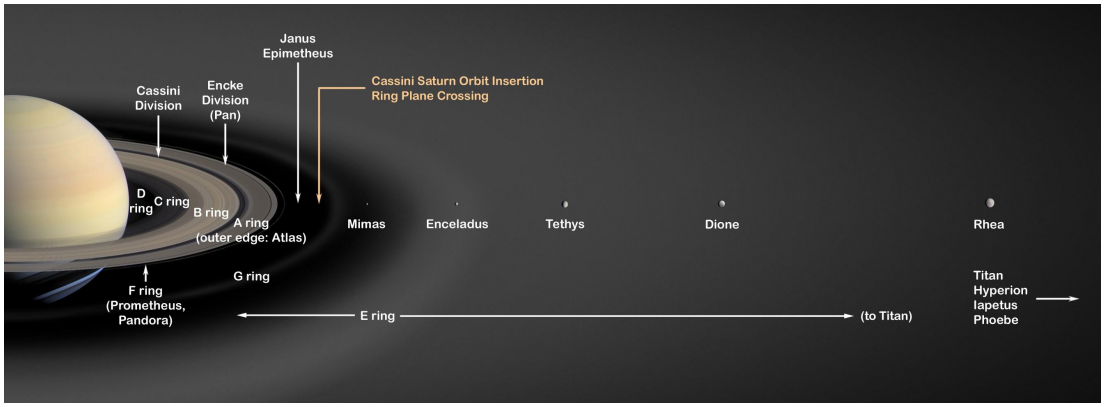


Figure 1.10: Overview of letters of Saturn rings. Adopted from https://en.wikipedia.org/wiki/Rings_of_Saturn.

The interpretation of *in-situ* observations was difficult because the recorded signal was not only produced by the dust but also by the ambient plasma, the difference of their spectra provided a tool for separation of dust and plasma effects [Aubier *et al.*, 1983].

The letter names have been given to the rings in the order of their discovery (Fig. 1.10). The main rings (from the outward direction) are known as C, B, and A. The Cassini Division is the largest gap in the rings and separates the rings B and A. Also a number of fainter rings has been discovered. The D ring is exceedingly faint and closest to the planet.

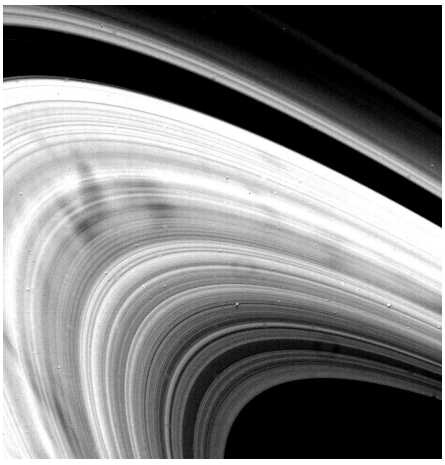


Figure 1.11: Spoke pattern observed by Voyager. Adopted from https://photojournal.jpl.nasa.gov/catalog/PIA02275.

The F ring is narrow and just outside the A ring. There are two other far fainter rings named G and E. The dust grains in Saturn's rings are composed primarily of water-ice and range from microns to meters in size [Cuzzi *et al.*, 1984]. One of the most interesting features observed in the Saturn's ring system by both Voyager 1 and 2 was the nearly radial spokes [Synnott *et al.*, 1981; Smith *et al.*, 1982], which were possibly noticed earlier in ground-based observations [Robinson, 1980].

The spokes are confined in the dense central B ring with the inner edge at about 1.52 and the outer edge at about 1.95 of the Saturn radius. They have their inner ring boundary at ≈1.72 of Saturn radius and an outer boundary at approximately the outer edge of the B ring [Hill and Mendis, 1982]. A typical spoke pattern is seen in Fig. 1.11. The spokes exhibit a characteristic wedge shape. Numerous formation theories were proposed to explain the spokes existence. According to predictions, the Cassini spacecraft would detected spokes at the arrival to Saturn in 2004. However, contrary to predictions Cassini didn't observe spokes, until September 2005. The variability in spoke observations has a seasonal effect and these seasonal variations can be a consequence of the variable plasma density near the ring (Fig. 1.12).

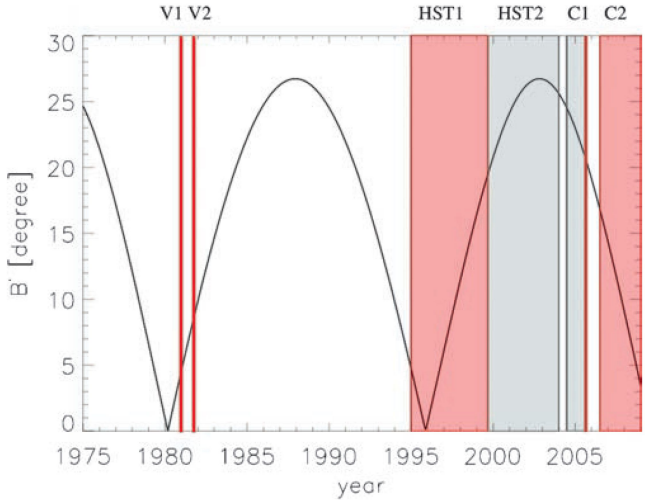


Figure 1.12: Variation of spokes with the solar elevation angle, B. Adopted from Dougherty *et al.* [2009].

The plasma density is a function of the solar elevation angle, B and it is generated mainly from the rings due to photoelectron production and ionization of neutrals by photo-sputtering [Farrell *et al.*, 2006; Mitchell *et al.*, 2006]. Another theories suggest a formation of Saturn's spokes by lightning-induced electron beams [Jones *et al.*, 2006]. The characteristics of dust and plasma varies from one ring to another. The dust and plasma characteristics of the E and F rings and the spokes of Saturn are shown in Tab. 1.4.

During cruise of the Cassini spacecraft to Saturn, the CDA instrument detected "stream" of tiny dust grains (less than 20 nm) coming from the ring system [Srama *et al.*, 2006; Kempf *et al.*, 2005a]. The grain were composed predominantly of oxygen, silicon, and iron [Kempf *et al.*, 2005b]. Because Saturn's main rings consisted primarily made of water-ice, stream grains are suspected to be the impurities in the water-ice ring material rather than the bulk composition of the grains themselves.

	$n_e(cm^{-3})$	$T_e(K)$	$n_d(cm^{-3})$	$r_d(\mu m)$
Saturn's F ring	$10 - 10^2$	$10^5 - 10^6$	< 30	< 1
Saturn's E ring	10	$10^5 - 10^6$	$10^{-7} - 10^{-8}$	~ 1
Saturn's spokes	$0.1 - 10^2$	$2 \cdot 10^4$	1	≤ 1

Table 1.4: Typical parameters of the dust and plasma in the F, and E Saturn's rings and its spokes (data adopted from Goertz [1989]).

During the flybys of the moon Enceladus, Cassini observed water ice geysers erupting from its south pole (Fig. 1.13) [Hansen *et al.*, 2006; Porco *et al.*, 2006; Spahn *et al.*, 2006]. This observation supports an idea that Enceladus can supply the dust into the Saturn's E ring [Hansen *et al.*, 2006; Spahn *et al.*, 2006; Kempf *et al.*, 2008, 2010]. The scientists started to suspect an existance of a pocket of liquid water near the surface of the moon that can be a source of eruptions driving the geysers plume.

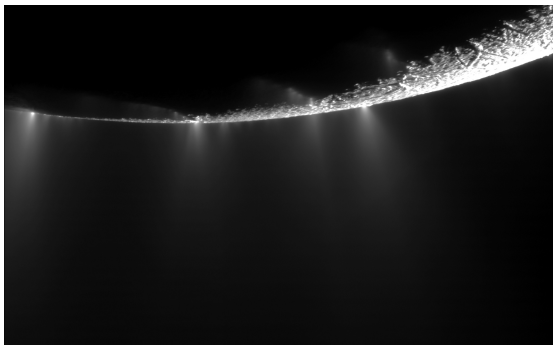


Figure 1.13: Enceladus plumes. Adopted from https://www.nasa.gov/mission_pages/cassini/multimedia/pia11688.html.

During the passing through the Enceladus plumes in 2008, the ion neutral mass spectrometer and ultraviolet imaging spectrograph on the spacecraft detected water, carbon dioxide and various hydrocarbons [Perry *et al.*, 2010; Teolis *et al.*, 2010; Hansen *et al.*, 2011; Waite *et al.*, 2006].

Due to the mapping of the surface features by infrared spectrometer, the much higher temperature than their surroundings was found. Throughout next flybys in another geometry, Cassini produced a detailed and high-resolution mosaic image of the southern pole of the moon with its "tiger stripes" (Fig. 1.14).



Figure 1.14: Tiger stripes on Enceladus. Adopted from https://saturn.jpl.nasa.gov/resources/4342/.

Almost after ten years, Cassini entered to the Saturn's orbit, and NASA reported an evidence about the presence of an internal global salty ocean between the surface icy crust and moon's rocky core [Patthoff and Kattenhorn, 2011; Thomas *et al.*, 2016]. This discovery put Enceladus between the most likely places to host alien microbial life in our solar system. To ensure protection and prevent biological contamination of the moons of Saturn,

the spacecraft finished its almost 20-year long journey by entering to the Saturn's atmosphere on 15th September 2017.

Saturn's E ring dynamics

Existing remote sensing and *in-situ* measurements indicate that the E ring is asymmetric in a peculiar way for reasons that are not yet understood [Showalter *et al.*, 1991]. The global structure of the E ring varies with the longitude relative to the Sun. It is more "compressed" at noon ansa and a fainter but more extended at midnight ansa. In other words, it has an egg-shaped structure with the blunt side facing to the Sun. In addition to the azimuthal asymmetry, the E ring is also not centered at the ring plane, except near the orbit of Enceladus at 3.95 R_s. For both the noon and midnight ansae, the ring inside the Enceladus' orbit is displaced southward and the ring outside 3.95 R_s is diplaced northward [Hamilton, 1993]. Some of the observed asymmetries can be comprehended by considering the effects of solar radiation pressure and the shadows created by the planet and the main rings [Hedman *et al.*, 2012]. Hovewer, current ring theories cannot explain features like the azimuthal brightness asymmetry between the noon and midnight ansae.

There are two key parameters needed for understanding of E ring asymmetries. The first is the orbital precession of ring grains [Horányi *et al.*, 1992]. Orbital precission rates depend on the grain properties (e.g., size, charge-to-mass ratio, efficiency in a response to the radiation pressure) and the conditions in the magnetosphere. The second is the recently discovered noon-to-midnight electric field [Wilson *et al.*, 2013; Andriopoulou *et al.*, 2014], which has a particular importance in driving of the E ring dynamical evolution.

The E ring asymmetries have been observed through both remote sensing observations and *in-situ* measurements by the CDA instrument. While the camera images convincingly demonstrated the day–night contrast, they cannot deliver the details of dust interactions with the magnetosphere. As opposed to remote sensing, *in-attitudesitu* measurements provide not only the E ring dust density profile but also its size distribution, which is crucial for understanding of the responsible processes. Unfortunately, the well-calibrated CDA measurements provide only a limited coverage. On the other hand, measurements by the Radio and Plasma Wave Science (RPWS) instrument, realized extensive coverage throughout the E ring while operated in a mode sensitive to dust particle impacts.

RPWS dust detection and data analysis

RPWS [Gurnett *et al.*, 2004] consists of three nearly orthogonal 10 m long, 2.5 cm diameter electric field antennas (E_U, E_V, E_W) and they act as large area "dust impact detectors". The E_U and E_V antennas are often used together in a dipole configuration, whereas E_W is typically operated in a monopole mode, measuring the voltage relative to the spacecraft (SC) body. Hypervelocity impacts of dust grains on the antenna and/or spacecraft surfaces generate expanding plasma clouds that can be (partially) recollected to generate transient voltage signals detectable by antenna instruments, such as RPWS [Scarf *et al.*, 1982; Aubier *et al.*, 1983; Meyer-Vernet, 1986; Wang *et al.*, 2006; Zaslavsky *et al.*, 2012; Malaspina *et al.*, 2014; Andersson *et al.*, 2015; Ye *et al.*, 2014, 2016; Kellogg *et al.*,

2016]. Dust detection by RPWS is minimally limited by the spacecraft attitude and thus can provide continuous measurements with a good temporal/spatial coverage. The antennas are connected to a set of receivers, yielding two types of measurements: power spectra and waveform captures [Gurnett *et al.*, 2004]. Individual dust impact pulses are best recognized in the waveforms, while the power spectrum has been used to estimate the average size/mass in regions with high dust impact rates. Three different types of RPWS data can be used for the E ring dynamic study:

1. Dust flux and size distribution based on individual dust impact signal waveforms. The analysis of waveforms provides information about each impact event and can be used to derive the size distribution and flux. The local dust density is derived for the relative spacecraft-dust velocity.

2. Integrated dust-mass flux based on the voltage power spectra density. The power spectrum calculated from RPWS data can be turned into a relevant observable, based on the works of Aubier *et al.* [1983] and Meyer-Vernet [1986].

3. Dust count rates from the onboard dust detection algorithm. When WBR (Wide Band Receiver) is not scheduled to capture high-resolution data, the onboard dust detection function is enabled to provide dust counts with a time resolution of 64 seconds [Gurnett *et al.*, 2004].

The laboratory capability to simulate the response of RPWS to dust impacts allows calibration measurements using a scaled down model of the Cassini spacecraft (SC). The laboratory effort can deliver needed insight into the generation of impact signal and its dependence on the impact speed/location, SC potential, and other parameters of interest.

Now we could see importance of the processes of interaction of the plasma particles and solar radiation with dust in formation of our interplanetary medium, especially environments like the Moon, planetary rings, comets, and Earth magnetosphere. In next two sections, we focus on elementary charging processes of dust grains and on their creation and destruction due to various physical processes presented in mentioned environments. The last two sections behind the goals of the work are devoted to investigations of the photoemission of dust in the linear electrodynamic trap and to studies of dust impacts from antenna signals on a scaled down model of the Cassini spacecraft. Both chapters are accompanied with the discussion of obtained results.

Chapter 2

Charging of dust grains

Objects in space are exposed to plasma particles and struck by ultraviolet photons. Net current then determines resulting charge of an object (e.g., dust or spacecraft). The precise charging history of dust grains depends on it's properties (material, size, shape [Richterová *et al.*, 2012] and surface character [Pavlů *et al.*, 2006a]) and on the ambient plasma (plasma composition, density, and temperature, and photon flux). Because the charging by any process does not occur instantaneously, but varies according to the different grain's charging history, rarely more than one charge equilibrium state exists [Meyer-Vernet, 1982].

The collection of plasma ions and electrons is not the only possible charging mechanism. Electrons can also be emitted from the grain surface due to thermionic, photoelectron, and secondary electron emission processes. These processes are important for dust charging in the upper atmosphere, in interplanetary space [Whipple, 1981; Mendis, 2002], and in some laboratory experiments, for instance, in thermal plasmas [Fortov *et al.*, 1996a,b], or in plasmas induced by UV irradiation [Fortov *et al.*, 1998], with photoelectric charging of particles [Sickafoose *et al.*, 2000], and with charging by electron beams [Walch *et al.*, 1995].

In contrast to the situation when the plasma electrons are collected and the grain charge is negative, the emission of electrons charges the grain positively and, under certain conditions (e.g., if primary electrons are energetic enough to release secondary electrons or if grain is irradiated by UV photons), can result in an overall positive charge.

Due to emission processes mentioned above, always two-component systems of dust and emitted electrons coexist. Such a system serves as the simplest model for investigations of different processes associated with emission of charged particles [Yakubov and Khrapak, 1989; Khrapak *et al.*, 1999].

The equilibrium potential (charge) of the grain is determined by a balance of the fluxes that are collected by the grain surface and emitted from it. The dust equilibrium electrical charge, Q for Maxwellian distributions of plasma components was calculated by many authors [Northrop, 1992; Mendis and Rosenberg, 1994; Schaffer and Burns, 1995; Horányi, 1996]. In following sections, we will briefly describe emission processes listed above from isolated dust grain.

2.1 Charging of isolated dust grains

There is a considerable number of processes which can contribute to the charging of dust grains. The time evolution of the dust charge, Q can be expressed according to the equation

$$\frac{dQ}{dt} = \sum_k I_k \,, \tag{2.1}$$

where particular charging mechanism produces a current I_k across the grain's boundary and this current I_k is a function of the grain properties and plasma conditions. In our Solar System, the most dominant charging currents are: plasma electron (I_e) and ion (I_i) collection and photoelectric effect (I_{ph}). We note that the processes as a production of secondary electrons (I_{sec}) due to a high energy of plasma particles or the thermionic effect (I_{th}) for heated grains play a minor role in dust charging. The dust charge is related to the surface potential, φ_s of the grain as

$$Q = C\varphi_s \,, \tag{2.2}$$

where C is the capacitance of the grain in the plasma. For a spherical grain with radius R satisfying $\mathrm{R} \ll \lambda_\mathrm{D}$ [Whipple, 1981], the capacitance is

$$C = 4\pi\varepsilon_0 R \,. \tag{2.3}$$

There is also process which can limit those above. Once the dust grain possesses large charge (i.e., high surface potential φ_s and correspondingly strong electric field), the field emission prevents its further charging [Müller and Tsong, 1969; Draine and Salpeter, 1979a]. The equilibrium value of the grain's surface potential is established when net current becomes to zero ($dQ/dt = 0$ in eq. 2.1).

2.2 Ion and electron collections

The basic charging model of a isolated grain immersed in the plasma is based on the "orbital-motion limited" (OML) theory. The total current I_α caused by plasma particles species α with a polar velocity distribution $f_\alpha(\omega, \varphi, \theta)$ that is symmetric in θ is given by

$$I_\alpha = 2\pi Z_\alpha e \int_{\omega_1}^{\infty} \int_0^{\pi/2} S_\alpha \cdot \sigma_\alpha(\omega) f_\alpha(\omega, \varphi) \omega^3 \sin\varphi \, d\varphi \, d\omega \,, \tag{2.4}$$

where S_α is a sticking coefficient (usually assumed as $S_\alpha = 1$) and $\sigma_\alpha(\omega)$ is a physical cross section for plasma particles with velocity ω. The simplest case is when f_α is Maxwellian [e.g., Whipple, 1981]. For Maxwellian distributions of electrons and ions characterized by temperatures T_e and T_i the particle currents are [Whipple, 1981]:

$$I_e = I_{oe} \exp(e\varphi_s / k_b T_e) \qquad \varphi_s < 0 \tag{2.5}$$

$$I_e = I_{oe}(1 + e\varphi_s / k_b T_e) \qquad \varphi_s > 0 \tag{2.6}$$

$$I_i = I_{oi} \exp(-z_i e\varphi_s / k_b T_e) \qquad \varphi_s > 0 \tag{2.7}$$

$$I_i = I_{oi}(1 - z_i e\varphi_s / k_b T_e) \qquad \varphi_s < 0 \,, \tag{2.8}$$

where z_i is the electronic charge of the ions and coefficents I_{oe}, I_{oi} describes currents for $\varphi_s = 0$. If the drift velocity is much smaller than the thermal velocities, the coefficients can be simplified to

$$I_{o\alpha} = 4\pi a^2 n_\alpha q_\alpha (kT_\alpha / 2\pi m_\alpha)^{1/2} \,, \tag{2.9}$$

where n_α is the number density, q_α the charge, T_α the temperature, and m_α the mass of the plasma species. The negative equilibrium potential, φ_s (floating potential) for collecting of plasma electrons and ions is according to eq. 2.1

$$I_{oe} \exp(e\varphi_s / k_b T_e) - I_{oi} \exp(1 - z_i e\varphi_s / k_b T_i) = 0. \tag{2.10}$$

The solution is

$$\varphi_s = K_\varphi T_e \,, \tag{2.11}$$

where coefficient $K_\varphi = K_\varphi(T_e/T_i, m_i/m_e)$ can be find numerically.

The potential φ_s generally ranges from –10 V to +10 V. The largest negative potentials are achieved at high plasma temperatures and for sufficiently high n_e ($I_e \gg I_{ph}$). The equilibrium surface potential, φ_s when the charging is by plasma attachment only is possible to find using the Spitzer's formula [Spitzer, 2004]

$$\varphi_s = -\beta \frac{kT_e}{e} \,, \tag{2.12}$$

where the parameter β changes according to plasma ion type, H^+, O^+, S^+, and S^{++}, respectively and reach the values of (2.5, 3.6, 3.9, and 3.4) [Havnes *et al.*, 1990].

The charging time constant of an uncharged grain to reach an equilibrium value is proportional to the temperature of electrons T_e, grain radius, R and plasma density, n

$$\tau = K_\tau \frac{T_e^{1/2}}{Rn} \,, \tag{2.13}$$

where the coefficient $K_\tau = K_\tau(T_i/T_e, m_i/m_e)$ can be determined again by numerical calculations [Chunshi and Goree, 1994].

2.3 Secondary electron emission

The secondary electron emission is the process where energetic primary plasma particles hitting a surface cause a release of secondary electrons. The process can occur due to both electron or ion impacts.

2.3.1 Electron impact

The electron approaches the dust grain surface and follows one of the scenarios: (1) it is reflected from the surface, (2) it enters the grain and stops inside, or (3) it enters the dust grain, loses a part of the kinetic energy and then leaves the grain. The lost energy goes into exciting electrons of the dust material. If the gained energy is high enough, electrons can escape from the grain.

The secondary electron emission can lead to either positive or negative charge of the dust grain. The charge polarity depends on the energy of incident electrons.

The process can lead to high values of the charge for high energies (20 keV) of primary electrons, as found Švestka *et al.* [1993], while low energies (< 50 eV) often result in the negative charge. The parameter describing the process is the total secondary emission yield, σ defined as a sum of backscattered electrons η and true secondary electrons δ

$$\sigma = \delta + \eta \,. \tag{2.14}$$

The yield of "true secondary emission" is defined as the ratio of emitted secondary electrons to primary electrons, while the backscattered electron yield is the ratio of reflected plus escaped electrons to primary electrons. The grain is charged positively when $\sigma > 1$. The well known Sternglass formula is often used for a description of the secondary emission yield [Sternglass, 1954; Jonker, 1952]

$$\frac{\sigma}{\sigma_{max}} = \frac{E}{E_{max}} \exp\left(2 - 2\sqrt{\frac{E}{E_{max}}}\right) , \tag{2.15}$$

where E is the energy of primary electrons, $\mathrm{E_{max}}$ is the energy of maximum of the yield, σ_{max}. It works well for large planar samples, where the electrons are assumed to escape only from one surface side (the side at which the primary electrons enter). For micron-sized dust grains the secondary electrons are not limited to the point of incidence of primary electrons and may exit from the whole grain surface. Thus, the secondary emission yield for small dust grains is higher than that determined by the Sternglass formula [Chow *et al.*, 1994]. Chow *et al.* [1993] discussed the yield equation of Jonker [1952] theoretically but a satisfactory explanation provided yet a Monte-Carlo model of the secondary emission by Richterová *et al.* [2004]. This model takes into account properties of the dust grain which can affect the total yield of the secondary emission, namely the size and shape of the grains [Richterová *et al.*, 2012] or their formation to clusters [Richterová *et al.*, 2016].

2.3.2 Ion impact

The ion approaching to a dust grain surface with a low kinetic energy (below 1 keV) can be neutralized by the tunnelling electrons. The energy released during this process may be sufficient to excite additional electrons which can then be emitted from the surface.

The number of emitted electrons depends on the available potential energy after electron–ion neutralization. A maximum available energy is determined by the difference of the ionization potential energy, E_i and the work function, W_d of the material. The energy necessary to release another electron from the material is equal to work function, thus the condition for the secondary emission is $E_i - W_d > W_d$.

On the other hand, for the incident ions with energies above 10 keV, the secondary electron yields can be substantially larger than unity. Draine and Salpeter [1979b] showed that the emission due to such high-energy ions hitting the dust surface may be the same as that of the electrons.

The energetic ions may enter into the dust grain and stop immediately (i.e., stick on the surface) or may pass further and lose their energy during a passage through material. This energy can go into excitation of the electrons that may escape from the grain surface.

2.4 Electron and ion field emissions

The electron field emission from a dust grain surface occurs when its surface electric field is between 10^6 and 10^7 V/cm^{-1} [Whipple, 1981]. Because of smallness of dust grains, a relatively small dust charge can produce a large electric field on the grain surface. The surface electric field of a small spherical dust grain of a radius R is approximately φ_s/R, where φ_s is the surface potential. This means that the electron field emission is important for the dust grains of radii of the order of microns and smaller and can limit their charging.

Not only the emission of negative charges can limit the maximum attainable surface potential of the grain. The ion field emission plays a similar role when a high positive charge is reached. The emission of positive ions can be caused by three main processes: (1) field desorption, (2) field ionization, and (3) field evaporation [Good and Muller, 1956; Gomer, 1961; Jeřáb *et al.*, 2007].

In the case of field desorption, the atoms or molecules of an adsorbed gas are ionized in the strong electric field at the surface and subsequently desorbed by the repulsive electric force.

Field ionization is the process during that the atoms of a surrounding gas get ionized by a strong electric field close to the surface and after the ionization are repulsed away as ions.

Field evaporation is similar to the field desorption but the emitted ions originate in the grain material.

The importance of each of these processes in field ion emission depends on a contamination and type of the surrounding gas and also on the material of the grain surface and on the adsorbed layer [Pavlů *et al.*, 2006b; Jeřáb *et al.*, 2007]. It means that both electron and ion field emissions may set limits to the maximum attainable surface potential in space [Draine and Salpeter, 1979b].

According to the Fowler-Nordheim theory, the limiting surface potential for a conductive negatively charged dust grain with a radius of R (in unit of μm) [Mendis and Axford, 1974; Northrop, 1992] is

$$\varphi_s(V) \approx -10^3 R(\mu m)\,, \tag{2.16}$$

which is equivalent to limiting electric field 10^9V/m. For the positively charged dust, the limit is higher [Draine and Salpeter, 1979b]

$$\varphi_s(V) \approx +3 \cdot 10^4 R(\mu m)\ . \tag{2.17}$$

The limiting surface potentials of dielectric dust particles can be much lower. Čermák *et al.* [1995], and later Sternovsky *et al.* [2001] found in the same experiment a limiting field of $+5 \cdot 10^8$ ($+3 \cdot 10^8$) V/m for micron sized glass grains as compared to $+3 \cdot 10^{10}$ V/m given by Draine and Salpeter [1979b]. The limiting field of $-2 \cdot 10^8$ V/m has been found for negatively charged 5 μm sized glass grains [Pavlů *et al.*, 2004].

The limiting surface potentials may be easily reached by very small dust grains. Tiny dust grains (less than 20 nm) detected by spacecraft missions around Saturnian and Jovian systems have very likely limited amount of the charge with respect to the equilibrium potential due to field emission processes. Observations by Ulysses [Švestka *et al.*, 1996] may indicate the existence of dust with the mass of a few times 10^{-18} kg that has extremely high surface potentials (near 10^4 V).

But, according to eq. 2.17, the field emission should have limited the charge to $\leq 2 \cdot 10^3$ V if the dust material density is $\approx 10^3\,\mathrm{kg/m^3}$. However, Švestka *et al.* [1996] stated that the measurement of dust charges by the Ulysses dust detector is a subject to large uncertainties.

Based on the Fowler-Nordheim theory [Fowler and Nordheim, 1928; Good and Muller, 1956], the size current density of tunnelling electrons is

$$i_f \approx \frac{E}{\varphi_s t^2(E^{\frac{1}{2}}, \varphi_s)} \cdot \exp\left(\frac{W^{\frac{2}{3}}}{E} v(E^{\frac{1}{2}}, W)\right) , \tag{2.18}$$

where E is the electric field, W is the grain work function, v and t are tabulated weak functions of E and W [Pavlů *et al.*, 2006b].

2.5 Photoemission

The photoelectrons are emitted when a flux of photons with the energy ($h\nu$) larger than the photoelectric work function (W) of the dust grain incidents the grain surface. The photoemission process depends on: (i) the wavelength of the incident light, and (ii) the properties of the dust grain material.

The mechanism contributes to make the dust more positively charged. Work function of the lattice material gives the minimum energy for photoelectron to overcome the surface potential barrier. Most of the metals has the photoelectric work function $\mathrm{W} < 5\,\mathrm{eV}$ (e.g., $\mathrm{W_{Ag}} = 4.46\,\mathrm{eV}$, $\mathrm{W_{Cu}} = 4.45\,\mathrm{eV}$, $\mathrm{W_{Al}} = 4.2\,\mathrm{eV}$. There is also a number of materials, e.g., carbides with low work functions, $\mathrm{W} = 2.18$–$3.50\,\mathrm{eV}$, borides with work functions, $\mathrm{W} = 2.45$–$2.92\,\mathrm{eV}$, oxides of metals with work functions ranging from $\mathrm{W_{Cs_2O}} = 1.95\,\mathrm{eV}$ to $\mathrm{W_{ZrO_2}} = 4.05\,\mathrm{eV}$. The materials with the low work function are widely used as photocathodes in multiplier tubes.

The maximum charge of the grain due to photoemission can be estimated from an energetic balance. The energy of the incoming photon has to be high enough to excite an electron with the kinetic energy larger than the grain photoelectric work function W and grain potential which is positive ($\varphi_s = Q/4\pi\varepsilon_0 R$). Thus, the minimum energy of photon which excites an electron should be $h\nu \geq W + eQ/4\pi\varepsilon_0 R$, where e is the elementary charge and ε_0 vacuum permitivity. This implies that the maximum attainable charge by photoemission is

$$Q = 4\pi\varepsilon_0 R \frac{(h\nu - W)}{e} . \tag{2.19}$$

Because the dust grain surface is positive due to photoemission, i.e. $\varphi_s > 0$, only an energetic fraction of the photoelectrons can overcome the dust grain potential and escape.

The surface potential is determined by the balance between the photoelectrons returned back and the photoelectrons escaped from the dust grain surface. The photoemission current for a photon flux J_p and for $\varphi_s > 0$ is, roughly [Rosenberg *et al.*, 1996; Goertz, 1989]

$$I_{ph} = \pi R^2 e J_p Q_{abs} Y_p \exp\left(-\frac{\mathrm{e}\varphi_\mathrm{s}}{\mathrm{k_b T_p}}\right) , \tag{2.20}$$

where Q_{abs} is the efficiency of the absorption of photons (usually taken as $Q_{abs} \approx 1$ for $2\pi R/\lambda > 1$, where λ is the wavelength of the incident photons [Evans, 1993]), Y_p is the photoelectron yield, and T_p is Maxwellian average temperature of photoelectrons.

Unfortunately, sometimes the assumption of a Maxwellian distribution is not fulfilled and require some modification It has to be noted that the exponential factor in equation 2.20 must be taken into account only if the photoelectrons have sufficient energy to overcome the potential barrier of the positively charged dust grain.

Now let's consider dust grain with a negative surface potential (i.e., $\varphi_s \leq 0$). In this case, photoelectrons are not returned back to the dust grain surface, i.e., all photoelectrons are emitted. This leads to a constant photoemission current

$$I_{ph} = \pi R^2 e J_p Q_{abs} Y_p \,. \tag{2.21}$$

In laboratory or in the space, the situation is more complicated, because the source of UV light (UV lamp or Sun) contains not only one UV line but whole spectrum of UV lines of variable and even changing intensity. In general, the photoemission current from a irradiated surface $A(R)$ is

$$I_{ph} = A e F_{ph} \,, \tag{2.22}$$

where coefficient F_{ph} is integral product due to integration of photoelectric efficienty of absorption $Q_{abs}(h\nu, R)$, photoelectric yield $Y_p(h\nu, R)$ and solar spectral photon density flux $S(h\nu, R)$ over the range of available energies with corresponding energy distribution of emitted photoelectrons $f(\varepsilon)$

$$F_{ph} = \int_{h\nu=W(R)+\varepsilon_{MIN}}^{\infty} Q_{abs}(h\nu, R) Y_p(h\nu, R) S(h\nu, R) \int_{\varepsilon_{MIN}}^{\varepsilon_{MAX}} f(\varepsilon)\, d\varepsilon\, d(h\nu) \,. \tag{2.23}$$

The size dependent efficiency factor (ratio between the effective and geometric cross section) for absorption of photons Q_{abs} can be calculated using Mie-theory and refractive index of the material.

The number of electrons released per absorbed photon, the yield function Y_p, was predicted to be a function of dust size [e.g., Gail and Sedlmayr, 1980] and must be determined for each material experimentally. The yield function for conductors was found to be close to that for bulk materials (flat half space surfaces) except for very small dust particles of radius of only a few nanometers, where the yield increases by a factor of several hundreds in such cases [Müller *et al.*, 1988; Schleicher *et al.*, 1993].

The energy distribution of released photoelectrons $f(\varepsilon)$ has a cut-off at a maximum energy (ε_{MAX}) which equals to difference of the photon energy $h\nu$ and the work function W. The minimum energy required for a released photoelectron to escape is $\varepsilon_{MIN} = 0$ for $\varphi_s \leq 0$ and $\varepsilon_{MIN} = e\varphi_s$ for $\varphi_s \geq 0$.

Accurate determination of equation 2.23 is difficult because the solar UV spectrum varies with time and since the absorption efficiency (Q_{abs}) depends on material and geometric properties which are usually not fully known [McGuire and Hapke, 1995; Hirst *et al.*, 1994].

An approximate expression of F_{ph} due to the uncertainties in evaluating of equation 2.23 [Wallis and Hassan, 1983] is

$$F_{ph} = 3 \cdot 10^{10} \frac{\chi}{r^2} \exp\left(-\frac{e\tilde{\varphi}}{k_b T_p}\right) \,, \tag{2.24}$$

where the factor r^{-2} takes care about the decrease of the photon flux with heliocentric distance in astronomical units with $\tilde{\varphi} = \max[0, \varphi_\mathrm{s}]$, χ is an efficiency factor close to 0.9 for metallic or graphitic grains and to 0.1 for icy grains. A typical average temperature of photoelectrons is $\mathrm{k_b T_p} \approx 1.3$ eV [Manka, 1973].

2.5.1 Work function

The work function is a minimum energy required to extract an electron from the surface of solid material to the vaccum. The work function also characterise the surface properties of the material, the crystal phase or contamination.

The photoelectric work function and thermionic work function are same for metals. In case of insulators, they can be different.

The value of the photoelectric work function (W) is often affected by impuritites inplanted in the material and by absorbed molecules on surface.

Experimental measurements on sodium [Herrmann *et al.*, 1978; Schumacher *et al.*, 1984] and silver [Schmidt-Ott *et al.*, 1980; Smith, 1965] nanometer sized particles revealed that the work function of these particles is different from bulk values.

The theoretical models consider the Coulomb potential interaction between the leaving electron and remaining positive particle. In model of Makov *et al.* [1988], the work function W(R) of spherical metal particle with radius R is related to the work function of planar material W_∞ according to

$$W(R) = W_\infty + \frac{3}{8}\frac{e^2}{4\pi\varepsilon_0}\frac{1}{R}\,, \tag{2.25}$$

on the other hand for dielectric spherical particle Brus [1983] calculated

$$W(R) = W_\infty + \frac{q^2}{2R}\frac{\varepsilon_r - 1}{\varepsilon_r}\,, \tag{2.26}$$

where W_∞ is the work function of planar material and ε_r is relative permitivity of dielectric sphere.

The work function of the material W determines the threshold of the photoelectron yield Y which related to the photon energy $h\nu$ by the Fowler–Nordheim law [Fowler, 1931]

$$Y(h\nu) \propto (h\nu - W)^2\,, \tag{2.27}$$

valid also for small particles.

2.5.2 Photoelectron yield

The photoelectric yield denotes the probability of ejection of an electron after the absorption of a photon.

An electron is excited somewhere in the volume of the sample and loses energy during its journey to the surface through interactions with electrons and with phonons of matter. As a result, the fraction of electrons which escape goes roughly as $\mathrm{C}\exp(-\mathrm{x}/\mathrm{l_e})$, where x is the distance which the electron traveled, l_e is the electron escape length and C norming constant.

When the photon attenuation length l_a exceeds l_e, the electrons excited deep inside a bulk sample can not reach the surface. Small size of grain limits the

distance from electron excitation point to surface, so the photoelectron yield is enhanced. The photon attenuation length depends on absorption properties of the material as

$$l_a = \frac{\lambda}{4\pi \mathrm{Im(m)}}\,, \tag{2.28}$$

where λ is the wavelength in vacuum and $m(\lambda)$ is the complex refractive index of absorbing material.

For a highly anisotropic materials like graphite the dielectric function is a tensor. For example for graphite the tensor can be diagonalized

$$\frac{1}{l_a} = \frac{4\pi}{\lambda}\left[\frac{2}{3}Im(m_\perp) + \frac{1}{3}Im(m_\parallel)\right]\,, \tag{2.29}$$

where $m_\perp$ and $m_\parallel$ are for the perpendicular and parallel electric field, respectively. The l_a is possible compute with using of dielectric functions [Draine and Lee, 1984; Laor and Draine, 1993].

A series of experiments conducted by Schmidt-Ott *et al.* [1980]; Burtscher and Schmidt-Ott [1982]; Burtscher *et al.* [1984]; Müller *et al.* [1988] on free silver spheres with radii between 27 and 54 Å found photoelectron yields exceeding the expectations by factor of several. A detailed and accurate model for the above geometrical effect is not yet available. A theoretical calculations of Faraci *et al.* [1989] was able to reproduce the results, but only with the assumption that the escape probability of electron depends only on its energy and is independent of its direction of motion.

The estimates for size-dependent yields are based on Watson [1973] simplified model. This model is developed from imagination about the photoemission for bulk material. The photoelectron yield for different geometries of surface y' than plane is possible to determine integration over the volume V of absorbing material

$$Y^{'} = \frac{\int C \exp(-\frac{x}{l_e})(\nabla.\mathbf{S})\mathrm{d}V}{\int(\nabla.\mathbf{S})\mathrm{d}V}\,, \tag{2.30}$$

where $\mathbf{S}$ is Poynting vector and its divergence $(-\nabla.\mathbf{S}/\hbar\omega)$ represents absorbed light in unit volume of the material. In case of unmagnetic optically anisotropic material, the photoelectric yield (eq. 2.30) (with using of Poynting theorem) changes into form

$$Y^{'} = \frac{\int C \exp(-\frac{x}{l_e})(\mathbf{E}^*.\mathbf{E})\mathrm{d}V}{\int(\mathbf{E}^*.\mathbf{E})\mathrm{d}V}\,. \tag{2.31}$$

The electric field $\mathbf{E}$ inside the spherical grain for incident planar electromagnetic wave is possible establish from Mie scattering [van de Hulst, 1957] theory with expand of electric field on real and imaginary part $\mathbf{E} = \mathbf{M_v} + i\mathbf{M_u}$ and found two solutions of the scalar wave equations [Bednář, 1980].

A solution of eq. 2.31 for bulk material with boundary value problem

$$\mathbf{E}^* \cdot \mathbf{E} = K \exp(-x/l_a)\,, \tag{2.32}$$

comes to form

$$Y_b = \frac{C l_e}{l_e + l_a}\,. \tag{2.33}$$

The photoelectron yield enhancement E_a (ratio of dust sphere yield $Y^{'}$ to yield of bulk material Y_b) can be with solution of Mie scattering theory found as

$$E_a = \frac{Y^{'}}{Y_b} = \frac{l_e + l_a}{l_e} \frac{\int_0^R \exp(-(r-R)/l_e) F(r) 4\pi r^2 \mathrm{d}r}{\int_0^R F(r) 4\pi r^2 \mathrm{d}r}\,, \tag{2.34}$$

where function $F(r)$ has form

$$F(r) = \frac{1}{k^2 r^2} \sum_{n=1}^{\infty} (2n-1) |j_n(z)|^2 \times \left\{ |c_n|^2 \left[|D_n|^2 + \frac{n(n+1)}{|z|^2} \right] + |d_n|^2 \right\} \tag{2.35}$$

and can be calculated numerically based on Wiscomb's formula with use of FORTRAN code PE-DING.FOR of Ding [1994]. The photoelectron yield enhancement results of Ding [1994] model for silicate and graphite grains are in Fig. 2.1 – left and Fig. 2.1 – right. The absolute photoelectron yield can be obtained

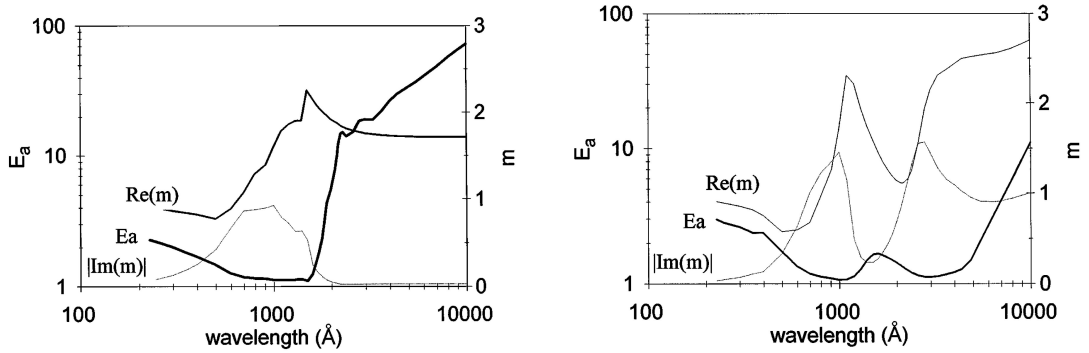


Figure 2.1: The photoelectron yield enhancements for silicate (left) and graphite (right) grains of 100 nm radii. Adopted from Ding [1994].

by multiplying yield enhancement factors with published yield values [Ballester *et al.*, 1995] see adopted Fig. 2.2. How Watson [1972, 1973] correctly pointed out, the yields of submicron particles are expected to be enhanced relative to the bulk yields, because of the finite electron escape length. Draine [1978] displayed

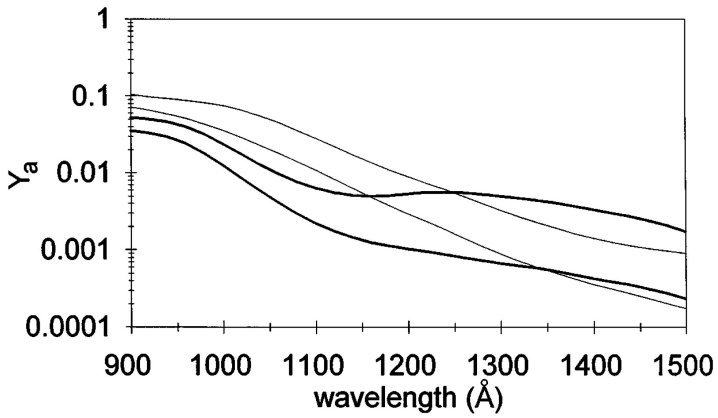


Figure 2.2: The absolute photoelectron yield Y$^{'}$ for silicate (thin curves) and graphite (thick curves) grains with radii 10 nm (upper curve) and 100 nm (lower curve). Adopted from Ballester *et al.* [1995].

yield measurements from experiments on bulk samples of materials of interest, including graphite, lunar dust, and silicon carbide and showed, that the bulk graphite yield measured by Feuerbacher and Fitton [1972] is unusually low, and lies more than an order of magnitude below the yields for anthracene [Fujihira *et al.*, 1973]. The higher value of the graphite yield suggest also Quemerais *et al.* [1985] measurements. Clearly, the yields for graphite grains are highly uncertain and the situation for silica is no better compare Quemerais *et al.* [1985] and Watson [1973]. Feuerbacher *et al.* [1972] also measured the yield for a powdered sample of lunar dust, and found that Y decreases rapidly as photon energy is decreased below 14 eV . However, they noted that the use of the powdered sample might result in yields that are too low.

2.5.3 Photoconductivity

Alvarez [1975, 1977b] measured the effects of ultraviolet (UV), visible, and infrared (IR) irradiation on the electrical conductivity of lunar samples, including the lunar soils for two different sample temperatures 100 K and 295 K (Fig. 2.3 – left and right). The relative change of their surface electrical conductivity to the conductivity in darkness was about a 10^1 increase for the IR and a 10^6 increase for the UV. To reach same increase of the surface conductivity as by radiation is necessary to heat the sample to temperature of around 800 °C [Olhoeft *et al.*, 1973, 1974].

These large changes in conductivity with irradiation can lead to large movements of electrical charge across the solar terminator on the lunar surface.

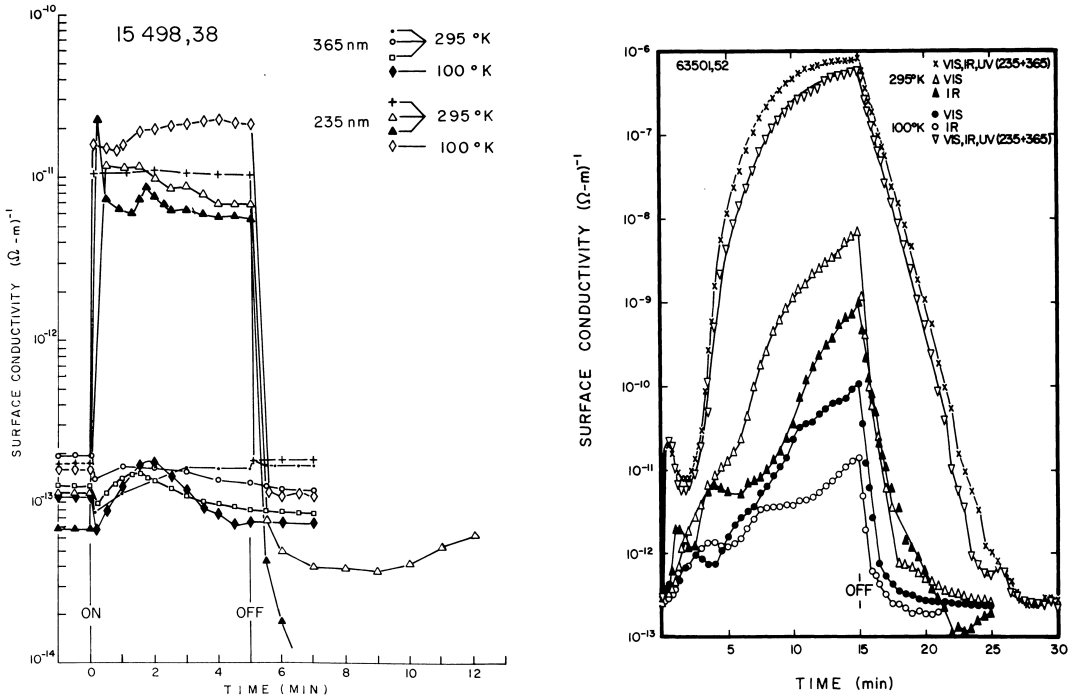


Figure 2.3: Change of photoconductivity of lunar samples. Comparision of change of photoconductivity for different UV wavelengths (left) and comparision of change of photoconductivity for UV and IR irradiation (right). Adopted from Alvarez [1975, 1977b].

2.6 Thermionic effect

One of the important charging processes when the dust grain charge up positively is thermionic emission [Sodha and Guha, 1971; Rosenberg *et al.*, 1999].

A dust grain heated to a high temperature may thermionically emit electrons or ions from its surface. The thermionic emission process may be induced by laser pulse, by infrared (IR) heating [Rosenberg *et al.*, 1999] or by hot filaments surrounding the dust grain. For extremely high temperatures of dust grain T_d, the electrons in dust may reach a sufficient energy to escape from its surface.

Normally, temperatures above 1000 K only are considerable for threshold of the process. Therefore the most refractive dust materials like carbon and silicates close to the Sun are relevant [Isobe and Satheesh-Kumar, 1992]. The thermoionic current density i_{th} can be obtained from the Richardson equation (e.g., [Richardson, 1901; Evans, 1993])

$$i_{th} = A{T_d}^2 \exp\left(-\frac{W}{k_b T_d}\right) , \tag{2.36}$$

where $A = \lambda_c(1-r)A_0$. The $\mathrm{A_0} = 4\pi \mathrm{e m_e k_b}^2/\mathrm{h}^3 = 120\,\mathrm{A cm^{-2} K^{-2}}$ is a universal constant, T_d grain temperature, W grain work function, r reflectance of the surface potential barier (usually neglected) and λ_c is a material correction factor.

To the equation 2.36 is usually neccesary included the decrese of the work function due to the Schottky effect [Schottky, 1914]. The thermionic current I_{th} for spherical negatively charged dust grain with radius R is

$$I_{th} = 4\pi R^2 A{T_d}^2 \exp\left(-\frac{|W-\Delta W|}{k_b T_d}\right) , \tag{2.37}$$

where ΔW provides lowering of the surface barrier by Schottky electric field F

$$\Delta W = \sqrt{\frac{e^3 F}{4\pi\varepsilon_0}} . \tag{2.38}$$

When the grain is positively charged, the electrons have to overcome the floating potential as well as the dust surface barrier. The thermionic current for a positively charged grain is [Delzanno *et al.*, 2004]

$$I_{th} = 4\pi R^2 A{T_d}^2 \left(1 + \frac{e\varphi_s(R)}{k_b T_d}\right) \exp\left(-\frac{W + e\varphi_s(R)}{k_b T_d}\right) . \tag{2.39}$$

The experimental value of coefficient A can vary from $32\,\mathrm{A cm^{-2} K^{-2}}$ for pure metals to $160\,\mathrm{A cm^{-2} K^{-2}}$ for oxide and composite surfaces [Wolf, 1995]. The dependence is also caused by the geometry, different crystallographic faces [Smith, 1954] and as well as possible impurities in the material.

2.7 Radioactivity

The radioactivity in form of trapped radioactive nuclei in the grains in space may establish a charging mechanism through both the escape of the emitted charged primaries from the radioactive nuclei and the escape of the secondary

electrons excited by a charged primaries through its passage to the surface. The amount of ordinary radioactivity material in bodies is insignificant for charging effects [Whipple, 1981].

On the other hand, there were also made some Earth's experiments with beta-active CeO_2 particles of 1 μm in diameter activated in the nuclear reactor [Fortov *et al.*, 1999]. Also, the dust grains formed in nova and supernova may have significant radioactive levels Yanagita [1977], particularly ^{22}Na or ^{26}Al which are β emitters. The charging due to β emission changes with the size of the grain and tend to larger grains be positively charged. The satellites sometimes carry quantities of radioactive materials in connection with certain types of experiments, or as a power source.

Such sources are usually well shielded, but may source of possible charging mechanisms for spacecraft. Then, each such source has to be evaluated individually as a possible source of charging.

2.8 Contact charging

One of the most interesting phenomena is charge transfer between two different insulators or metals in contact. The transfer can be due to ions, electrons, or fragments of material carrying charge (such as small charged dust paticles) [Harper, 1967].

The complexity of the charge transfer problem is illustrated by the fact that even the well-defined electrification system may show different properties in different ambient atmospheres, for different temperatures or for different kinds of contact.

The theoretical studies of the charging of insulators are in general at a rather inconclusive stage. The main effort is being concentrated on electron transfer models since results from many electrification experiments [e.g., Arridge, 1967; Davies, 1967a, 1969] can be interpreted in this way. However, there is also evidence for the existence of other kinds of charging.

Contact charging described by electron transfer model is treated on the basis of band theory. The electrons are transferred from material with a lower work function, W_1 to the another one with a larger work function W_2, when these materials are brought into contact. The model works well for metal-metal contacts and the amount of transferred charge is $Q = C\varphi$. The size of contact potential is proportional to differences of work functions of both materials $\varphi = (W_1 - W_2)/e$. The size of the capacitance of the system C depends on size, shape, geometrical arrangement and surface properties of object in the contact [Lowell, 1975].

In case of charging of insulators, the situation is more complicated, no unified theory is known. The insulator contact charging is usually interpreted due to localized energy levels inside the forbidden energy gap of the insulator. These levels can exist due to impurities, defects, or the presence of surface states and can be filled up to a certain energy level. The size of the level is called as the "effective" work function of the insulator. The insulator charges positively when it is in contact with materials of larger work function.

In case of metal-insulator contact the charge is a linear function of the metal work function [Lowell and Rose-Innes, 1980; Lee, 1994].

It has also been found that the contact charge can accumulate due to repeating of contacts. This phenomenon is poorly understood and can be caused by increasing contact area as well as increased charge penetration into the insulator.

The charging processes depend on the properties of surfaces. Even the oxidized surface of the metal can rapidly change size of the contact potential [Harper, 1967]. Harper [1967] developed a model for the changes of the contact potential when a metal surface is oxidized.

2.9 Frictional charging

The sliding of two surfaces has a large effect on the transferred contact charge [O'Neill and Foord, 1975]. However, the sliding mode of electrification might not always be called "frictional charging" because the effect of sliding can simply increase area of contact between the materials only. The evidence that friction may give rise charging comes from experiments on the rubbing of two apparently identical surfaces together [Rudge, 1914; Shaw, 1927; Henry, 1953]. The study by Henry [1953] demonstrated that the asymmetry of the rubbing action plays an important role as well.

Henry [1953] concluded that the friction concentrated on a smaller area of one surface give rise to a strong temperature gradient across the contact.

The frictional charging (or triboelectric charging) mechanism is not necessary to be associated to one special kind of carrier. The heating of a contact point can tend to transfer of charged material particles as well as increase the mobility of ions and electrons. The charge carriers diffuse to the colder part of the contact so charging this surface negatively if the carriers are electrons and/or negative ions or the charging is positive if there are positive ions. There are experimental results showing both positive and negative charge transfer [i.e., Shaw, 1927; Shaw and Hanstock, 1930; Henry, 1957].

On the other hand, the frictional electrification study by Cunningham [1964] provides relationship between the charge transferred and work against the force of friction and supported the idea of Henry [1957] that frictionally generated charge may dominate in charge transfer. A study by Zimmer [1970] is another example that heat generation is involved in frictional charging.

Triboelectric charging is rarely discussed for grains. Sternovsky *et al.* [2002] tried to determine parameters of the grains (as their size, surface potential and work function) from contact charging. The triboelectric charging is frequently invoked as a mechanism for charging of windblown grains. The rubbing of grains increases the surface charge because increases the fraction of the area in contact [Lowell and Rose-Innes, 1980; Harper, 1967].

Strong electric fields observed near dust devils [Freier, 1960] may arise from triboelectricity and may occur on Mars [Melnik and Parrot, 1998; Farrell *et al.*, 1999]. Spectacular lightning discharges observed in volcanic plumes may also result from triboelectric charging of dust [Gilbert *et al.*, 1991; Anderson *et al.*, 1965].

In addition to the above dust currents, charging can also result from dust fragmentation and dust-dust collisions with charge exchange. These two mechanisms may be important in thunderclouds [e.g., Chiu, 1978].

2.10 Grain charging in the solar system

Charge of a single dust grain can vary with the local plasma conditions of our solar system. A comparision between the two most important currents I_e eq. 2.5 and I_{ph} eq. 2.22 can help to quantify significance of each of these currents. Situating of $\varphi_s = 0$, we can for referenced equations find [Mukai *et al.*, 2001]

$$\frac{I_{ph}}{I_e} = \frac{3.7 \cdot 10^2 \chi}{n_e {T_e}^{1/2}(eV) r^2} \,. \tag{2.40}$$

The typical conditions in interplanetary space are electron temperature $T_e \approx$ 10 eV and electron density $\mathrm{n_e} \approx 10^6\,\mathrm{m}^{-3}$. According to eq. 2.40, the photoelectric effect dominates to considerable distances from the Sun. Only low photoelectron yield of dust material and electron density $\mathrm{n_e} \gtrsim 10^7\,\mathrm{m}^{-3}$ (eq. 2.40) can setup that $I_{ph} \sim I_e$ for $r \gtrsim 1\,\mathrm{AU}$. The plasma particle currents (I_e, I_i, I_{sec}) usually dominate at magnetosheric conditions where n_e is in the range of $10^7 - 10^8\,\mathrm{m}^{-3}$ [e.g., Hartquist *et al.*, 1992].

The surface potential φ_s of a spherical grain is proportional to the charge number Z_d

$$Z_d = (4\pi\varepsilon_0 R/e)\varphi_s(V) \approx 700\varphi_s(V)R(\mu)\,. \tag{2.41}$$

The effect of secondary electrons becomes important with increasing plasma temperature, which makes the surface potential less negative and eventually positive. Since ejected secondary electrons have approximately Maxwellian velocity distributions with fairly low temperatures (1 to 5 eV), they cannot overcome high positive surface potentials and the positive potentials will normally stay below $\approx +10$ V. Since photoelectrons also have low temperature energy distributions (1 to 3 eV), they can neither produce high positive dust surface potential.

Chapter 3

Creation and destruction of dust grains

3.1 Dust production by comets

The comets are able to emit dust in tails in large quantities. From this reason the comets appear as the main source of interplanetary dust. The meteoroids (as the remnants of disintegrated comets) and sporadic meteoroids (resulting from dissolved meteoroids streams) can produce dust in mutual collisions.

According to the orbital distribution of dust, the short-period comets would be a suitable candidates for sources of interplanetary dust. According to calculations of Dohnanyi [1972] and Grün *et al.* [1985] it is necessary to supply about 10 tons/s to keep the interplanetary dust cloud in steady state. However, calculatated amount of dust emitted by short-period comets gives only 250 kg/s of dust remained in bound orbits. Detailed studies of comets Encke and d'Arrest by Sekanina and Schuster [1978b,a] showed that this value may be even overestimated. Direct injection of dust from comets therefore does not appear as the main supply for the interplanetary dust.

However, the recent models of Nesvorný *et al.* [2010] and Poppe [2015] of relative contribution of asteroids and cometary material to zodiacal light have shown that asteroidal particles produced by the main belt collisions cannot produce the zodiacal cloud emission at large ecliptic latitudes simply because the main belt asteroids have generally small orbital inclinations. Based on the models the authors propose that $\geq 90\%$ of the zodiacal cloud emission at mid-infrared wavelengths originates from dust grains released by Jupiter-family comets, and $\leq 10\%$ comes from the long period Oort-cloud comets and/or asteroid collisions.

3.2 Plasma induced sputtering and alteration

The energy deposited into a grain by ion or electron impacts alter the target material and can cause its erosion through process known as sputtering. The interaction occurs due to momentum transfer between the ions and the atoms of the target or by the electronic excitation of atoms or molecules by the incident plasma ions and electrons [Fenyö *et al.*, 1990].

The sufficiently high-energy ions cause sputtering of the dust material or can

be built in the dust surface and may later diffuse outside the grain [Beránek *et al.*, 2010]. The amount of sputtered material which can be in neutral or ionized state depends on the material of the grain, on the energy and type of the incident ions and on the angle of incidence.

Energetic impacts can cause via electronic excitations more efficient production of H_2 and O_2 in H_2O [Brown *et al.*, 1984] than the UV desorption by photons do [Westley *et al.*, 1995].

Finally, impacting ions can also alter the grains material by implantation into it [e.g., Roth, 1983]. For example, an implantation of plasma protons into carbon can lead to formation of CH_4. An implanted H can compete for O in silicates to form hydroxyl groups (–OH) or even water H_2O. Chemical effects leading to material loss like discussed above are referred as chemical sputtering.

Bond breaking reactions and momentum transfer collisions can cause displacements and locally heat the material lattice. This may produce amorphous regions in some crystalline materials. The typical examples are the amorphous rims on lunar grains [Taylor, 1982] and amorphous regions in some interplanetary dust particles (IDPs) grains [Bradley, 1994].

Displacements and agitations can lead to formation of "tracks" along the path of ions. The tracks formed by solar flare ions can help to determine exposure ages of collected IDPs grains. The disturbances along the particles paths may induce an ion-enhanced diffusion. Therefore, material species can diffuse to the grain surface. Agitation, defect formation, and ion-enhanced diffusion of volatiles lead to sputtering. Further sputtering yield enhancements may occur due to nonlinear sputtering when the energy deposited by ions raises sufficiently the grain temperature.

The erosion of lunar material due to sputtering was found to be only 0.03 Å per year [Ashworth, 1978]. However, on ice particles sputtering has a 100 times higher efficiency [Lanzerotti *et al.*, 1978]. Therefore the lifetime of ice particles in the outer solar system is much shorter than the lifetime of mineral grains.

The experiments with sputtering of glass dust grains levitated in electrodynamic trap by 2 keV Ar^+ ions [Vyšinka *et al.*, 2016] revealed increase of sputtering yield from one SiO_2 molecules per incident ion to 1.6 while the grain was simultaneously bombarded by the intense 1 keV electron beam. Similar experiments on gold [Pavlů *et al.*, 2007] afforded sputerring yield for different type of incident ions and various distances from the Sun. The measurements also shown that the initial shape of the grain changed due to the sputtering process.

The interplanetary material is modified to the depth of ion penetration after long-term exposure. Sputtering can then modify stoichometry. Johnson and Baragiola [1991] expected depletion of O in the surface regions on silicates. However, Bradley [1994] have found O-excesses in the irradiated surface regions of IDP's caused by –OH formation by impacting protons. Mg and Ca appear to be depleted in irradiated rims of IDPs whereas these regions are enriched in O, S, Fe, and Ni [Bradley, 1994].

A sputtering of organics by fast light ions like H^+ and He^+ leads to depletion of volatiles from organics and gradually produces a carbonaceous residue. An electronic sputtering is extremely efficient in the sputtering of organics and dominates in the sputtering of ices as well.

3.3 Electrostatic fragmentation of charged grains

On the charged grain surface, charges of some polarity are mutually repulsed and generate electric field. The electrostatic force can exceed the tensile strength of the grain material and may disintegrate a large grain into smaller fragments.

The Maxwell's stress force F is given by $F = \frac{1}{2}\varepsilon_0 E^2$ where E is the electric field on the grain surface, and ε_0 denotes the dielectric constant of the vacuum.

The surface charge density σ_0 for a spherical grain with a radius R and a surface electric potential φ_s is

$$\sigma = Q/4\pi R^2 = \varepsilon E = \varepsilon\varphi_s/R\,, \tag{3.1}$$

where Q means the total charge of the grain and ε is the dielectric constant of the grain material.

For an irregularly shaped grains the charge distribution on the surface is non-uniform. Mukai [1991] calculated the stress force for the irregularity on the surface. In this model, the roughness of spherical grain with a radius R is represented by a part of a sphere with a small radius of curvature ρ (see Fig. 3.1).

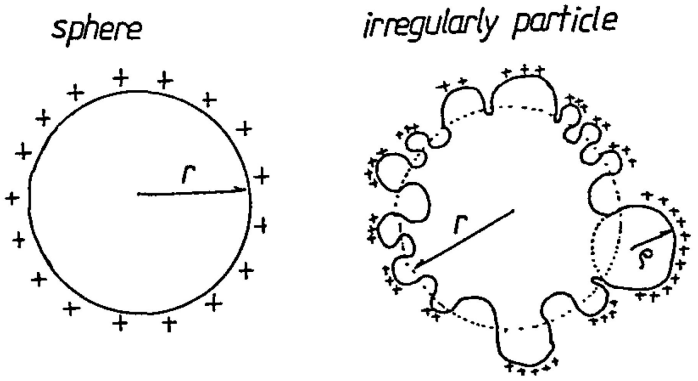


Figure 3.1: Charge distribution on the surface of spherical and irregularly shaped grain. Adopted from Mukai [1991].

The charge density σ at a spot with a radius ρ is given by

$$\sigma = \varepsilon\frac{\varphi_s}{\rho}\,. \tag{3.2}$$

Consequently, the stress tensor force F_i on this position becomes

$$F_i = F\left(\frac{R}{\rho}\right)^2\,. \tag{3.3}$$

The stress force F_i at curved surface is significantly stronger than F expected at the average surface of a sphere.

According to equation 3.1 and relation for Maxwell's stress force we can determine the critical radius R_c for the electrostatic fragmentation threshold

$$R_c = \sqrt{\frac{\varepsilon_0{\varphi_s}^2}{2F_{th}}}\,, \tag{3.4}$$

where F_{th} is the tensile strength of grain material. The value of tensile strength F_{th} varies for different materials over a wide range from $\approx 10^{-3}$ MPa for loose aggregates like snow flakes or fluffy grains to $10^1 - 10^3$ MPa for silicates or metals [Grün *et al.*, 1984]. The experimental values of tensile strength for Al_2O_3 grains in radii range 1–7 μm provided measurements by Švestka *et al.* [1993] in the electrodynamic trap. However, the value of determined tensile strength could be affected by the electric field applied on the trap electrodes.

When the disruption started at a sufficiently high potential φ_s and the critical radius R_c is larger than the grain radius, the process should continue in avalanche as the new smaller fragments would be inevitably unstable. However, in the case of nonspherical particles, everything may end with the breakaway of particularly acute protuberances.

If the characteristic radius of curvature remains smaller than R_c and the disruption does not stop, then a new stabilizing mechanism becomes active and limits the electric field intensity E and the tensile force. The field emission, which sharply decreases the charge and potential of the grain and halts the electrostatic disruption [Opik, 1956]. Mendis and Rosenberg [1992] discussed observations of electrostatic disruption as a possible reason for the so-called striae in some comet tails [Sekanina and Farrell, 1976; Hill and Mendis, 1980].

The particles are also disrupted due to the fast increase of electric charge, e.g., due to exposure to stream of energetic electrons ($E \approx 1 - 10$ keV). The grain potential may become as high as $\varphi_s = 60 - 300\,V$ and the tensile strength of grains estimated assuming this mechanism is quite realistic $10^{-3} - 10^{-1}$ MPa.

Another evidence for this mechanism was provided by measurements of concentration of very small dust grains in the vicinity of Halley's comet. The measurements revealed a sharp peak in the spatial distribution of small particles at distance 180 000 km away from the comet core, in the cometopause region.

The change in the concetration might be result of electrostatic disruption of larger grains due to the abrupt change of the plasma temperature from $T \leq 1$ eV within the cometopause to $T \geq 10$ eV beyond. Similar processes are likely to occur in planetary magnetospheres [Fechtig *et al.*, 1979] where a macroscopic body crosses the Earth's auroral region (filled with an energetic particles, $T \approx 1$ to 10 keV) may exceed the critical value for electrostatic fragmentation.

3.4 Coagulation of charged and neutral dust grains

Coagulation of dust grains is process when during collisions larger particles are produced. The process is important for the formation of the spectrum of masses in space. The growth of dust grains of different sizes from a gaseous medium is proceeds in several steps.

The first step is homogeneous nucleaction due to condensation of liquid droplets or solid particles from a uniform cold gas in the absence of preexisting nuclei [Latimer, 1982]. This is a slow process and results in the production of grains smaller than a few microns.

The next step involves condensation of atoms and molecules onto already existing nuclei that risen earlier, and the size of grains increases. The condensa-

tion rate is higher in this case but not by orders of magnitude [Latimer, 1982]. Meanwhile, the pressure of surroundig neutral gas decreases, and the rate of condensation is reduced. Both processes nucleation and condensation require a high degree of supersaturation of the neutral gas. In most cases the degree of supersaturation decreases with time and eventually falls below the value needed for further condensation.

Further grow of the grains is possible only by coagulation of the already-existing particles. The coagulation process involves grain–grain sticking collisions.

The aggregation process of small grains with neglecting fragmentation can be studied via the coagulation equation [Safranov, 1972].

The effects of electrostatic attraction (or repulsion) on coagulation of colliding particles were discussed by Horányi and Goertz [1990]. The number of large grains increases in the case of oppositely charged particles and decreases for a like same sign charges.

3.5 Melting and evaporation of grains

The evaporation process plays a role close to the Sun. Röser and Staude [1978] shown expected temperatures for interplanetary particles and found with Lamy [1974] dust free zones caused due to evaporation, 24 $R_\odot$ for iron, 10 $R_\odot$ for olivine, 4 $R_\odot$ for obsidian, 1.5 $R_\odot$ for graphite and quartz, where $R_\odot$ is the solar radius.

However, Mukai and Yamamoto [1979] calculated that a particle of suitable size and material would spend a prolonged time outside the evaporation zone, oscillating in and out under the interplay of evaporation, radiation pressure, and Poynting-Robertson drag. This effect should lead to a measurable enhancement of spatial dust density. Most particles in this region will probably evaporate completely. Nevertheless, with the temperatures of melting materials in the range 1000 – 1500 K [Röser and Staude, 1978] the edges of dust free zones should be observable in the near infrared.

Indeed, structures of enhanced infrared emission have been observed and have been interpreted as the edges of dust free zones [McQueen, 1968; Peterson, 1967].

Pure ice is predicted to evaporate at heliocentric distance 3 AU [Hanner, 1981], where its equilibrium temperature is 170 K. In case of its contamination with dark material the limit may be farther out than 4 AU. Ice particles should not be expected in the inner heliosphere. However, they are the main constituent of interplanetary dust in the outer Solar system.

3.6 Impact ionization process

Impact ionization is process when the high velocity impacting particle hits a solid surface and produces ions from the particle as well as from the target material.

The shock wave ionization model describes the impact process as a sequence of phases [Drapatz and Michel, 1974].

At first, the particle is compressed by a shock to high pressures and temperatures. The material of the target and the grain is ionized and thermoelectrons

are produced. A plasma cloud with local thermodynamic equilibrium is set on and it starts to isentropically expand.

At the beginning the plasma is quite dense and has ability to shield external electric fields. According to velocity of cloud expansion, after few nanoseconds the plasma density falls down that causes decoupling of ions and electrons in the cloud. The plasma cloud is separated on two independent sets of particles electrons and ions and the ability to shield external field is lost. Charged particles are driven just by external electric fields.

Depending on the impact velocity and mass of impinging particle, the particle can be partially (surface ionization) or completely (volume ionization) evaporated [Mocker *et al.*, 2013].

For volume ionization (impact velocities greater than 20 km/s) the energy of impacting particle is high enough to dissociate the molecules and even ionize the atoms.

In case of surface ionization (impact velocities less than 10 km/s), the ions are generated predominantly from the surface. The input energy is insufficient to vaporize the particle completely, but it is large enough to fragment particle into small droplets. Mainly inpurities with low ionization potential (alkali metals) are ionized after diffusion through the liquid material to the surface [Drapatz and Michel, 1974]. The impact charge yield can be expressed as a function of impactor mass and velocity by standard empirical formula

$$Q = \text{const.m}^{\alpha}\text{v}^{\beta}\,, \tag{3.5}$$

where Q is the generated ion or electron charge, m is the mass of grain, v impact velocity, and α and β are constants: $\alpha = 1$, $\beta = 3.5$ for impacts of iron particles on tungsten target [Dietzel *et al.*, 1973].

The standard empirical formula eq. 3.5 is the most often used equation for recollected charge despite the unknown uncertainties of Q. Amount of produced Q varies with the angle of incidence and composition of the impinging particle and the target material. Overview of impact charge yield relations adopted from the literature and extended by Collette *et al.* [2014] measurements was shown in Table 1.

One of the more important parameters of impact plasma is the temperature of species which are produced (electron and ions). Friichtenicht *et al.* [1971] assumed thermal equilibrium of the impact plasma and derived plasma temperatures from the degree of ionisation in a multi-element target via the Saha equation. They quoted values of ≈ 0.5 eV invariant with velocity over the range of 17–47 km/s.

Collette *et al.* [2016] measured recollected charge between the model spacecraft and antenna as a function of the spacecraft potential relative to the chamber wall. With a two-parameter nonlinear least squares fit of energetic distribution they obtained temperature of electrons 4.3 eV and ions 4.6 eV for slow impact speed 4 km/s. For higher speed 20 km/s, the temperature of ions was established as 23 eV and temperature of electrons decreased to 0.6 eV.

In another experiment performed by Ratcliff *et al.* [1997], the impacts of iron particles on rhodium target were investigated. The temperature of ions was found between 10 and 60 eV for a wide range of impact speeds and variety of ions species. The ion temperature were calculated from the widths of the ion mass lines in a time-of-flight arrangement.

Chapter 4

Goals of the thesis

In previous sections, we discussed the importance of the charging processes caused by plasma particles and solar radiation on the charge of dust grains and conditions of grain sputtering and alteration. It was shown that the dust can serve also as a source of plasma particles due to impact ionization process. This process allows us to study a composition of dust particles in mass spectrometers related to space applications [Sternovsky *et al.*, 2007; Kempf *et al.*, 2012; Srama *et al.*, 2006].

All these processes play a key role in the interplanetary medium with important consequences for environments like the lunar surrounding, planetary rings, cometary tails, and the Earth's magnetosphere. Investigations *in-situ* are complicated because complex specialized instruments on the various spacecraft measure only results of a combination of several processes acting simultaneously under particular conditions. Nevertheless, they may be studied in laboratory setups where these processes can be separated or the influence of a surrounding environment can be suppressed. Last but not least, laboratory experiments use precisely defined conditions and parameters.

In the interplanetary space, relevant charging processes are interactions with electrons and ions of the solar wind and photons from solar UV radiation. For example, the dayside lunar surface is positively charged as a consequence of the photoemission current. In this case, an equilibrium surface charge leads to the electric potential that prevents further photoelectrons to escape. All other charging currents are small and they are balanced by a portion of photoelectrons with energies above the surface potential and this portion as well as the photoelectron energy depends on the work function of the dust grain material. Since the direct spacecraft measurements are difficult, we finish the development of a unique experimental setup with a linear electrodynamic trap. The original set-up allowed to charge dust grains of various materials (conductive or dielectric) with the beams of particles (electrons and ions) but did not allow investigations of the photoemission. Thus, we introduce laboratory measurements (including development of corresponding experimental facility) of the photoemission from lunar dust simulant (Minnesota Lunar Simulant, MLS-1) samples of micrometer sizes. In a series of experiments, we store a single (charged) dust grain in an electrodynamic trap and expose it to electron and/or ion beams with variable energies and to photons from the UV source.

Hypervelocity impacts of dust particles on the antenna and/or spacecraft sur-

faces generate expanding plasma clouds that are (partially) recollected and generate transient voltage signals detectable by antennas of instruments like the RPWS (Radio Plasma Wave Science) onboard the Cassini spacecraft [Gurnett *et al.*, 2004]. Voyager and Cassini observed such spikes in conjunction with a passage through the rings of Saturn [Gurnett *et al.*, 1983; Wang *et al.*, 2006] and in a connection with Jovian dust streams. However, the profiles of the responses to the dust impacts are strongly influenced by the spacecraft potential that is determined predominantly by photoemission. In the laboratory conditions, the impact ionization process can be studied in the setup with a linear dust accelerator which provides impact velocities high enough to reach the threshold of the impact ionization process. In the thesis, we use the dust accelerator situated at the IMPACT (Institute for Modeling Plasma, Atmospheres and Cosmic Dust) facility in Boulder. This facility was equipped with the reduced Cassini spacecraft model with antennas in monopole and dipole configurations that allows us to study the proportionality between the amplitude and shape of produced antenna signals and preselected parameters of grains as well as effects of the spacecraft potential.

We can formulate particular tasks of the thesis as:

(1) To complete the experimental set-up based on a linear electrodynamic trap with the UV source, and to design and to build all necessary electronic circuits for measurements of the charge-to-mass ratio of the captured grain.

(2) To test a whole system of measurements of the photon flux for a variety of working gases (He, Ar, Ne, H_2) and UV source operation modes.

(3) To determine parameters of the captured grain (the grain size, its surface potential and work function) using a time evolution of charging/discharging processes and to compare these parameters for irregularly shaped and spherical grains.

(4) To design and fabricate a new simplified scaled down model (approximately 1:20) of the Cassini spacecraft for the IMPACT facility and to investigate iron grain impacts onto the Cassini spacecraft model in both monopole and dipole configurations of RPWS instrument for various spacecraft potentials, velocities and masses of the grains.

(5) To analyze the measured data and to find possible relationships between simulation results and the data measured by Cassini in Saturn rings.

Chapter 5

Photoemission study of dust in linear electrodynamic trap

The number of photoelectrons as well as their energy depends on the photoelectron yield and the work function of the dust grain material. Many authors tried to determine this parameter, but the direct measurements are difficult for insulators and especially for small irregular samples.

Sickafoose *et al.* [2000] studied photoelectric charging of dust particles 90 – 160 μm in diameter composed of Zn, Cu, graphite, and glass in two different experimental setups: for single grains dropped through the UV beam, and grains dropped through photoelectron sheath above the photoemitting surface. They found out that the UV iluminated grains are more positive than non-iluminated grains and the grains dropped through a photoelectron sheath are strictly negative.

Sternovsky *et al.* [2002] determined the work function of a lunar regolith simulant (JSC-1) using the contact charging method. The dust was dropped on substrates from different materials. They found that the contact charging with oxidized metal surfaces only slightly depends on the effective work function of oxidized surfaces. The effective work functions of two different samples of the lunar analog were determined by extrapolation as 5.8 and 5.6 eV.

Abbas *et al.* [2006] investigated the photoemission yield from lunar dust samples brought by the Apollo and Luna missions. They found that this yield is a rising function of the grain size and has a tendency to saturate for the largest investigated grains. However, the saturated value was an order of magnitude larger than that reported for bulk materials with a similar composition [Feuerbacher *et al.*, 1972].

For this reason we developed a new experimental setup with a linear electrodynamic trap in which we can study these processes separately on a single dust grain in conditions relevant to space.

One grain caught in the linear electrodynamic trap was irradiated by the UV source that can operate with a variety of gases (He, Ne, Ar, H_2, etc.). The distinct lines He I (21.2 eV) and He II (40.8 eV) in the He discharge and rich spectra of Ar and Ne can be used for determinations of photoemission parameters of the grain [Nouzák *et al.*, 2016]. The first photoemission charging by the Lymann UV line as the dominant UV line in the solar spectrum is introduced as well.

In next few sections, we briefly explain important characteristics of our exper-

imental setup, the UV source and measurement techniques for a determination of parameters of dust grains. In the last section, we describe experimental results obtained from MLS-1 (Minnesota Lunar Simulant 1) and MF (Melamine Formaldehyde) grain measurements.

5.1 Experimental setup

The base of our experimental set-up for study of charging processes of a single dust grain is a linear electrodynamic trap (in the center of Fig. 5.1). A more open design of the linear trap along the main axes in comparision to another type of traps [Paul and Steinwedel, 1956] is useful for photoemission investigations, because it eliminates production of photoelectrons on electrodes of the trap.

The charged dust grain can be suspended in an effective potential of this trap. The effective potential is formed by three independent RF fields, which have dominant quadrupole terms with minimum of the effective potential in the center of the trap [Beránek *et al.*, 2012]. These fields are generated by electric potentials on rods of the electrodynamic trap.

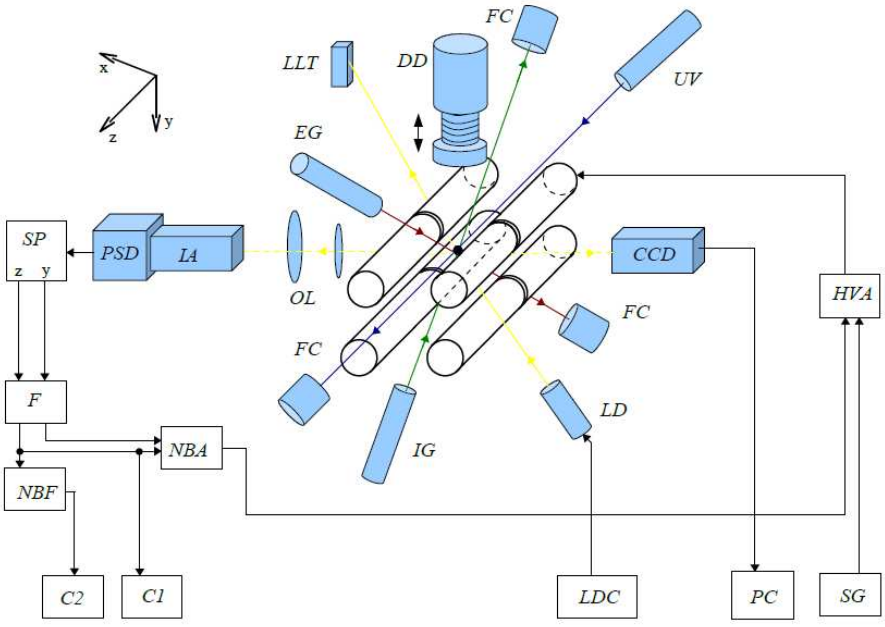


Figure 5.1: Experimental setup with linear electrodynamic trap (FC – Faraday cup, EG – electron gun, IG – ion gun, UV – UV source, DD – dust dropper, IA – image amplifier, PSD – position sensitive detector, PC – personal computer, HVA – high voltage amplifier, OL – optical lenses, LLT – laser light trap, SP – signal processor, F – filter, NBF – narrow band filter, NBA – narrow band amplifier, C1,C2 – counters, LDC – laser diode control, SG – signal generator, CCD – CCD camera).

The rods are supplied by eight high voltage amplifiers (HVA). Each of them can produce the voltage up to 5 kV with a frequency limit of 10 kHz. Input harmonic signal with a time window for shooting charged particles is provided by the programmable signal generator (SG).

Dust grains are shaken out mechanically from the dust dropper (DD). Inside the dust dropper, there is a cup with a small cone hole in the center. Grains are transported to the small hole by mechanical vibrations. Dust grains then fall to the potential mimimum of the trap. The falling grain can be charged by particle sources and become trapped in this efective potential. Three different types of particle sources can be used for charging: electron gun (EG), ion gun (IG) and differentially pumped UV lamp (UV).

Currents from these sources are measured by gridless Faraday cups (FCs) [Nouzák, 2010]. Particular currents are stabilized by feed-back loops.

The charged grain caught in the trap is irradiated by a red laser diode with the maximum power 100 mW and wavelength 638 nm. The wavelength of light is choosed according to sizes of investigated grains (up to 1 μm in diameter) and sensitivity of an optical amplifier. The beam from a laser diode (LD) is modulated by the laser diode controler (LDC) at the frequency of 50 kHz, which allows us to use the synchronous optical detection technique of light scattered by the grain and to increase the signal to noise ratio. Light scattered by the levitated grain is focused throught system of the lenses (OL) to an image amplifier (IA) and detected by a position sensitive detector (PSD) (surface PIN diode) that converts the optical signal to electrical signals connected to the signal processor (SP).

The processor unit provides a projected position of the grain image on a plane of PSD in form of two electrical signals which describe the grain motion. These signals are also used for active damping/stabilization of dust grain oscilations [Čermák *et al.*, 1995]. After damping two of three independent oscillations of the grain, only one electrical signal describing the grain motion remains. This signal is amplified with the narrow-band amplifier (NBA) and its frequency, f_x is measured precisely with the connected frequency counter (C2). From the measured oscillation frequency of the grain, f_x it is possible to determine its charge-to-mass ratio according to "trap equation"

$$\frac{Q}{m} = \frac{4\pi^2\sqrt{2}f_x f_{AC} {r_0}^2}{\lambda_z V_z}\,, \tag{5.1}$$

where f_{AC}, V_z are the frequency and amplitude of the trap supply and r_0, λ_z are geometric parameters of the trap (see Beránek *et al.* [2012] for details). The Q/m evolution is recorded throughout experiments.

During Q/m measurements, the grain is kept in an electrical center of the trap. An electrical force for compensation of the gravity is achieved by the DC voltage applied on top and bottom electrodes. The compensation voltage U_G is indirectly proportional to the Q/m ratio of the grain

$$U_G \approx \frac{g}{0.15 \cdot 10^{-3}[m^{-1}]} \left(\frac{Q}{m}\right)^{-1}\,, \tag{5.2}$$

where g is the gravitational acceleration.

5.1.1 Electron gun

The experimental setup is equipped with a commercial electron gun, SPECS EQ 22/35 with the available energy range of 100 eV – 5 keV. The spot size of the

electron beam can be adjusted down to 50 μm. The size of the emission current is controllable in the range of 0.01–250 μA and can be measured by the gridless Faraday cup situated opposite to the electron gun. The electron beam is sampled according to the time window in the harmonic signal of the trap, because the electrons would be deflected by the trap field which would influence the measurements. The electronic cuircuit inside the electron gun power unit ensures that electrons from the electron gun enter the trap exactly when the electrodynamic field of the trap is zero and also allows change of the width of the time window.

5.1.2 Ion gun

As a source of ions, the ion gun SPECS IQE 12/38 with the energy range of 100 eV – 5 keV is used. The ion gun IQE 12/38 is divided into three different stages, ionization, focusing and deflection.

The ionization chamber consists of the anode in the form of a grid cylinder and an Ω-shaped iridium ribbon cathode. A cylinder around these electrodes forms the ionization chamber and also acts as repeller.

A conical extractor electrode accelerates ions out of the plasma area and forms the ion beam. After the ion beam succesfully passes the output aperture, the double system of lenses focuses it on the sample.

A pair of deflection plates is used for electrostatic deflection of the ion beam from the main axis of the ion source. The sampler with deflection electrodes placed between ion source and vacuum chamber allows ion source modulation according to the width of time window in the electrodynamic field of the trap. The maximum operating current is 10 μA at energy of 5 keV. The power supplies of the electron and ion guns are remotely controlled via IEC 488 or RS 232 interface.

5.1.3 UV source

As the UV source we use differentially pumped UV discharge lamp from the SPECS company (UVS10/35). A high intensity photon beam is directed windowless onto the grain by discharge and guide capillaries. The beam guide capillary of length 200 mm is 1.3 mm in diameter and can be replaced with smaller one with 0.8 mm in diameter. The inner diameter of the collimating capillary determines the photon flux output. The small capillary diameter ensures good coliminating conditions of the UV beam and eliminates creation of background photoelectrons on rods of the trap. The guide capillary is differentially pumped that allows UHV conditions in the experimental chamber during the operation of the UVS 10/35.

The UV source is based on hollow cathode construction and the UV radiation originates in the area of the cathode fall and positive column of the glow discharge. A pin anode is at positive high voltage and extends into the quartz discharge capillary. The cathode is made from a material that guarantees a high cathode fall and low sputter rate.

The UV source can operate with a variety of noble and other gases (He, Ne, Ar, Kr, Xe, H_2, etc.) and can be run with extremely high portions of He II, Ne II, etc. excitation lines in addition to the high intesities of He I, Ne I, etc. The ratio of He II/He I, Ne II/Ne I can be adjusted by change of pressure conditions in

differential pumping stages of the UV source.

The typical working conditions of the UV lamp are [Specs, 2006]:

- The pressure in the discharge capillary: $0.1 - 5\,\mathrm{mbar}$.
- The pressure in the first pumping stage: $5 \cdot 10^{-3} - 5 \cdot 10^{-1}\,\mathrm{mbar}$.
- The pressure in the second pumping stage: $1 \cdot 10^{-6} - 1 \cdot 10^{-4}\,\mathrm{mbar}$.
- Discharge current in the main capillary: $20 - 120\,\mathrm{mA}$.
- Initial break-down voltage: $6.5\,\mathrm{keV}$.
- Discharge voltage: 650–700 V for He I and 300–400 V for Ne I.
- Input power: 120 W.

The UV source power unit allows to add 6 kV for a intial breakdown of the working gas in discharge capillary. After this breakdown the voltage falls down to value given by the type of the working gas and only discharge current is possible to change. The operational range of discharge current is between 20–120 mA. The 20 mA is a limit for UV discharge extinguish and 120 mA is a limit of power unit and cooling ability of the UV source. The manufacturer of the UV source recommends maximum runing operational discharge current 100 mA.

Maximum available energy of photons depends on type of working gas. The highest excitation energy 53 eV has He with its line $\mathrm{He\,II}_{\gamma\delta}$. But, its intensity is less than 100 times lower than most abundant $\mathrm{He\,I}_{\alpha}$ line with energy 21.2 eV and 20 times lower than $\mathrm{He\,II}_{\alpha}$ line (40.8 eV) [Cardona and Ley, 1978]. Relative intensities of lines depend on condition of the discharge and can vary with the impurities of the working gases.

The third gridless Faraday cup, which behaves also as the UV light trap, is situated against the UV source and can measure UV flux of the UV source.

5.1.4 Vacuum system

The experimental setup consists of few different vacuum parts: experimental chamber, ion gun and UV source. Vaccum connection with distribution of working gases is shown in Fig. 5.2.

The electrodynamic trap is located in the center of the experimental chamber.

The ion gun and UV source together with the electron gun, laser beam colimator, Faraday cups, and dust dropper are connected to the experimental chamber. The ultimate pressure is $2 \cdot 10^{-8}$ mbar in the chamber and allows operation of the experiment in the UHV conditions.

The experimental chamber is connected through electro-pneumatic valve to the main turbo pump Pfeiffer TMU 520 and vacuum gauges or aditional ion pump. The turbopump TMU 520 is pumped with smaller flow turbopump Pfeiffer TMU 071 and backed by TriScroll 300 from Varian.

The ion gun and UV source have differential pumping consisting of turbopumps Pfeiffer HiPace 80 backed by TriScroll 300 in the case of the second differential pumping stage of the UV source and Pfeiffer HiCube Eco diaphragm pump in case of the ion gun. The first stage of the UV source differential pumping is connected directly to the dry pump TriScroll 300.

The experimental setup is equipped with the system for a distribution of working gases (He, Ar, and H_2) for the ion gun and UV source. The distribution

system doesn't allow use different types of gases for simultaneous operation of the ion gun and UV source. As the damping gas is used He, which is connected directly through the sapphire UHV valve to the main chamber.

The pressure is measured by different types of gauges: Pirani gauges for forvac measurements, thermocouple gauge for setup working conditions of UV source, cold-cathode gauges for measuring ultimate pressure in the main chamber and between the TMU 520 and TMU 071. The cold-cathode gauge is also used for setup of working pressure conditions of the ion gun.

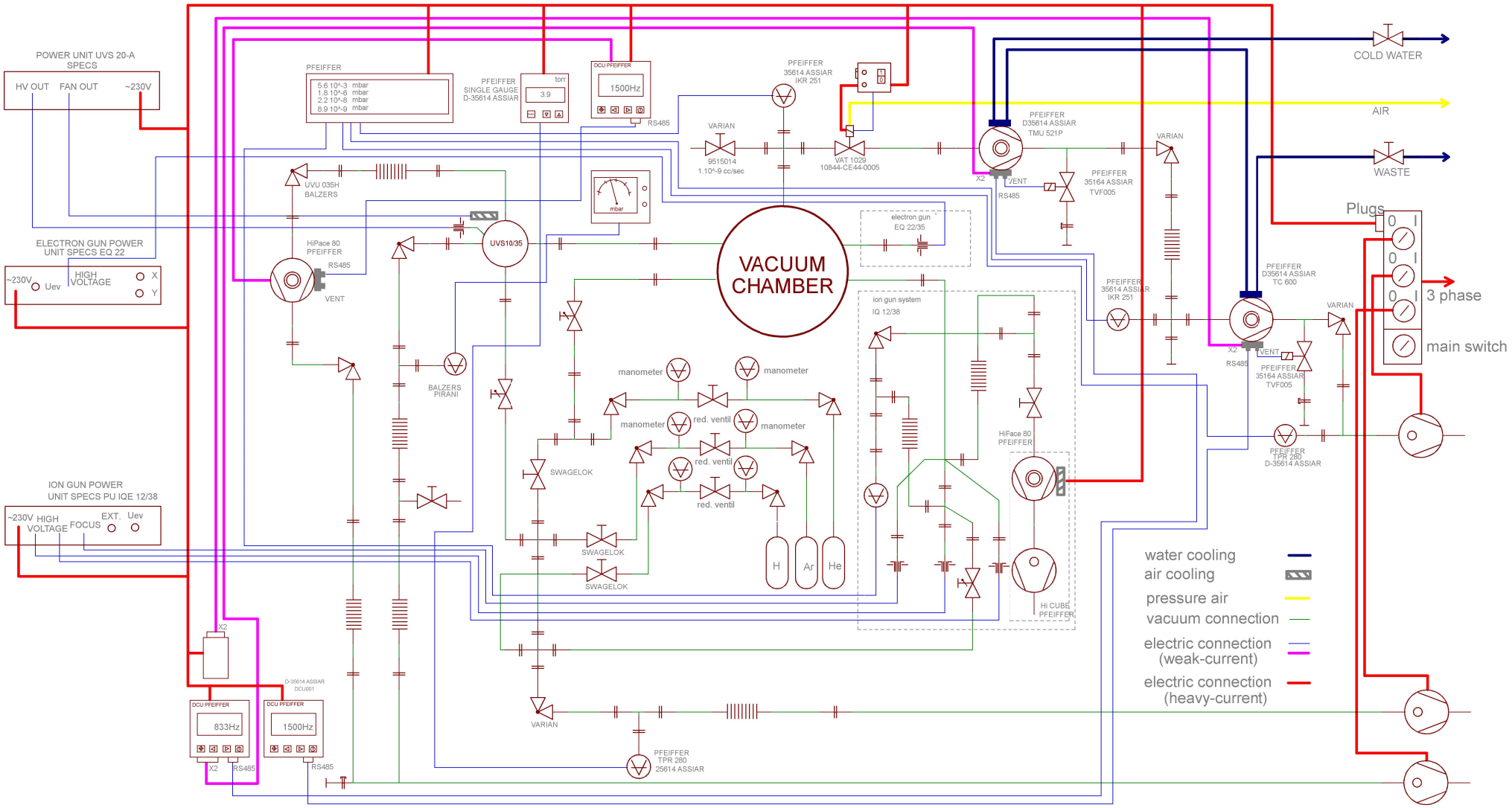


Figure 5.2: Vacuum and electronic schematics of the experimental setup.

5.2 Measurement techniques

Several measurement methods to determine parameters of the grain (mass, its surface potential) and parameters of the UV source (photon energy and flux) have been developed.

5.2.1 Determination of the grain mass

The method for determination of the mass is based on the Millikan experiment [Millikan, 1913] and was in detail described by Žilavý *et al.* [1999]. When the grain has small amount of charge itself (thousand of elementary charges) it is possible to measure changes of individual elementary charges. The change of the grain charge (change of its frequency) can be induced by the electron or ion guns. For this purpose, it is necessary precisely tune the current and the time window for a particular shot.

Then the change of the charge (i.e., frequency, note that the mass of the grain changes negligibly) can happen in small steps as it demonstrates Fig. 5.3. From a step in the frequency f_x coresponding to one elementary charge we can easily determine the mass of the grain

$$m = \frac{e f_x}{(\frac{Q}{m})\Delta f_x} \,. \qquad (5.3)$$

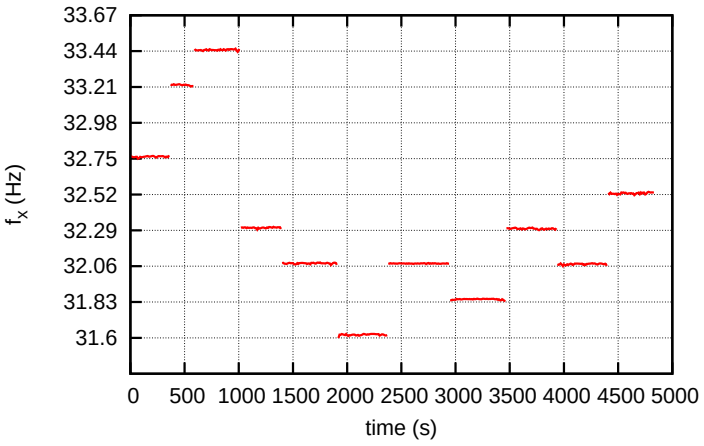


Figure 5.3: Individual elementary changes of the grain charge.

The method doesn't require any assumptions on the measured grain (its size, shape, or even material).

5.2.2 I–V characterictеristics

The method is based on charging of dust with ions of a higher energy (e.g., 1 keV) and consecutive bombardement by ions with the energy lower than the equilibrium potential of dust Čermák *et al.* [1995].

Because the ions with a lower energy can't reach the grain, the grain is slowly discharged by secondary electrons produced due to the impact of ions on the electrodes of the trap or walls of the vaccum chamber.

The discharging current is proportional to the grain surface potential for the fixed energy and current of ions.

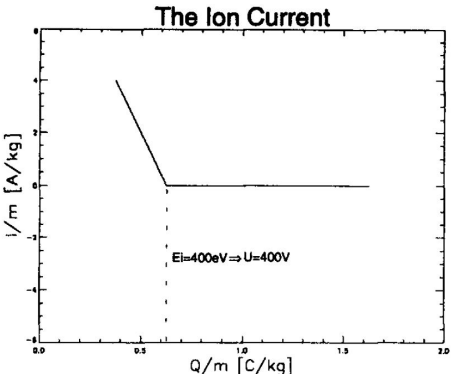


Figure 5.4: Change of the slope in the I–V characteristics equivalent to the energy of incident ions. Adopted from Čermák *et al.* [1995].

When dust is dicharged below the potential equivalent to the energy of incident ions, the ions start interact again with the grain and reduce the discharging current Čermák [1994]; Čermák *et al.* [1995]. This moment is represented by the change of the slope in the I–V characteristics (Fig. 5.4). The break point matches to equality of the grain surface potential and energy of incident ions. Exactly at this point, we know the surface potential of the grain and its charge-to-mass ratio.

From equation 2.2, it is easy to determine the capacitance of the grain. With assumptions of grain sphericity and knowledge of the grain mass density, ρ we can calculate size, R and mass, m of the grain from Q/m and φ

$$R = \sqrt{\frac{3\varepsilon_0}{\rho}\varphi\left(\frac{Q}{m}\right)^{-1}}, \tag{5.4}$$

$$m = \frac{4}{3}\pi\frac{1}{\sqrt{\rho}}\left[3\varepsilon_0\varphi\left(\frac{Q}{m}\right)^{-1}\right]^{\frac{3}{2}}. \tag{5.5}$$

The disadvantages of this method are less accuracy caused by derivation of discharging characteristics and its impossible use of smaller dust grains (they have for the same surface potential too large Q/m values).

5.2.3 Determination of UV photon flux

The estimation of the UV photon flux is based on photoelectron saturation currents measured by a gridless Faraday cup (Fig. 5.5) [Nouzák *et al.*, 2013].

The absence of the grids ensures that photoelectrons cannot be generated on their surfaces and influence the current measurement. The gridless Faraday cup (FC) is used as an integral energy analyzer. It consists of two coaxial electrodes of a special shape and a collector [Thomas *et al.*, 2005] which was covered by a micrometer-thick Au layer to define the photoelectron yield and work function of the FC collector.

The voltage, U on two coaxial electrodes and zero potential on the collector set up a potential barrier with effective height that the photoemitted electrons have to overcome when they want to leave the collector area.

The current from the collector at a given voltage, U_0 is proportional to the total number of electrons with energies between $eU_0 = E_i$ and $eU_{max} = E_{max}$ according to

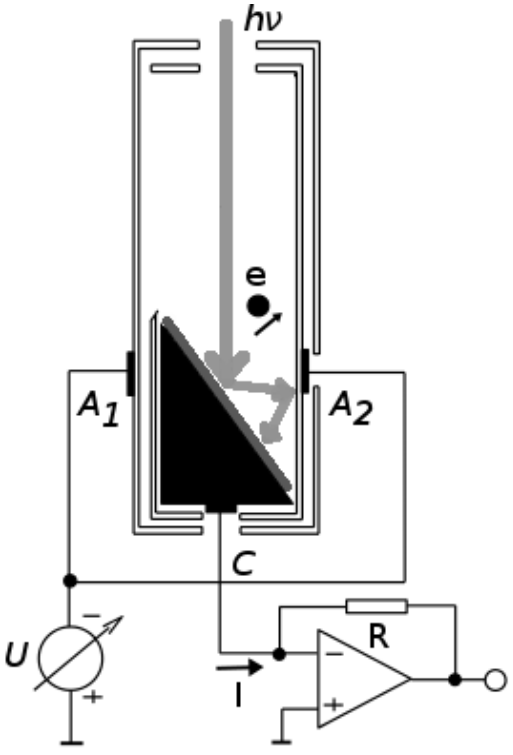


Figure 5.5: Principle of the gridless Faraday cup measurements.

$$I(E_i) = \int_{E_i}^{E_{max}} N(E)dE \tag{5.6}$$

where U_{max} is the voltage necessary to set up a potential barrier for electrons in the energy distribution with the maximum energy E_{max}. The energy distribution of the electrons $N(E)$ can be obtained by differentiation of eq. 5.6 with respect to E_i. The collector current is measured by the current–voltage convertor connected to a 16 bit ADC [Nouzák, 2010]. The voltage sweep on electrodes A_1 and A_2 (Fig. 5.5) is generated by a 16 bit DAC. Both circuits are controlled via an I^2C interface allowing flexibility when connected to the data acquisition system of the experimental setup.

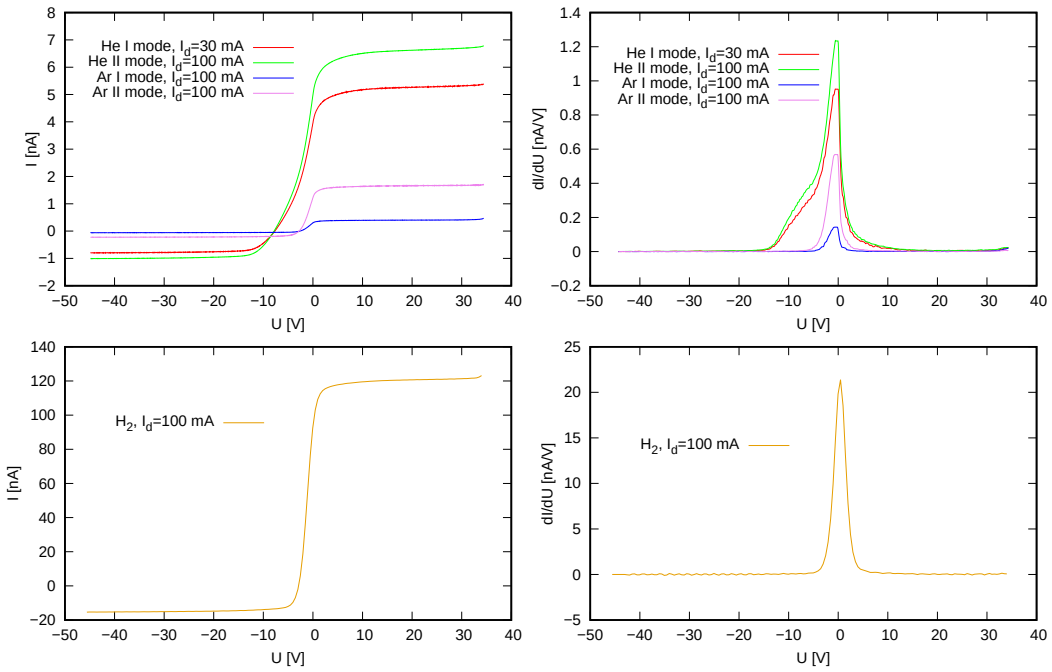


Figure 5.6: Photoelectron integral (left column) and differential (right column) energy distributions measured by the gridless Faraday cup for different gasses (He, Ar, and H_2) and various operation modes of the UV lamp.

Typical integral characteristics measured for the discharge in the He, Ar, and H_2 gas are depicted in Fig. 5.6 – left. Their corresponding differential characteristics are in Fig. 5.6 – right. The differentiation of characteristics is performed numerically and actually, doesn't contain information about the electron energy distribution from the collector (C in Fig. 5.5) only. Approximately 1.4 % (for He I line) and 100 % (for He II line, due to a total reflection at the collector) of the incident UV light [Palik, 1985] is reflected to the second electrode A_2 of the FC (see the saturated currents in the integral characteristics). A second reflection from the electrode A_2 is approximately 0.2 % (for He I line) and 10 % (for He II line) and has minimal consequences for saturation current measurements. In this geometry with the top angle of the FC collector 29°, the incident light can hit the electrode A_1 only after seven reflections between the electrode A_2 and the FC collector and its current contribution is negligible. The kinetic energy of released photoelectrons cannot exceed the energy of He II photons.

For the positive voltage U=35 V on A_1 and A_2, we can suppose that the photoelectrons from C and A_2 are attracted to electrodes A_1 and A_2. In the current measurement, only the photoelectrons from the collector C can participate

because the photoelectrons from A_2 cannot leave an area of the electrode. The saturated current for a positive voltage corresponds to the collector saturated current created by He I photoelectrons only.

In the case of the negative voltage U= –45 V on A_1 and A_2, the photoelectrons from the collector C are returned and only photoelectrons from A_2 participate in the current measurement, i.e., He II photoelectrons dominate.

5.3 Experimental results

This chapter summarizes results obtained in course of the photoemission investigation. For experiments we choosed two samples of MLS-1 grains (Fig. 5.7) as a suitable lunar regolith candidate, glass, and MF grains. The MF grains were studied for two reasons: their sphericity (easy to compare with results for irregular samples) and problems with determination of their work function from field emission measurements. The detailed description of results can be found in attached publications [A2]–[A4].

5.3.1 Photoemission of lunar dust simulant

The surface of the Moon covered by a layer of dust grains is exposed to particles from the solar wind. On the sunlit side of the Moon, the photoemission dominates other charging processes and the work function of grains determines the maximum energy of photoelectrons originated from the Moon surface. Consequently, the irradiated lunar surface is positively charged as a consequence of the photoemission current. On the dayside, an equilibrium potential +4 V is established and the charged surface prevents further escape of photoelectrons. The photoemission parameters of lunar grains as the photoelectron yield or work function are key parameters which characterise the processes of photoemission charging.

A determination of the work function *in-situ* is desirable, but probably impossible because we can observe only an equilibrium state of charging due to different charging processes. Nevertheless, it is possible to investigate it on a single dust grain in laboratory conditions.

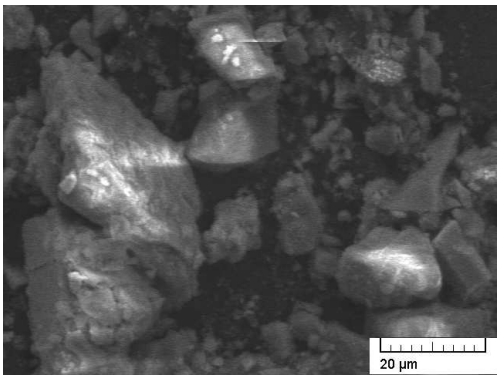


Figure 5.7: SEM picture of MLS-1 grains.

In following sections, we briefly describe measurement techniques which we used for a determination of the work function and photoemission yield of the grain.

Measurement technique

The measurement technique uses the current–voltage (I–V) plot method (variation to subsec. 5.2.2) for at least two but rather more UV emission lines.

When the dust grain is charged more than would be given by the highest emission line (eq. 2.19) presented in the discharge and the UV source is turned on, the background photoelectrons start to discharge the grain and to reduce its potential. When the grain reaches the potential corresponding to the line

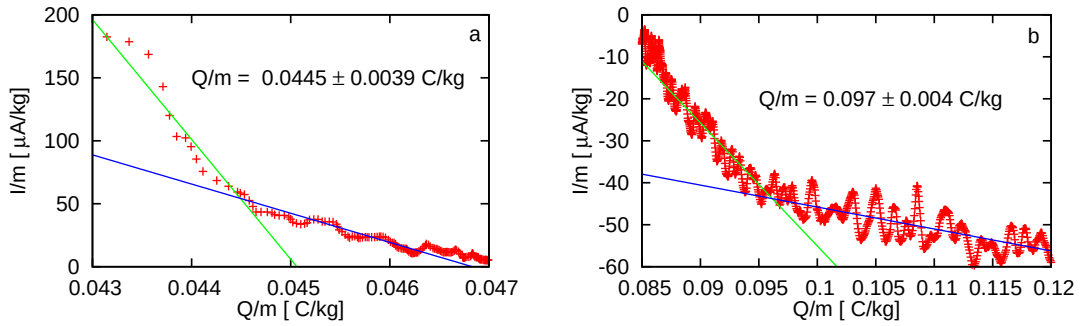


Figure 5.8: Examples of I–V plots. (a) I–V plot recorded during charging by a group of He I lines. (b) I–V plot recorded during discharging of the grain by He II lines.

in the discharge, the photoelectrons start to leave the grain and to reduce the discharge current. A time derivation of measured Q/m (t) during the experiment determines the discharging current

$$\frac{d}{dt}\left(\frac{Q}{m}\right) = \frac{I}{m}\,. \tag{5.7}$$

The plot I/m versus Q/m is called the I–V plot, because Q/m is proportional to the grain potential. Every change of the discharge current, for example due to transition over another emission line of the UV source, is recorded in the I–V plot and is visualized as a knee in the plot. The example of the knee determination is in Fig. 5.8.

Determination work function

The key point of the work function estimation is finding a relation between the grain potential and its specific charge for at least two emission lines.

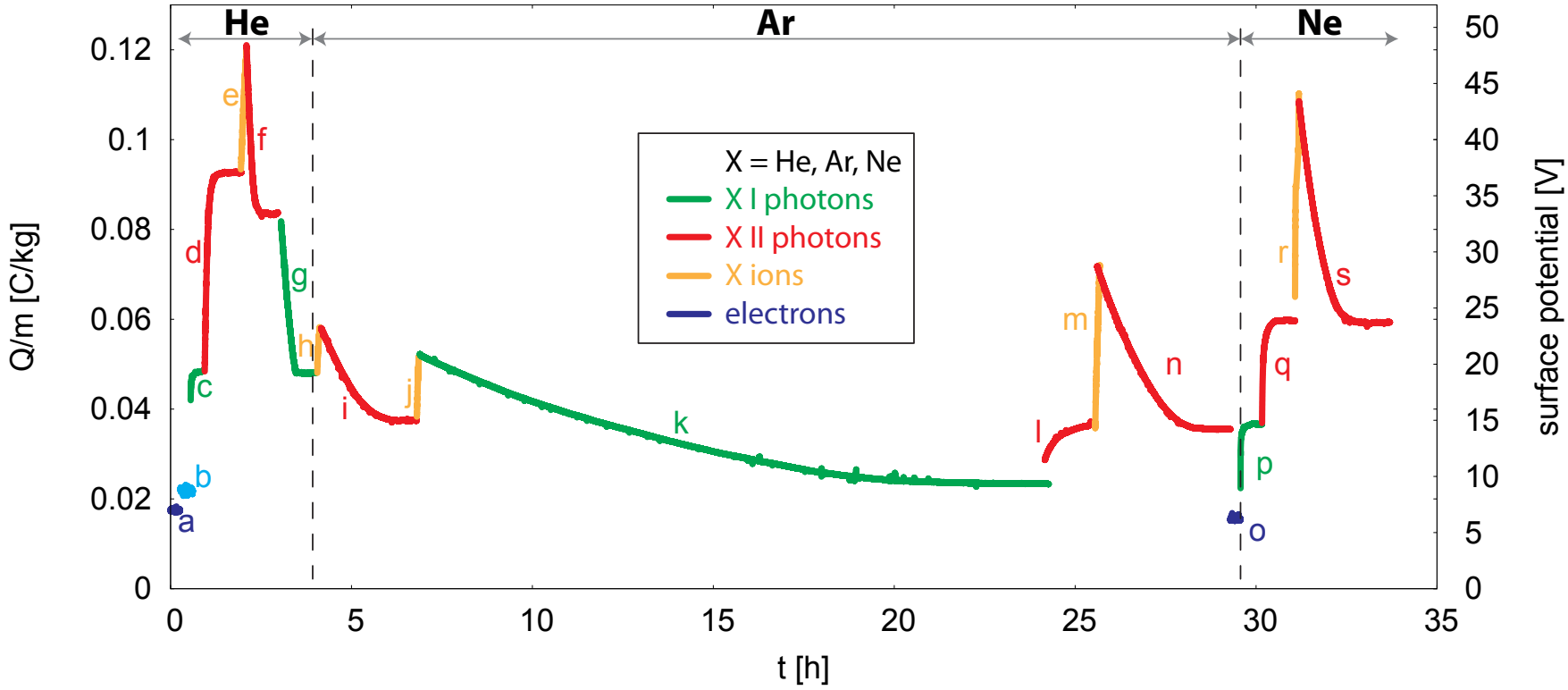


Figure 5.9: Charging and discharging procedure of the grain for three different gases in the UV source. Adopted from [Nouzák *et al.*, 2016].

We made a full sequence of grain charging and discharging in three different gases to identify a sufficient amount of lines (Fig. 5.9). In Tab. 5.1, the list of charge-to-mass ratios and emisson lines identified in the discharges of He, Ar, and Ne for two MLS-1 grains is presented.

The resulting work functions for two grains are shown in Fig. 5.10. The position of the points on the horizontal axis is given by the energy of a particular emission line. The vertical axis provides the grain specific charge. The error bars show the uncertainties of the linear fits of I–V plots. The determined values of $W_{4.7\mu m} = (5.9 \pm 0.3)$ eV and $W_{4.0\mu m} = (5.1 \pm 0.7)$ eV are in an accordance with the value of $W \approx 5.8$ eV for the JSC-1 lunar regolith simulant obtained by the contact charging method [Sternovsky *et al.*, 2002].

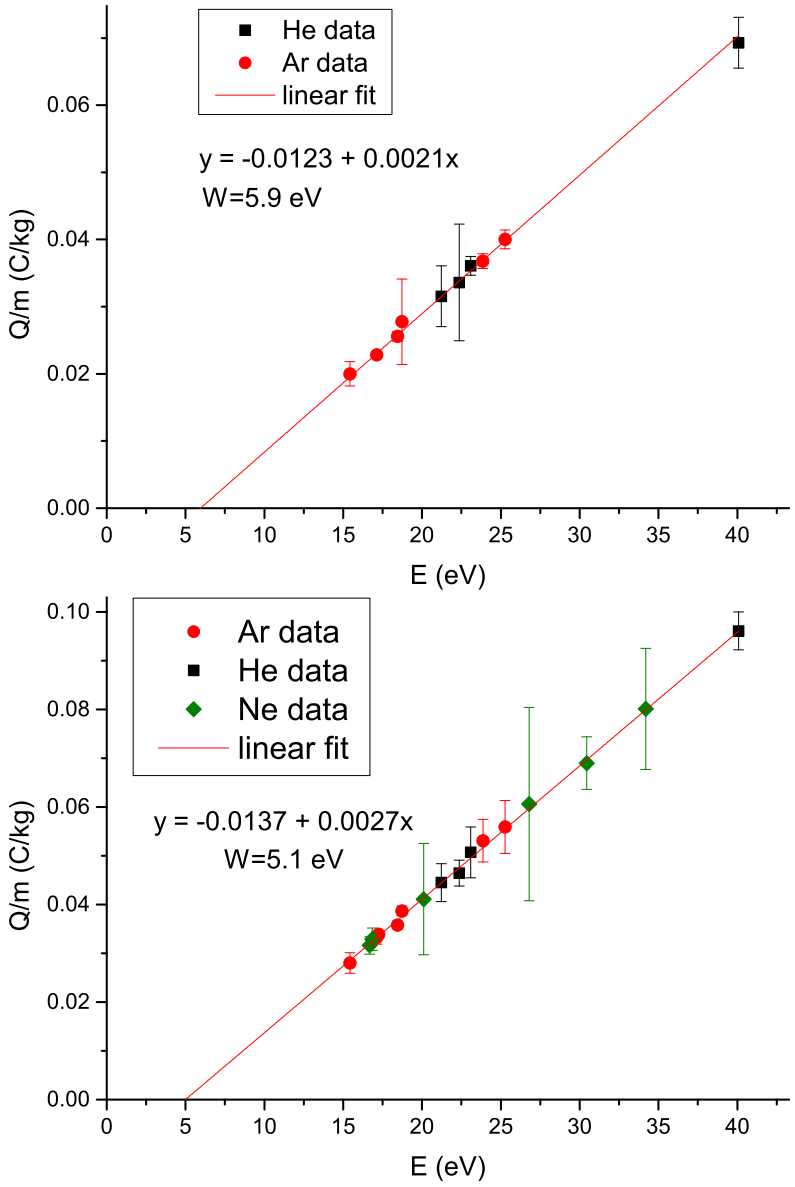


Figure 5.10: The work functions determined for two MLS-1 grains. Adopted from [Nouzák *et al.*, 2016].

Emission line	Excitation energy (eV)	Wavelength (nm)	Q/m $_{d_{ef} \approx 4.7\,\mu m}$(C/kg)	Q/m $_{d_{ef} \approx 4.0\,\mu m}$(C/kg)
Ar I	15.43	80.35	0.0200 ± 0.0018	0.0280 ± 0.0021
Ar II	17.13	72.38	0.0228 ± 0.0005	0.0332 ± 0.0013
Ar II	17.26	71.83	0.0256 ± 0.0007	0.0339 ± 0.0007
Ar II	18.44	67.23	0.0278 ± 0.0064	0.0358 ± 0.0008
Ar II	23.87	51.94	0.0368 ± 0.0011	0.0387 ± 0.0010
Ar II	25.26	49.08	0.0400 ± 0.0014	0.0559 ± 0.0054
He I	21.22	58.43	0.0316 ± 0.0045	0.0445 ± 0.0039
He I	23.08	53.72	0.0361 ± 0.0014	0.0507 ± 0.0052
He II	40.82	30.93	0.0703 ± 0.0038	0.0971 ± 0.0039
Ne I	16.67	74.38		0.0316 ± 0.0018
Ne I	16.85	73.58		0.0329 ± 0.0023
Ne I	20.14	61.96		0.0411 ± 0.0114
Ne II	26.82	46.26		0.0606 ± 0.0198
Ne II	30.45	40.72		0.0690 ± 0.0054
Ne II	34.21	36.25		0.0801 ± 0.0124

Table 5.1: Table of emission lines identified in the different discharges.

Glass dust grains are also space-related (material composition relevant to lunar dust material [Hill *et al.*, 2007]) and well suitable for studies of their interaction with plasma particles and UV radiation due to their sphericity. The UV photoemission properties of glass grains were also studied [Nouzák *et al.*, 2014]. The work function of those grains was established by a similar method like in the case of MLS-1 grains as $W_{5.4\,um} = (4.7 \pm 1.5)\,eV$. The smaller value of the determined work function for glass grains suggests that it is probably influenced by the shape and purity of the grain material.

Melamin formaldehyde (MF) grains are widely used in laboratory dusty plasma experiments, because they are available in a broad range of sizes and they have low-mass density, monodispersity, sphericity and good optical reflectivity.

Nevertheless, many authors have found that some parameters of MF grains can change during particular experiments. The variations of the parameters depend on types of the plasma environment.

One of very important parameters is the work function of MF resin grains. Pavlů *et al.* [2006a] tried to estimate the work function of MF grains from discharging of these grains by field emission using the Fowler–Nordheim method. Because the resulting plots were neither stable nor linear, the authors couldn't determine reliable the work function, thus they estimated the value in a very broad range (1.4–7.5 eV).

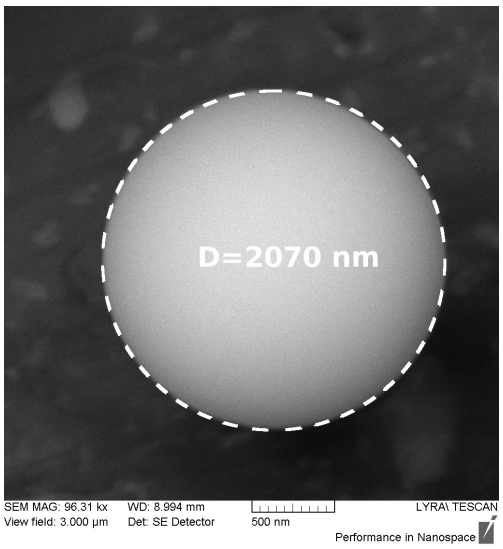


Figure 5.11: SEM picture of a spherical MF grain.

We used the UV photoemission method for investigations of the MF work function [Vyšinka *et al.*, 2017]. This method has one huge advantage, it does not involve any particles (electrons or ions), which usually cause some disorders in the material of the grain, but uses photons instead. In addition, the maximum surface potential is given by the maximum energy of UV photons (up to 50 eV), which means that the photoemission keeps the surface potential of the grain low and can't destroy organic bonds like in the case of charging by electrons to field emission limit. In summary, the method is considerate to the grain material. The work function of the MF grain was establish $W = (4.4 \pm 0.2)\,eV$.

To check a possible influence of low-energy (400 eV) electrons on the work function, the grain was bombarded for 35 hours and the work function was determined again. The measured value of the work function was $W' = (4.5 \pm 0.2)\,eV$. Moreover, there is no evidence that a specific capacitance of the grain has changed in course of the experiment.

Photoemission yield

The photoemission yield as the ratio of a number of incoming photons to emitted electrons was determined by the photon flux measuring technique (described in chapter 5.2.3).

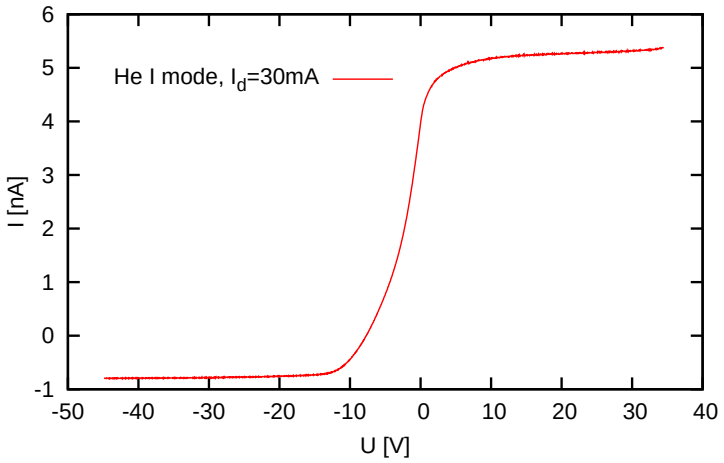


Figure 5.12: Photoelectron integral energy distribution measured by the gridless Faraday cup in the He I mode.

The gridless Faraday cup measurement in the He I mode represents typical integral energy distribution characteristics (Fig. 5.12). The saturated current for the He I mode is

$$I_{\mathrm{He\,I+He\,II}} \approx 5.3 \cdot 10^{-9}\,\mathrm{A}\ . \tag{5.8}$$

In this mode, the ratio of He I and He II photons should be 1:4 [Specs, 2006]. The contribution of He I photons into the saturated current is

$$I_{\mathrm{He\,I}} \approx 3.6 \cdot 10^{-9}\,\mathrm{A}\ . \tag{5.9}$$

The photon density for the He I mode (supposing quantum yield of the gold sample in FC $\eta_{\mathrm{gold}}(21.2eV) \approx 0.12$ Nitta *et al.* [2010]) measured by the gridless Faraday cup is

$$I_{\mathrm{ph,He\,I}} \approx 1.6 \cdot 10^{14}\,\frac{\mathrm{ph}}{\mathrm{s.sr}}\,, \tag{5.10}$$

and the approximate photon flow on the grain is

$$\Gamma \approx 33789\,\frac{\mathrm{ph}}{\mathrm{s}}\,. \tag{5.11}$$

Since the charging current is proportional to the photon flow, Γ and the photoelectron yield of the grain, η_{dust} is defined as

$$I^0_{\mathrm{ph,He\,I}} = e\Gamma\eta_{\mathrm{dust}}\,, \tag{5.12}$$

we can determine the photoelectron yield of the grain as

$$\eta_{\mathrm{dust}}(21.2\,eV) = 0.05\,. \tag{5.13}$$

This value is in a good agreement with measurements of Feuerbacher *et al.* [1972] on powdered samples of the lunar dust (48 % of glass, 18 % of Al_2O_3)

$\eta_{\text{lunar}}(21.2eV) \approx 0.02$. However, Feuerbacher *et al.* [1972] pointed out that the measurements of the photoelectron yield on powdered sample might result in yields that are too low; for isolated particle the yield can be significantly larger [Weingartner and Draine, 2001].

Chapter 6

Investigation of dust impact from antenna signals

Assuming that the antenna signal generation process is charge recollection from the impact plasma, the polarity and the amplitude of the detected signal is determined by: (1) the total generated impact charge (which in turn depends on the dust mass and the impact speed), (2) the surface potential of the SC/antenna that controls the fraction of the recollected charge, (3) the measurement mode (dipole/monopole), (4) the impact location (material properties, potential geometry effects).

Two different models were proposed by Gurnett *et al.* [1983] for converting the charge to a voltage pulse after the impacts on the spacecraft body.

First model is called the antenna collection model. It supposes that the voltage pulse in the dipole configuration of antennas is created due to collection of different amount of charge on these antennas. It is very unlikely that the impact will symmetrically occur in the middle of dipole, thus the charge collected by one antenna will be always larger than on the other one. The amplitude of the voltage pulse ΔV_{ANT} can be written as

$$\Delta V_{ANT} = \alpha \frac{Q}{C_{ANT}}\,, \tag{6.1}$$

where α is a collection coefficient, C_{ANT} is the antenna capacitance and Q is the charge produced due to the impact. The collection coefficient depends on geometry of the spacecraft and antennas.

The second model is called spacecraft collection model, because the signal is produced as a response on the charge recollected by the spacecraft body. Since the plasma cloud is formed close to the huge surface of the spacecraft body in comparision to surface of antennas, the spacecraft body is efficient collector and amplitude of the voltage pulse is given by

$$\Delta V_{SC} = \frac{Q}{C_{SC}}\,, \tag{6.2}$$

where C_{SC} is capacitance of spacecraft. The corresponding signal on the monopole antenna, ΔV_{MON} is related to the amplitude of the voltage pulse, ΔV_{SC} of the spacecraft body through a geometric coupling constant, Γ ($\Delta V_{MON} = \Gamma \Delta V_{SC}$).

In most studies, the particles hitting directly the antennas are neglected because the spacecraft body is a much bigger target. On the other hand, impacts

directly on the antenna would produce a much larger signal, especially if the antenna is biased and nearly all charge of one sign is recollected by antenna.

In the case of direct impacts on the antennas, in both the dipole and monopole configurations, the amplitudes of generated signals will follow equation 6.1 with collection coefficient close to 1.

Oberc [1996] suggested that besides processes of recollection of impact charges by the spacecraft body and the antennas, also voltage pulses due to the electric field created by the charge separation inside the expanding plasma cloud are generated. The other possible way for producing of the voltage pulses is induction of these pulses by escaping charges of the impact cloud [Meyer-Vernet *et al.*, 2014].

Pantellini *et al.* [2012] suggested that strong voltage pulses can be produced due to charging of the antenna with a temporary interruption of the photoelectron return current. Most of the photoelectrons emitted by the antenna have high eccentricity orbits and are located in a large distance from the antenna. Even a small energetic kick given by the expanding cloud of impact plasma can be sufficent to change the azimuthal velocity of photoelectrons and to disconnect them from the corresponding ballistic trajectory. This mechanism is not applicable on the spacecraft with a small antenna radius (WIND) or in a large distances from the Sun (Cassini).

Since the mechanism of destabilization of the photoelectrons suggested by Pantellini *et al.* [2012] is negligible due to small radii of the antennas on the Wind spacecraft, Meyer-Vernet *et al.* [2014] argued that there is only one mechanism which can explain production of positive pulses on the Wind spacecraft by nanodust remains – electron recollection. A plasma cloud generated during the impact of nanometer sized dust grains on a spacecraft body is too weak for production of the voltage pulses observed by the STEREO spacecraft between individual antennas and spacecraft body.

6.1 Experimental setup for antenna signal study

The Cassini RPWS instrument consists of three nearly orthogonal 10 m long, 2.5 cm in diameter electric field antennas, depicted in Fig. 14 [Gurnett *et al.*, 2004] as E_U, E_V, and E_W. The antenna elements are made of beryllium-copper and are silver plated on the exterior surface. The E_U and E_V antennas are often connected together in a dipole configuration, while E_W is typically operated in a monopole mode, measuring thus the antenna voltage relative to the SC body. This is also the configuration used in the experiments described below.

A simplified and scaled down model (approximately 1:20) of the Cassini spacecraft was designed and fabricated for the purpose of the measurements. Fig. 6.1 – left shows the main elements of the model that consists of the cylindrical DC body, the HGA on the top and the magnetometer boom. The antennas are electrically isolated from the body and are mounted on a small block. The body is machined out of aluminum, while the antennas are made out of 1.6 mm diameter, 50 cm long stainless steel rods. The size of the Cassini model was chosen to fit the available vacuum chamber without interference. The chamber is about 1 m in diameter and 1.5 m long (Fig. 6.1 – right). Both the body and antennas are coated with graphite to ensure an electrically uniform surface [Robertson *et al.*, 2004].

There are designated 10 different impact locations on the model. Each of these is a small, 1–3 cm^2 patch of tungsten foil attached to the body or antennas using conductive tape or using screws. The impact locations used in the experiments described below are mounted approximately at the middle of the antennas and on the top of the HGA. All impacts are perpendicular to targets.

The benefits of using tungsten patches for the impact experiments are easier handling and cleaning, and a more direct comparability of measurements from different locations and with those of previous investigations, e.g., Collette *et al.* [2015]. Tungsten also offers a high impact yield and thus a better signal-to-noise ratio.

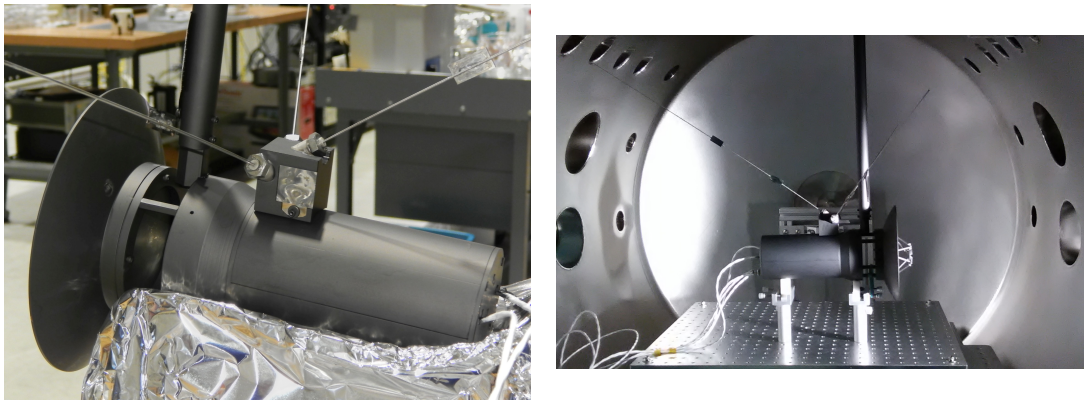


Figure 6.1: Simplified model of the Cassini spacecraft (left) and its location in the interaction chamber of the accelerator (right).

The RPWS antennas on Cassini are connected to one or more receivers that are selectable by command and cover different frequency ranges. The wideband receiver, operating with a passband of 60 Hz – 10.5 kHz or 0.8 – 75 kHz, serves as the front end electronics for on-board dust detection function. The recorded data can be processed into two types of measurements: power spectra and waveform captures [Gurnett *et al.*, 2004]. Individual dust impact pulses are best recognized in the waveforms, while the power spectrum has been used to estimate the average size/mass in regions with frequent dust impacts.

The actual schematics of the RPWS receivers is not publicly available, however, it is reasonable to assume that they operate as high input impedance voltage followers. The lab model is equipped with the electronics shown in Fig. 6.2 for both the dipole (antennas E_U and E_V) and monopole (E_W) configurations.

There are several features worth mentioning: (1) all three antennas and the SC body can be independently biased through a 10 MΩ resistor; (2) each element is connected to a voltage follower through ac-coupling with a long time constant; (3) differential amplifiers are then used to measure the voltage difference between the elements in the dipole and monopole configurations.

This setup has several advantages over that used in previous laboratory measurements by Collette *et al.* [2015, 2016], including higher fidelity resemblance to signal dust impact detection by the spacecraft. The circuit also achieved higher signal-to-noise ratios (SNRs) due to the differential amplifier. The circuit has a bandwidth of 50 Hz – 100 kHz and a voltage gain of approximately 100. The electronic boards are housed inside the cylindrical body of the Cassini model.

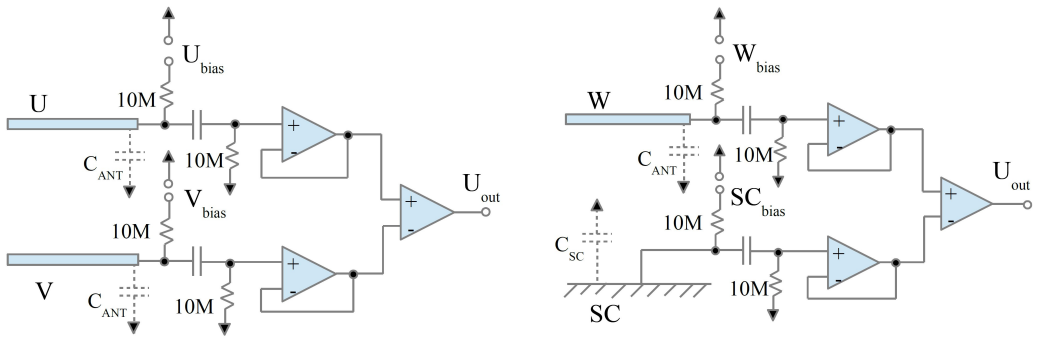


Figure 6.2: Electronic equipment of the Cassini model spacecraft.

It is important for the interpretation of results to discuss how electric signals are generated on the antennas. The first important mechanism is the charge collection on the antenna element and/or the SC body. The only way for the collected charge to leak from the element is through the parallel connection of two 10 MΩ resistors. The time constant of discharging is then $\tau = RC_i$, where R = 5 MΩ and i = U, V, W or SC for the different elements.

There are two important implications of this concept. One is that the capacitance of the elements can be determined from the time constant of discharging. And second, the signal from the charge collection can be clearly identified from discharging time constant and thus separated from other signal generation mechanisms discussed in the introduction of chapter 6.

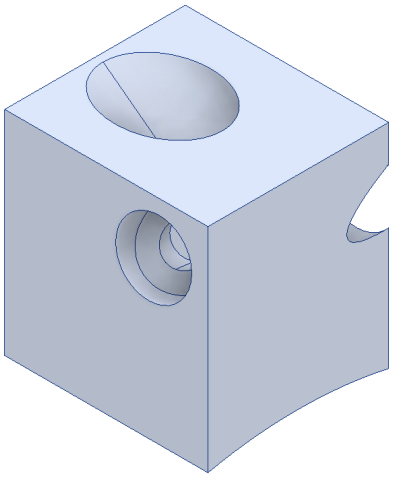


Figure 6.3: Mounting block for the antennas.

It is added for completeness that two sets of antennas together with their mounting block (see Fig. 6.3) were manufactured. The two sets were similar, but in one of them guard cylinders are inserted between the antenna and the mounting block.

The guard cylinders are hard wired to the ground and their role is to eliminate (or significantly reduce) any capacitive signal coupling between the antennas and the SC. The lab data taken by two different antenna designs showed no qualitative differences.

The laboratory measurements were performed in the dust accelerator facility operated at the University of Colorado. Its operation principle is described by Shu *et al.* [2012]. The principal schema of the experimental equipment with the dust accelerator is shown in Fig. 6.4. The charged dust released from the dust source is accelerated in the space of acceleration rings of the Pelletron type linear dust accelerator. Dust acelerated by the potential difference goes through the connected beam-line. The beam-line is equipped with three charge sensitive amplifier detectors (CSAs) [Srama and Auer, 2008]. The first two of them are used for determination of parameters of the grain, its charge, mass, and velocity.

The grain parameters are compared in real time with required grain parameters by the fast FPGA of the selection unit (PSU). Then, the grain is released to the last CSA and farther to the interaction chamber or is reflected on the inner wall of the beam-line by the deflection system.

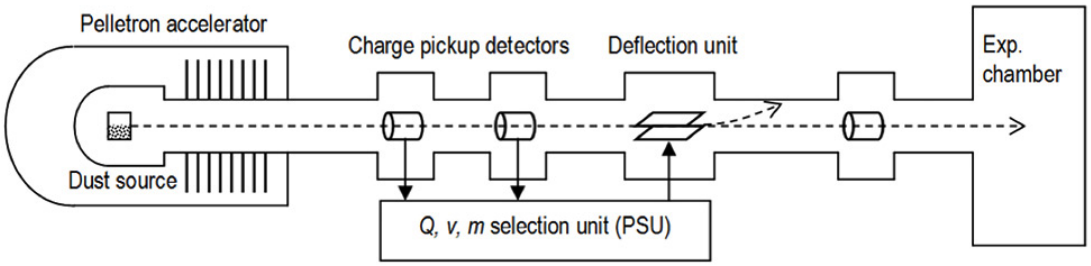


Figure 6.4: The experimental equipment with the linear dust accelerator. Picture adopted from the IMPACT facility website: http://impact.colorado.edu/facilities.html#dal.

Iron dust particles used for studies were accelerated to velocities of 4–25 km/s with characteristic distributions shown in Fig. 6.5 and directed to one of the designated impact locations.

The chamber was evacuated by a large turbomolecular pump and the measurements were performed in vacuum around 10^{-6} torr. A linear moving stage and an optional rotary motion feedthrough are used to reposition the model without breaking vacuum. The power supplies, including those providing the electric bias voltages and the data acquisition are located outside a vacuum. A fast digital storage scope is used for acquisition of antenna signals. The mass and velocity of each particle is determined by CSAs.

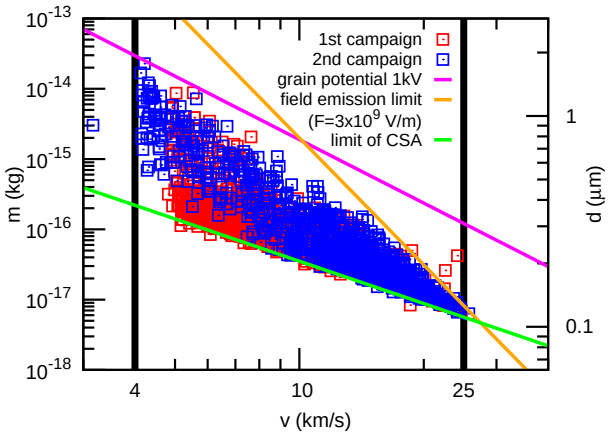


Figure 6.5: The mass-velocity distribution of the iron particles used for the measurements. Adopted from Nouzák *et al.* [2017].

6.2 Experimental results

The amount of collected charge from the impact depends on the applied bias voltages of the spacecraft and antennas. For simplicity, we kept the antennas and spacecraft on the same potential and a bias voltage was applied between the spacecraft and vacuum chamber. One dipole antenna with constant bias voltages of –25; –10; –5; 0; +5; +10, and +25 V was bombarded. The response of the electronics to the dust impacts for positive bias voltages can be seen in Fig. 6.6 The measured signals for negative biases had the same shape as those recorded

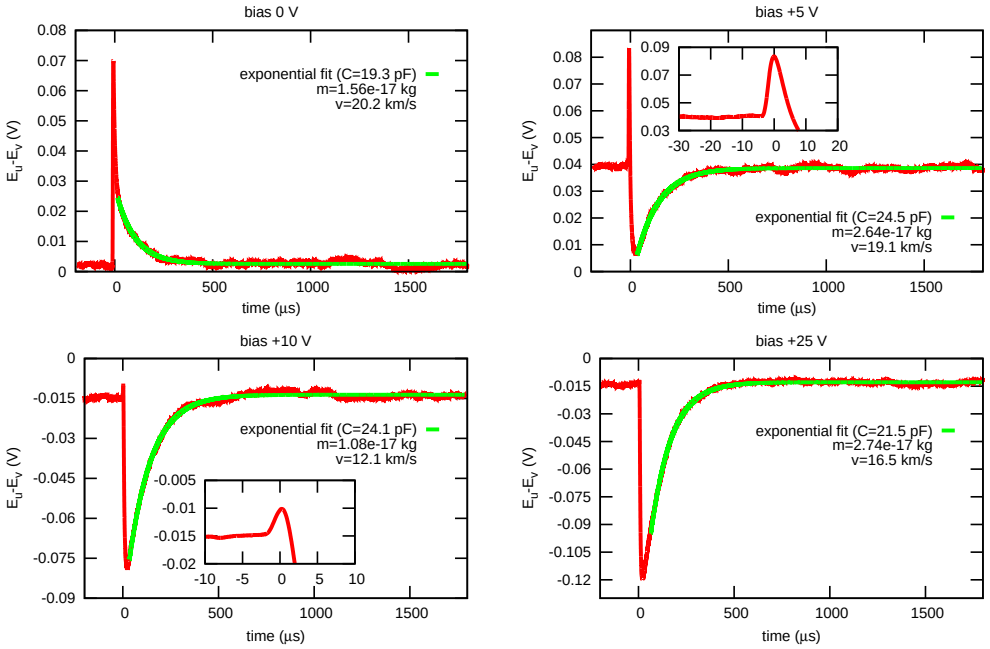


Figure 6.6: The impact signals detected by the antennas in a dipole configuration (E_U was bombarded) and an illustration of a determination of the time constant of the signals. The inserts show details of the positive spikes. Adopted from Nouzák *et al.* [2017].

for +25 V but with the opposite polarity. We observed interesting feature for positive biases (+5 V and +10V), the sharp positive-going peak foregoing a slower negative-going signal. We called it pre-peak. The slow negative-going signal is from the net recollection of electrons from the impact plasma by the applied positive bias voltage and its exponential decay corresponds to the characteristic RC time constant of the electronics (Fig. 6.2). On the other hand, the short positive spike cannot be caused by the charge collection because it is much shorter than the time constant of the measuring circuits.

Hovewer, the induced (or image) charge of the created impact plasma cloud can produce such fast spike. Because the thermal speed of the electrons in the impact cloud is much higher than the ions, the electrons may quickly escape from the attractive potential of the antenna and leave behind a net positive space charge (ions) that induces a positive signal on the antenna, see sketch in Fig. 6.8.

The pre-peak is diminishing with an increasing bias voltage (Fig. 6.6) as fewer electrons escape. The 0 V bias case in Fig. 6.6 is a special case where the pre-peak is also clearly visible.

The pre-peaks were observed for both the dipole and monopole antenna configurations. In the case of dust impacts occurring on the SC body, the polarity of the pre-peaks was negative due to the electronic circuit (Fig. 6.2).

Because the parameters of the impact plasma cloud are same for shooting on the E_U and the HGA antenna, we compared the derivation of produced signals in both geometries for zero biases. As we can see in Fig. 6.7, the time response of the pre-peak part is different.

In the case of E_U antenna, the signal has an uniform shape caused by the

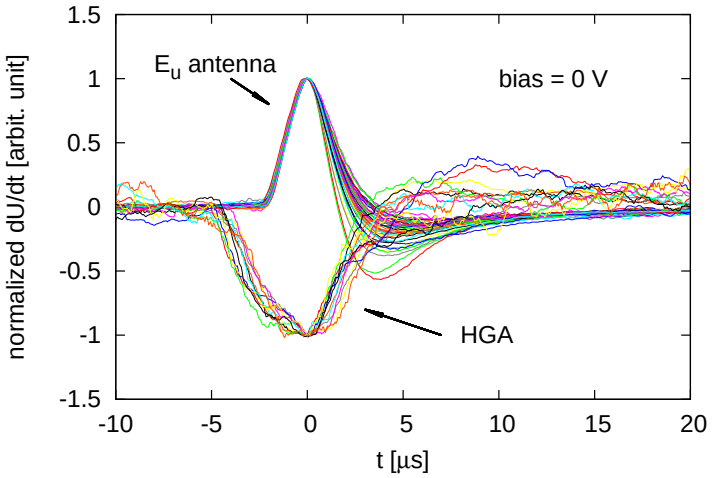


Figure 6.7: A comparison of the derivations of the pre-peaks for 0 V bias measured from dust impacts on the E_U antenna and the HGA. Adopted from Nouzák *et al.* [2017].

limited bandwidth of the amplifiers.

On the other hand, the signals for a dust impact on the HGA have a longer duration because the HGA is much larger than both monopole and dipole antennas and it takes much longer to diminish the image charge from the HGA and signals are thus not limited by the amplifier.

The size of the collected charge from the impact cloud is proportional to the voltage measured by electronics and the capacitance of the antenna (C_{ANT}) or spacecraft (C_{SC}). The capacitances can't be measured directly, but they can be calculated from the time constants of detected signals (Fig. 6.6).

The time constant determined from the exponential fit of the discharging profiles allows calculations of the capacitance based on the assumption that it is discharged through the 5 MΩ resistor (see Fig. 6.2).

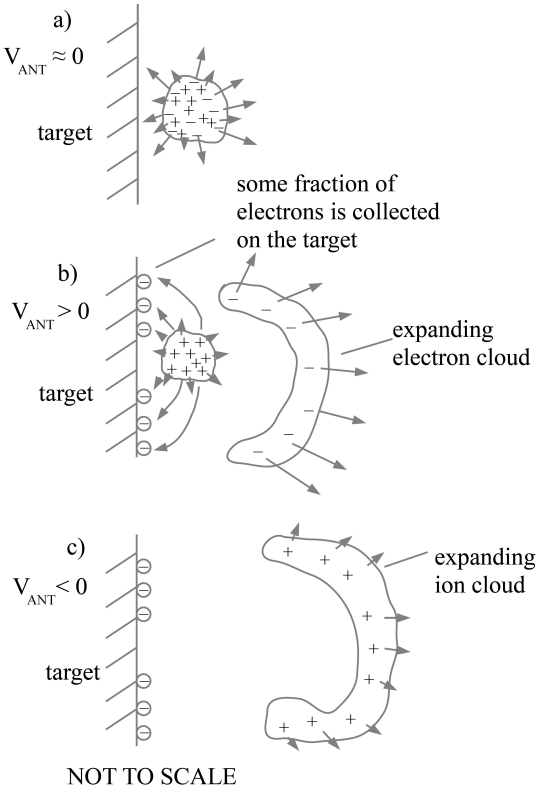


Figure 6.8: Sketch of impact plasma evolution.

The capacitances of the antenna and spacecraft were determined from about 1600 impacts (collected in two data sets) and their histograms are shown in Fig. 6.9.

Since the determined capacitances have a wide spread values mainly due to a noise, the Gaussian fits were made to each distribution and the mean values were used for further processing. The capacitances of the antennas for dipole and monopole configurations were determined as 20.9 pF and 20.4 pF, respectively (see Fig. 6.9 – left and middle). The capacitance of the spacecraft was determined from impacts on the HGA dish as 118.6 pF (Fig. 6.9 – right).

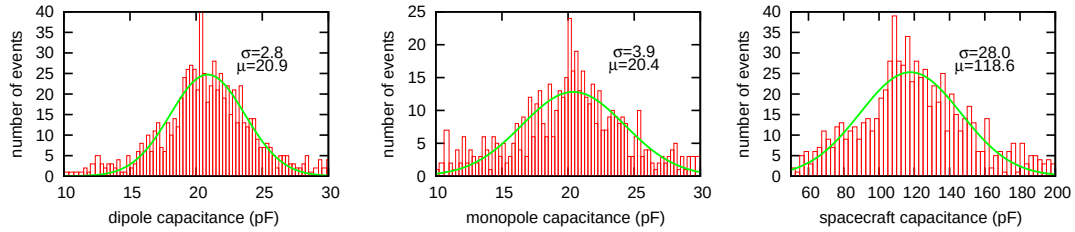


Figure 6.9: Determination of capacitances: Capacitance of the dipole antenna (left), monopole antenna (middle) and spacecraft (right).
Adopted from Nouzák *et al.* [2017].

The experimental set-up provides a large variety of possible configurations with different impact locations and different bias voltages applied on various parts of the model. Thus, the analysis of the signals recorded by the dipole antenna and the monopole antenna was restricted to the dust impacts onto dipole antenna only. Any notable response was found to the dust impacts onto the spacecraft body (HGA) or onto the monopole antenna in the dipole antenna signal. This fact doesn't mean that the dipole antenna is not capable of registration of impacts onto the spacecraft body but rather that the plasma plumes generated at HGA were well shielded from the dipole antennas. Moreover, the impact target was in the middle of HGA and thus there should be no difference in the charge potentially collected by both E_U and E_V parts. A new series of experiments should be carried out to clarify whether the impacts onto different parts of the spacecraft can or cannot produce detectable signals on the dipole antenna. On the other hand, the impacts onto the dipole antenna often result in a detectable response on the monopole antenna (Fig. 6.10). The records shown in this figure belong to the

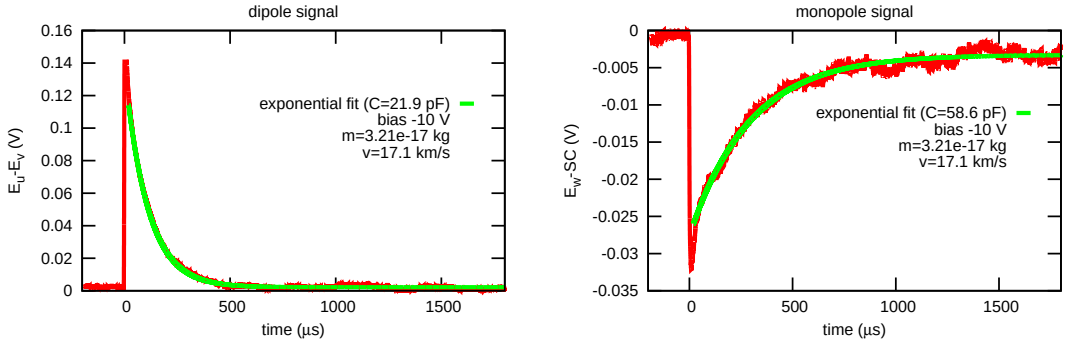


Figure 6.10: Demonstration of a response of the monopole antenna on the impacts onto the dipole antenna.

impact of the $3.21 \cdot 10^{-17}$ kg grain with the velocity of 17.1 km/s. A relatively large impulse registered by the dipole antenna is shown in the left panel and its much smaller counterpart recorded simultaneously by the monopole antenna is

depicted in the right panel of Fig. 6.10. The opposite polarity of the signals is consistent with the scheme in Fig. 6.2 and capacitive coupling between the dipole and spacecraft body. However, a partial recollection of the charge generated at the dipole antenna and its contribution to the monopole signal cannot be excluded. It should be noted that such a clear response is not frequent, the signals on the monopole antenna are usually close to the noise level. The response of the monopole antenna to the impacts onto the dipole is statistically quantified in Figs. 6.11 and 6.12.

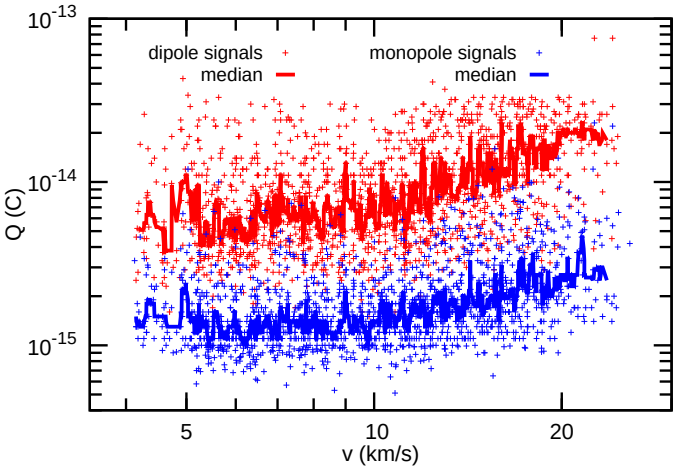


Figure 6.11: The amplitudes of impulses generated by impacts onto the dipole antenna and a response in the monopole configuration as a function of the impact velocity.

Fig. 6.11 shows the amplitudes of impulses generated by impacts onto the dipole antenna as a function of the impact velocity. Since this figure combines all impacts regardless of the bias, the amplitudes are converted into a collected charge. The red crosses show the charges registered by the dipole antenna, whereas the monopole antenna responses are in blue. The data are very noisy and thus the floating medians computed over 15 consecutive points are given as lines of corresponding colors. The red and blue medians exhibit a very similar trend in spite of the fact that typical peaks recorded in the noise of used amplifiers expressed in units of a charge are about 0.8 fC. In order to quantify a level of similarity of the trends in Fig. 6.11, a ratio of charges registered by two antennas is plotted in Fig. 6.12.

The format is the same as that in Fig. 6.11 and one can see that this ratio is approximately constant ≈ 5.5. The constant ratio again suggests that the signal registered by the monopole antenna is produced by the capacitive coupling to the dipole antenna. The large spread of individual points in Fig. 6.12 is probably caused by the fact that the signals registered by the monopole antenna are close to a noise level but the ratio of impulse amplitudes in Fig. 6.10 is about 5, i.e., in a good agreement with the value of the median in Fig. 6.12. Assuming that the monopole response is due to a capacitive coupling, the capacitance between the dipole and monopole antennas should be about 4 pF that seems to be rather large but possible value. However, this value is determined for the spacecraft model placed in the vacuum chamber and scaling of these results to the real Cassini spacecraft operating in the free space is rather difficult.

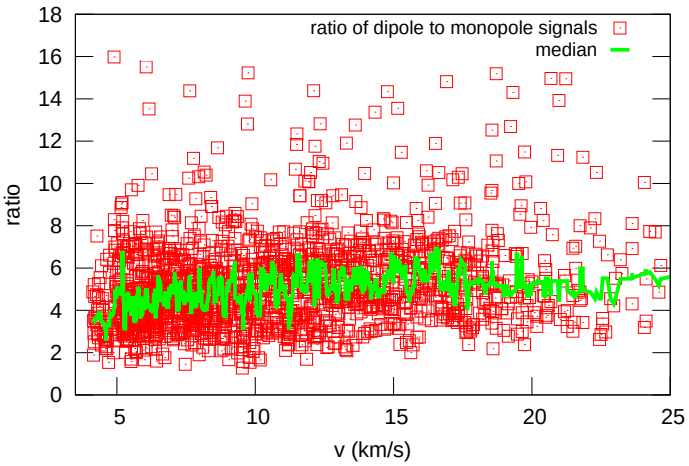


Figure 6.12: A ratio of charges registered by dipole and monopole antennas as a function of the impact velocity.

The data from the E and G ring crossings of the Cassini spacecraft were analyzed. Most of the dust impacts exhibit overshooting behavior, see typical waveforms observed on dipole and monopole antennas in Fig. 6.13. The time analysis of all impacts on the dipole in the E ring crossing and the monopole in the G ring crossing suggests that almost all registered dust impacts have been limited by bandwidth of wideband reciever (10.5 kHz) on board of the Cassini spacecraft [Gurnett *et al.*, 2004]; see normalized derivations for monopole and dipole antennas (Fig. 6.14). The waveforms were mirrored to the same polarity for easiest comparison.

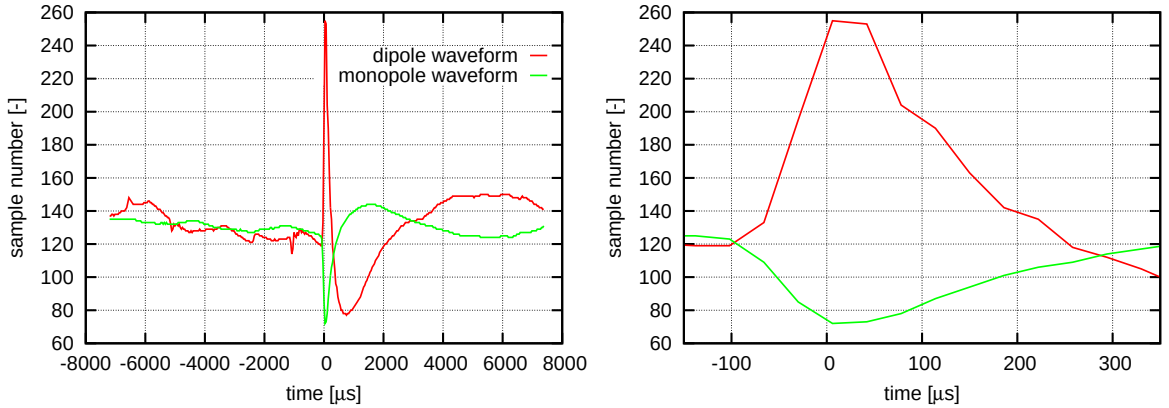


Figure 6.13: Comparison of dust impact waveforms for dipole and monopole antennas (left) and their zoom around zero time (right).

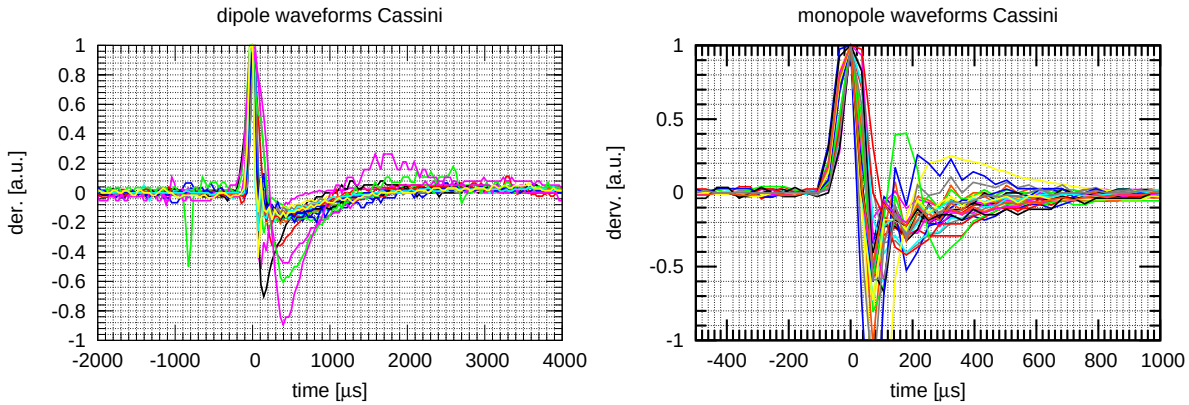


Figure 6.14: Comparison of the normalized derivation of dust impact waveforms for dipole (left) and monopole antennas (right).

Chapter 7

Conclusions

In the interplanetary medium, the interaction of plasma particles and photons with dust grains leads to their charging or their sputtering and alteration. On the other hand, dust impacts on the solid surfaces cause a creation of plasma particles. In the thesis, we focused on two particular problems: (a) an influence of the photoemission from lunar dust micrometer-sized samples because the parameters of this important process were studied only occasionally; and (b) on dust impacts to the antennas of the Cassini model to help with interpretations of the spacecraft measurements. We can summarize our results as:

(1) The experimental set-up with a linear electrodynamic trap was complemented with the UV source. The system was designed and built, and the necessary electronic equipment was developed (including the system for a compensation of the gravity acting on the grain, active damping and control of grain oscillations, and a sampling system for electron and ion beams). Furthermore, a system for measurement of intensities of electron, ion, and photon beams was prepared and tested. The Labview program for continuous controlling of all electronic parts and for on-line recording of the charge-to-mass ratio during the experiment was developed.

(2) The UV source was tested and we estimated its photon flux for He, Ar, Ne, H_2 discharges in different working modes from the current measured by a gridless Faraday cup. We identified a peak of electrons with almost Maxwellian energy distribution with a temperature about 1.65 eV for the He discharge [Nouzák *et al.*, 2013]; indicated a presence of the He I excitation line, and found that a ratio of saturated currents of positive and negative branches of integral characteristics could be used as a measure of the intensity ratio of He I/He II emission lines.

(3) Photoemission parameters of spherical glass, MLS-1 (lunar simulant), and MF (melamine formaldehyde resin) grains were studied. The values for mentioned grains are: spherical glass ($W = (4.7 \pm 1.5)\,\mathrm{eV}$, $\eta\,(21.2\,\mathrm{eV}) = 0.04$) [Nouzák *et al.*, 2014], MLS-1 (lunar dust simulant) ($W_{4.7\mu\mathrm{m}} = (5.9 \pm 0.3)\,\mathrm{eV}$, $W_{4.0\mu\mathrm{m}} = (5.1 \pm 0.7)\,\mathrm{eV}$, $\eta\,(21.2\,eV) = 0.05$) [Nouzák *et al.*, 2016], and MF ($W = (4.4 \pm 0.2)\,\mathrm{eV}$) [Vyšinka *et al.*, 2017]. Note that a value of the work function for MLS-1 is similar to the value obtained for the JSC-1 lunar regolith simulant by [Sternovsky *et al.*, 2002] that used the contact charging method. A comparision of work functions of spherical glass and irregular

shaped MLS-1 grains revealed a clear dependence of the work function on the composition of particular dust grains.

(4) We prepared the reduced Cassini spacecraft model and used the dust accelerator at the IMPACT facility in Boulder to test dust impacts on its antennas in monopole and dipole configurations [Nouzák *et al.*, 2017]. We found that: dipole antennas are greatly insensitive to dust impacts on the spacecraft body or the monopole antenna (in agreement with Ye *et al.* [2016]); and a polarity of the signals changes with the polarity of the bias potential. We observed the overshoot signals for positive values of the bias potential on the antenna and spacecraft and found that a size of the pre-shoot part changes with the size of the positive bias. In the case of shooting to the HGA (High Gain Antenna) dish, no signals were registered on the dipole antennas.

(5) We compared the data from dust impacts on the Cassini model with the data registered, when Cassini spacecraft crossed E and G rings. The analysis showed that the most impact signals exhibit overshoots where a pre-spike part is limited by a bandwidth of electronics of the wide-band receiver (10.5 kHz). However, the signals measured on the Cassini model are much faster because a limit of the electronics is 100 kHz. For further comparisons of simulation results with Cassini spacecraft data, a new design of the Cassini model electronics that will be more similar to the wideband receiver would be necessary.

Finally, we can conclude that all goals of the thesis were fulfilled. Nevertheless, many new tasks also arose. For example, our experiments revealed a surprising feature that dust impacts on the dipole antenna often generate a detectable signal on the monopole antenna and no physical explanation exists yet for such observation.

As a final conclusion, we note that the particular results of the studies were presented at various international conferences (e.g., European Geosciences Union General Assembly, Vienna, Austria 2013–2017, the 8$^{\text{th}}$ International Conference on the Physics of Dusty Plasmas, Prague, Czech Republic 2017, Dusty Plasma in Application, Odessa, Ukraine 2013, 2017, the 3$^{\text{rd}}$ International Workshop on Diagnostics and Simulation of Dusty Plasmas, Kiel, Germany, 2015, the 14$^{\text{th}}$ Workshop on the Physics of Dusty Plasmas, Auburn, Alabama, USA, 2015) and were published in attached publications [A1]–[A5].

Appendix

The appendix is based on the work of Beránek *et al.* [2010]. It serves for better understandig of principles of the linear electrodynamic trap and the relation between charge-to-mass ratio of the grain and parameters of the trap determined from equations of motion.

Principles of a linear electrodynamic trap

The linear electrodynamic trap is based on generation an effective potential with the minimum in the center of the trap. One of the solutions are following electric potentials in the main axes of the trap [Beránek *et al.*, 2010]

$$\varphi_z = \lambda_z V_z \frac{xy}{{r_0}^2} \cos \omega t \tag{7.1}$$

$$\varphi_x = \lambda_{xy} V_{xy} \frac{yz}{{r_0}^2} \cos \omega t \tag{7.2}$$

$$\varphi_y = \lambda_{xy} V_{xy} \frac{xz}{{r_0}^2} \cos \omega t \ , \tag{7.3}$$

where λ_z and $\lambda_{xy} = \lambda_x = \lambda_y$ are geometric parameters of the trap and V_z, V_{xy} are the amplitudes of mentioned potentials. We can see that the potentials φ_x a φ_y represent the electric potential of the electrostatic quadrupole. The potential, φ_z represents an additional potential, which prevents to escape of the dust grain in the main axis z (in the case of the electrostatic quadrupole, the charged particle is not anyway held in the main axis).

The overall electric potential is according to principle of superposition, in a form

$$\varphi = \frac{\cos \omega t}{{r_0}^2} \left[(x+y) \lambda_{xy} V_{xy} z + \lambda_z V_z xy \right] \ . \tag{7.4}$$

The force occurring on the charged grain is necessary to establish an efective potential of the electric potential mentioned above. The effective potential really acts on the grain and has meaning of the gravitional potential in a mechanical analogy. The gradient of the effective potential, $\mathrm{u_{eff}}$ [Gerlich, 1992] describes the equation of motion of the charged dust grain

$$m\ddot{\mathbf{r}} = -\nabla u_{eff} = -\frac{Q^2}{4m\omega^2} \nabla |\mathbf{E}(\mathbf{r})|^2 \, . \tag{7.5}$$

The intensity of the electric field $\mathbf{E}(\mathbf{r})$ is equal to a gradient of the electric potential (eq. 7.4) in a form

$$\nabla \varphi = \frac{\lambda_z V_z \cos \omega t}{{r_0}^2} \left[Cz + y, Cz + x, C(x+y) \right] \ , \tag{7.6}$$

where C is the ratio coefficient of voltage amplitudes and the geometrical factor

$$C = \frac{\lambda_{xy} V_{xy}}{\lambda_z V_z} \,. \tag{7.7}$$

The equation of motion (eq. 7.5) with an algebraic expression simplifying has a form

$$m\ddot{\mathbf{r}} = -\frac{Q^2 {\lambda_z}^2 {V_z}^2}{4m\omega^2 {r_0}^4} \nabla \left| [Cz + y, Cz + x, C(x + y)] \right|^2 \tag{7.8}$$

$$= -\frac{Q^2 {\lambda_z}^2 {V_z}^2}{2m\omega^2 {r_0}^4} \Big\{ (Cz + x) + C^2(x + y), (Cz + y) \tag{7.9}$$

$$+C^2(x + y), (Cz + y)C + (Cz + x)C \Big\}$$

$$= -\frac{Q^2 {\lambda_z}^2 {V_z}^2}{2m\omega^2 {r_0}^4} \begin{pmatrix} C^2 + 1 & C^2 & C \\ C^2 & C^2 + 1 & C \\ C & C & 2C^2 \end{pmatrix} . \begin{pmatrix} x \\ y \\ z \end{pmatrix} , \tag{7.10}$$

where on the last line is a transition to the matrix representation. Now, we have system of three ordinary differential equations, which are linked together and their solution would be rather complicated.

The easiest solution can be found with diagonalization of matrix and made consecutive to the different coordinate system $(x, y, z) \rightarrow (x', y', z')$. In new (dashed) coordinates, the equation of motion is

$$m\ddot{\mathbf{r}}' = -\frac{Q^2 {\lambda_z}^2 {V_z}^2}{2m\omega^2 {r_0}^4} \begin{pmatrix} 2 & 0 & 0 \\ 0 & 4C^2 + 1 - \sqrt{8C^2 + 1} & 0 \\ 0 & 0 & 4C^2 + 1 + \sqrt{8C^2 + 1} \end{pmatrix} . \begin{pmatrix} x' \\ y' \\ z' \end{pmatrix} . \tag{7.11}$$

This equation is easy to rewrite into a more clear and readable form

$$\ddot{\mathbf{r}}' + \frac{Q^2 {\lambda_z}^2 {V_z}^2}{2m^2\omega^2 {r_0}^4} \begin{pmatrix} 2 & 0 & 0 \\ 0 & 4C^2 + 1 - \sqrt{8C^2 + 1} & 0 \\ 0 & 0 & C^2 + 1 + \sqrt{8C^2 + 1} \end{pmatrix} . \mathbf{r}' = 0 \,.$$

We obtained a set of three ordinary differential equations, which is not linked together and its solutions in the coordinate system (x', y', z') are the eigen-oscillations of the grain

$$\Omega_i = \frac{Q}{m} \frac{\lambda_z V_z}{2\omega {r_0}^2} \begin{cases} \sqrt{2} & ; i = x' \\ \sqrt{4C^2 + 1 - \sqrt{8C^2 + 1}} & ; i = y' \\ \sqrt{4C^2 + 1 + \sqrt{8C^2 + 1}} & ; i = z' \,. \end{cases} \tag{7.12}$$

With puff of the damping gas into the main chamber or with electronic damping it is possible to damp oscillations of the grain in directions, y' and z', to investigate only the oscillation in the x' axis. Damping of motion in unwanted directions is important for the farther analysis of the signal by synchronous detection of motion (signal around only one eigen-frequency is analyzed). From the equation for eigen-oscillation in x' we can obtain explicit relation between charge-to-mass ratio of the dust grain and a geometry of the trap r_0 with amplitude V_z and frequency ω of potentials on its electrode

$$\frac{Q}{m} \approx \frac{\sqrt{2} {r_0}^2}{\lambda_z} \frac{\omega \Omega_{x'}}{V_z} \,. \tag{7.13}$$

This relation is just approximate and it is valid within an adiabatic aproximation only. The precise expression is possible to obtain from solution of the Mathieu differential equation [Abramowitz and Stegun, 1972]. Its solution is equation 7.13 with the correction factor

$$\frac{1}{\sqrt{1+\left(k\frac{\Omega_{x'}}{\omega}\right)^2}} \quad ; k = 1.8 \ . \tag{7.14}$$

Bibliography

M. M. Abbas, D. Tankosic, P. D. Craven, J. F. Spann, A. LeClair, E. A. West, J. C. Weingartner, A. G. G. M. Tielens, J. A. Nuth, R. P. Camata, and P. A. Gerakines. Photoelectric emission measurements on the analogs of individual cosmic dust grains. *Astrophys. J.*, 645:324–336, March 2006.

M. Abramowitz and I. Stegun. *Handbook of Mathematical Functions with Formulas, Graphs, and Mathematical Tables.* U.S. Department of Commerce, Dover, Ch. 20. Mathieu Functions, 1972.

R. Alvarez. Lunar and terrestrial sample photoconductivity. In *Proc. Lunar Sci. Conf. 6th*, volume 3, pages 3187–3197, 1975.

R. Alvarez. Photoconductive effects on lunar and terrestrial fines. In *Proc. Lunar Sci. Conf. 8th*, volume 1, pages 1277–1290, 1977b.

H. Alvén. On the origin of the solar system (Oxford: Clarendon). *Quarterly Journal of the Royal Astronomical Society*, 8:215–226, 1954.

E. Anders. Pre-biotic organic matter from comets to asteroids. *Nature*, 342:255–257, 1989.

R. Anderson, S. Gathman, J. Hughes, S. Björnsson, S. Jónasson, D. C. Blanchard, C. B. Moore, H. J. Survilas, and B. Vonnegut. Electricity in volcanic clouds: Investigations show that lightning can result from charge-separation processes in a volcanic crater. *Science*, 148(3674):1179–1189, 1965.

L. Andersson, T. D. Weber, D. Malaspina, F. Crary, R. E. Ergun, G. T. Delory, C. M. Fowler, M. W. Morooka, T. McEnulty, A. I. Eriksson, and D. J. Andrews. Dust observations at orbital altitudes surrounding Mars. *Science*, 350(6261):aad0398–1–aad0398–3, 2015.

M. Andriopoulou, N. Roussos, C. Krupp, M. Paranicas, M. Thomsen, S. Krimigis, M. K. Dougherty, and K.-H. Glassmeier. Spatial and temporal dependence of the convective electric field in Saturn's inner magnetosphere. *Icarus*, 229:57–70, 2014.

R. G. C. Arridge. The static electrification of nylon 66. *Brit. J. Appl. Phys.*, 18:1311–1316, 1967.

D. G. Ashworth. Lunar and planetary impact erosion. In *Cosmic Dust, ed. by J. A. M. McDonnell, Wiley, Chichester*, pages 427–526, 1978.

M. G. Aubier, N. Meyer-Vernet, and B. M. Pedersen. Shot noise from grain and particle impacts in Saturn's ring plane. *Geophys. Res. Lett.*, 10(1):5–8, 1983.

T. W. Backhouse. The luminous cirrus clouds of June and July. *Meteorol. Mag.*, 20:133, 1885.

J. L. Ballester, Y. Shi, and E. Dwek. Photoelectron yield of silicate and graphite grains. *J. Opt. Soc. Am. B*, 12(7):1211–1214, 1995.

B. B. Balsley, W. L. Ecklund, and D. C. Fritts. VHF echoes from the high-latitude mesosphere and lower thermosphere: Observations and interpretations. *American Meteorological Society.*, 40:2451–2466, 1983.

B. Baron, D. Hoover, and F. Williams. Vacuum ultraviolet photoelectric emission from amorphous ice. *J. Chem. Phys.*, 68(4):1997–1999, 1978.

J. Bednář. *Pozoruhodné jevy v atmosféře.* Academia, Praha, 1980.

O. E. Berg, H. Wolf, and J. W. Rhee. Lunar soil movement registered by the Apollo 17 cosmic dust experiment. In *In: Interplanetary Dust and Zodical Light, Lecture Notes Phys., ed. by H. Elsässer and H. Fechtig,*, volume 48, page 233. Springer (Berlin), 1975.

M. Beránek, I. Čermák, Z. Němeček, and J. Šafránková. Trapping charged microparticles in the linear quadrupole trap. In *Proceedings of contributed papers WDS – part II*, pages 112–120. Matfyzpress (Praha), 2010.

M. Beránek, I. Čermák, Z. Němeček, J. Šafránková, M. Jeřáb, and J. Pavlů. Linear trap with three orthogonal quadrupole fields for dust charging experiments. *Rev. Sci. Instrum.*, 93(115109), 2012.

P. A. Bernhardt, G. Ganguli, M. C. Kelley, and Swartz W. E. Enhanced radar backscatter from space-shuttle exhaust in the ionosphere. *J. Geophys. Res.*, 100(A12):23811–23818, 1995.

N. Borisov and U. Mall. Charging and motion of dust grains near the terminator of the moon. *Planet. Space. Sci.*, 54:572–580, 2006.

F. Boulanger, P. Cox, and A. P. Jones. Course 7: Dust in the interstellar medium. In *F. Casoli; J. Lequeux; F. David. Infrared Space Astronomy, Today and Tomorrow*, volume 70, pages 251–335, 1950.

J. P. Bradley. Chemically anomalous, preaccretionally irradiated grains in interplanetary dust from comets. *Science*, 265:925–929, 1994.

E. Bron, F. Le Petit, and J. Le Bourlot. Efficient ortho-para conversion of H2 on interstellar grain surfaces. *Astron. Astrophys.*, A27:1–17, 2016.

W. L. Brown, W. M. Augustyniak, K. J. Marcantonio, E. H. Simmons, J. W. Boring, R. E. Johnson, and C. T. Reimann. Electronic sputtering of low temperature molecular solids. *Nucl. Instrum. Methods Phys. Res., Sect. B*, 1:307–314, 1984.

D. E. Brownlee. Cosmic dust: Collection and research. *Annu. Rev. Earth Pl. Sc.*, 13:147–173, 1985.

L. E. Brus. A simple model for the ionization potential, electron affinity, and aqueous redox potentials of small semiconductor crystallites. *J. Chem. Phys.*, 79(11):5566–5571, 1983.

M. J. Burchell, S. A. J. Fairey, P. Woyniakiewicz, D. E. Brownlee, F. Horz, A. T. Kearsley, T. H. See, P. Tsou, A. Westphal, S. F. Green, J. M. Trigo-Rodríguez, and G. Domingúez. Characteristics of cometary dust tracks in stardust aerogel and laboratory calibrations. *Meteorit. Planet. Sci.*, 43(1/2):23–40, 2008.

J. A. Burns, M. R. Showalter, J. N. Cuzzi, and J. B. Pollack. Physical processes in Jupiter's ring: clues to its origin by Jove! *Icarus*, 44(2):339–360, 1980.

H. Burtscher and A. Schmidt-Ott. Enormous enhancement of van der Waals forces between small silver particles. *Phys. Rev. Lett.*, 48(25):1734–1737, 1982.

H. Burtscher, A. Schmidt-Ott, and H. C. Siegmann. Photoelectron yield of small silver and gold particles suspended in gas up to a photon energy of 10 eV. *Z. Phys. B*, 56(3):197–199, 1984.

M. Cardona and L. Ley. *Photoemission in Solids I.* Springer Berlin, New York, 1978.

J. D. Cassini. Découverte de la lumiere celeste qui paroist dans le zodiaque. *Paris: Académie Royale des Sciences*, 1683.

J. Childrey. Britannia Baconica or the natural rarities of England, Scotland and Wales (London). 1661.

C. S. Chiu. Numerical study of cloud electrification in an axisymetric, time dependent cloud model. *J. Geophys. Res.*, 83(C10):5025–5049, 1978.

J. Y. N. Cho and M. C. Kelley. Polar mesosphere summer radar echoes: Observations and current theories. *Rev. Geophys.*, 31(3):243–265, 1993.

V. W. Chow, D. A. Mendis, and M. Rosenberg. Role of grain size and particle velocity distribution in secondary electron emission in space plasmas. *J. Geophys. Res.*, 98(A11):19065–19076, 1993.

V. W. Chow, D. A. Mendis, and M. Rosenberg. Secondary emission from small dust grains at high electron energies. *IEEETPS*, 22(2):179–186, 1994.

C. Chunshi and J. Goree. Fluctuations of the charge on a dust grain in a plasma. *IEEE Trans. Plasma Sci.*, 22(2):5025–5049, 1994.

Ch. F. Chyba and G. D. McDonald. The origin of life in the solar system: Current issues. *Annu. Rev. Earth Pl. Sc.*, 23:215–249, 1995.

A. Collette, E. Grün, D. Malaspina, and Z. Sternovsky. Micrometeoroid impact charge yield for common spacecraft materials. *J. Geophys. Res.*, 119(8):6019–6026, 2014.

A. Collette, G. Meyer, D. Malaspina, and Z. Sternovsky. Laboratory investigation of antenna signals from dust impacts on spacecraft. *J. Geophys. Res.*, 120(7):5298–5305, 2015.

A. Collette, D. Malaspina, and Z. Sternovsky. Characteristic temperatures of hypervelocity dust impact plasmas. *J. Geophys. Res.*, 121(9):8182–8187, 2016.

G. Cremonese and M. Fulle. Sodium in comets. In *Earth, Moon, and Planets*, volume 79, pages 209–220, 1997.

G. H. Cremonese, H. Rauer, and I. A. U. Fitzsimmous. *Circular no. 6643, Central Bureau for Astronomical Telegrams*. Smithsonian Astrophysical Observatory, Cambridge, 1997a.

G. Cremonese, H. Boehnhardt, J. Crovisier, H. Rauer, A. Fitzsimmons, M. Fulle, J. Licandro, D. Pollacco, G. P. Tozzi, and R. M. West. Neutral sodium from comet Hale-Bopp: A third type of tail. *Astrophys. J.*, 490:L199–L202, 1997b.

D. R. Criswell and B. R. De. Intense localized charging in the lunar sunset terminator region: Development of potentials and fields. *J. Geophys. Res.*, 82(7):999–1004, 1977.

D. R. Criswell and B. R. De. Intense localized charging in the lunar sunset terminator region: Supercharging at the progression of sunset. *J. Geophys. Res.*, 82(7):1005–1007, 1977.

D. R. Criswell. Horizon-glow and the motion of lunar dust. in: Grard, R. J. L. (ed.). *Photon and Particle Interactions with Surfaces in Space. D. Reidel Publishing Co., Dordrecht, Holland*, 37:545–556, 1973.

R. G. Cunningham. Frictional electrification of belts of insulating materials. *J. Appl. Phys.*, 35(8):2332–2337, 1964.

J. N. Cuzzi, J. J. Lissauer, L. W. Esposito, J. B. Holberg, E. A. Marouf, and G. L. Tyler. Saturn's rings – properties and processes. *In: Planetary rings (A85-34401 15-88). Tucson, AZ, University of Arizona Press*, pages 73–199, 1984.

D. K. Davies. The examination of the electrical properties of insulators by surface charge measurements. In *J. Sci. Instrum.*, volume 44, pages 521–524, 1967a.

D. K. Davies. Charge generation on dielectric surfaces. *J. Phys. D*, 2(11):1533–1537, 1969.

U. de Angelis, V. Formisano, and M. Giardano. Ion plasma waves in dusty plasmas: Hallay's comet. *J. Plasma Phys.*, 40(3):399–406, 1988.

U. de Angelis. The physics of dusty plasmas. *Phys. Scr.*, 45(5):465–474, 1992.

G. L. Delzanno, G. Lapenta, and M. Rosenberg. Attractive potential around thermionically emitting microparticle. *Phys. Rev. Lett.*, 92(3):1–4, 2004.

S. F. Dermott, D. D. Durda, K. Grogan, and T. J. J. Kehoe. *Asteroids III*. Number ISBN 0-8165-2281-2. The University of Arizona Press, Tucson, Arizona 85721, 2002.

H. Dietzel, G. Eichhorn, H. Fechtig, E. Grün, H. J. Hoffmann, and J. Kissel. The HEOS 2 and HELIOS micrometeroid experiments. *J. Phys. E: Sci. Instrum.*, 6(3):209–217, 1973.

Y. Ding. Photoelectron yield enhancement of small graphite and silicate dust grains. Diploma thesis, Division of physical sciences Emporia State Univesity, 1994.

N. Divine. The comet Halley dust and gas environment. *ESA SP*, 174:25–47, 1981.

J. S. Dohnanyi. Interplanetary objects in review, statistics of their masses and dynamics. *Icarus*, 17:1–48, 1972.

M. K. Dougherty, L. W. Esposito, and S. M. Krimigis. *Saturn from Cassini-Huygens*. Springer, 2009.

B. T. Draine and H. M. Lee. Optical properties of interstellar graphite and silicate grains. *Astrophys. J.*, 285:89–108, 1984.

B. T. Draine and E. E. Salpeter. Destruction mechanisms for interstellar dust. *Astrophys. J.*, 231:438–455, 1979.

B. T. Draine and E. E. Salpeter. On the physics of dust grains in hot gas. *Astrophys. J.*, 231(1):77–94, 1979.

B. T. Draine, W. G. Roberg, and A. Dalgarno. Magnetospheric hydrodynamic shock waves in molecular clouds. *Astrophys. J.*, 264:485–507, 1983.

B. T. Draine. Photoelectric heating of interstellar gas. *Ap. J. Suppl.*, 36(4):595–619, 1978.

B. T. Draine. Interstellar dust grains. *Annu. Rev. Astron. Astrophys.*, 41(1):241–289, 2003.

S. Drapatz and K. W. Michel. Theory of shock-wave ionization upon high-velocity impact of micrometeorites. *Z. Naturforsch.*, 29a:870–879, 1974.

I. Čermák, E. Grün, and J. Švestka. New results in studies of electric charging of dust particles. *Adv. Sp. Res.*, 15(10):(10)59–(10)64, 1995.

I. Čermák. Laboruntersuchung elektrischer Aufladung kleiner Staubteilchen. Dissertation, MPI-K Heidelberg, 1994.

A. Evans. *The Dusty Universe*. by Evans, A. Ellis Horwood, New York: Wiley and Sons, 1993.

G. Faraci, A. R. Pennisi, and G. Margaritondo. Mechanism of photoelectron yield enhancement from Ag clusters. *Phys. Rev. B*, 40:4209–4211, 1989.

W. M. Farrell, M. L. Kaiser, M. D. Desch, J. G. Houser, S. A. Cummer, D. M. Wilt, and G. A. Landis. Detecting electrical activity from Martian dust storms. *J. Geophys. Res.*, 104(2):3795–3801, 1999.

W. M. Farrell, M. D. Desch, M. L. Kaiser, W. S. Kurth, and D. A. Gurnett. Changing electrical nature of Saturn's rings: Implications for spoke formation. *Geophys. Res. Lett.*, 33(L07203):1–4, 2006.

H. Fechtig, E. Grün, and G. E. Morfill. Micrometeoroids within ten earth radii. *Planet. Space. Sci.*, 27(4):511–531, 1979.

D. Fenyö, B. U. R. Sundqvist, B. R. Karlsson, and R. E. Johnson. Molecular-dynamics study of electronic sputtering of large organic molecules. *Phys. Rev. B*, 42(4):1895–1902, 1990.

K. Ferriere. The interstellar environment of our galaxy. *Rev. Mod. Phys.*, 73(4):1031–1066, 2001.

B. Feuerbacher and B. Fitton. Experimental investigation of photoemission from satellite surface materials. *J. Appl. Phys.*, 43(4):1563–1572, 1972.

B. Feuerbacher, M. Anderegg, B. Fitton, L. D. Laude, R. F. Willis, and R. J. L. Grard. Photoemission from lunar surface fines and the lunar photoelectron sheath. In *Proceedings of the 3rd Lunar Science Conference (Geochim. Cosmochim. Acta Suppl.)*, volume 4, pages 2655–2663, 1972.

J. G. Flynn, P. Bleuet, J Borg, J. P. Bradley, F. E. Brenker, S. Brennan, D. E. Bridges, J. Brownlee, E. S. Bullock, M. Burghammer, Z. R. Clark, B. C. Dai, Ch. P. Daghlian, Z. Djouadi, S. Fakra, T. Ferroir, Ch. Floss, I. A. Franchi, Z. Gainsforth, P. Gallien, J.-P. Gillet, G. A. Grant, P. G. Graham, S. F. Green, F. Grossemy, P. R. Heck, G. F. Herzog, P. Hoppe, F. Hörz, J. Huth, K. Ignatyev, H. A. Ishii, K. Janssens, D. Joswiak, A. T. Kearsley, H. Khodja, A. Lanzirotti, J. Leitner, L. Lemelle, H. Leroux, K. Luening, G. J. MacPherson, K. K. Marhas, M. A. Marcus, G. Matrajt, T. Nakamura, K. Nakamura-Messenger, T. Nakano, M. Newville, D. A. Papanastassiou, P. Pianetta, W. Rao, Ch. Riekel, F. J. M. Rietmeijer, D. Rost, C. S. Schwandt, T. H. See, J. Sheffield-Parker, A. Simionovici, I. Sitnitsky, J. Ch. Snead, F. J. Stadermann, T. Stephan, R. M. Stroud, J. Susini, Y. Suzuki, R. S. Sutton, S. Taylor, N. Teslich, D. Troadec, P. Tsou, A. Tsuchiyama, K. Uesugi, B. Vekemans, E. P. Vicenzi, L. Vincze, A. J. Westphal, P. Wozniakiewicz, E. Zinner, and M. E. Zolensky. Elementary composition of comet 81P/Wild 2 samples collected by Sturdust. *Science*, 314(5806):1731–1735, 2006.

M. Fomenkova and Ch. Sherwood. Carbon in comet Halley dust particles. *AIP Conference Proceedings*, 310(193):193–202, 1994.

M. Fomenkova. On the organic refractory component of cometary dust. In K. Altwegg, P. Ehrenfreund, J. Geiss, and W. F. Huebner, editors, *Composition and origin of cometary materials*, volume 8 of *Proceedings of an ISSI Workshop, 14–18 September 1998, Bern, Switzerland*, page 109, 1998.

V. Formisano and G. Moreno. Helium and heavy ions in the solar wind. *La Rivista del Nuovo Cimento*, 1(3):365–422, 1971.

V. E. Fortov, A. P. Nefedov, O. F. Petrov, A. A. Samarian, and A. V. Chernyschev. Particle ordered structures in a strongly coupled classical thermal plasma. *Phys. Rev. E*, 54(3):R2236–R2239, 1996a.

V. E. Fortov, A. P. Nefedov, O. F. Petrov, A. A. Samarian, A. V. Chernyschev, and A. M. Lipaev. Experimental observation of Coulomb ordered structure in sprays of thermal dusty plasmas. *JETP Lett.*, 63(3):187–192, 1996b.

V. E. Fortov, A. P. Nefedov, O. S. Vaulina, A. M. Lipaev, V. I. Molotkov, A. A. Samaryan, V. P. Nikitskii, A. I. Ivanov, S. F. Savin, A. V. Kalmykov, A. Ya. Soloviev, and P. V. Vinogradov. Dusty plasma induced by solar radiation under microgravitational conditions: An experiment on board the Mir orbiting space station. *JETP Lett.*, 87(6):1087–1097, 1998.

V. E. Fortov, A. P. Nefedov, V. I. Vladimirov, L. V. Deputatova, V. I. Molotkov, V. A. Rykov, and A. V. Khudyakov. Dust particles in a nuclear-induced plasma. *Phys. Lett. A*, 258(4–6):305–311, 1999.

R. H. Fowler and L. Nordheim. Electron emission in intense electric fields. *Proceedings of Royal Society of London A*, 119(781):173–181, 1928.

R. H. Fowler. The analysis of photoelectric sensitivity curves for clean metals at various temperatures. *Phys. Rev.*, 38(1):45–56, July 1931.

J. W. Freeman and M. Ibrahim. Lunar electric fields, surface potential and associated plasma sheaths. *Earth Moon Planets*, 14(1):103–114, 1975.

G. D. Freier. The electric field of a large dust devil. *J. Geophys. Res.*, 65(10):3504–3504, 1960.

J. F. Friichtenicht, N. L. Roy, and D. G. Becker. The cosmic dust analyzer: Experimental evaluation of an impact ionization model. In *Evolutionary and Physical Properties of Meteoroids, Proceedings of IAU Colloq. 13 held in Albany, NY*, pages 299–310, 1971.

M. Fujihira, R. Hirooka, and H. Inokuchi. Photoemission from compounds containing benzene, naphthalene and anthracene ring systems. *Chem. Phys. Lett.*, 19(4):584–587, 1973.

H. P. Gail and E. Sedlmayr. On the photoelectric yield of insulating dust grains. *Astron. Astrophys.*, 86(3):380–385, 1980.

M. J. Genge, C. Engrand, M. Gounelle, and S. Taylor. The classification of micrometeorites. *Meteorit. Planet. Sci.*, 43(3):497–515, 2008.

D. Gerlich. Inhomogeneous RF fields: A versatile tool for the study of processes with slow ions. *Adv. Chem. Phys.*, 82(1), 1992.

J. S. Gilbert, S. J. Lane, R. S. J. Sparks, and T. Koyaguchi. Charge measurements on particle fallout from a volcanic plume. *Nature*, 349:598–600, 1991.

B. J. Gladman, J. A. Burns, M. J. Duncan, and H. F. Levison. The dynamical evolution of lunar impact ejecta. *Icarus*, 118(2):302–321, 1995.

C. K. Goertz. Dusty plasmas in the solar system. *Rev. Geophys.*, 27(2):271–292, 1989.

R. Gomer. *Field Emission and Field Ionization, vol. 9, , Harvard monographs in applied science edn.* Harvard University Press, Cambridge, 1961.

R. H. Good and E. W. Muller. *Encyklopedia of Physics, vol. XXI - Electron Emission, Gas Discharges I, chap. 2.* Springer-Verlag, Heidelberg, 1956.

J. N. Goswami, R. E. McGuire, R. C. Reedy, D. Lal, and R. Jha. Solar flare protons and alpha particles during the last three solar cycles. *J. Geophys. Res.*, 93(A7):7195–7205, 1988.

E. Grün and M. Horányi. A new look at Apollo 17 LEAM data: Nighttime dust activity in 1976. *Planet. Space. Sci.*, 89:2–14, 2013.

E. Grün, G. E. Morfill, and D. A. Mendis. In *Planetary Rings, edited by A. Brahic and R. Greenberg*, page 275, University of Arizona, 1984. Press: Tucson, AZ.

E. Grün, H. A. Zook, H. Fechtig, and R. H. Giese. Collisional balance of the meteoritic complex. *Icarus*, 62:244–272, 1985.

E. Grün, H. A. Zook, M. Baguhl, H. Fechtig, M. S. Hanner, J. Kissel, B. A. Lindbad, G. Linkert, I. B. Mann, J. A. M. McDonnell, G. E. Morfill, C. Polanskey, R. Riemann, G. Schwehm, and N. Siddique. Ulysses dust measurements near Jupiter. *Science*, 257(5076):1550–1552, 1992.

E. Grün, H. A. Zook, M. Baguhl, A. Balogh, S. J. Bame, H. Fechtig, R. Forsyth, M. S. Hanner, M. Horányi, J. Kissel, B. A. Lindbad, D. Linkert, G. Linkert, I. B. Mann, J. A. M. McDonnell, G. E. Morfill, J. L. Phyllips, C. Polanskey, G. Schwehm, N. Siddique, P. Staubach, J. Švestka, and A. Taylor. Discovery of Jovian dust streams and interstellar grain by Ulysses spacecraft. *Nature*, 362:428–430, 1993.

D. A. Gurnett, E. Grün, D. Gallagher, W. S. Kurth, and F. L. Scarf. Micron-sized particles detected near Saturn by the Voyager plasma wave instrument. *Icarus*, 53(2):236–254, 1983.

D. A. Gurnett, W. S. Kurth, D. L. Kirchner, G. B. Hospodarsky, P. Averkamp, T. F. Zarka, A. Lecacheux, R. Manning, A. Roux, P. Canu, N. Cornilleau-Wehrlin, P. Galopeau, A. Meyer, R. Boström, G. Gustafsson, J.-E. Wahlund, L. Ahlen, H. O. Rucker, H. P. Ladreiter, W. Macher, L. J. C. Woolliscroft, H. Alleyne, M. L. Kaiser, M. D. Desch, W. M. Farrell, C. C. Harvey, P. Louarn, P. J. Kellogg, K. Goetz, and A. Pedersen. The Cassini radio and plasma wave science investigation. *Space Sci. Rev.*, 114(1–4):395–463, 2004.

J. S. Halekas, R. P. Lin, and D. L. Mitchell. Large negative lunar surface potentials in sunlight and shadow. *Geophys. Res. Lett.*, 32(L09102):1–4, 2005.

D. P. Hamilton and J. Burns. Ejection of dust from Jupiter's gossamer ring. *Nature*, 364:695–699, 1993.

D. P. Hamilton. Motion of dust in a planetary magnetosphere: Orbit-averaged equations for oblateness, electromagnetic, and radiation forces with application to Saturn's E ring. *Icarus*, 101(2):244–264, 1993.

M. S. Hanner. On the detectability of ice grains in the comae of comets. *Icarus*, 47(3):342–350, 1981.

C. J. Hansen, L. W. Esposito, A. I. F. Stewart, J. Colwell, A. Hedrix, W. Pryor, D. Shemansky, and R. West. Enceladus' water vapor plume. *Science*, 311(5766):1422–1425, 2006.

C. J. Hansen, D. E. Shemansky, L. W. Esposito, A. I. F. Stewart, and B. R. Lewis. The composition and structure of the Enceladus plume. *Geophys. Res. Lett.*, 38(L11202):1–5, 2011.

M. Hapgood. Modelling long-term trends in lunar exposure to the Earth's plasmasheet. *Ann. Geophys.*, 25:2037–2044, 2007.

W. R. Harper. *Contact and frictional electrification*. Oxford at the Clarendon Press (Oxford University Press), London, 1967.

T. W. Hartquist, O. Havnes, and G. E. Morfill. The effects of dust on the dynamics of astronomical and space plasmas. *Fund. Cosm. Phys.*, 15:107–142, 1992.

C. M. Hartzell, X. Wang, D. J. Scheeres, and M. Horányi. Experimental demonstration of the role of cohesion in electrostatic dust lofting. *Geophys. Res. Lett.*, 40(6):1038–1042, 2013.

O. Havnes, T. K. Aanesen, and F. Melandsø. On dust charges and plasma potentials in a dusty plasma with dust size distribution. *J. Geophys. Res.*, 95(A5):6581–6585, 1990.

O. Havnes, U. de Angelis, R. Bingham, C. K. Goertz, G. E. Morfill, and V. Tsytovich. On the role of dust in the summer mesopause. *Journal of Atmospheric and Terrestrial Physics*, 52(6–8):637–643, 1990a.

O. Havnes, J. Trøim, T. Blix, W. Mortensen, L. I. Næsheim, E. Thrane, and T. Tønnesen. First detection of charged dust particles in the Earth's mesosphere. *J. Geophys. Res.*, 101(A5):10839–10847, 1996a.

M. M. Hedman, J. A. Burns, D. P. Hamilton, and M. R. Showalter. The three-dimensional structure of Saturn's E ring. *Icarus*, 217(1):322–338, 2012.

G. H. Heiken, D. T. Vaniman, and B. M. French. Lunar sourcebook a user's guide to the Moon. *Cambridge University Press, Cambridge*, 1991.

R. Hellmich and H. U. Keller. The comet Halley dust and gas environment. *Icarus*, 47(3):325–332, 1981.

P. S. H. Henry. The role of asymmetric rubbing in the generation of static electricity. *Br. J. Appl. Phys.*, 4(2):S31–S36, 1953.

P. S. H. Henry. Generation of static on solid insulators. In *J. Text. Inst. Proc.*, volume 48, pages P5–P25, 1957.

A. Herrmann, E. Schumacker, and L. Wöste. Preparation and photoionization potentials of molecules of sodium, potassium, and mixed atoms. *J. Chem. Phys.*, 68(5):2327–2336, 1978.

J. R. Hill and D. A. Mendis. On the origin of striae in cometary dust tails. *Astrophys. J.*, 242:395–401, 1980.

J. R. Hill and D. A. Mendis. The dynamical evolution of the Saturnian ring spokes. *J. Geophys. Res.*, 87(A9):7413–7420, 1982.

E. Hill, M. J. Mellin, B. Deane, Y. Liu, and L. A. Taylor. Apollo sample 70051 and high- and low-Ti lunar soil simulants MLS-1A and JSC-1A: Implications for future lunar exploration. *J. Geophys. Res.*, 112, 2007.

E. Hirst, P. H. Kaye, and J. R. Gruppy. Light scattering from nonspherical airborne particles: Experimental and theoretical comparisons. *Appl. Optics*, 33(30):7180–7186, 1994.

U. P. Hoppe, Ch. Hall, and J. Röttger. First observation of summer polar mesospheric backscatter with a 224 MHz radar. *Geophys. Res. Lett.*, 15(1):28–31, 1988.

U. P. Hoppe, D. C. Fritts, I. M. Reid, P. Czechowsky, C. M. Hall, and T. L. Hansen. Multiple-frequency studies of the high-latitude summer mesosphere : implications for scattering processes. *Journal of Atmospheric and Terrestrial Phys.*, 52(10/11):907–926, 1990.

M. Horányi and C. K. Goertz. Coagulation of dust particles in a plasma. *Astrophys. J.*, 361:155–161, 1990.

M. Horányi, J. Burns, and D. P. Hamilton. The dynamics of Saturn's E ring particles. *Icarus*, 97:248–259, 1992.

M. Horányi, G. Morfill, and E. Grün. The dusty ballerina skirt of Jupiter. *J. Geophys. Res.*, 98(A12):21245–21251, 1993.

M. Horányi, G. Morfill, and E. Grün. Mechanism for the acceleration and ejection of dust grains from Jupiter's magnetosphere. *Nature*, 363:144–146, 1993.

M. Horányi, B. Walch, S. Robertson, and D. Alexander. Electrostatic charging properties of Apollo 17 lunar dust. *J. Geophys. Res.*, 103(E4):8575–8580, 1998.

M. Horányi. Charged dust dynamics in the solar system. *Annu. Rev. Astron. Astrophys.*, 34:383–418, 1996.

F. Hoyle and Ch. Wickramasinghe. *Comets and the Origin of Life*. D. Reidel Publishing Company, 1981.

W. F. Huebner and D. C. Boice. Comets as a possible source of prebiotic molecules, 1992.

P. Žilavý, Z. Němeček, and J. Šafránková. Size and density determination of a spherical particle in the dust charging experiment. In *Proceedings of contributed papers WDS – part II*, page 252–257. Matfyzpress (Praha), 1999.

S. Isobe and A. Satheesh-Kumar. Charging of dust grains in the solar dust ring and its effect. In J.-C. Gerard A. Brahic and J. Surdej, editors, *Observations and Physical Properties of Small Solar System Bodies*, volume 30 of *Proceedings of the Liege International Astrophysical Colloquium, Institut d'Astrophysique, Liege: Universite de Liege, Institut d'Astrophysique*, page 257, 1992.

M. Jeřáb, I. Richterová, J. Pavlů, J. Šafránková, and Z. Němeček. Influence of charging conditions on field ion emission from dust grains. *IEEE Trans. Plasma Sci.*, 35(2):292–296, 2007.

E. K. Jessberger. Rocky cometary particulates: Their elemental, isotopic and mineralogical ingredients. In K. Altwegg, P. Ehrenfreund, J. Geiss, and W. F. Huebner, editors, *Composition and origin of cometary materials*, volume 8 of *Proceedings of an ISSI Workshop, 14–18 September 1998, Bern, Switzerland*, page 91, 1998.

R. E. Johnson and R. Baragiola. Lunar surface: Sputtering and secondary ion mass spectrometry. *Geophys. Res. Lett.*, 18(11):2169–2172, 1991.

T. V. Johnson, G. Morfill, and E. Grün. Dust in Jupiter's magnetosphere: An Io source? *Geophys. Res. Lett.*, 7(50):305–308, 1980.

G. H. Jones, N. Krupp, H. Kruger, E. Rousoss, W.-H. Ip, D. G. Mitchell, S. M. Krimigis, J. Woch, A. Lagg, M. Franz, M. K. Dougherty, C. S. Arridge, and H. J. McAndrews. Formation of Saturn's ring spokes by lightning-induced electron beams. *Geophys. Res. Lett.*, 33(L21202):1–6, 2006.

J. L. H. Jonker. On the theory of secondary electron emission. *Phillips Res. Rep.*, 7:1–20, 1952.

M. C. Kelley. The effect of cluster ions on anomalous VHF backscatter from the summer polar mesosphere. *Geophys. Res. Lett.*, 14(10):1031–1034, 1987.

P. J. Kellogg, K. Goetz, and S. J. Monson. Dust impact signals on the wind spacecraft. *J. Geophys. Res.*, 121(2):966–991, 2016.

S. Kempf, R. Srama, M. Horányi, M. Burton, S. Helfert, G. Moragas-Klostermeyer, M. Roy, and E Grün. High-velocity streams of dust originating from Saturn. *Nature*, 433:289–291, 2005a.

S. Kempf, R. Srama, F. Postberg, M. Burton, S. F. Green, S. Helfert, J. K. Hillier, N. McBride, J. A. McDonnell, G. Moragas-Klostermeyer, M. Roy, and E. Grün. Composition of Saturnian stream particles. *Science*, 307(5713):1274–1276, 2005b.

S. Kempf, U. Beckmann, G. Moragas-Klostermeyer, F. Postberg, R. Srama, T. Economou, J. Schmidt, F. Spahn, and E. Grün. The E ring in the vicinity of Enceladus: I. spatial distribution and properties of the ring particles. *Icarus*, 193(2):420–437, 2008.

S. Kempf, U. Beckmann, and J. Schmidt. How the Enceladus dust plume feeds Saturn's E ring. *Icarus*, 206(2):446–457, 2010.

S. Kempf, R. Srama, E. Grün, A. Mocker, F. Postberg, J. K. Hillier, M. Horányi, Z. Sternovsky, B. Abel, A. Beinsen, R. Thissen, S. Jürgen, F. Spahn, and N. Altobelli. Linear high resolution dust mass spectrometer for a mission to the Galilean satellites. *Planet. Space. Sci.*, 65(1):10–20, 2012.

S. A. Khrapak, A. P. Nefedov, O. F. Petrov, and O. S. Vaulina. Dynamical properties of random charge fluctuations in a dusty plasma with different charging mechanisms. *Phys. Rev. E and Erratum in Phys. Rev. E*, 59(5):6017–6022, 1999.

H. Kimura, H. Okamoto, and T. Mukai. Radiation pressure and the Poynting-Robertson effect for fluffy dust particles. *Icarus*, 157(2):349–361, 2002.

J. Kissel, R. Z. Sagdeev, J. L. Bertaux, V. V. Angarov, J. Audouze, J. E. Blamont, K. Buchler, E. N. Evlanov, H. Fechtig, M. N. Fomenkova, H. von Hoerner, N. A. Inogamov, V. N. Khromov, W. Knabe, F. R. Krueger, Y. Langevin, V. B. Leonas, A. C. Levasseur-Regourd, G. G. Managadze, S. N. Podkolzin, V. D. Shapiro, S. R. Tabaldyev, and B. V. Zubkov. Composition of comet Halley dust particles from Vega observations. *Nature*, 321:280–282, 1986.

R. L. Klein, K. S. Budil, T. S. Perry, and D. R. Bach. The interaction of supernova remnants with interstellar clouds: Experiments on the Nova laser. In *Lawrence Livermore National Laboratory*, pages 1–48, 2002.

H. Klinkrad. *Space Debris Models and Risk Analysis*. Number ISBN 3-540-25448-X. Springer-Verlag, Berlin Heidelberg New York, 2006.

S. Koutchmy and P. Lamy. Propagating inhomogeneities in the dust tail of comet West 1975. *Nature*, 273:522–524, 1978.

P. L. Lamy. Interaction of interplanetary dust grains with the solar radiation field. *Astron. Astrophys.*, 35(2):197–207, 1974.

L. J. Lanzerotti, W. L. Brown, J. M. Poate, and W. M. Augustniak. Low energy cosmic ray erosion of ice grains in interplanetary and interstellar media. *Nature*, 272:431–433, 1978.

L. J. Lanzerotti. *Solar-terrestrial physics*. Number ISBN 978-80-246-1342-0. Encyclopedia of physical science and technology, Academic Press, SanDiego, 1987.

A. Laor and B. T. Draine. Spectroscopic constrains on the properties of dust in active galactic nuclei. *Astrophys. J.*, 402(2):441–468, 1993.

J. M. Latimer. Formation of planetary systems. In *Lunar and Planetary Exploration*, page 182, Toulouse: Capadues, 1982.

L.-H. Lee. Dual mechanism for metal-polymer contact electrification. *J. Electrost.*, 32(1):1–29, 1994.

H. Leroux, F. J. M. Rietmeijer, M. A. Velbel, A. J. Brearley, D. Jacob, F. Langenhorst, J. C. Bridges, T. J. Zega, R. M. Stroud, P. Cordier, R. P. Harvey, M. Lee, M. Gounelle, and M. E. Zolensky. A TEM study of thermally modified comet 81P/Wild 2 dust particles by interactions with the aerogel matrix during the Stardust capture process. *Meteorit. Planet. Sci.*, 43(1/2):97–120, 2008.

Jer-Chyi Liou and H. A. Zook. Comets as a source of low eccentricity and low inclination interplanetary dust particles. *Icarus*, 123(2):421–502, 1996.

Jer-Chyi Liou, H. A. Zook, and F. D. Stanley. Kuiper belt dust grains as a source of interplanetary dust particles. *Icarus*, 124(2):429–440, 1996.

J. Lowell and A. C. Rose-Innes. Contact electrification. *Adv. Phys.*, 29(6):947–1023, 1980.

J. Lowell. Contact electrification of metals. *J. Phys. D*, 8:53–63, 1975.

G. Makov, A. Nitzan, and L. E. Brus. On the ionization-potential of small metal and dielectric particles. *J. Chem. Phys.*, 88(8):5076–5085, April 1988.

D. M. Malaspina, M. Horányi, A. Zaslavsky, K. Goetz, L. B. III. Wilson, and K. Kersten. Interplanetary and interstellar dust observed by the Wind/WAVES electric field instrument. *Geophys. Res. Lett.*, 41(2):266–272, 2014.

R. H. Manka. Plasma and potential at the lunar surface. *Photon and Particle Interactions with Surfaces in Space*, 37:347–361, 1973.

J. A. M. McDonnell, P. L. Lamy, and G. S. Pankiewicz. Physical properties of cometary dust. In R. L. Newburn, Jr., M. Neugebauer, and J. Rahe, editors, *IAU Colloq.: Comets in the post-Halley era*, volume 116 of *Astrophysics and Space Science Library*, pages 1043–1073, 1991.

A. F. McGuire and B. W. Hapke. An experimental study of light scattering by large, irregular particles. *Icarus*, 113(1):134–155, 1995.

R. M. McQueen. Infrared observations of the outer solar corona. *Astrophys. J.*, 154:1059–1076, 1968.

O. Melnik and M. Parrot. Electrostatic discharge in Martian dust storms. *J. Geophys. Res.*, 103(A12):29107–29117, 1998.

D. A. Mendis and W. I. Axford. Satellites and magnetospheres of the outer planets. *Annu. Rev. Earth Pl. Sc.*, 2:419–474, 1974.

D. A. Mendis and M. Rosenberg. Some aspects of dust-plasma interactions in the cosmic environment. *IEEE Trans. Plasma Sci.*, 20(6):929–934, 1992.

D. A. Mendis and M. Rosenberg. Cosmic dusty plasma. *Annu. Rev. Astron. Astrophys.*, 32:419–463, 1994.

D. A. Mendis, H. L. F. Houpis, and M. L. Marconi. The physics of comets. In *Fundamentals of Cosmic Physics*, volume 10, 1985.

D. A. Mendis. *Advances in Dusty Plasmas: Proceedings of the International Conference on Physics of Dusty Plasmas*. World Scientific Publishing, Singapore, 1996.

D. A. Mendis. Progress in the study of dusty plasmas. *Plasma Sources Sci. T.*, 11:A219–A228, 2002.

S. Messenger. Identification of molecular-cloud material in interplanetary dust particles. *Nature*, 404:968–971, 2000.

N. Meyer-Vernet, A. Lecacheux, and B. M. Pedersen. Constraints on Saturn's E ring from the Voyager 1 radio astronomy instrument. *Icarus*, 123(0145):113–128, 1996.

N. Meyer-Vernet, M. Moncuquet, K. Issautier, and A. Lecacheux. The importance of monopole antennas for dust observations: Why Wind/WAVES does not detect nanodust. *Geophys. Res. Lett.*, 41:2716–2720, 2014.

N. Meyer-Vernet. Flip-flop of electric potential of dust grains in space. *Astron. Astrophys.*, 105(1):98–106, 1982.

N. Meyer-Vernet. Voyager 2 at Uranus – grain impacts in the ring plane. *Geophys. Res. Lett.*, 13(7):617–620, 1986.

R. A. Millikan. On the elementary electrical charge and the Avogadro constant. *Phys. Rev.*, 2(2):109–143, 1913.

C. J. Mitchell, M. Horányi, O. Havnes, and C. C. Porco. Saturn's spokes: Lost and found. *Science*, 311(5767):1587–1589, 2006.

E. W. Müller and T. T. Tsong. Field ion microscopy, principles and applications. *American Elsevier Pub. Co.*, 1969.

U. Müller, A. Schmidt-Ott, and H. Burtscher. Photoelectric quantum yield of free silver particles near threshold. *Z. Phys. B – Cond. Matter*, 73:103–106, 1988.

A. Mocker, K. Hornung, E. Grün, S. Kempf, A. Collette, K. Drake, M. Horányi, T. Munsat, L. O'Brien, Z. Sternovsky, and R. Srama. On the application of a linear time-of-flight mass spectrometer for the investigation of hypervelocity impacts of micron and sub-micron sized dust particles. *Planet. Space. Sci.*, 89:47–57, 2013.

G. E. Morfill, E. Grün, and T. V. Johnson. Dust in Jupiter's magnetosphere: Physical processes. *Planet. Space. Sci.*, 28:1087–1100, 1980.

T. Mukai and T. Yamamoto. A model of the circumsolar dust cloud. *Publ. Astron. Soc. Japan*, 31:585–596, 1979.

T. Mukai, J. Blum, A. M. Nakamura, R. E. Johnson, and O. Havnes. *Interplanetary Dust*. Springer-Verlag, Heidelberg, 2001.

T. Mukai. Electrostatic fragmentation of irregularly shaped particles. In *Origin and Evolution of Interplanetary Dust*, pages 371–374. Kluwer Academic Publishers, 1991.

T. Nakamura, A. Tsuchiyama, T. Akaki, K. Uesugi, T. Nakano, A. Takeuchi, Y. Suzuki, and T. Noguchi. Bulk mineralogy and three-dimensional structures of individual stardust particles deduced from synchrotron X-ray diffraction and microtomography analysis. *Meteorit. Planet. Sci.*, 43(1–2):247–259, 2008.

D. Nesvorný, P. Jenniskens, H. F. Levison, W. F. Bottke, D. Vokrouhlický, and M. Gounelle. Cometary origin of the zodical cloud and carboneceous micrometeorites. Implications for hot debris disks. *Astrophys. J.*, 713(2):816–836, 2010.

E. P. Ney. Star dust. *Science*, 195(4278):541–546, 1977.

K. Nitta, M. Takahashi, H. Miyake, Y. Yamano, and K. Yto. A measurement of light intensity and quantum yield in photoelectron emission from satellite surface materials in the 30–250 nm range. In *XXIVth Int. Symp. on Discharges and Electrical Insulation in Vacuum*, pages 1–4, 2010.

T. Nitter and O. Havnes. Dynamics of dust in a plasma sheath and injection of dust into the plasma sheath above Moon and asteroidal surfaces. *Earth Moon Planets*, 56(1):7–34, 1992.

T. Nitter, T. K. Aslaksen, F. Melandsø, and O. Havnes. Levitation and dynamics of a collection of dust particles in a fully ionized plasma sheath. *IEEE Trans. Plasma Sci.*, 22(2):159–172, 1994.

T. Nitter, O. Havnes, and F. Melandsø. Levitation and dynamics of charged dust in the photoelectron sheath above surfaces in space. *J. Geophys. Res.*, 103(A4):6605–6620, 1998.

T. G. Northrop. Dusty plasmas. In *Phys. Scr.*, volume 45, pages 475–490. 5, 1992.

T. G. Northrop. Physics of dusty plasmas: An historical overview. In P. K. Shukla, D. A. Mendis, and T. Desai, editors, *Advances in Dusty Plasmas, Proceedings of the International Conference on Physics of Dusty Plasmas*, pages 3–19, 1997.

L. Nouzák, J. Pavlů, J. Šafránková, and Z. Němeček. Photoelectron energy distribution from an Au target measured by a gridless Faraday cup. In *Proceedings of contributed papers WDS – part II*, page 48–53. Matfyzpress (Praha), 2013.

L. Nouzák, J. Pavlů, J. Šafránková, and Z. Němeček. Investigation of the photoemission from glass dust grains. In *Proceedings of contributed papers WDS – Physics*, page 361–370. Matfyzpress (Praha), 2014.

L. Nouzák, I. Richterová, J. Pavlů, Z. Němeček, and J. Šafránková. Investigations of photoemission from lunar dust simulant. *IEEE Trans. Plasma Sci.*, 44(4):512–518, 2016.

L. Nouzák, S. Hsu, D. Malaspina, F. M. Thayer, S.-Y. Ye, Z. Sternovsky, J. Pavlů, Z. Němeček, and J. Šafránková. Laboratory modeling of dust impact detection by the Cassini spacecraft. *Planet. Space. Sci.*, pages 1–15, 2017.

L. Nouzák. Systém stabilizace proudu zdrojů částic. Bakalářská práce, MFF UK Praha, 2010.

P. Oberc. Electric antenna as a dust detector. *Adv. Sp. Res.*, 17(12):(12)105–(12)110, 1996.

G. R. Olhoeft, D. W. Strangway, and A. L. Frisillo. Lunar sample electrical properties. In *Proc. Lunar Sci. Conf. 4th*, volume 3, pages 3133–3149, 1973.

N. Olhoeft, A. L. Frisillo, and D. W. Strangway. Electrical properties of lunar soil sample 15301,38. *J. Geophys. Res.*, 79(11):1599–1604, 1974.

B. C. O'Neill and T. R. Foord. Contact and tribo charging of polymer surfaces. In *Proc. Static Electrification Conf.*, pages 104–114, 1975.

E. J. Opik. Interplanetary dust and terrestrial accretion of meteoric matter. *Irish Astronomical Journal*, 4(3/4):84–135, 1956.

J. Oró, A. Lazeano, and P. Ehrenfreund. *Comets and the Origin and Evolution of Life*. Springer-Verlag (eds. P. J. Thomas et al.), Berlin Heidelberg, 2006.

J. Oró. Comets and the formation of biochemical compounds on the primitive Earth. *Nature*, 190(4774):389–390, 1961.

E. D. Palik. *Handbook of Optical Constants of Solids*. Academic Press, Boston, 1985.

F. Pantellini, S. Belheouane, N. Meyer-Vernet, and A. Zaslavsky. Nano dust impacts on spacecraft and boom antenna charging. *Astrophys. Space Sci.*, 341(2):309–314, 2012.

D. A. Patthoff and S. A. Kattenhorn. A fracture history on Enceladus provides evidence for a global ocean. *Geophys. Res. Lett.*, 38(L18201):1–16, 2011.

W. Paul and H. Steinwedel. *German patent nr. 944 900*. USA Patent 2939958, 1956.

J. Pavlů, Z. Němeček, J. Šafránková, and I. Čermák. Emission from nonconductive negatively charged dust grains. *IEEE Trans. Plasma Sci.*, 32(4):607–612, 2004.

J. Pavlů, I. Richterová, J. Šafránková, and Z. Němeček. Impact of surface properties on the dust grain charging. *Adv. Sp. Res.*, 38(11):2558–2563, 2006a.

J. Pavlů, A. Velyhan, I. Richterová, J. Šafránková, Z. Němeček, J. Wild, and M. Jeřáb. Ion beam effects on dust grains: 2—Influence of charging history. *Vacuum*, 80(6):542–547, 2006b.

J. Pavlů, I. Richterová, Z. Němeček, J. Šafránková, and J. Wild. The sputtering of dust grains: Aspects of experimental observations. *IEEE Trans. Plasma Sci.*, 35(2):297–302, 2007.

M. A. Pelizzari and D. R. Criswell. Differential photoelectric charging of nonconducting surfaces in space. *J. Geophys. Res.*, 83(A11):5233–5244, 1978.

M. E. Perry, B. Teolis, H. T. Smith, R. L. McNutt Jr., G. Fletcher, W. Kasprzak, B. Magee, D. G. Mitchell, and J. H. Waite Jr. Cassini INMS observations of neutral molecules in Saturn's E-ring. *J. Geophys. Res.*, 115(A10206):1–11, 2010.

A. W. Peterson. Experimental detection of thermal radiation from interplanetary dust. *Astrophys. J.*, 148:L37–L39, 1967.

A. R. Poppe. An improved model for interplanetary dust fluxes in the outer solar system. *Icarus*, 264:369–386, 2015.

C. C. Porco, P. Helfenstein, P. C. Thomas, A. P. Ingersoll, J. Wisdom, R. West, G. Neukum, T. Denk, R. Wagner, T. Roatsch, S. Kieffer, E. Turtle, A. McEwen, T. V Johnson, J. Rathbun, J. Veverka, D. Wilson, J. Perry, J. Spitale, A. Brahic, J. A. Burns, A. D. DelGenio, L. Dones, C. D. Murray, and S. Squyres. Cassini observes the active south pole of Enceladus. *Science*, 311(5766):1393–1401, 2006.

F. Postberg, S. Kempf, R. Srama, S. F. Green, J. K. Hillier, N. McBride, and E. Grün. Composition of jovian dust stream particles. *Icarus*, 183(1):122–134, 2006.

A. Quemerais, A. Seignac, M. Priol, and J. Lefevre. Optical and photoelectric properties of materials of astrophysical interest, 1985.

P. R. Ratcliff, M. J. Burchell, M. J. Cole, T. W. Murphy, and F. Allahdadi. Experimental measurements of hypervelocity impact plasma yield and energetics. *Int. J. Impact Engng.*, 20(6–10):663–674, 1997.

G. Reid. Ice particles and electron "bite-outs" at the summer polar mesopause. *J. Geophys. Res.*, 95(D9):13891–13896, 1990.

R. Reinhard. The comet Halley micrometeoroid hazard. *ESA*, SP-153:7–15, 1997.

J. J. Rennilson and D. R. Criwsell. Surveyor observations of lunar horizon-glow. *Moon Planets*, 10(2):121–142, 1974.

O. W. Richardson. On the negative radiation from hot platinum. *Philosophical of the Cambridge Society*, 11:286–295, 1901.

I. Richterová, Z. Němeček, J. Šafránková, and J. Pavlů. A model of secondary emission from dust grains and its comparison with an experiment. *IEEE Trans. Plasma Sci.*, 32(2):617–622, 2004.

I. Richterová, Z. Němeček, M. Beránek, J. Šafránková, and J. Pavlů. Secondary emission from non-spherical dust grains with rough surfaces: Application to lunar dust. *Astrophys. J.*, 761(108):1–5, 2012.

I. Richterová, Z. Němeček, J. Pavlů, J. Šafránová, and J. Vaverka. Secondary emission from clusters composed of spherical grains. *IEEE Trans. Plasma Sci.*, 44(4):505–511, 2016.

S. Robertson, Z. Sternovsky, and B. Walch. Reduction of asymmetry transport in the annular Penning trap. *Phys. Plasmas*, 11(5):1753–1756, 2004.

L. J. Robinson. Closing in on Saturn. *Sky Telescope*, 60(6):481–481, 1980.

M. Rosenberg, D. A. Mendis, and Sheehan D. P. UV-induced Coulomb crystallization of dust grains in high-pressure gas. *IEEE Trans. Plasma Sci.*, 24(6):1422–1430, 1996.

M. Rosenberg, D. A. Mendis, and Sheehan D. P. Positively charged dust crystals induced by radiative heating. *IEEE Trans. Plasma Sci.*, 27(1):239–242, 1999.

J. Roth. Chemical sputtering. In *Topics in Applied Physics, Sputtering by particle bombardement II*, volume 52, pages 91–146. Springer-Verlag, 1983.

S. Röser and H. J. Staude. The zodiacal light from 1500A to 60 micron. *Astron. Astrophys.*, 67(3):381–394, 1978.

W. A. D. Rudge. On the electrification produced during the raising of a cloud of dust. *Proc. R. Soc. London A*, 90(618):256–271, 1914.

V. S. Safranov. *Evolution of the Protoplanetary Cloud and the Formation of the Earth and the Planets*. NASA TT F-677, 1972.

R. Z. Sagdeev. Small-size dust particles near Halley's comet. *Adv. Sp. Res.*, 9(3):263–267, 1989.

S. A. Sandford, J. Aléon, C. M. O'D. Alexander, S. Bajt, G. A. Baratta, J. Borg, J. P. Bradley, D. E. Brownlee, J. R. Brucato, M. J. Burchell, H. Busemann, A. Butterworth, S. J. Clemett, G. Cody, L. Colangeli, G. Cooper, L. D'Hendecourt, Z. Djouadi, J. P. Dworkin, G. Ferrini, H. Fleckenstein, G. J. Flynn, I. A. Franchi, M. Fries, M. K. Gilles, D. P. Glavin, M. Gounelle, F. Grossemy, Ch. Jacobsen, L. P. Keller, A. L. D. Kilcoyne, J. Leitner, G. Matrajt, A. Meibom, V. Mennella, S. Mostefaoui, L. R. Nittler, M. E. Palumbo, D. A. Papanastassiou, F. Robert, A. Rotundi, Ch. J. Snead, M. K. Spencer, F. J. Stadermann, A. Steele, T. Stephan, P. Tsou, T. Tyliszczak, A. J. Westphal, S. Wirick, B. Wopenka, H. Yabuta, R. N. Zare, and M. E. Zolensky. Organics captured from Comet 81P/Wild 2 by the Stardust spacecraft. *Science*, 314(5806):1720–1724, 2006.

B. D. Savage and J. S. Mathis. Observed properties of interstellar dust. *Ann. Rev. Astron. Astrophys.*, 17:73–111, 1979.

F. L. Scarf, D. A. Gurnett, W. S. Kurth, and R. L. Poynter. Voyager 2 plasma wave observations at Saturn. *Science*, 215(4532):587–594, 1982.

L. E. Schaffer and J. A. Burns. Stochastic charging of dust grains in planetary rings: Diffusion rates and their effect on Lorentz resonances. *J. Geophys. Res.*, 100(A1):213–234, 1995.

B. Schleicher, H. Burtscher, and H. C. Siegmann. Photoelectric quantum yield of nanometer metal particles. *Appl. Phys. Lett.*, 63(9):1191–1193, 1993.

A. Schmidt-Ott, P. Schurtenberger, and H. C. Siegmann. Enormous yield of photoelectrons from small particles. *Phys. Rev. Lett.*, 45(15):1284–1287, 1980.

W. Schottky. Über den Einfluss von Strukturwirkungen, besonders der Thomsonschen Bildkraft, auf die Elektronenemission der Metall. *Phys. Z.*, 15:872–878, 1914.

H. Schulze, J. Kissel, and E. K. Jessberger. In Y. J. Pendleton, editor, *From Stardust to Planetesimals*, volume 122 of *Astronomical Society of the Pacific Conference Series*, page 397, 1997.

E. Schumacher, M. Kappes, K. Marti, P. Radi, M. Schär, and B. Schmidhalter. Metal-clusters: Preparation, properties, theory. *Ber. Bunsenges. Phys. Chem.*, 88(3):220–228, 1984.

R. Schwenn. *Encyclopedia of Astronomy and Astrophysics*. Nature Publishing Group, Dirac House, Temple Back, Bristol, UK, 2001.

Z. Sekanina and J. A. Farrell. Evidence for fragmentation of strongly nonspherical dust particles in the tail of comet West 1976 VI. In *Solid particles in the solar system*, pages 267–270. Dordrecht, D. Reidel Publishing Co., 1976.

Z. Sekanina and H. E. Schuster. Dust from periodic comet Encke: Large grains in short supply. *Astron. Astrophys.*, 68(3):429–435, 1978.

Z. Sekanina and H. E. Schuster. Meteoroids from periodic comet d'Arrest. *Astron. Astrophys.*, 65(1):29–35, 1978.

P. E. Shaw and R. F. Hanstock. Triboelectricity and friction. *Proc. R. Soc. London A*, 128:474–479, 1930.

P. E. Shaw. Electrical separation between identical solid surfaces. *Proc. Phys. Soc.*, 39:449–452, 1927.

J. Shirley and R. Fairbridge. *Encyclopedia of Planetary Sciences. Encyclopedia of Earth Sciences Series.* Springer, 1997.

M. R. Showalter, J. A. Burns, J. N. Cuzzi, and J. B. Pollack. Jupiter's ring system: New results on structure and particle properties. *Icarus*, 69:458–498, 1987.

M. R. Showalter, J. N. Cuzzi, and S. M. Larson. Structure and particle properties of Saturn's E ring. *Icarus*, 94:451–473, 1991.

A. Shu, A. Collette, K. Drake, E. Grün, M. Horányi, S. Kempf, A. Mocker, T. Munsat, P. Northway, R. Srama, Z. Sternovsky, and E. Thomas. 3MV hypervelocity dust accelerator at the Colorado Center for Lunar Dust and Atmospheric Studies. *Rev. Sci. Instrum.*, 83(7):5108–1–5108–8, 2012.

A. A. Sickafoose, J. E. Colwell, M. Horányi, and S. Robertson. Photoelectric charging of dust particles in vacuum. *Phys. Rev. Lett.*, 84(26):6034–6037, March 2000.

J. A. Simpson. Introduction to the galactic cosmic radiation. In *Composition and origin of cosmic rays, ed. M. M. Shapiro*, volume 107, pages 1–24. Reidel (Amsterdam), 1983.

S. F. Singer and J. E. Stanley. In I. Halliday and B. A. McIntosh, editors, *Solid particles in the solar system*, volume 80, pages 329–333. Springer Netherlands, 1980.

S. F. Singer and E. H. Walker. Electrostatic dust transport on the lunar surface. *Icarus*, 1(1–6):112–120, 1962.

B. A. Smith, L. A. Soderblom, R. Beebe, J. Boyce, G. Briggs, M. Carr, S. A. Collins, A. F. Cook II, G. E. Danielson, M. E. Davies, G. E. Hunt, A. Ingersoll, T. V. Johnson, H. Masursky, J. McCauley, D. Morrison, T. Owen, C. Sagan, E. M. Shoemaker, R. Strom, V. E. Suomi, and J. Veverka. The Galilean satellites and Jupiter: Voyager 2 imaging science results. *Science*, 206(4421):927–950, 1979.

B. A. Smith, L. A. Soderblom, T. V. Johnson, A. P. Ingersoll, S. A. Collins, E. M. Shoemaker, G. E. Hunt, H. Masursky, M. H. Carr, M. E. Davies, A. F. Cook, J. Boyce, G. E. D., Danielson, O. Tobias, C. Sagan, R. F. Beebe, J. Veverka, R. G. Strom, J. F. McCauley, D. Morrison, G. A. Briggs, and V. E. Suomi. The Jupiter system through the eyes of Voyager 1. *Science*, 204(4396):951–972, 1979.

B. A. Smith, L. Soderblom, R. Batson, P. Bridges, J. Inge, H. Masursky, E. Shoemaker, R. Beebe, J. Boyce, G. Briggs, A. Bunker, S. A Collins, C. J. Hansen, T. V. Johnson, J. L. Mitchell, R. J. Terrile, A. F. Cook II, J. Cuzzi, J. B. Pollack, G. E. Danielson, A. P. Ingersoll, M. E. Davies, G. E. Hunt, D. Morrison, T. Owen, C. Sagan, J. Veverka, R. Strom, and V. E. Suomi. A new look at the Saturn system: The Voyager 2 images. *Science*, 215(4532):504–537, 1982.

G. F. Smith. Thermionic and surface properties of tungsten crystals. *Phys. Rev.*, 94(2):295–308, 1954.

J. M. Smith. Nonequilibrium ionization in wet alkali metal vapors. *AIAA J.*, 3(4):648–651, 1965.

M. S. Sodha and S. Guha. Physics of collodial plasmas. *Adv. Plasma Phys.*, 4:219–309, 1971.

F. Spahn, J. Schmidt, N. Albers, M. Hörning, M. Makuch, M. Seiß, S. Kempf, R. Srama, V. Dikarev, S. Helfert, G. Moragas-Klostermeyer, A. K. Krivov, M. Sremčević, A. J. Tuzzolino, T. Economou, and E. Grün. Cassini dust measurements at Enceladus and implications for the origin of the E ring. *Science, New Series*, 311(5766):1416–1418, 2006.

Specs. Small spot UV source. Technical report, SPECS, 2006.

L. Spitzer. *Physical processes in the interstellar medium.* Wiley-VCH Verlag, Weinheim, 2004.

R. Srama and S. Auer. Low-charge detector for the monitoring of hyper-velocity micron-sized dust particles. *Measurement Science and Technology*, 19(5):1–8, 2008.

R. Srama, S. Kempf, G. Moragas-Klostermeyera, S. Helfert, T. J. Ahrens, N. Altobelli, S. Auer, U. Beckmann, J. G. Bradley, M. Burton, V. V. Dikarev, T. Economou, H. Fechtig, S. F. Green, M. Grande, O. Havnes, J. K. Hillier, M. Horányi, E. Igenbergs, E. K. Jessberger, T. V. Johnson, H. Kruger, G. Matt, N. McBride, A. Mocker, P. Lamy, D. Linkert, G. Linkert, F. Lura, J. A. M. McDonnell, D. Mohlmannn, G. E. Morfill, F. Postberg, M. Roy, G. H. Schwehm, F. Spahn, J. Švestka, V. Tschernjawskin, A. J. Tuzzolinoe, R. Waschn, and E. Grün. In situ dust measurements in the inner Saturnian system. *Planet. Space. Sci.*, 54(9–10):967–987, 2006.

L. Starukhina. Water detection on atmosphereless celestial bodies: Alternative explanations of the observations. *J. Geophys. Res.*, 106(E7):14701–14710, 2001.

T. Stephan, D. Rost, E. P. Vicenzi, E. S. Bullock, G. J. MacPherson, A. J. Westphal, Ch. J. Snead, G. J. Flynn, S. A. Sandford, and M. E. Zolensky. TOF-SIMS analysis of cometary matter in Stardust aerogel track. *Meteorit. Planet. Sci.*, 43(1–2):233–246, 2008a.

T. Stephan, G. J. Flynn, S. A. Sandford, and M. E. Zolensky. TOF-SIMS analysis of cometary particles extracted from Stardust aerogel. *Meteorit. Planet. Sci.*, 43(1–2):285–298, 2008b.

E. J. Sternglass. *Theory of secondary electron emission under electron bombardment.* Sci. Pap. 1772, Westinghouse Res. Lab., Pittsburgh, Pa., 1954.

Z. Sternovsky, Z. Němeček, J. Šafránková, and A. Velyhan. Ion field emission from micrometer-sized spherical glass grains. *IEEE Trans. Plasma Sci.*, 29(2):292–297, 2001.

Z. Sternovsky, S. Robertson, A. Sickafoose, J. Colwell, and M. Horányi. Contact charging of lunar and Martian dust simulants. *J. Geophys. Res.*, 107(E11):15–1–15–8, 2002.

Z. Sternovsky, K. Amyx, G. Bano, M. Landgraf, M. Horányi, S. Knappmiller, S. Robertson, E. Grün, R. Srama, and S. Auer. Large area mass analyzer instrument for the chemical analysis of interstellar dust particles. *Rev. Sci. Instrum.*, 78(014501):1–10, 2007.

Z. Sternovsky, P. Chamberlin, M. Horányi, S. Robertson, and X. Wang. Variability of the lunar photoelectron sheath and dust mobility due to solar activity. *J. Geophys. Res.*, 113(A10104):1–4, 2008.

W. G. Stroud, W. Nordberg, W. R. Bandeen, F. L. Bartman, and P. Titus. Rocket-grenade observation of atmospheric heating in the arctic. *J. Geophys. Res.*, 64(9):1342–1343, 1959.

J. Stubbs, R. R. Vondrak, and W. M. Farrell. A dynamic fountain model for lunar dust. *Adv. Sp. Res.*, 37(1):59–66, 2006.

S. P. Synnott, C. F. Peters, B. A. Smith, and L. A. Morabito. Orbits of the small satellites of Saturn. *Science*, 212(4491):191–192, 1981.

S. R. Taylor. *Planetary science: A lunar perspective*. Lunar and Planetary Institute, Houston, Texas, 1982.

B. D. Teolis, M. E. Perry, B. A. Magee, J. Westlake, and J. H. Waite. Detection and measurements of ice grains and gas distribution in the Enceladus plume by Cassini's Ion Neutral Mass Spectrometer. *J. Geophys. Res.*, 115(A9):1–12, July 2010.

J. D. Thomas, G. S. Hodges, D. G. Seely, N. A. Moroz, and T. J. Kvale. Performance enhancement study of an electrostatic Faraday cup detector. *Nucl. Instrum. Methods Phys. Res., Sect. A*, 536(1–2):11–21, 2005.

P. C. Thomas, R. Tajeddine, M. S. Tiscareno, J. A. Burns, J. Joseph, T. J. Loredo, and P. Helfenstein. Enceladus's measured physical libration requires a global subsurface ocean. *Icarus*, 264:37–47, 2016.

G. E. Thomas. Mesospheric clouds and the physics of the mesopause region. *Rev. Geophys.*, 29(4):553–575, 1991.

A. G. G. M. Tielens and L. J. Allamandola. Composition, structure, and chemistry of interstellar dust. In *NASA Technical Memorandum 88350*, page 1–74. NASA, Ames Research Center, 1985.

A. G. G. M. Tielens. The composition of interstellar dust. In *The Role of Dust in the Formation of Stars*, page 280–287. Springer-Verlag, 1996.

P. Tsou, D. E. Brownlee, S. A. Sandford, F. Horz, and M. E. Zolensky. Wild 2 and interstellar sample collection and Earth return. *J. Geophys. Res.*, 108(E10):3–1–3–21, 2003.

V. N. Tsytovich. Dust plasma crystals, drops, and clouds. *Physics-Uspekhi*, 40(1):53–94, 1997.

J. C. Ulwick, K. D. Baker, M. C. Kelley, B. B. Balsley, and W. L. Ecklund. Comparison of simultaneous MST radar and electron density probe measurements during STATE. *J. Geophys. Res.*, 93(D6):6989–7000, 1988.

H. C. van de Hulst. *Light scattering by small particles*. John and Sons, Inc., New York, 1957.

J. Vaverka, I. Richterová, J. Pavlů, J. Šafránková, and Z. Němeček. Lunar surface and dust grain potentials during the Earth's magnetosphere crossing. *Astrophys. J.*, 825(133):1–10, 2016.

F. Verheest. *Waves in Dusty Plasmas*. Dordrecht: Kluwer Academic, 2000.

J. Švestka, I. Čermák, and E. Grün. Electric charging and electrostatic fragmentation of dust particles in laboratory. *Adv. Sp. Res.*, 13(10):199–202, 1993.

J. Švestka, S. Auer, M. Baguhl, and E. Grün. Measurement of dust electric charges by the Ulysses and Galileo dust detectors. In B. A. S. Gustafson and M. S. Hanner, editors, *Physics, Chemistry and Dynamics of Interplanetary Dust*, volume 104, pages 481–484. San Francisco: Astron. Soc. of the Pacific Press, 1996.

N. Vilmer. Solar flares and energetic particles. *Phil. Trans. R. Soc. A*, 370(1970):3241–3268, 2012.

U. von Zahn and W. Meyer. Mesopause temperatures in polar summer. *J. Geophys. Res.*, 94(D12):14647–14651, 1989.

M. Vyšinka, Z. Němeček, J. Šafránková, J. Pavlů, J. Vaverka, and J. Lavková. Sputtering of spherical SiO_2 samples. *IEEE Trans. Plasma Sci.*, 44(6):1036–1044, 2016.

M. Vyšinka, L. Nouzák, J. Pavlů, Z. Němeček, J. Šafránková, and I. Richterová. MF microspheres: Helping or puzzling tool? *IEEE Trans. Plasma Sci.*, PP(99):1–9, 2017.

J. H. Waite, M. R. Combi, W.-H. Ip, T. E. Cravens, R. L. McNutt, W. Kasprzak, R. Yelle, J. Luhmann, H. Niemann, D. Gell, B. Magee, G. Fletcher, J. Lunine, and W.-L. Tseng. Cassini ion and neutral mass spectrometer: Enceladus plume composition and structure. *Science*, 311(5766):1419–1422, 2006.

B. Walch, M. Horányi, and S. Robertson. Charging of dust grains in plasma with energetic electrons. *Phys. Rev. Lett.*, 75(5):838–840, 1995.

M. K. Wallis and M. H. A. Hassan. Electrodynamics of submicron dust in the cometary coma. *Astron. Astrophys.*, 121(1):10–14, 1983.

Z. Wang, D. A. Gurnett, T. F. Averkamp, A. M. Persoon, and W. S. Kurth. Characteristics of dust particles detected near Saturn's ring plane with the Cassini Radio and Plasma Wave instrument. *Planet. Space. Sci.*, 54(9–10):957–966, 2006.

X. Wang, M. Horányi, Z. Sternovsky, S. Robertson, and G. E. Morfill. A laboratory model of the lunar surface potential near boundaries between sunlit and shadowed regions. *Geophys. Res. Lett.*, 34(L16104):1–5, 2007.

W. D. Watson. Heating of interstellar H I clouds by ultraviolet photoelectron emission from grains. *Astrophys. J.*, 176:103–110, 1972.

W. D. Watson. Photoelectron emission from small spherical particles. *J. Opt. Soc. Am.*, 63(2):164–165, 1973.

W. D. Watson. Interstellar molecule reactions. *Rev. Mod. Phys.*, 48(4):513–553, 1976.

S. J. Weidenshilling. Dust to planetesimals: Settling and coagulation in the solar nebula. *Icarus*, 44(1):172–189, 1980.

J. C. Weingartner and B. T. Draine. Photoelectric emission from interstellar dust: Grain charging and gas heating. *Astrophys. J. Suppl. S.*, 134(4):263–281, June 2001.

M. S. Westley, R. A. Baragiola, R. E. Johnson, and G. A. Baratta. Photodesorption from low-temperature water ice in interstellar and circumsolar grains. *Nature*, 373:405–407, 1995.

E. C. Whipple. Potentials of surfaces in space. *Reg. Prog. Phys.*, 44(11):1197–1250, 1981.

D. Whitehouse. *Renaissance Genius: Galileo Galilei and His Legacy to Modern Science*. Sterling Publishing Company, Inc. p. 100, 2009.

R. F. Willis, M. Anderegg, B. Feuerbacher, and B. Fitton. Photoemission and secondary electron emission from lunar surface material. In Grard R. J. L., editor, *Photon and Particle Interactions with Surfaces in Space*, pages 389–401. Springer, Dordrecht, 1973.

J. K. Wilson, J. Baumgardner, and M. Mendillo. Three tails of comet Hale-Bopp. *Geophys. Res. Lett.*, 25(3):225–228, 1998.

R. J. Wilson, F. Bagenal, P. A. Delamere, M. Desroche, B. L. Fleshman, and V. Dols. Evidence from radial velocity measurements of a global electric field in Saturn's inner magnetosphere. *Geophys. Res. Lett.*, 118(5):2122–2132, 2013.

B. Wolf. *Handbook of ion sources*. CRC Press, Darmstadt, Germany, 1995.

I. T. Yakubov and A. G. Khrapak. Thermophysical and electrophysical properties of low temperature plasma with condensed disperse phase. *Sov. Tech. Rev. B. Therm. Phys.*, 2:269–337, 1989.

S. Yanagita. Electric charge of grains and interstellar radioactivity. *Astrophys. Space Sci.*, 49(2):L11–L15, 1977.

S.-Y. Ye, D. A. Gurnett, W. S. Kurth, T. Averkamp, S. Kempf, H. W. Hsu, R. Srama, and E. Grün. Properties of dust particles near Saturn inferred from voltage pulses induced by dust impacts on Cassini spacecraft. *J. Geophys. Res.*, 119(8):6294–6312, 2014.

S.-Y. Ye, D. A. Gurnett, and W. S. Kurth. In-situ measurements of Saturn's dusty rings based on dust impact signals detected by Cassini RPWS. *Icarus*, 279:51–61, 2016.

A. Zaslavsky, N. Meyer-Vernet, I. Mann, A. Czechowski, K. Issautier, G. Le Chat, F. Pantellini, K. Goetz, M. Maksimovic, S. D. Bale, and J. C. Kasper. Interplanetary dust detection by radio antennas: Mass calibration and fluxes measured by STEREO/WAVES. *J. Geophys. Res.*, 117(A05102):1–13, 2012.

E. J. Zeller, L. B. Ronca, and P. W. Levy. Proton-induced hydroxyl formation on the lunar surface. *J. Geophys. Res.*, 71(20):4855–4860, 1966.

E. Zimmer. Die elektrostatische Aufladung von hochpolymeren Isolierstoffen. *Kunststoffe*, 60:465–465, 1970.

H. A. Zook and E. McCoy. Large scale lunar horizon glow and a high altitude lunar dust exosphere. *Geophys. Res. Lett.*, 18(11):2117–2120, 1991.

H. A. Zook. Spacecraft measurements of the cosmic dust flux. In Schmitz B. Peucker-Ehrenbrink B., editor, *Accretion of Extraterrestrial Matter Throughout Earth's History*, pages 75–92. Springer, Boston, MA, 2001.

Papers attached to the thesis

proceedings: A1 Nouzák et al. [2013]
Nouzák, L., Pavlů, J., Šafránková, J., and Němeček, Z., Photoelectron Energy Distribution from an Au Target Measured by a Gridless Faraday Cup In: Šafránková, J. and Pavlů, J. (Eds.) *WDS'13 Proceedings of Contributed Papers: Part II - Physics of Plasmas and Ionized Media*, Prague, Matfyzpress, 2013, pp. 48–53. ISBN 978-80-7378-102-6.

proceedings: A2 Nouzák et al. [2014]
Nouzák, L., Richterová, I., Pavlů, J., Němeček, Z., and Šafránková, J., Investigations of the Photoemission from Glass Dust Grains In: Šafránková, J. and Pavlů, J. (Eds.) *WDS'14 Proceedings of Contributed Papers: Part II - Physics of Plasmas and Ionized Media*, Prague, Matfyzpress, 2013, pp. 361–370. ISBN 978-80-7378-102-6.

paper: A3 Nouzák et al. [2016]
Nouzák, L., Richterová, I., Pavlů, J., Němeček, Z., and Šafránková, J., Investigations of Photoemission From Lunar Dust Simulant *IEEE Trans. Plasma Sci.*, 2016, **44**(4), 512–518. DOI: 10.1109/TPS.2015.2493885

paper: A4 Vyšinka et al. [2017]
Vyšinka, M., Nouzák, L., Pavlů, J., Němeček, Z., Šafránková, J., and Richterová, I., MF Microspheres: Helping or Puzzling Tool? *IEEE Trans. Plasma Sci.*, 2017.

paper: A5 Nouzák et al. [2017]
Nouzák, L., Hsu, S., Malaspina, D., Thayer, F. M., Ye, S.-Y., Sternovsky, Z., Pavlů, J., Němeček, Z., and Šafránková, J., Laboratory modeling of dust impact detection by the Cassini spacecraft *Planetary and Space Science*, 2017.

Nouzák et al. [2013]

Photoelectron Energy Distribution from an Au Target Measured by a Gridless Faraday Cup

L. Nouzák, J. Pavlů, J. Šafránková and Z. Němeček
Charles University in Prague, Faculty of Mathematics and Physics, Prague, Czech Republic.

Abstract. In the interstellar and interplanetary space, small objects of micrometer size—dust grains—are present. These grains are charged by impact of particles from the Sun: electrons, ions, and UV photons. In our laboratory, we study charging of a single grain by UV irradiation. Our photon source (differentially pumped discharge lamp) works with noble gases (He in our case), and can operate with different intensity ratios of emission lines (i.e., HeI/HeII ratios). As the first step to control the presence of HeI (21.22 eV) and HeII (40.82 eV) lines and corresponding intensity ratios, we introduce simple measurements of photoelectron energy distribution using a gridless Faraday cup (FC). In this paper, our experimental results confirm a presence of HeI line in the discharge and its dependence on the magnitude of the discharge current and on pressure conditions in the differential pumping stages of the lamp. Measured energy distribution characteristics indicate a presence of photoemitted electrons of Maxwellian energy distribution with the temperature of about 1.6 eV and the electrons with energies in the range of 5–14 eV that probably correspond to the valence band structure of gold. A SIMION model was used to give an evidence that these electrons are not produced by a complicated configuration of the electric field within the gridless FC.

Introduction

Dust grains can be charged in plasma by different mechanisms [*Morfill*, 1996]. In our solar system, the most important charging processes are photoemission due to UV irradiation from the Sun, attachment of charged particles from the solar wind, and secondary electron emission caused by energetic solar wind electrons [e.g., *Boehnhardt and Fechtig*, 1987; *Northrop*, 1992]. As a consequence of the balance of different charging processes on sunlit and dark sides of the Moon, a number of interesting phenomena arise (dust horizon glow, dust fountains, and dust levitation) observed since the Apollo missions [*McCoy and Criswell*, 1974]. In the interstellar space, the photoemission plays mostly a dominant role. Irradiated surfaces of dust are charged positively as a consequence of photoemission and an equilibrium is established when the electric potential of charged grain prevents the escape of further photoelectrons. At the surface of the grain, a surface potential is established typically in the range of +5 V to +10 V, which depends on the properties of the bulk grain material. In the case of sole photoemission charging, the maximum attainable surface potential, ϕ of the dust grain meets equation

$$\phi = \frac{1}{e}(h\nu - W) \ . \tag{1}$$

From this equation, it is seen that the surface potential of the grain depends on its work function, W and on the energy of incident light, $h\nu$. The charging time, τ of the grain up to this maximum surface potential can be estimated as

$$\tau \approx \frac{C\phi}{\eta I_{ph}} \ . \tag{2}$$

The dependence of the charging time on parameters of the grain (i.e., grain capacitance C, maximum attainable surface potential, ϕ, and quantum yield, η) is obvious but the charging time depends on the photon flux, I_{ph} as well.

In the paper, we present first results of an application of the UV lamp to study charging processes of levitated grains. The first step to this task is the examination of the UV source.

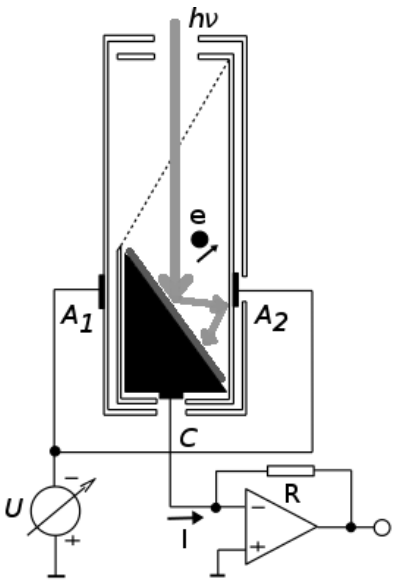


Figure 1. Sketch of the gridless Faraday cup. The electrodes A_1 and A_2 are connected to the same voltage U, which can be sweeped. The collector C is situated through the current-voltage convertor on zero potential.

Experimental setup

Our photon source is a differentially pumped discharge lamp (Specs UVS 10/35). This lamp works with He gas and can operate with different HeI/HeII intensity ratios. Furthermore, the photon flux of the lamp depends on its discharge current. As it was shown in (1) and (2), the photoemission from dust grains depends on the energy of the photons. For this purpose it is necessary to control the presence of HeI (21.22 eV) and HeII (40.82 eV) lines and their ratio and to determine both the photon flux and energy.

The estimation of the flux is based on photoelectron saturation currents. The determination of the HeI/HeII intensity ratio is derived from the distribution of photoelectrons which are generated during the interaction of the UV light with the gold target. For both types of measurements we use a gridless Faraday cup (Fig. 1). The absence of the grids ensures that photoelectrons cannot be generated on their surfaces and influence the current measurement.

The gridless Faraday cup (FC) is used as an integral energy analyzer. It consists of two coaxial electrodes of a special shape and a collector [*Thomas et al.*, 2005] which is covered by a micrometer-thick Au layer. In our case, a voltage U on two coaxial electrodes and the collector on zero potential sets up a potential barrier with effective height that the photoemitted electrons must overcome when they leave the collector area. As a consequence of a contact potential (created by a contact of a stainless steel and the Au layer), this potential barrier can be affected.

Fig. 2 left shows the collector current vs the barrier potential that is representing the integral energy spectrum. The collector current is measured by the current-voltage convertor connected to a 16 bit ADC [*Nouzák*, 2010]. The energy distribution measurements use a sweeping voltage on electrodes A_1 and A_2 (Fig. 1) that is provided by a 16 bit DAC. Both circuits are controlled via an I^2C interface allowing flexibility when connected to a PC .

The current at a given voltage U_0 is proportional to the total number of electrons with

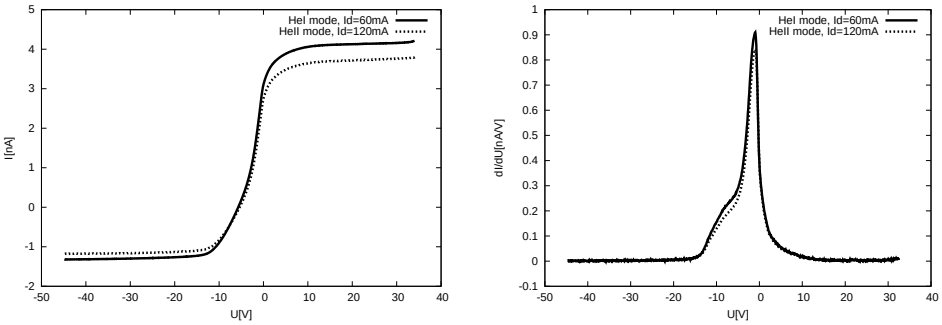


Figure 2. Integral (left) and differential (right) photoelectron characteristics (the solid line—mode for max. HeI intensity with the discharge current $I_d = 60\,\mathrm{mA}$, the dotted line—mode for max. HeII intensity with the discharge current $I_d = 120\,\mathrm{mA}$).

energies between $eU_0 = E_i$ and $eU_{max} = E_{max}$

$$I(E_i) = \int_{E_i}^{E_{max}} N(E)\,\mathrm{d}E\ , \tag{3}$$

where U_{max} is the voltage necessary to set up a potential barrier for electrons in the energy distribution with the maximum energy E_{max}. The energy distribution of the electrons, $N(E)$ is obtained by differentiation of (3) with respect to E_i. In our case, the differentiation is performed numerical. Typical integral characteristics measured for the discharge in the He gas are depicted in Fig. 2 left, while the corresponding differential characteristics are in the right part. Actually, they doesn't contain information about the electron energy distribution from the collector (C in Fig. 1) only, but approximately 1.4 % (for HeI line) and 100 % (for HeII line, due to a total reflection at the collector) of the incident UV light [*Palik*, 1985] is reflected to the other electrode A_2 of the FC (see the saturated currents in the integral characteristics). A second reflection from the electrode A_2 is approximately 0.2 % (for HeI line) and 10 % (for HeII line) of the light reflected on the FC collector and has minimal consequences for saturation current measurements. A top angle of the FC collector is 29 °. In this geometry, the incident light can fall on the electrode A_1 only after seven reflections between the electrode A_2 and the FC collector. Thus, the current contribution from the electrode A_1 would be negligible. The kinetic energy of the photoelectrons cannot exceed the energy of HeII photons. For positive voltage $U \approx 35V$ on A_1 and A_2 we can suppose that the photoelectrons from C and A_2 are attracted to electrodes A_1 and A_2. In the current measurement, only the photoelectrons from collector C can participate because the photoelectrons from A_2 cannot leave an area of the electrode. The measured saturated current for a positive voltage corresponds to the collector saturated current created by HeI photoelectrons. The situation is analogous for the negative voltage $U \approx -45V$ on A_1 and A_2. The photoelectrons from the collector C are returned and only photoelectrons from A_2 in the current measurement participate (HeII photoelectrons). The photoelectrons from both the collector and electrode A_1 overlap in Fig. 2 between these voltages. However, if we deal with the largest branch only (corresponding to photoemission from collector), then we get the photoelectron energy distribution as depicted in Fig. 3 by reversing the x axis.

Numerical simulation

A numerical model of the FC was created in SIMION [*SIMION*, 2013]. In our geometry, we generated photoelectrons with a Maxwellian energy distribution with the kinetic temperature of $kT = 1.6\,\mathrm{eV}$ and a cosine angular distribution [*Greenwood*, 2002] at one point of the center of the FC collector. Although, in the real experiment, the number of high-energy photoelectrons

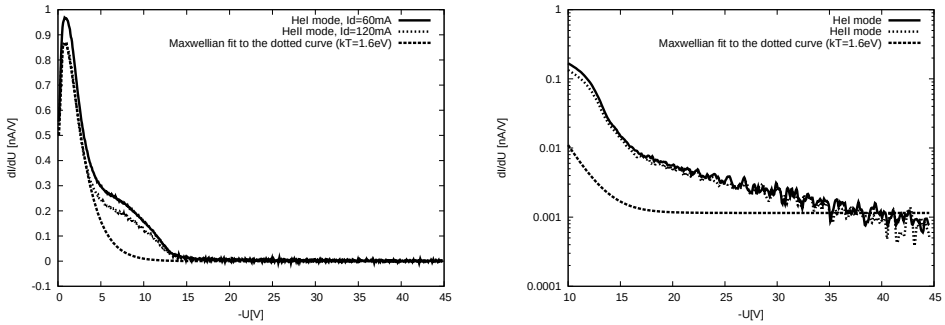


Figure 3. Photoelectron energy distribution function (left) and its detailed view in semi-log scale (right). The solid line—mode for max. HeI intensity, the dotted line—mode for max. HeII intensity, the dashed line—Maxwellian fit to the dotted line.

(i.e., those at photon energy reduced by work function) is small, their influence is non-negligible. However, they are not included in the simulation and thus it cannot describe associated effects. In the real experiment, an irradiated area of the FC collector by the UV beam is not significant and the excitation volume of the material for photoelectron emission is larger than one point as we suppose in our simulation. This approximation is justified because a change of the barrier potential along the distance of the UV beam diameter is negligible.

The dependence of the current of escaping electrons on the adjusted potential represents the simulated integral characteristics (Fig. 4 left). Because a part of the incident light is reflected from the collector area to the electrode A_2, photoelectrons of the same Maxwellian distribution were generated at both photon–electrode points of incidences. A generation of the distribution from A_1 wasn't included in the simulation because this electrode almost doesn't participate in the photoelectron production. The sum of the integral characteristics was obtained by a superposition of the characteristics from the collector and the electrode A_2 of the FC after scaling to the measured characteristics.

Results and discussion

In the left part of Fig. 2, one can see the integral photoelectron distribution characteristics for two different working modes of the differentially pumped discharge lamp. In these modes, measurements were performed for two discharge currents ($I_d = 60\,\mathrm{mA}$, $I_d = 120\,\mathrm{mA}$). From the characteristics we can easily establish the saturated currents for the negative branch of the characteristics that represents the saturated current from the electrode A_2 ($I = 1.3\,\mathrm{nA}$) and the positive branch which corresponds to the saturated current from the collector C ($I = 4.2\,\mathrm{nA}$). From the ratio of these currents we can quantify the amount of radiation reflected towards the electrode A_2 (≈ 30 %). Since mainly the HeII photons are reflected, this ratio gives us an approximate ratio of HeI/HeII photons in the UV beam. Corresponding differential characteristics are plotted in Fig. 2 right. Only a part of the characteristics with the negative voltage at the electrodes is used. In this part (Fig. 3 left), we can find some interesting regions. In the first region (0–5 V), there are electrons with a Maxwellian distribution with a temperature of 1.6 eV. Next, there are electrons with energies between 5 and 14 eV which probably correspond to the valence band structure of gold. In the last region, we can observe a slow decrease into the saturation region (see details in the right panel of Fig. 3). This can signalize a presence of the HeI excitation line. We didn't observe any variations of the energy spectrum at about 36 V which would indicate a presence of the HeII extinction line in the discharge—as aforementioned HeII line should be seen in the other branch only. Note that the characteristics are actually

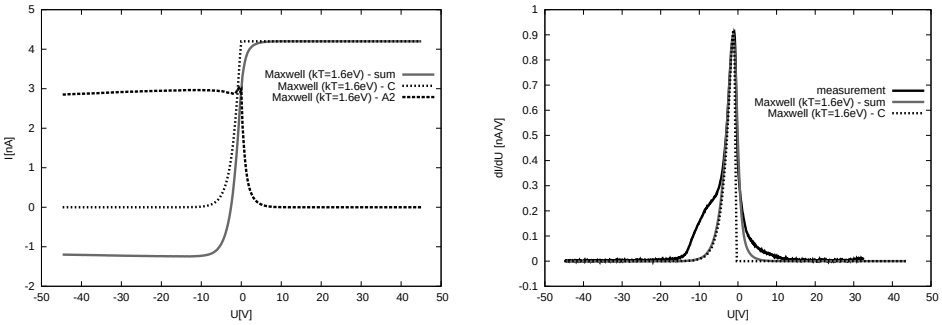


Figure 4. SIMION simulation: integral (left) and differential (right) characteristics for electrons with a cosine angular distribution and a Maxwell energy distribution generated from: C—doted line, electrode A_2 of the FC—dashed line, solid grey line is a superposition of both, measurement—solid black line.

displaced with respect to the band energies as

$$E_k = h\nu - W \tag{4}$$

with work function, W of gold (the material used for the FC collector).

In Fig. 4 left, there are shown integral characteristics obtained from our simulation for electrons with the Maxwellian energy distribution ($kT = 1.6\,\mathrm{eV}$) and cosine angular distribution after re-scaling number of electrons to the equivalent current. The doted line depicts a distribution generated from the collector C. The dash part represents the distribution from the electrode A_2. The last part is a superposition of both. In Fig. 4 right, corresponding differential characteristics are shown. By comparing the characteristics from the simulation, it is obvious that the distribution from the electrode A_2 shapes the total distribution (the solid grey line) for positive voltages (0–8 V). Despite it, the shape of the sum characteristic is not sufficient (compare the measurement—solid black line with the model—solid grey line in Fig. 4 right). The reason is in the absence of valence band electrons in the model calculation. For better match, it would be necessary to create a more sophisticated model.

We compared the measured energy spectrum of the photoelectrons ejected from the collector (Fig. 5) with the UPS [ultraviolet photoelectron spectroscopy, e.g., *Cardona and Ley*, 1974] spectrum in Fig. 6 [adapted from *Surface Science Western*, 2013]. Taking into account that (a) the collector surface is contaminated by a layer of unknown composition that was created during an exposition to open air and (b) the poor resolution of our detector, one can note a qualitative similarity of both spectra. We believe that our measurements are able to provide a reliable spectrum of photoelectrons after cleaning of the collector surface.

Conclusion

We can conclude that:

- We identified a peak of electrons with almost Maxwellian energy distribution with a temperature about 1.65 eV.
- The difference between the data obtained by the FC and a hemispherical analyzer (compare Fig. 5 with Fig. 6) are most probably caused by a low energy resolution of our energetic analyzer (gridless FC with electronics).
- We identified a bend of the energy distribution characteristics (see detail in the semi-log scale in the right panel of Fig. 3 at about 16 V) that can indicate a presence of the HeI excitation line in the discharge.

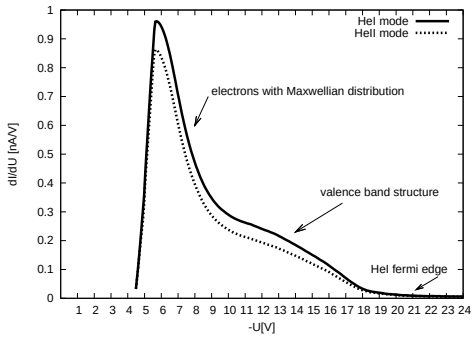


Figure 5. Measured electron energy distribution from air contaminated gold (solid line—mode for max. HeI intensity, dotted line—mode for max. HeII intensity).

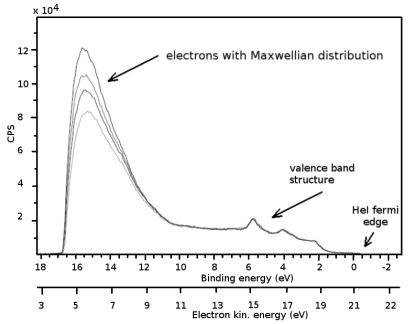


Figure 6. UPS spectrum of standard sputter-cleaned gold [adapted from *Surface Science Western*, 2013]. The diagram shows a peak of electrons with the Maxwellian distribution, valence band electrons and HeI Fermi edge.

- We didn't observe any bending of the energy distribution characteristics in the region of about 36 V (see Fig. 3) indicating a presence of the HeII extinction line. It is clearly caused by a total reflection of HeII photons from the collector to the other electrode. On the other hand, the ratio of saturated currents of positive and negative branches of integral characteristics could be used as a measure of the HeI/HeII emission line intensity ratio.
- We developed a simple model in the SIMION software package. The model includes a generation of electrons from electrodes C and A_2 with a Maxwellian distribution, but it doesn't include valence band electrons generated from these electrodes.

Acknowledgment. This work was supported by the Grant Agency of the Charles University under project number 1410213 and by the Czech Grant Agency project No. 209/11/1412.

Reference

J. E. McCoy, D. R. Criswell. Evidence for a high altitude distribution of lunar dust. Proc. Lunar Sci. Conf. 5th, 2991–3005, 1974.

G. Morfill. Solar system — the enigma of Jupiter's ring. Nature, 381(6580), 279–280, May 1996.

T. G. Northrop. Dusty plasmas. Physica Scripta, 45(5), 475–490, May 1992.

H. Boehnhardt and H. Fechtig. Electrostatic charging and fragmentation of dust near P/Giacobini-Zinner and P/Halley. Astronomy and Astrophysics, 187(1–2), 824–828, November 1987.

J. D. Thomas, G. S. Hodges , D. G. Seely , N. A. Moroz , T. J. Kvale. Performance enhancement study of an electrostatic Faraday cup detector. Nucl. Instrum. Methods Phys. Res. Sect. A, 536, 11–21, 2005.

E. D. Palik. Handbook of Optical Constants of Solids, Academic Press, Boston, 1985.

SIMION [software package], http://simion.com/ [2013-10-17].

J. Greenwood. The correct and incorrect generation of a cosine distribution of scattered particles for Monte-Carlo modelling of vacuum systems. Vacuum, 67, 217–222, 2002.

L. Nouzák. Stabilization system for particle sources, Bachelor thesis (in Czech), MFF UK, Praha, 2010.

M. Cardona, L. Ley. Photoemission in Solids I, Springer Berlin, Heidelberg, New York, 1978.

Surface Science Western at the University of Western Ontario, UPS spectrum of sputter-cleaned gold [online], http://sprocket.ssw.uwo.ca/xpsfiles/ups.pdf [2013-10-17].

Nouzák et al. [2014]

WDS'14 Proceedings of Contributed Papers — Physics, 361–370, 2014. *ISBN 978-80-7378-276-4* © *MATFYZPRESS*

Investigations of the Photoemission from Glass Dust Grains

L. Nouzák, I. Richterová, J. Pavlů, Z. Němeček, and J. Šafránková
Charles University in Prague, Faculty of Mathematics and Physics, Prague, Czech Republic.

Abstract. Dust grains are present on the surface of the Moon and can be charged by particles from the Sun (photons, electrons, and ions). We present laboratory measurements of photoemission from a single glass grain of micron size (a lunar analogue material). The grain is caught in the electrodynamic trap and irradiated by UV source with distinct He I (21.2 eV) and He II (40.8 eV) lines. The grain specific charge is evaluated from the grain oscillation frequency in the electrodynamic trap. In our measurements, we determine grain surface potential,its size, and work function from the time evolution of the charging by He I and He II photons. First results indicate that the work function of the glass grain is about 4.7 eV.

Introduction

Dust grains are present in diverse astrophysical environments. Where they can be charged by a variety of processes. In our solar system, the most important charging processes are photoemission due to UV or X-ray radiations from the Sun [*Kreplin et al.*, 1962], attachment of the solar wind particles, and secondary electron emission [e.g., *Anderegg et al.*, 1972; *Boehnhardt and Fechtig*, 1987; *Northrop*, 1992].

The lunar surface is composed of rocks and regolith, which has been created by meteoroid impacts. The size of the regolith grains range from centimeters to submicron sizes [*Heiken et al.*, 1974]. The smaller grains are often called a lunar dust or simply dust. As a consequence of the balance of various charging processes on both dayside and nightside of the Moon, a number of interesting phenomena arises (dust horizon glow, dust fountains, and dust levitation). These phenomena were observed throughout the Apollo missions [*McCoy and Criswell*, 1974; *Criswell*, 1973]. Irradiated surface of the Moon on the dayside is charged positively as a consequence of photoemission current [*Manka*, 1973]. An equilibrium charge on dayside is established when the electric potential [$\approx +4\tilde{\mathrm{V}}$, *Manka*, 1973] of the charged surface prevents the escape of further photoelectrons because all other charging currents are small and they are balanced by a portion of photoelectrons with energies above this surface potential. On the other hand, the nightside part is charged negatively [potential of ≈ -40 V, *Manka*, 1973] by the ambient electrons. An investigation of the occurring charging processes in situ is complicated, because we can observe only the equilibrium state that results from the charging, nevertheless, we can study these charging processes separately on a single dust grain in laboratory conditions.

In this paper, we investigate the photoemission from a single glass dust grain (as a lunar analogue material) levitating in the electrodynamic trap. We present our first experimental results including the work function estimation for a dielectric body.

Experimental setup

The heart of the experimental setup is a linear electrodynamic trap (situated in the center of Fig. 1). A single charged grain is held in an effective potential, which is formed by three independent oscillating fields with dominant quadrupole terms [*Beránek et al.*, 2012]. These fields are generated by AC voltages applied to rods of the trap, which are supplied by high voltage amplifiers (HVA). A signal generator (SG) provides a harmonic signal with a time window for shooting of the charged particles. The grains are shaken out from the dust dropper (DD) at the beginning of each particular measurement. Three independent particle sources

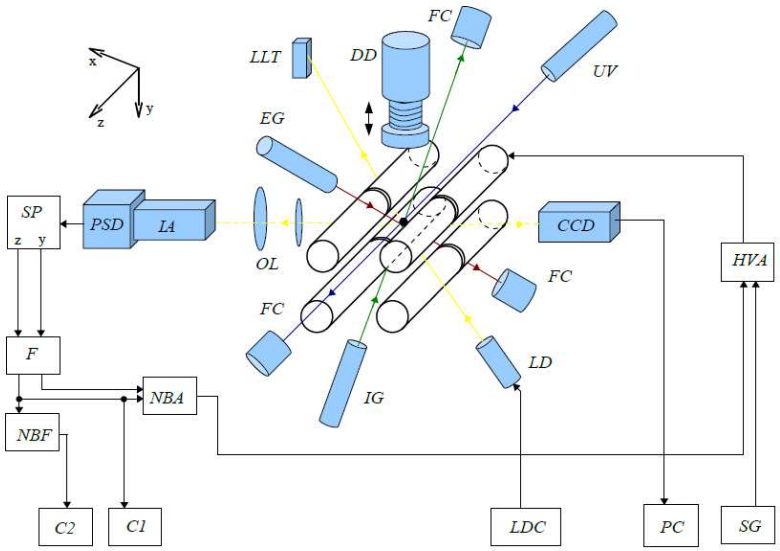


Figure 1. Experimental set-up — electrodynamic trap (FC—Faraday cup, EG—electron gun, IG—ion gun, UV—UV source, DD—dust dropper, IA—image amplifier, PSD—position sensitive detector, PC—personal computer, HVA—high voltage amplifier,OL—optical lenses, LLT—laser light trap, SP—signal processor, F—filter, NBF—narrow band filter, NBA—narrow band amplifier, C1,C2—counters, LDC—laser diode control, SG—signal generator, CCD—CCD camera).

can be used for charging of the grain: electron gun (EG), ion gun (IG), and UV source (UV). Particular particle currents are measured by gridless Faraday cups (FC) [*Thomas et al.*, 2005] with detection electronics [*Nouzák*, 2010]. A Faraday cup situated in front of the UV source measures a photon flux. The photon flux is determined from the photoelectron current generated after an interaction of the UV beam with the Faraday cup collector [*Nouzák*, 2013].

The laser beam generated by the laser diode (LD) is modulated by the diode controller (LDC) and scattered by a trapped grain. A part of the scattered light is projected via an optical lens system (OL) onto the image amplifier (IA) and to the position sensitive detector (PSD). This detector converts the amplified light spot to electrical signals for a signal processor (SP). An algorithm is applied to calculate a current position of the grain from the signal. The grain oscillates in three independent directions and position signals from signal processor are used for active damping or stabilization of the oscillations to left only one direction of the secular oscillations for measurements. The frequency of the position signal from PSD is measured by the connected counter (C2). A charge-to-mass ratio (Q/m) of the grain is determined from its secular frequency f_x as

$$\frac{Q}{m} = \frac{4\pi^2\sqrt{2}f_x f_{AC}{r_0}^2}{\lambda_z V_z} , \tag{1}$$

where f_{AC}, V_z are the frequency and amplitude of the trap supply and r_0, λ_z are geometric parameters of the trap [see *Beránek et al.*, 2012, for details]. The Q/m evolution is recorded in course of experiments.

For a correct Q/m estimation, it is necessary to keep the grain in an electrical center of the trap. This is achieved by an electrical force that compensates the gravity force (DC voltage applied on top and bottom electrodes). The DC voltage U_G (in a linear approximation of the electrostatic potential around the center of the trap in the vertical direction) is indirectly

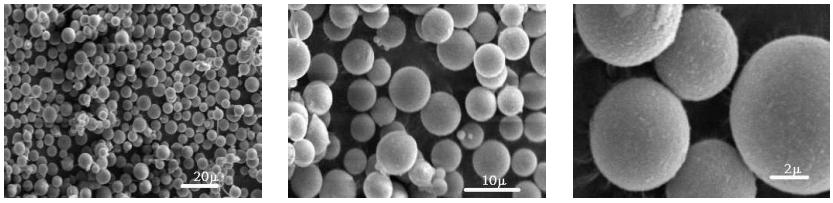


Figure 2. Glass dust grains of 3–8 μm in diameter. The panels differ by magnification.

proportional to the Q/m ratio of the grain

$$U_G \approx \frac{g}{0.15 \cdot 10^{-3}[\mathrm{m}^{-1}]} \left(\frac{Q}{m}\right)^{-1} \quad , \tag{2}$$

where g is the gravity acceleration.

Photoemission study

The charge-to-mass ratio of the grain (Q/m) is directly proportional to its surface potential (ϕ) [*Pavlů et al.*, 2008] according to the equation

$$\frac{Q}{m} = C_\mathrm{m}\phi \ , \tag{3}$$

through the grain specific capacitance C_m (ratio of the grain capacitance and mass).

The photoemission is studied on glass grains (see Fig. 2). These grains have spherical shape and we can easily calculate their specific capacitance C_m

$$C_\mathrm{m} = \frac{C}{m} = \frac{3\varepsilon_0}{\rho R^2} , \tag{4}$$

where ρ is the mass density of the grain ($\rho_\mathrm{glass} = 2400\,\mathrm{kg/m^3}$) and R its radius.

In the case of sole photoemission charging by monochromatic light with an energy $h\nu$, the maximum attainable surface potential, ϕ_max of the dust grain would meet the equation

$$\phi_\mathrm{max} = \frac{1}{\mathrm{e}}(\mathrm{h}\nu - \mathrm{W}) \ , \tag{5}$$

where W is a work function of the grain and determination of the work function would be straightforward. In laboratory conditions, the situation is more complex for two reasons:

(1) We use a differentially pumped capillary discharge ultraviolet source [*Specs*, 2009] which can operate with a variety of gases (He, Ne, Ar, etc.). For the current experiment, we use the He discharge with the strongest He I (21.2 eV) and He II (40.8 eV) emission lines. However, presence of other lines in the discharge (see Tab. 1) complicates investigations of the photoemission charging.

(2) Parts of the UV beam either from the photon source or reflected from different surfaces inside the vacuum vessel produce a photoelectron background in the chamber. Some of the electrons reach the grain and decrease the surface potential of the grain. In this case, the maximum surface potential of the grain given by the equation (5) is not reached. On the other hand, if the emission lines with higher energies are present in the discharge, the potential can exceed the value given by eq. (5). In order to account for these difficulties, we have developed a method of work function determination that uses two or more UV emission lines. This technique employs so-called current–voltage (I–V) plot method.

Table 1. Excitation energies, wavelengths and relative intensities in He. Adapted from user manual of the UV source [*Specs*, 2009].

Emission line	Excitation energy (eV)	Wavelength (nm)	Relative intensity
He I_{α}	21.22	58.4	100
He $I_{\beta\gamma}$	23.09 / 23.75 / 24.05	53.7 / 52.2 / 51.5	< 2 each
He $I_{satellites}$	24.21 / 24.31 / 24.38 / 24.42	51.2 / 51.0 / 50.8 / 50.7	
He II_{α}	40.82	30.4	20[a]
He II_{β}	48.38	25.63	2[a] each
He $II_{\gamma\delta}$	51.02 / 52.32 / 53.0	24.28 / 23.69 / 23.39	< 1[a] each

Measuring procedure

The study of the photoemission is based on observations of the time evolution of the grain charge under varying conditions (Fig. 3). The time sequence of measurements was as it follows (the abbreviation is the same as in Fig. 3).

(a) We charged the grain by 0.6 keV electrons. The value of the Q/m ratio at maximum of the secondary electron emission yield according to *Žilavý et al.* [1998] was used for an approximate estimation of the surface potential ($\approx 8.6\,\mathrm{V}$) of the grain for further charging (the thin line, for reference only).

(b) Simultaneously, we turn on the photon source and we set up pressure conditions to maximum presence of He I photons in the discharge (He I mode). The equilibrium grain potential increased due to a new emission current.

(c) We switched off the electron beam and we follow the evolution of the Q/m under He I photons.

(d) When the equilibrium was reached, we set the photon source to mode with the maximum of He II photons (He II mode). The grain charge increased and it reached a new equilibrium value.

(e) Since we need to charge the grain to higher potentials for the discharging current–voltage plot, we charged the grain by 1 keV He ions from the ion source.

(f) After the ion source turned off, the grain slowly discharged by photoelectrons from the background.

(g) As the grain achieved equilibrium, we switched the photon source back to the mode with maximum amount of He I photons and the grain continued discharging by photoelectrons from the background.

Current–voltage plot method

The principle of the current–voltage (I–V) plot method is based on calculation of a time derivative of discharging/charging characteristics Q/m(t) (see, e.g., Fig. 3). The charging current can be determined as a derivative of this characteristics:

$$\frac{\mathrm{d}}{\mathrm{dt}}\left(\frac{Q}{m}\right) = \frac{I}{m}\ . \tag{6}$$

We plot this derivative (I/m(t)) as a function of the Q/m ratio (note that Q/m is proportional to potential). For explanation of the method, let us consider only one charging current due to photoemission. The form of this charging current is proportional to photoelectron energy distribution. This distribution is unknown, and it will be a subject of future investigations. In

[a]Relative intensities of the lines depend on conditions of the discharge.

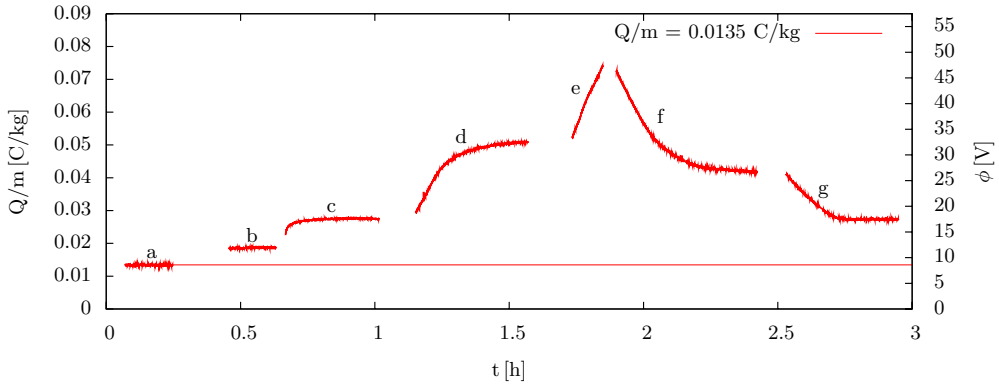


Figure 3. The time evolution of the photoemission charging (from left to right: charging by 0.6 keV electrons (a), charging by 0.6 keV electrons and He I photons (b), charging by He I photons (c), charging by He II photons (d), charging by 1 keV He ions (e), discharging by He I photoelectrons from background (f), discharging by He II photoelectrons from background (g); the thin line is a reference only for Q/m from charging by 0.6 keV electrons).

the present paper, we assume that this distribution has a Maxwellian profile [*Sternovsky et al.*, 2008] and the photocurrent can be written:

$$I_{\mathrm{ph}}(\phi) \approx I^0_{\mathrm{ph}} \mathrm{e}^{-\frac{e\phi}{\mathrm{k_b T_{ph}}}} \ , \tag{7}$$

where T_{ph} is a photoelectron temperature (generally $\mathrm{k_b T_{ph}} \approx 2\mathrm{eV}$), I^0_{ph} is the photoelectron flux, e elementary charge, and ϕ grain potential. Background current caused by reflected UV light is proportional to surface potential of the grain and can be expressed as [*Žilavý et al.*, 1998]:

$$I_{\mathrm{back}}(\phi) = I^0_{\mathrm{back}} \left(1 + \frac{e\phi}{E_{\mathrm{back}}}\right) \alpha \ , \tag{8}$$

where α is a sticking coefficient, I^0_{back} is background current for $\phi = 0$ of the grain and E_{back} is energy of produced background photoelectrons.

Now, we can examine I–V plots obtained from discharging curves (parts f and g in Fig. 3). In the case of part f, after charging to $Q/m \approx 0.07$ C/kg by ions, the grain is discharged by He II and He I photoelectrons [approximate ratio 4:1, *Specs*, 2009] from background to the surface potential, where the energetic part of He II photoelectrons distribution generated from grain appears. This discharging continues until the equilibrium of these currents is established (zero point on y-axis of the I–V characteristic). The first part of discharging (Fig. 4f, with dotted line) can be expressed in terms of eqs. (3, 6, 8) as

$$\frac{I}{m} = \frac{Q}{m} A_{\mathrm{back,He\,II_{mode}}} + \frac{I^0_{\mathrm{back,\,He\,II_{mode}}} \alpha}{m} \ , \tag{9}$$

where

$$A_{\mathrm{back,\,He\,II_{mode}}} = \frac{I^0_{\mathrm{back,\,He\,II_{mode}}}}{m C_{\mathrm{m}}} \frac{e\alpha}{E_{\mathrm{back}}} \ . \tag{10}$$

Investigation of the second part of characteristic is more complicated, because there are two currents. Using approximation $\frac{e\phi}{\mathrm{k_b T_{ph}}} \ll 1$ (we are far from potential corresponding temperature of generated photoelectrons ($\mathrm{k_b T_{ph}} \approx 2\,\mathrm{eV}$)) resulting current can be expressed similarly to (9)

$$\frac{I}{m} = \frac{Q}{m} \left(A_{\mathrm{back,\,He\,II_{mode}}} - B_{\mathrm{ph,\,He\,II}}\right) + \frac{1}{m} \left(I^0_{\mathrm{back,\,He\,II_{mode}}} \alpha + I^0_{\mathrm{ph,\,He\,II}}\right) \ , \tag{11}$$

where

$$B_{\mathrm{ph,\,He\,II}} = \frac{eI^0_{\mathrm{ph,\,He\,II}}}{mC_{\mathrm{m}}\mathrm{k_b}\mathrm{T_{ph}}} \ . \tag{12}$$

As we can see from eq. (9, 11), these approximations describe straight lines in a plot of I/m vs Q/m (i.e., I–V plot).

From the I–V plot (e.g., in Fig. 4f), we can easily establish, the point where the charging current given by photoemission changes to the discharging current caused by photoelectrons from background. Such point could be identified by change of the slope of the Q/m(I/m) curve. The Q/m determined this way (we use linear regression of currents (9, 11) for better estimation) is proportional to the surface potential, ϕ, given by equation (5) for a corresponding emission line.

The mathematical description for I–V plot in Fig. 4g is more complicated, because background current will change [ratio of He II photoelectrons to He I photoelectrons 1:4, *Specs*, 2009] and charging photocurrent form He II photons is necessary to add to both lines (9 for He I mode, 11 for He I mode). The line for "background" (background photoelectrons and He II photocurrent, see Fig. 4g) can be described with equation 11 (for He I mode). But the second part of I–V plot after addition of He II photocurrent can be expressed like

$$\frac{I}{m} = \frac{Q}{m}\left(A_{\mathrm{back,\,He\,I_{mode}}} - B_{\mathrm{ph,\,He\,II}} - B_{\mathrm{ph,\,He\,I}_{\beta\gamma}}\right) + \frac{1}{m}\left(I^0_{\mathrm{back,\,He\,I_{mode}}}\alpha + I^0_{\mathrm{ph,\,He\,II}} + I^0_{\mathrm{ph,\,He\,I}_{\beta\gamma}}\right) \ , \tag{13}$$

In the case of charging characteristics we can make similar consideration about background and charging currents. The first part of I–V characteristic (Fig. 4c) can be thus described by eq. 11 (for He I mode) but another charging current appears in the second part, because surface potential of the grain is below the energy of different less intense emission line denoted as $\mathrm{He\,I}_{\beta\gamma}$. This part of characteristic we can express like

$$\begin{aligned}\frac{I}{m} = \frac{Q}{m}&\left(A_{\mathrm{back,\,He\,I_{mode}}} - B_{\mathrm{ph,\,He\,II}} - B_{\mathrm{ph,\,He\,I}_{\beta\gamma}} - B_{\mathrm{ph,\,He\,I}}\right) \\ &+\frac{1}{m}\left(I^0_{\mathrm{back,\,He\,I_{mode}}}\alpha + I^0_{\mathrm{ph,\,He\,II}} + I^0_{\mathrm{ph,\,He\,I}_{\beta\gamma}} + I^0_{\mathrm{ph,\,He\,I}}\right) \ .\end{aligned} \tag{14}$$

The established Q/m value in this case will correspond to this unknown emission line.

Results and discussion

In Fig. 4, there are I–V plots established from charging/discharging parts through the whole experiment. Since the current is obtained as a derivative of the measured charge the plots are rather noisy. Nevertheless, we were able to fit the I–V plots by two straight lines in three cases. The equilibrium surface potential corresponding to charging by He II photons was overcome by charging with ions (see Fig. 3e). In I–V plot from charging by He II photons, we can see no features, which could signalize a presence of any distinct emission line. Based on I–V characteristics (Fig. 4), we were able to identify three relevant charge to mass ratios

$$\left(\frac{Q}{m}\right)_{\mathrm{a}} = (26 \pm 1)\,\mathrm{mC/kg} \ , \left(\frac{Q}{m}\right)_{\mathrm{b}} = (28.8 \pm 1.7)\,\mathrm{mC/kg} \ , \left(\frac{Q}{m}\right)_{\mathrm{c}} = (56.8 \pm 1.7)\,\mathrm{mC/kg}\,, \tag{15}$$

sequenced

$$\left(\frac{Q}{m}\right)_{\mathrm{a}} < \left(\frac{Q}{m}\right)_{\mathrm{b}} < \left(\frac{Q}{m}\right)_{\mathrm{c}} \ . \tag{16}$$

We assume that two of them are related to He I and He II emission lines. An energetic distance of the investigated emission lines is known (see Tab. 1)

$$\phi_{\mathrm{He\,II}} - \phi_{\mathrm{He\,I}} = 19.6\,\mathrm{V} \ . \tag{17}$$

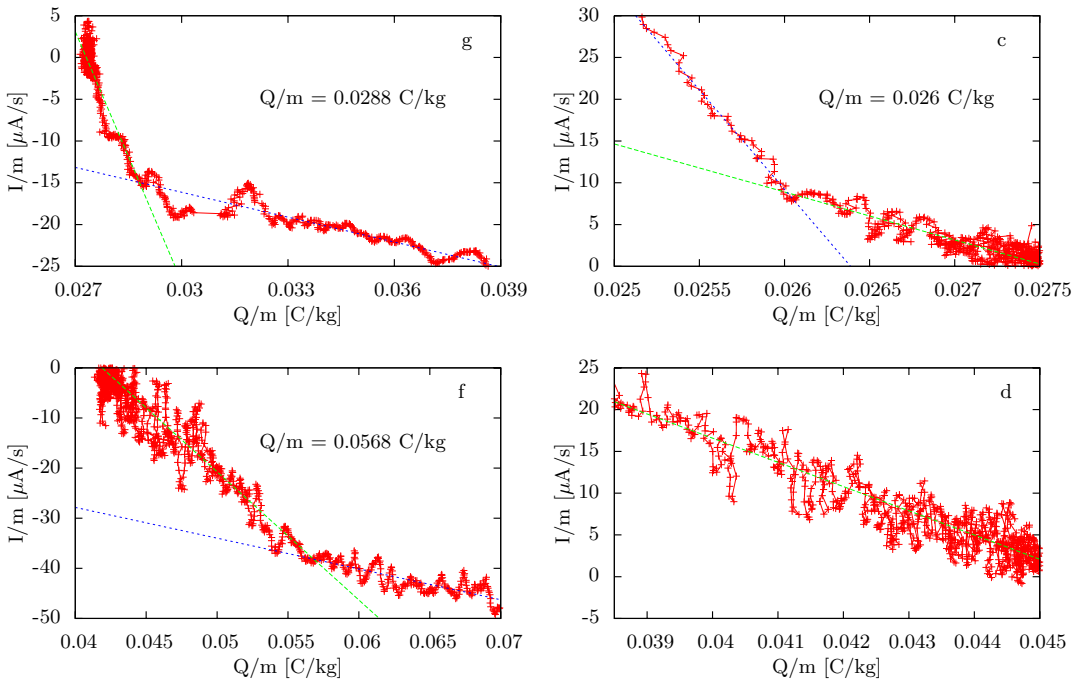


Figure 4. I–V characteristics obtained from discharging curves (parts f and g in Fig. 3) and from charging curves (parts c and d in Fig. 3), straight lines are the best linear fits of the currents.

If we suppose, that the specific capacitance of the grain didn't change during measurement (e.g., helium ions used for charging didn't change structure or even size of the grain) we can expect following relation

$$\frac{\phi_{\mathrm{He\,I}}}{\phi_{\mathrm{He\,II}}} = \frac{\left(\frac{Q}{m}\right)_{\mathrm{He\,I}}}{\left(\frac{Q}{m}\right)_{\mathrm{He\,II}}} . \tag{18}$$

According to relations (16) only three options of eq. (18) are possible — a:b, b:c, a:c. With use of eq. (17) we can calculate $\phi_{\mathrm{He\,I}}$ and $\phi_{\mathrm{He\,II}}$ for each option:

$$\phi_{\mathrm{He\,I}} = 182.0\,\mathrm{V}\ , \phi_{\mathrm{He\,II}} = 201.6\,\mathrm{V}\ , \tag{19}$$

$$\phi_{\mathrm{He\,I}} = 20.2\,\mathrm{V}\ , \phi_{\mathrm{He\,II}} = 39.6\,\mathrm{V}\ , \tag{20}$$

$$\phi_{\mathrm{He\,I}} = 16.5\,\mathrm{V}\ , \phi_{\mathrm{He\,II}} = 36.1\,\mathrm{V}\ . \tag{21}$$

Obviously, the first option doesn't have any physical sense. The second value leads to work function of about 1 eV (which is incredibly low even for cesium [a]). Only last option for surface potentials

$$\phi_{\mathrm{He\,I}} = (16.5 \pm 1.5)\,\mathrm{V},\ \phi_{\mathrm{He\,II}} = (36.1 \pm 1.5)\,\mathrm{V} \tag{22}$$

seems to be right. The surface potential of the grain for $(\mathrm{Q/m})_{\mathrm{b}} = 0.0288\,\mathrm{C/kg}$ was determined as $\phi_{\mathrm{He\,b}} = (18.3 \pm 1.5)\,\mathrm{V}$, thus corresponding emission line was

$$h\nu_{\mathrm{He\,I}_{\beta\gamma}} = (23 \pm 1.5)\,\mathrm{eV}\ . \tag{23}$$

[a] http : //en.wikipedia.org/wiki/Work_function#References

As we can see (compare calculated value with Table 1), this value probably corresponds to the energy of the He I$_{\beta\gamma}$ emission line.

From (4), we can obtain the specific grain capacitance, $C_m = 1.57\,\mathrm{mF/kg}$ and approximate size of the grain, $R \approx 2.7\mu\mathrm{m}$. According to (5) we can also establish the work function of the grain as

$$W = (4.7 \pm 1.5)\,\mathrm{eV}\ . \tag{24}$$

The calculated value of the grain work function is in accordance with the values obtained by *Hiroyoshi and Haruhisa* [2005] or *Okamura et al.* [2009]. These values were obtained for the bulk material, but our measurement was done on small spherical particles. According to theories of *Brus* [1983] and *Makov et al.* [1988], the work function depends on the curvature of the surface, however, the change of the work function for grains with radius in the range of micrometers would be negligible. The work function of the grain would be equal to the work function of the bulk material. The size effect would be noticeable for grains in the nanometer range, only.

With extrapolation of line (9) in Fig. 4f to zero potential of the grain, we obtained background photocurrent for He II mode and zero potential of the grain as

$$I^0_{\mathrm{back,\,He\,II_{mode}}} = -6.6 \cdot 10^{-19}\mathrm{A} \approx 4\,\mathrm{electrons/s}\ . \tag{25}$$

Assuming sticking coefficient $\alpha = 1$ we can calculate (9) photocurrent from grain (for zero potential)

$$I^0_{\mathrm{ph,\,He\,II}} = 2.2 \cdot 10^{-17}\,\mathrm{A}\ . \tag{26}$$

Similar considerations we can make for Fig. 4g. The sum of background current and He II charging current was determined as

$$I^0_{\mathrm{ph,\,He\,II}} + I^0_{\mathrm{back,He\,I_{mode}}}\alpha = 2.7 \cdot 10^{-18}\,\mathrm{A}\ . \tag{27}$$

Extrapolated tangent of line gives equation

$$A_{\mathrm{back,\,He\,I_{mode}}} - B_{\mathrm{ph,\,He\,II}} = -0.001\ \mathrm{s}^{-1}\ . \tag{28}$$

From last two equations (27, 28) we can evaluate of background current $I^0_{\mathrm{back,\,He\,I_{mode}}}$ and photocurrent $I^0_{\mathrm{ph,\,He\,II}}$ for He I mode

$$I^0_{\mathrm{back,\,He\,I_{mode}}} = 1.3 \cdot 10^{-18}\,\mathrm{A}, \mathrm{I}^0_{\mathrm{ph,\,He\,II}} = 1.4 \cdot 10^{-18}\,\mathrm{A}\ . \tag{29}$$

Similarly, we can derive from eq. (11, 13 for He II mode)

$$I^0_{\mathrm{ph,\,He\,I_{\beta\gamma}}} = 5.1 \cdot 10^{-17}\,\mathrm{A}\ . \tag{30}$$

and from equations (13, 14) determine size of charging current from He I photons

$$I^0_{\mathrm{ph,\,He\,I}} = 9.4 \cdot 10^{-17}\,\mathrm{A}\ . \tag{31}$$

The gridless Faraday cup measurement [*Nouzák*, 2013] in He I mode gave integral energy distribution characteristic Fig. 5. Saturated current for He I mode

$$I_{\mathrm{He\,I+He\,II}} \approx 5 \cdot 10^{-9}\,\mathrm{A}\ . \tag{32}$$

In this mode should be ratio of He I and He II photons 1:4 [*Specs*, 2009]. The contribution of He I photons in this saturated current is

$$I_{\mathrm{He\,I}} \approx 3.5 \cdot 10^{-9}\,\mathrm{A}\ . \tag{33}$$

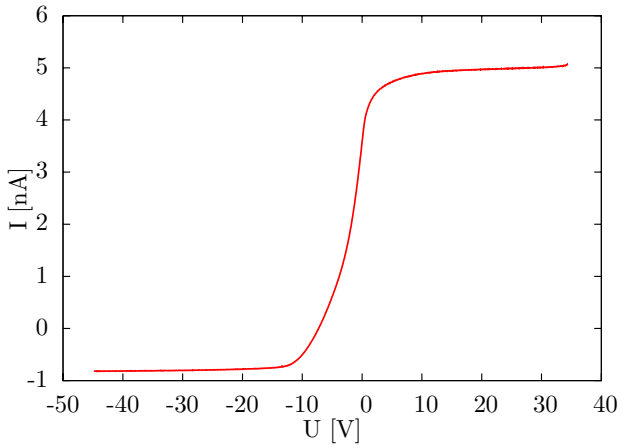


Figure 5. Photoelectron integral energy distribution measured by gridless Faraday cup in He I mode.

Photon density for He I mode (supposing quantum yield of the stainless steel sample in FC $\eta_{\mathrm{st.steel}}(21.2\,\mathrm{eV}) \approx 0.12$ [*Feuerbacher and Fitton*, 1972] measured by gridless Faraday cup is

$$I_{\mathrm{ph,\,He\,I}} \approx 1.6 \cdot 10^{14}\ \frac{\mathrm{ph}}{\mathrm{s.sr}}\ . \tag{34}$$

Approximate photon flow on grain is

$$\Gamma \approx 14384\ \frac{\mathrm{ph}}{\mathrm{s}}\ . \tag{35}$$

Since charging current is proportional to photon flow Γ and photoelectron yield of the grain η_{dust}

$$I^0_{\mathrm{ph,\,He\,I}} = e\Gamma\eta_{\mathrm{dust}}\ , \tag{36}$$

we can determine photoelectron yield of the grain as

$$\eta_{\mathrm{dust}}(21.2\,\mathrm{eV}) = 0.04\ . \tag{37}$$

This value is in good agreement with measurements of *Feuerbacher et al.* [1972] on powdered sample of lunar dust (48% of glass, 18% of Al_2O_3) $\eta_{\mathrm{lunar}}(21.2\,\mathrm{eV}) \approx 0.02$. However, *Feuerbacher et al.* [1972] point out that the measurement of the photoelectron yield on powdered sample might result in yields that are too low; for isolated particle the yield can be significantly larger [*Weingartner and Draine*, 2001].

Summary

We can conclude that:

- The radius of the investigated grain was $R \approx 2.7\,\mu$m and its mass was $m = 2 \cdot 10^{-13}$ kg.
- We have measured the time evolution of the photoemission charging of the glass grain illuminated by a He discharge lamp containing He I and He II photons. Observations have shown that the $\mathrm{He\,I}_{\beta\gamma}$ emission line in the He discharge plays a role in charging.
- We estimated the surface potential of the grain for two different photon energies and determined a specific capacitance of the grain.
- We determined the photoelectric yield for the glass dust grain with radius of $R \approx 2.7\,\mu$m and photons of energy 21.2 eV as $\eta_{\mathrm{dust}} \approx 0.04$.
- The work function of the glass grain was established as $\mathrm{W} = (4.7 \pm 1.5)\,\mathrm{eV}$.

Acknowledgment. This work was supported by the Grant Agency of the Charles University under project number 1410213 and by the Czech Grant Agency project No. 209/11/1412.

Reference

M. Anderegg, B. Feuerbacher, B. Fitton, L. D. Laude, and R. F. Willis. Secondary electron emission characteristics of lunar surface fines. P. Lunar Planet. Sci. C. 3th, 2665–2669, 1972.

M. Beránek, I. Čermák, Z. Němeček, J. Šafránková, M. Jeřáb, and J. Pavlů. Linear trap with three orthogonal quadrupole fields for dust charging experiments. Rev. Sci. Instrum. 93, 115109, 2012.

H. Boehnhardt and H. Fechtig. Electrostatic charging and fragmentation of dust near P/Giacobini-Zinner and P/Halley. Astron. Astrophys., 187 (1–2), 824–828, 1987.

L. E. Brus. A simple model for the ionization potential, electron affinity, and aqueous redox potentials of small semiconductor crystallites. J. Chem. Phys. 79, 5566–5571, 1983.

D. R. Criswell. Horizon-glow and the motion of lunar dust. in: Grard, R.J.L. (Ed.), Photon and Particle Interactions with Surfaces in Space. D. Reidel Publishing Co., Dordrecht, Holland, 545–556, 1973.

B. Feuerbacher, M. Anderegg, B. Fitton, L.D. Laude, and R. F. Willis. Photoemission from lunar surface fines and the lunar photoelectron sheath. P. Lunar Planet. Sci. C. 3th, 2655–2663, 1972.

B. Feuerbacher and B. Fitton. Experimental Investigation of Photoemission from Satellite Surface Materials. J. Appl. Phys., 43, 4, 1563–1572, 1972.

G. H. Heiken, D. T. Vaniman, and B. M. French. Lunar Sourcebook a User's Guide to the Moon. Cambridge University Press, Cambridge, 1991.

K. Hiroyoshi, F. Haruhisa. Charging of insulating glass caused by contact with plates. IEEJ Trans. Fund. Mater., 125, 2, 179–184, 2005.

R. W. Kreplin, T. A. Chubb, and H. Friedman. X-ray and Lyman-alpha emission from the Sun as measured from the NRL SR-1 satellite. J. Geophys. Res., 67, 6, 2231–2253, 1962.

G. Makov, A. Nitzan, and L. E. Brus. On the ionization potential of small metal and dielectric particles. J. Chem. Phys. 88, 5076–5085, 1988.

R. H. Manka. Plasma and potential at the lunar surface. in: Grard, R.J.L. (Ed.), Photon and Particle Interactions with Surfaces in Space. D. Reidel Publishing Co., Dordrecht, Holland, 347–361, 1973.

J. E. McCoy, D. R. Criswell. Evidence for a high altitude distribution of lunar dust. P. Lunar Planet. Sci. C. 5th, 2991–3005, 1974.

G. Morfill. Solar system — the enigma of Jupiter's ring. Nature, 381 (6580), 279–280, 1996.

T. G. Northrop. Dusty plasmas. Physica Scripta, 45(5), 475–490, 1992.

L. Nouzák. Stabilization system for particle sources, Bachelor thesis (in Czech), MFF UK, Praha, 2010.

L. Nouzák, J. Pavlů, J. Šafránková, and Z. Němeček, Photoelectron Energy Distribution from an Au Target Measured by a Gridless Faraday Cup, in *WDS'13 Proceedings of Contributed Papers: Part II — Physics of Plasmas and Ionized Media* (eds. J. Šafránková and J. Pavlů), Prague, Matfyzpress, 48–53, 2013.

S. Okamura, T. Iwao, M. Yumoto, H. Miyake, K. Nitta. Measurement of Photoelectron Emission by Vacuum Ultraviolet Ray Irradiation, AIP Conf. Proc. 1087, 544, 2009.

J. Pavlů, I. Richterová, Z. Němeček, J. Šafránková, and I. Čermák. Interaction between single dust grains and ions or electrons: laboratory measurements and their consequences for the dust dynamics. Faraday Discuss., 137, 139–155, 2008

Specs UV-source UVS 10/35, user manual, Specs, 2009.

Z. Sternovsky, P. Chamberlin, M. Horanyi, S. Robertson, and X. Wang. Variabillity of the lunar photoelectron sheath and dust mobility due to solar activity, J. Geophys. Res., 113, 1–4, 2008

J. D. Thomas, G. S. Hodges, D. G. Seely, N. A. Moroz, T. J. Kvale. Performance enhancement study of an electrostatic Faraday cup detector. Nucl. Instrum. Methods Phys. Res. Sect. A, 536, 11–21, 2005.

J. C. Weingartner and B. T. Draine. Photoelectric emission from interstellar dust: grain charging and gas heating, Astrophys. J. Suppl. S., 134, 263–281, 2001.

P. Žilavý, Z. Sternovský, I. Čermák, Z. Němeček and J. Šafránková. Surface potential of small particles charged by the medium — energy electron beam. Vacuum, 50, 1–2, 139–142, 1998.

Nouzák et al. [2016]

This article has been accepted for inclusion in a future issue of this journal. Content is final as presented, with the exception of pagination.

Investigations of Photoemission From Lunar Dust Simulant

Libor Nouzák, Ivana Richterová, Jiří Pavlů, Zdeněk Němeček, and Jana Šafránková

***Abstract*— The surface of the Moon is covered by a layer of dust grains. On the sunlit side, the photoemission dominates other charging processes and the work function of grains determines the maximum energy of the originated photoelectrons and, consequently, the grain surface potential. We present laboratory measurements of the work function on a single micrometer-sized lunar dust simulant captured in an electrodynamic trap and irradiated by UV photons. The first results indicate that the work function of lunar dust simulant Minnesota Lunar Simulant grains exceeds 5 eV. We suggest that a slight difference between the work functions determined for two grains is probably caused by the shape effect. The photoelectron yield in the energy range of about 20 eV (58 nm) estimated from the measurements is around 0.05 and it is in good agreement with the previous results.**

***Index Terms*— Dusty plasmas, electron emission, particle charging, photoemission.**

I. Introduction

THE SURFACE of the Moon is composed of rocks and lunar regolith, formed during a long period of meteoroid impacts [1]. The lunar regolith, a fragmental layer of broken, melted, or otherwise altered debris from the original bedrock, consists of grains less than 1 cm in size [1]. Regolith thickness on the *maria* is typically a few meters [2], [3], but in older highland regions, it can reach 10–15 m. The lunar soil is a subcentimeter fraction of the lunar regolith. It is cohesive, dark to light gray, very fine-grained, loose, and clastic material primarily derived from mechanical disintegration of rocks. The finest composite of the lunar soil material is often called lunar dust [4], [5]. As a consequence of mechanical crashing, lunar dust grains have sharp edges [6], [7].

The sharp gradient in a UV flux from the Sun across the solar terminator (the boundary between day and night sides of the Moon) may generate clouds of electrostatically charged dust. This dust can be set into a motion across the Moon as the terminator moves. The Surveyor and Apollo missions discovered some phenomena (horizon glow [8] and streamers [5]) above the lunar surface probably caused by a light scattered off electrostatically charged dust clouds at the terminator region [9]–[11]. Unexplained glows were even noted by ground-based observations [12], [13]. However, Horányi *et al*. [14] recently reported *in situ* lunar dust observations along the orbit of the Lunar Atmosphere and Dust Environment Explorer mission. They found no evidence of the lunar dust at high altitudes that could account for the lunar horizon glow or streamers.

The irradiated lunar surface is positively charged as a consequence of the photoemission current [15], [16]. On the dayside, an equilibrium charge is established when the electric potential (+4 V, [15]) of the charged surface prevents further photoelectrons to escape. All other charging currents are small and they are balanced by a portion of photoelectrons with energies above the surface potential. The number of photoelectrons as well as their energy depends on the work function of the dust grain material, but the direct measurements of this parameter is difficult for insulators [17] and especially for small irregular samples.

Sternovsky *et al*. [18] determined the work function of a lunar (Johnson Space Center (simulant) (JSC-1)) regolith simulant using contact charging of dust falling on substrates from different materials. The contact charging with oxidized metal surfaces was found to be independent on the work function. The effective work functions of the lunar analog determined by extrapolation were 5.8 and 5.6 eV for two different samples. Abbas *et al*. [19] investigated the photoemission yield from lunar dust samples brought by the Apollo and Luna missions. They found that this yield is a rising function of the grain size with a tendency for a saturation at largest investigated grains. However, the saturated value was an order of magnitude larger than that reported for bulk materials with a similar composition.

A determination of the work function from *in situ* measurements would be desirable, but it is probably impossible because we can observe only an equilibrium state that results from the charging by different processes. Nevertheless, we can investigate these charging processes separately on a single dust grain in laboratory conditions [20] or using numerical simulations [21].

In this paper, we introduce laboratory measurements of the photoemission from lunar dust simulant Minnesota Lunar Simulant (MLS-1) [22] samples of micrometer sizes. A single grain is captured in a linear electrodynamic trap of a special design [23] and irradiated by a UV source that can operate with a variety of gases (He, Ne, Ar, etc.). In measurements, we determine the grain size, its surface potential, and the work function using a time evolution of charging/discharging processes. The first results indicate that the work function of the lunar dust simulant is above 5 eV, very similar to the work function of glass grains [20]. The estimation of the

Manuscript received July 31, 2015; revised October 7, 2015; accepted October 11, 2015. This work was supported in part by the Czech Science Foundation under Grant GP13/25185P and Grant P209/11/1412 and in part by the Grant Agency of Charles University under Grant 1410213.

The authors are with the Faculty of Mathematics and Physics, Charles University in Prague, Prague 121 16, Czech Republic (e-mail: libor.nouzak@mff.cuni.cz; ivana.richterova@mff.cuni.cz; jiri.pavlu@mff.cuni.cz; zdenek.nemecek@mff.cuni.cz; jana.safrankova@mff.cuni.cz).

Color versions of one or more of the figures in this paper are available online at http://ieeexplore.ieee.org.

Digital Object Identifier 10.1109/TPS.2015.2493885

0093-3813 © 2015 IEEE. Personal use is permitted, but republication/redistribution requires IEEE permission.
See http://www.ieee.org/publications_standards/publications/rights/index.html for more information.

This article has been accepted for inclusion in a future issue of this journal. Content is final as presented, with the exception of pagination.

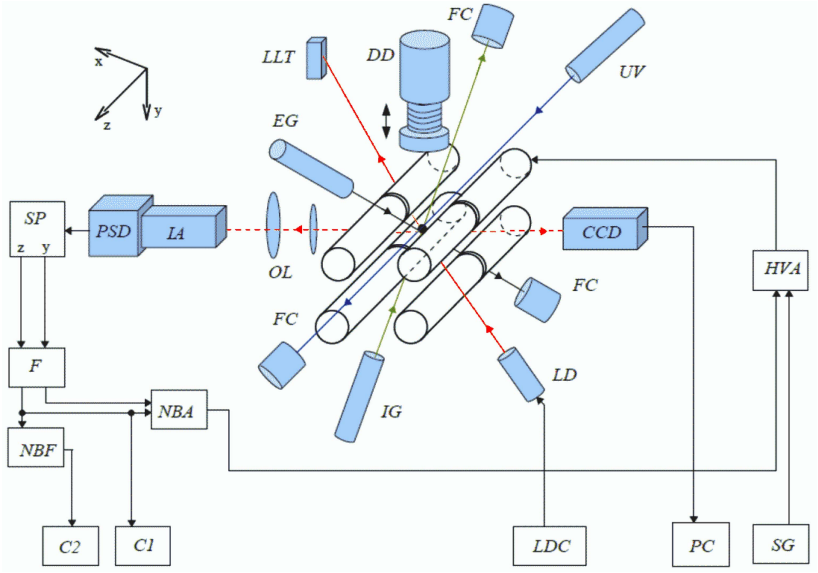


Fig. 1. Experimental setup—electrodynamic trap (FC—Faraday cup, EG—electron gun, IG—ion gun, UV—UV source, DD—dust dropper, IA—image amplifier, PSD—position sensitive detector, PC—personal computer, HVA—high voltage amplifier, OL—optical lenses, LLT—laser light trap, SP—signal processor, F—filter, NBF—narrowband filter, NBA—narrowband amplifier, C1 and C2—counters, LD—laser diode, LDC—LD control, SG—signal generator, CCD—charge-coupled device camera).

photoemission yield of one of the investigated grains provides a value of 0.05 for the ≈58-nm UV line.

II. Experimental Setup

The experimental setup is based on a linear electrodynamic trap (in the center of Fig. 1). The charged dust grain is caught in an effective potential that is formed by three-independent RF fields, all of them having dominant quadrupole terms [23]. The trap consists of four rods, each of them being divided into two parts and the rod parts are supplied by eight high voltage amplifiers. A harmonic signal with a time window for shooting charged particles is provided by a programmable signal generator. A grain is shaken out from a dust dropper, and the falling grain is charged by one of particle sources to be caught in the effective potential of the trap. Three particle sources can be used: 1) an electron gun; 2) an ion gun; and 3) a differentially pumped UV lamp (UV). The currents from particular sources are stabilized by a feedback loop and measured by the gridless Faraday cups (FCs). The measurements of the UV effects rely on the stability of the used UV source.

The measurements are based on a determination of the frequency of the grain oscillation within the trap. We use a synchronous optical detection of a light scattered by the grain. The light beam from a laser diode modulated by a controller (LDC) interacts with the levitating grain and a part of the scattered light is concentrated by a lens system (OL) onto an image amplifier and a position sensitive detector (PSD) that converts an optical signal to the electrical signal for a signal processor. The processor unit provides the position signal of the grain image that is used for damping/stabilization of dust grain oscillations. The signal from the PSD is amplified by a narrowband filter and its frequency f_x is measured by a frequency counter (C2). The charge-to-mass ratio of the grain is determined from its oscillation frequency, f_x

$$\frac{Q}{m} = \frac{4\pi^2\sqrt{2} f_x f_{\mathrm{AC}} r_0^2}{\lambda_z V_z} \tag{1}$$

where f_{AC} and V_z are the frequency and amplitude of the trap supply, and r_0 and λ_z are geometric parameters of the trap (see [23] for details). The Q/m evolution is recorded during the measurements.

III. Measurement Technique

The charge-to-mass ratio of the grain (Q/m) is directly proportional to its surface potential (ϕ) [24] through the grain specific capacitance C_m (the ratio of the grain capacitance and mass). This capacitance can be easily calculated for spherical grains, but an electron microscope photo (not shown) of an MLS-1 lunar simulant has shown that the grains are not spherical; they exhibit sharp edges and thus their specific capacitance is unknown.

In the case of photoemission charging by a monochromatic light with an energy of $h\nu$, the maximum attainable surface potential $\phi_{\max}$ of the dust grain would meet the equation

$$\phi_{\max} = \frac{1}{e}(h\nu - W) \tag{2}$$

where W is the work function of the grain, and its determination would be straightforward when C_m is known. In laboratory conditions, the situation is more complex for several reasons.

This article has been accepted for inclusion in a future issue of this journal. Content is final as presented, with the exception of pagination.

TABLE I
EMISSION LINES OF He, Ar, AND Ne GASES IDENTIFIED FROM Q/m VALUES OF TWO MLS-1 GRAINS OF DIFFERENT SIZES

Emission line	Excitation energy (eV)	Wavelength (nm)	$Q/m_{4.7\,\mu\mathrm{m}}$ (C/kg)	$Q/m_{4.0\,\mu\mathrm{m}}$ (C/kg)
Ar I	15.43	80.35	0.02 ± 0.0018	0.028 ± 0.0021
Ar II	17.13	72.38	0.0228 ± 0.0005	0.0332 ± 0.0013
Ar II	17.26	71.83	0.0256 ± 0.0007	0.0339 ± 0.0007
Ar II	18.44	67.23	0.0278 ± 0.0064	0.0358 ± 0.0008
Ar II	23.87	51.94	0.0368 ± 0.0011	0.0387 ± 0.001
Ar II	25.26	49.08	0.04 ± 0.0014	0.0559 ± 0.0054
He I	21.22	58.43	0.0316 ± 0.0045	0.0445 ± 0.0039
He I	23.08	53.72	0.0361 ± 0.0014	0.0507 ± 0.0052
He II	40.8	30.93	0.0703 ± 0.0038	0.0971 ± 0.0039
Ne I	16.67	74.38		0.0316 ± 0.0018
Ne I	16.85	73.58		0.0329 ± 0.0023
Ne I	20.14	61.96		0.0411 ± 0.0114
Ne II	26.82	46.26		0.0606 ± 0.0198
Ne II	30.45	40.72		0.069 ± 0.0054
Ne II	34.21	36.25		0.0801 ± 0.0124

1) We use a differentially pumped capillary discharge UV source [25] that can operate with a variety of gases (He, Ne, Ar, etc.), but investigations can be complicated by a presence of several emission lines in the discharge of each working gas. When no discharging background current is present, the maximum attainable surface potential $\phi_{\max}$ will be given by the emission line with the highest excitation energy.
2) A part of a UV light from the source or a possible reflected UV from surrounding surfaces can interact with walls of the vacuum vessel or with rods of the trap and produce background photoelectrons. Some of them can reach the grain and decrease its surface potential, and thus, the maximum surface potential of the grain will be lower than that given by (2).

On the other hand, if an emission line with the higher energy is present in the discharge and its intensity is sufficient, the surface potential can exceed the value given by (2). In such cases, the equilibrium grain potential is given by a balance of the photocurrent and the discharging background current.

The used UV source can operate in two modes differing by a pressure of the working gas and discharge current. In the mode denoted I (II), it predominantly emits lines with energies just below the first (second) ionization potential, but all other lines are emitted as well albeit with the depressed intensity. Table I shows the energies and corresponding wave lengths of lines that we were able to identify and that were used for the determination of the grain work function. We should note that these lines only partly correspond to a list of most intensive lines provided by the UV source manufacturer. The last two columns of Table I show the specific charges of two investigated grains, and a method of their estimation will be discussed later.

To overcome these difficulties, we have developed a method of a work function determination that uses two or more UV emission lines and employs the so-called current–voltage (I–V) plot technique [26]. Since I–V plots are a key technique for the determination of the work function, we briefly describe this method.

Let us assume that the grain is charged to a surface potential higher than that given by (2) when the UV source is switched ON. UV produces background electrons that discharge the grain and its potential starts to decrease. When the grain potential reaches the value of $\phi_{\max}$ corresponding to (2), the photoelectrons become to leave the grain and to reduce the discharging current.

The discharging current can be obtained as a derivative of the measured $Q/m(t)$ temporal profile

$$\frac{d}{dt}\left(\frac{Q}{m}\right) = \frac{I}{m}. \tag{3}$$

The plot I/m versus Q/m is called the I–V plot because Q/m is proportional to the grain potential. In this simple scenario, I/m consists of two components: 1) the background current I_{back}/m and 2) the photoemission current I_{photo}/m. One can expect that the dependence of both these components on Q/m can be approximated by straight lines in a vicinity of $\phi_{\max}$ [27]. Since I_{photo}/m is equal to zero above $\phi_{\max}$, the plot of the total current would exhibit a knee at Q/m corresponding to $\phi_{\max}$. The position of this knee can be determined from a bilinear fit of the I–V plot. This one point would be sufficient for a determination of the work function in an ideal case of a monochromatic light, but two or more points are needed in a real experiment.

IV. ESTIMATION OF THE WORK FUNCTION

The computation of the work function from measurements on a grain illuminated by the nonmonochromatic light is based on evaluation of records of charging/discharging characteristics. The key point is a relation between the grain potential and its specific charge. To simplify this task, we use the fact that the secondary electron emission under the bombardment by the 1-keV electron beam will charge the grain to $\approx$7 V of the surface potential [24], and the corresponding Q/m can be used for a rough estimation of the grain capacitance. The full measuring sequence for one dust grain is shown in Fig. 2 and a procedure is described in its captions. As it can be seen in Fig. 2, we applied three gases in order to identify a sufficient amount of lines and to decrease the error of the work function determination. The whole measurements proceed a long time because a rate of the Q/m determination is about 1 Hz, and the charging/discharging curves should be well sampled for computation of their derivatives.

This article has been accepted for inclusion in a future issue of this journal. Content is final as presented, with the exception of pagination.

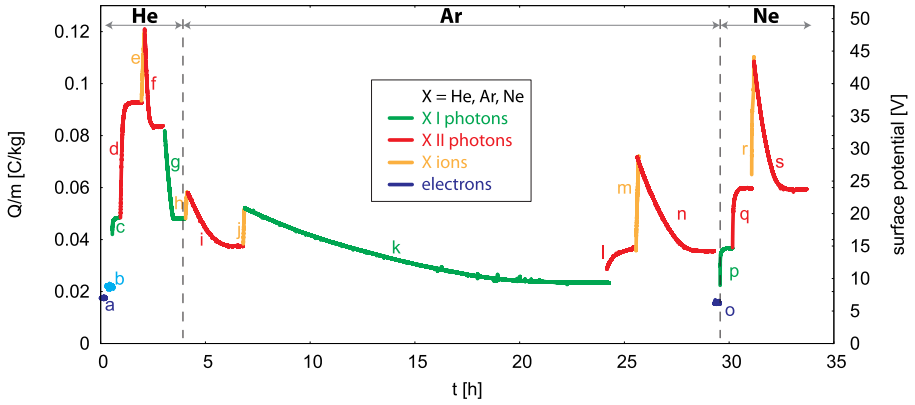


Fig. 2. Time evolution of the photoemission charging of the grain with a size of ≈4.0 μm. Charging/discharging procedure from left to right: (a) charging by 1-keV electrons, (b) charging by 1-keV electrons and He I photons, (c) charging by He I photons, (d) charging by He II photons, (e) charging by 1-keV He ions, (f) discharging by He II photoelectrons from the background, (g) discharging by He I photoelectrons from the background, (h) charging by 1-keV Ar ions, (i) discharging by Ar II photoelectrons from the background, (j) charging by 1-keV Ar ions, (k) discharging by Ar I photoelectrons from the background, (l) charging by Ar II photoelectrons, (m) charging by 1-keV Ar ions, (n) discharging by Ar II photoelectrons from the background, (o) discharging by 1-keV electrons, (p) charging by Ne I photoelectrons, (q) charging by Ne II photoelectrons, (r) charging by 1-keV Ne ions, and (s) discharging by Ne II photoelectrons from the background.

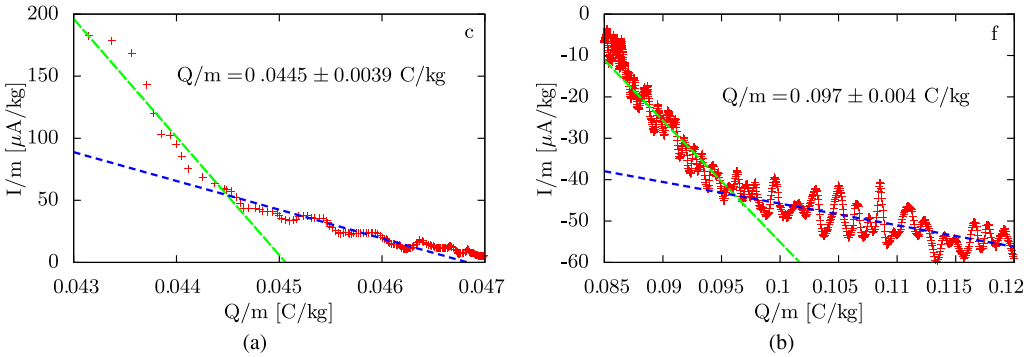


Fig. 3. Examples of I–V plots. (a) I–V characteristics recorded during the grain charging by He I lines [Fig. 2(c)]. (b) I–V characteristics that represent discharging of the grain by emission lines of He II groups [Fig. 2(f)].

Another reason for slow changes of the grain charge is that the precise determination of Q/m requires the grain oscillating around the trap center, thus the DC potential compensating a gravity should be simultaneously adjusted [24]. Fast changes of Q/m usually lead to grain loss and the experiment should start from the beginning. Nevertheless, we were able to measure the full sequence for one grain and the sequence limited to He and Ar emission lines for the second one.

We applied the I–V plot technique on all parts of the profile corresponding to the charging or discharging of the grain by the UV source with a special attention to the Q/m regions surrounding expected knees caused by the emission lines. According to theory, we would be able to identify plenty of lines (e.g., http://www.nist.gov/), but the Q/m data are noisy and the derivative increases the noise further. For this reason, we were able to find only the most intensive lines as it can be seen in Table I.

Fig. 3 presents two examples of I–V plots. First of them [Fig. 3(a)] was recorded during grain charging by He I lines [Fig. 2(c)], the second one [Fig. 3(b)] belongs to discharging of the grain charged by energetic ions to a surface potential exceeding the energies of He II groups of emission lines [Fig. 2(f)]. The ratio of Q/m corresponding to the intersection of two linear fits was recalculated to the grain potential using the grain specific capacitance that was determined in two steps. The first rough estimation was based on an assumption that the grain bombarded by 1-keV electrons is charged to 7 V. The value was later adjusted to achieve the best agreement between the distribution of measured surface potentials and possible energies of the UV lines.

The results of above described procedures applied on two grains from the Lunar Highlands Type lunar regolith simulant are shown in Fig. 4. The position of points on the horizontal axis is given by the energy of a particular emission line, and the vertical axis is marked in units of the grain specific charge. The error bars show propagated uncertainties of the linear fits to I–V plots; the thin line is a linear fit to depicted points that reflect the mentioned uncertainties. Under

This article has been accepted for inclusion in a future issue of this journal. Content is final as presented, with the exception of pagination.

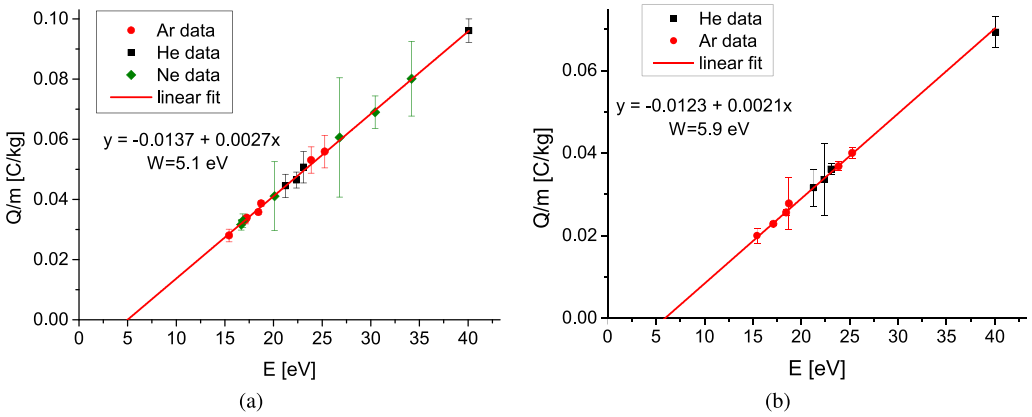


Fig. 4. Estimated work functions of two grains of different sizes using I–V plots. The grains used with an effective diameter of (a) 4 and (b) 4.7 μm.

assumptions that the potentials are given by (3) for each of identified UV lines, the points would lie on a straight line that intersects the horizontal axis at the energy equal to the grain work function. The investigated grains slightly differ by their dimensions and/or shapes. This fact can be described by their effective diameters calculated from the specific capacitance assuming a spherical shape. This effective diameter is 4 μm for the grain in Fig. 4(a) and 4.7 μm for that in Fig. 4(b). We should point out that it does not necessarily mean that the second grain is larger; as we mentioned, the difference can be caused by the different shapes of a particular grain.

The calculated values ($W_{4.7\ \mu\mathrm{m}} = (5.9 \pm 0.3)$ eV and $W_{4.0\ \mu\mathrm{m}} = (5.1 \pm 0.7)$ eV, respectively) of the grain work function are in a full accordance with the value of $W \approx 5.8$ eV obtained in [18] for the JSC-1 lunar regolith simulant by the contact charging method. We should note here that the work function of the glass grain [20] was determined as $W = (4.7 \pm 1.5)$ eV under the same conditions, also in agreements with the values obtained in [28] and [29] for the bulk material. According to the theories in [30] and [31], the work function would depend on the curvature of the surface, but this effect would be negligible for grains with a radius in the micrometer range but it would be seen for nanometer-sized grains. On the other hand, sharp edges that can be expected on the grain surface can lead to decrease of the measured work function. This means that the work function would be different for different parts of the grain surface, and this effect could be responsible for difficulties with a determination of breaks in I–V plots like those in Fig. 3.

V. Photoemission Yield

Estimates of background and photoemission currents belonging to particular emission lines of our UV source demonstrated in Fig. 3 could be used for the determination of the photoemission yield defined as a ratio of numbers of incoming photons and emitted electrons. The number of photons falling on the grain was determined from the total photoemission current measured by the FC with stainless steel collector under assumptions that the yield of this material for the most intensive He I emission line (21.2 eV) is ≈0.12 [32].

The diameter of the UV beam was estimated from the geometries of the source and experimental setup. The grain was expected to levitate in the center of the beam with the Gaussian intensity profile. The grain cross section was considered to be circular with an effective diameter determined from the grain specific capacitance. Under these assumptions, the photoemission yield η of the first grain (with a effective diameter of 4 μm) is

$$\eta_{\mathrm{dust}}(21.2\ \mathrm{eV}) = 0.05. \tag{4}$$

This value is in good agreement with measurements on a powdered sample of the lunar dust (48% of glass and 18% of Al_2O_3), $\eta(21.2\ \mathrm{eV}) = 0.02$ [33], and a silica solar cell covered by an indium oxide layer, $\eta(21.2\ \mathrm{eV}) = 0.07$ [32]. However, Feuerbacher *et al.* [33] point out that the measurement of the photoelectron yield on powdered sample might result in yields that are too low; the yield of an isolated particle can be significantly larger [34].

A value estimated by our procedure is similar to that found in [19] for the dust grains of micrometer diameters. However, we should note that the shape of grains investigated in our and their experiments were irregular, and thus a value of the yield would depend on the way used for a determination of the grain surface. We are using the effective diameter, and we believe that is a good approximation because it rises with an elongation of the grain and the same does the grain surface. Nevertheless, the grain shape is the most important source of the uncertainty of the yield determination.

VI. Conclusion

The main goal of this paper is to describe a procedure that allows a reliable determination of the work function of a single dust grain and its dependence on the grain material and on the energy of UV photons. The results of this preliminary study can be summarized as follows.

1) We observed time evolutions of the photoemission charging of two lunar dust simulant (MLS-1) grains illuminated by a UV discharge lamp emitting He I, He II, Ar I, Ar II, Ne I, and Ne II photons.

This article has been accepted for inclusion in a future issue of this journal. Content is final as presented, with the exception of pagination.

2) We calculated I–V plots and we identified several emission lines in He, Ar, and Ne discharges from the changes of charging/discharging currents.
3) We associated these lines with grain surface potentials (using corresponding Q/m ratio) and extrapolating them to zero grain potentials, we estimated work functions of the lunar simulant material.
4) The work functions of the lunar simulant grains were found to be $W_{4.7\ \mu\mathrm{m}} = (5.9 \pm 0.3)$ eV and $W_{4.0\ \mu\mathrm{m}} = (5.1 \pm 0.7)$ eV. We suggest that the difference of work functions can be connected with the effects of the grain shape.
5) We have determined the photoemission yield of the lunar dust MLS-1 material as ≈0.05 for 21.2-eV photons.

The effects of the grain shape on a value of the determined yield as well as on the determined work function will be subjects of consecutive studies.

ACKNOWLEDGMENT

The authors would like to thank Prof. D. Vítek for his useful suggestions and comments.

REFERENCES

[1] G. Heiken, D. Vaniman, and B. M. French, Eds., *Lunar Sourcebook: A User's Guide to the Moon*. Cambridge, U.K.: Cambridge Univ. Press, 1991.
[2] Y. Langevin and J. R. Arnold, "The evolution of the lunar regolith," *Annu. Rev. Earth Planet. Sci.*, vol. 5, no. 1, pp. 449–489, 1977.
[3] S. R. Taylor, *Planetary Science: A Lunar Perspective*. Houston, TX, USA: Lunar and Planetary Institute, 1982.
[4] D. S. McKay *et al.*, "The lunar regolith," in *Lunar Sourcebook: A User's Guide to the Moon*, G. Heiken, D. Vaniman, and B. French, Eds. Cambridge, U.K.: Cambridge Univ. Press, 1991, pp. 285–386.
[5] T. J. Stubbs, R. R. Vondrak, and W. M. Farrell, "A dynamic fountain model for lunar dust," *Adv. Space Res.*, vol. 37, no. 1, pp. 59–66, 2006.
[6] H. Heywood, "Particle size and shape distribution for lunar fines sample 12057,72," in *Proc. Lunar Sci. Conf.*, vol. 2. 1971, pp. 1989–2001.
[7] W. D. Carrier, G. R. Olhoeft, and W. Mendell, "Physical properties of the lunar surface," in *Lunar Sourcebook: A User's Guide to the Moon*, G. Heiken, D. Vaniman, and B. French, Eds. Cambridge, U.K.: Cambridge Univ. Press, 1991, pp. 475–594.
[8] D. A. Glenar, T. J. Stubbs, J. E. McCoy, and R. R. Vondrak, "A reanalysis of the Apollo light scattering observations, and implications for lunar exospheric dust," *Planet. Space Sci.*, vol. 59, pp. 1695–1707, Nov. 2011.
[9] J. E. McCoy and D. R. Criswell, "Evidence for a high altitude distribution of lunar dust," in *Proc. Lunar Sci. Conf.*, vol. 5. 1974, pp. 2991–3005. [Online]. Available: http://adsabs.harvard.edu/abs/1974LPSC....5.2991M
[10] D. R. Criswell, "Horizon-glow and the motion of lunar dust," in *Photon and Particle Interactions With Surfaces in Space* (Astrophysics and Space Science Library), vol. 37, R. J. L. Grard, Ed. Noordwijk, The Netherlands: Springer-Verlag, 1973, pp. 545–556.
[11] H. A. Zook and J. E. McCoy, "Large scale lunar horizon glow and a high altitude lunar dust exosphere," *Geophys. Res. Lett.*, vol. 18, no. 11, pp. 2117–2120, 1991.
[12] W. S. Cameron, "Manifestations and possible sources of lunar transient phenomena (LTP)," *Moon*, vol. 14, no. 1, pp. 187–199, Sep. 1975.
[13] W. S. Cameron, "Lunar transient phenomena catalog," NASA Goddard Spaceflight Center, Greenbelt, MD, USA, Tech. Rep. NSSDC/WDC-A-R&S v. 7803, Jul. 1978.
[14] M. Horányi *et al.*, "A permanent, asymmetric dust cloud around the Moon," *Nature*, vol. 522, no. 7556, pp. 324–326, 2015.
[15] R. H. Manka, "Plasma and potential at the lunar surface," in *Photon and Particle Interactions With Surfaces in Space* (Astrophysics and Space Science Library), vol. 37, R. J. L. Grard, Ed. Noordwijk, The Netherlands, Springer-Verlag, 1973, pp. 347–361.
[16] R. F. Willis, M. Anderegg, B. Feuerbacher, and B. Fitton, "Photoemission and secondary electron emission from lunar surface material," in *Photon and Particle Interactions With Surfaces in Space* (Astrophysics and Space Science Library), vol. 37, R. J. L. Grard, Ed. Noordwijk, The Netherlands: Springer-Verlag, 1973, pp. 389–401.
[17] A. A. Sickafoose, J. E. Colwell, M. Horányi, and S. Robertson, "Experimental investigations on photoelectric and triboelectric charging of dust," *J. Geophys. Res.*, vol. 106, no. A5, pp. 8343–8356, 2001.
[18] Z. Sternovsky, S. Robertson, A. Sickafoose, J. Colwell, and M. Horányi, "Contact charging of lunar and Martian dust simulants," *J. Geophys. Res. (Planets)*, vol. 107, no. E11, pp. 15-1–15-8, Nov. 2002.
[19] M. M. Abbas, D. Tankosic, P. D. Craven, J. F. Spann, A. LeClair, and E. A. West, "Lunar dust charging by photoelectric emissions," *Planet. Space Sci.*, vol. 55, nos. 7–8, pp. 953–965, 2007.
[20] L. Nouzák, I. Richterová, J. Pavlů, Z. Němeček, and J. Šafránková, "Investigations of the photoemission from glass dust grains," in *WDS'14 Proc. Contrib. Papers—Phys.*, Prague, Czech Republic, 2014, pp. 361–370.
[21] J. Vaverka, I. Richterová, J. Pavlů, J. Šafránková, and Z. Němeček, "Lunar surface and dust grain potentials during the Earth's magnetosphere crossing," *J. Geophys. Res.*, to be published.
[22] E. Hill, M. J. Mellin, B. Deane, Y. Liu, and L. A. Taylor, "Apollo sample 70051 and high- and low-Ti lunar soil simulants MLS-1A and JSC-1A: Implications for future lunar exploration," *J. Geophys. Res.*, vol. 112, no. E2, 2007, Art. ID E02006.
[23] M. Beránek, I. Čermák, Z. Němeček, J. Šafránková, M. Ječáb, and J. Pavlů, "Linear trap with three orthogonal quadrupole fields for dust charging experiments," *Rev. Sci. Instrum.*, vol. 83, no. 11, p. 115109, 2012.
[24] J. Pavlů, I. Richterová, Z. Němeček, J. Šafránková, and I. Čermák, "Interaction between single dust grains and ions or electrons: Laboratory measurements and their consequences for the dust dynamics," *Faraday Discuss.*, vol. 137, pp. 139–155, 2008.
[25] *SPECS UV-Source UVS 10/35, User Manual*, SPECS Surf. Nano Anal. GmbH, Berlin, Germany, 2009.
[26] I. Čermák, E. Grün, and J. Švestka, "New results in studies of electric charging of dust particles," *Adv. Space Res.*, vol. 15, no. 10, pp. 59–64, May 1995.
[27] P. Žilavý, Z. Sternovský, I. Čermák, Z. Němeček, and J. Šafránková, "Surface potential of small particles charged by the medium-energy electron beam," *Vacuum*, vol. 50, no. 1–2, pp. 139–142, 1998.
[28] H. Kitabayashi and H. Fujii, "Charging of insulating glass caused by contact with plates," *IEEJ Trans. Fundam. Mater.*, vol. 125, no. 2, pp. 179–184, 2005.
[29] S. Okamura, T. Iwao, M. Yumoto, H. Miyake, and K. Nitta, "Measurement of photoelectron emission using vacuum ultraviolet ray irradiation," in *Proc. AIP Conf.*, vol. 1087. Jan. 2009, pp. 544–549.
[30] L. E. Brus, "A simple model for the ionization potential, electron affinity, and aqueous redox potentials of small semiconductor crystallites," *J. Chem. Phys.*, vol. 79, no. 11, pp. 5566–5571, 1983.
[31] G. Makov, A. Nitzan, and L. E. Brus, "On the ionization potential of small metal and dielectric particles," *J. Chem. Phys.*, vol. 88, no. 8, pp. 5076–5085, 1988.
[32] B. Feuerbacher and B. Fitton, "Experimental investigation of photoemission from satellite surface materials," *J. Appl. Phys.*, vol. 43, no. 4, pp. 1563–1572, 1972.
[33] B. Feuerbacher, M. Anderegg, B. Fitton, L. D. Laude, R. F. Willis, and R. J. L. Grard, "Photoemission from lunar surface fines and the lunar photoelectron sheath," in *Proc. 3rd Lunar Sci. Conf.*, vol. 3. 1972, pp. 2655–2663.
[34] J. C. Weingartner and B. T. Draine, "Photoelectric emission from interstellar dust: Grain charging and gas heating," *Astrophys. J. Suppl. Ser.*, vol. 134, no. 2, p. 263, 2001.



Libor Nouzák was born in Česká Lípa, Czech Republic, in 1988. He received the M.S. degree from Charles University in Prague, Prague, Czech Republic, in 2012, where he is currently pursuing the Ph.D. degree with the Space Physics Laboratory.

His current research interests include the laboratory simulation of elementary processes in dusty plasmas, namely, photoemission.

This article has been accepted for inclusion in a future issue of this journal. Content is final as presented, with the exception of pagination.



Ivana Richterová was born in Český Brod, Czech Republic, in 1979. She received the M.S. and Ph.D. degrees from Charles University in Prague, Prague, Czech Republic, in 2003 and 2012, respectively.

She is currently a Senior Assistant with the Space Physics Laboratory, Department of Surface and Plasma Science, Faculty of Mathematics and Physics, Charles University in Prague. Her research is devoted to the laboratory investigation and modeling of elementary charging processes on dust grains.



Jiří Pavlů was born in Pardubice, Czech Republic, in 1977. He received the M.S. and Ph.D. degrees from Charles University in Prague, Prague, Czech Republic, in 2001 and 2005, respectively.

He is currently a Senior Assistant with the Space Physics Laboratory, Department of Surface and Plasma Science, Faculty of Mathematics and Physics, Charles University in Prague. His current research interests include the laboratory investigations of elementary processes on dust grains induced by electron, ion, and photon irradiations.



Zdeněk Němeček was born in Prague, Czech Republic, in 1947. He received the M.S., Ph.D., and D.Sc. degrees from Charles University in Prague, Prague, in 1971, 1982, and 1996, respectively.

He has held several leading positions with the Faculty of Mathematics and Physics, Charles University in Prague, since 1971. His current research interests include the solar wind interaction with the Earth's magnetosphere and the laboratory simulations of plasma processes.



Jana Šafránková was born in Teplice, Czech Republic, in 1947. She received the M.S., Ph.D., and D.Sc. degrees from Charles University in Prague, Prague, Czech Republic, in 1972, 1982, and 1996, respectively.

She has held several positions with the Faculty of Mathematics and Physics; she is currently the Head of the Space Physics Laboratory. Her current research interests include the solar wind and laboratory simulations of elementary processes in dusty plasmas.

Vyšinka et al. [2017]

MF Microspheres: Helping or Puzzling Tool?

Marek Vyšinka, Libor Nouzák, Jiří Pavlů, Zdeněk Němeček, Jana Šafránková, Ivana Richterová

***Abstract*—Melamine formaldehyde (MF) microspheres are widely used in dusty plasma experiments for their monodispersity, sphericity, low mass density, and well defined sizes. The paper summarizes problems that were encountered in numerous applications of these grains in different laboratory simulations. and the already published results are discussed in view of new experiments. The main results of this paper are connected with changes of the grain mass due to the decreased pressure and/or increased temperature and variations of the grain dimensions, its shape, and mass density under electron or ion bombardments. By contrast to the work function estimated from field emission properties, we have found the photoelectric work function (4.5 eV) being close to that expected. A sputtering of the grains using a 30 keV ion beam revealed their unexpected heterogeneity.**

***Index Terms*—Dust grains, dusty plasma, melamine formaldehyde (MF) resin, microspheres.**

I. Introduction

MELAMINE formaldehyde resin spheres are widely used by the dusty plasma community since they are available in a broad range of sizes and their low-mass density and a good optical reflectivity (see Table I adopted from Microparticles GmbH web pages http://microparticles.de/en/) facilitate different experimental techniques. Monodispersity and sphericity make estimations and calculations easier; the low-mass density enables easy grain levitation and the high reflectivity implicates easy optical detection. From this point of view, it seems that MF microspheres are an ideal sample not only for the dusty plasma research, but for many sorts of studies involving small particles; even more, they are offered in numerous alternatives with functional surfaces (dyed, metal covered, fluorescent, with magnetic layer, etc.).

Numerous dusty plasma experiments over the world used MF grains: their different sizes were used together onboard ISS within the PKE-Nefedov, PK-3 Plus, and PK-4 experiments, e.g., [1]–[3]; they were used as a kind of probes in order to study and to map electric fields (both horizontal and vertical) [4], [5] in low-pressure gas discharges; or to investigation of interactions between the plasma and magnetic field [6]; to study dust grains under the influence of crossed electric and magnetic fields in the sheath of an RF discharge [7]; or dust charge fluctuations in the sheath and at its boundaries [8], [9]; to determination of levitation limits within the sheath [10]; and to demonstration of vortex flow turbulence [11] in complex plasma experiments. Liu et al. [12] reported how the radiation pressure and gas drag forces act on a single MF microsphere and quantified the Epstein gas drag force coefficient. In space applications, Wang et al. [13] discussed a dust transport in the plasma investigating an origin of the lunar horizon glow.

TABLE I
SOME OF THE PROPERTIES OF MF PARTICLES (ADOPTED FROM THE PRODUCER WEB PAGES).

Property	MF particles
Density	1.51 g/cm^3
Refractive index	1.68
Particle diameter	0.3–12 μm
Monodispersity	CV $< 5\%$
Particle shape	spherical
Temperature stability	to 250 °C
Mechanical strength	robust
Stability in solvents without swelling	water, alcohols, all solvents and oils
Structure	hydrophilic, non-porous

Above a brief overview of the literature demonstrates how popular the MF grains are in fundamental laboratory studies. Nevertheless, many authors have found that some parameters of MF grains change during experiments and that these variations depend on types of the plasma environment and on applications of various diagnostic techniques (e.g., [14]–[16]). According to these papers, we already know that an exposition of MF grains to vacuum, plasma, and/or electron or ion beams can induce changes of the MF grain dimensions, mass density, shape, and electrical properties that can be attributed to the modification of the internal structure. Since this knowledge is spread over different reports, we summarize and comment the previous results and show the results of new observations with a motivation to help other experimenters to understand and to interpret their measurements.

The text is divided into the subsections devoted to different aspects of MF grains (work function, mass, size, mass density, adhesiveness of surface layers, etc.) or processes like field emission or ion sputtering. Each of these subsections starts with a short overview of already published experiments that are further discussed from the point of view of properties of MF grains, and continues with new results. The main attention is focused on an interaction of MF particles with energetic electrons or ions using two types of experiments but other possible sources of particle modifications are discussed as well.

II. Experimental techniques

The paper presents two complementary types of experiments. Scanning Electron Microscopy (SEM) is a widely used

This work was supported by the Czech Science Foundation project 16-05762S and LN thanks to the Grant Agency of Charles University for support by project 728616.

All authors are with the Charles University in Prague, Faculty of Mathematics and Physics, Prague, Czech Republic. e-mail: (see http://physics.mff.cuni.cz/kfpp/).

0000–0000/00$00.00 © 2014 IEEE

technique for scientific images under an assumption that the energetic electrons do not change the properties of investigated samples substantially. For this reason, we have varied the focus, scanned area, and electron beam intensity in course of the experiments. High intensities and long expositions were used to influence the grains, whereas very low intensities served for consecutive images that permit a quantification of results of the electron beam–grain interaction. The electron beam energy was 15 keV and the pressure in the experimental vessel varied from 10^{-2} to 10^{-3} Pa during experiments. The integrated-in Focused Ion Beam (FIB) operating with 30 keV gallium ions facilitated sputtering experiments.

A second type of our experimental set-ups is an electrodynamic quadrupole trap [17] which allows us to catch a single charged grain and to affect it by different beams of particles with a tunable energy. This particular experiment is conducted under ultra-high vacuum conditions (typically 10^{-7} Pa). The principles of this technique can be found in [14] and in [18], respectively, thus we repeat only basic features used in the present paper.

A single charged MF grain levitates in the effective potential of the trap and it can be bombarded by beams of UV photons and/or beams of electrons and/or ions. The only measurable quantity is a frequency of grain oscillations that is directly proportional to its charge-to-mass ratio (specific charge hereafter). A determination of all important quantities requires applications of dedicated techniques:

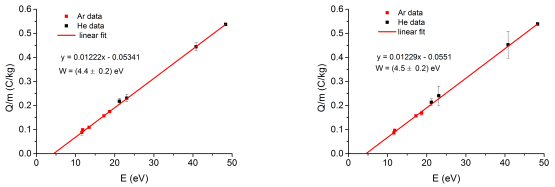
1) Grain mass: the charge of a slightly charged (about one hundred of elementary charges) grain is changed by one elementary charge up or down and a jump of the oscillation frequency is proportional to the grain mass.
2) Grain charge: it is computed from the specific charge and grain mass.
3) The surface potential: the grain is charged by the ion beam to a positive surface potential (that is approximately equal to the beam energy) and the beam energy is abruptly decreased. The beam ions are repulsed from the charged grain but it is gradually discharged by background electrons (originated mainly due to ionization of the residual gas in the vessel). When the grain potential becomes equal to the beam energy, an abrupt change of the discharging current is observed.
4) Grain specific capacitance: it can be calculated from its specific charge corresponding to the potential determined by the point 3).
5) Grain size: it is calculated from the capacitance under an assumption of the grain spherical shape.

If the mass determined by 1) and the estimated size by 5) do not match the known mass density, it can be interpreted as a non-spherical shape of the grain or mass density change.

III. Observations

A. Work function

As a first point, we discuss the work function that is a very important parameter for any estimation of the charge of illuminated dust grains, nevertheless, its determination is generally difficult for insulators due to their charging. For this reason,



(a) (b)

Fig. 1. Work functions of the MF grain calculated from identified emission lines of Ar I, Ar II, He I and He II prior to (left) and after (right) 35-hour treatment by the 0.4 keV electron beam.

Pavlu et al. [19] tried to estimate the work function of MF grains from observations of the field emission discharging of highly charged grains by the Fowler–Nordheim method. Since the resulting plots were neither linear nor stable, the authors were able to provide only a very broad range (1.4–7.5 eV) of work function values. Suggested causes of the spread of experimental data were variations of the electric capacitance caused by unpredictable changes of the grain dimensions or shapes due to a high surface electric field. It was one of the first experiments showing that the geometry/dimension of MF grains can be significantly influenced by their charge.

As a range of MF work functions established by [19] was rather broad, we applied the method based on the photoemission that was suggested by [20]. Impacts of UV photons lead to charging of the MF grain by photoelectron emission. The grain surface potential is given by the photon energy and the material work function according to Eq. 1.

$$\phi = \frac{1}{e}(h\nu - W) \tag{1}$$

where ϕ is the surface potential, h is the Planck constant, ν is the photon frequency, W is the work function and e is the elementary charge. A determination of the work function would be straightforward if a single UV line would be used. However, above mentioned problems with the surface electric field require the measurements with several photon energies. We used the UV lamp that mixes wavelengths according to discharge conditions and the work function was extrapolated from the measurements at the emission lines of argon (11.62 eV, 11.83 eV, 13.47 eV, 17.26 eV, and 18.72 eV) and helium (21.22 eV, 23.08 eV, 40.82 eV and 48.35 eV).

The extrapolated work function of the grain was W=(4.4 $\pm$ 0.2) eV (Fig. 1, left). To check a possible influence of the electron bombardment on the work function, the grain was bombarded for 35 hours by the 0.4 keV electron beam and the work function was determined again (Fig. 1, right). The observed change of the work function (4.5 ± 0.2) eV is within the estimated error of measurements. Moreover, the oscillations of the grain in the trap were stable and it suggests that a specific capacitance of the grain did not change in course of the experiments.

B. Mass and mass density changes in vacuum

A MF resin is known to be hydrophilic and the grains tend to absorb water from the air during their storage. In dry

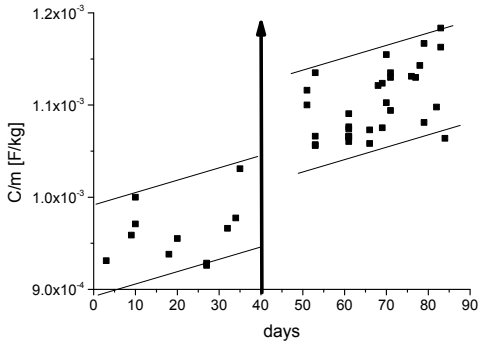


Fig. 2. An evolution of the specific capacitance of 10-micron MF grains in UHV conditions. The arrow marks the time of the grain baking at $240\,^{\circ}$C for 6 hours.

environments or at lower pressures, an evaporation of water or other volatile elements would lead to mass changes [15]. However, it is not clear whether these changes result in a decrease of the mass density and the dimensions are constant during the time or not. To clarify this point, we have revisited first systematic measurements of a evolution of the MF grain mass in UHV conditions by [14]. The authors carried out two particular experiments:

- Measurements of the mass loss rate of one weakly charged MF grain with diameter of $2.4\,\mu$m that was kept in UHV conditions (with the pressure of 10^{-6} Pa) and the specific charge was recorded for 6 days. Since an overall change of the specific charge was lower than that corresponding to one elementary charge, the whole change should be caused by the decrease of the particle mass.
- Measurements of a evolution of the specific capacitance of larger ($10\,\mu$m) grains for 40 days that were followed by 6 hours of baking at $240\,^{\circ}$C and by new measurements of the specific capacitance for next 45 days (see Fig. 2). During the observations, they used an assemblage of about 50 particles; each of them was measured only once to minimize the effects of bombardment with energetic electrons or ions. We cannot exclude an influence of these measurements on the grain parameters but this effect would be the same for each measured grain, thus the obtained trends are reliable.

Results of these two experiments can be summarized as:

(a) A monotonic increase of the specific charge with a rate of 0.011% a day that corresponds to the decrease of the mass of the grain with diameter of 2.4 μm with a rate of 1.2×10^{-18} kg/day (i.e., 0.015% a day).

(b) A monotonic increase of the specific capacitance of the 10 μm grain with a rate of about 0.09% a day during an exposition to UHV and the additional 6.3% increase during baking. The data are shown in Fig. 2 as squares, the thin straight lines show the average trend derived in two halves of the plot (prior to and after the baking), and their distance corresponds to an uncertainty of the grain diameter declared by the manufacturer. Note that Fig. 5 in [14] shows a reciprocal value of the specific capacitance in arbitrary units, thus the plot exhibits a decreasing trend of the depicted quantity, nevertheless, the initial data are the same.

The interpretation of results in terms of the mass density, volume, etc. requires additional assumptions and their application can lead to different results:

1) Assumptions of an unaffected grain diameter and measurements in (a) result in a decrease of the mass density with a rate of 0.011% a day. On the other hand, the assumption of a constant diameter (constant capacitance) and measurements in (b) provide a decrease of the mass density with a rate of 0.09% a day. An order of magnitude difference cannot be probably explained by different grain diameters used for measurements (2.4 and 10 μm, respectively) that could result in a different relative mass loss rate, thus this assumption should be abandoned.
2) The specific capacitance is inversely proportional to a product of the mass density and a square of the grain diameter. Measurements in (b) show an overall relative increase of the specific capacitance of about 8% (the effect of baking is not considered) and the assumption of the constant mass density thus requires a decrease of the grain diameter by 4%. Such a decrease is smaller than that reported by [16] in the discharge plasma but our assumption of the constant mass density would lead to the mass decrease to 88% of the original value that is probably too large if the mass loss rate determined in the measurements (a) is considered.
3) The principal assumption that the grains conserve their spherical shape is behind both scenarios discussed above. It seems to be very natural expectation but, in a light of phenomena that will be described in the further text, we should stress it out. For the sake of completeness, we are showing how the specific capacitance depends on the grain shape in Fig. 3. The plot depicts a ratio of capacitances of ellipsoid of revolution and sphere with the same volume. One can see that this ratio is always larger than unity. It means that the change of the grain shape could contribute to the observed increase of the specific capacitance.
4) Since our above considerations did not lead to a satisfactory conclusion, we suggest that the results of the experiment should be interpreted as simultaneous changes of the mass density and a volume of the grain. However, the data provided by the mentioned experiments are not sufficient for determination of a proportion of changes of these two parameters.

Nevertheless, the experiments undoubtedly confirmed a fact that MF grains loss their mass in the vacuum even if they are not affected by electron or ion bombardments, and allowed to determine the mass loss rate. The mass losses are accompanied with a decrease of grain dimensions and changes of the mass density. It would be interesting to know if the mass losses are

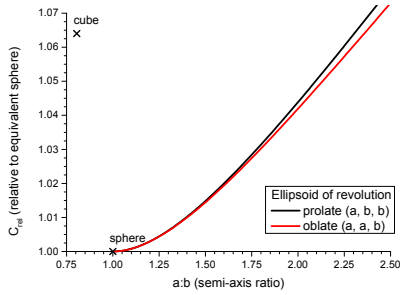


Fig. 3. A ratio of capacitances of the ellipsoid of revolution and sphere with the same volume as a function of the aspect ratio.

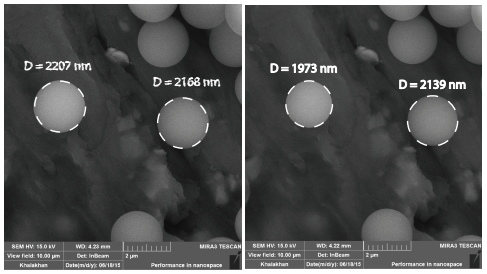


Fig. 4. Influence of the electron bombardment (the beam of 15 keV, with the intensity of 71 A/m^2) on the MF grain size. (a) prior to bombardment, (b) after 40-minute bombardment (the grain on the left side of both images was bombarded, the grain on the right side serves to a comparison).

proportional to the grain mass or to the grain surface but the experimental data are not sufficient to answer this question.

C. Evolution of the grain size under electron bombardment

The grains immersed in a plasma are bombarded by plasma particles. In a majority of applications, the plasma is non-isothermal and electrons are much hotter than the ions or neutral atoms that often follow the room temperature. Consequently, the energies of impinging electrons are larger and thus one would expect that the effects of a grain bombardment (if any) would be caused by electrons. [21], [22] studied an oxygen plasma etching and a layer deposition on the MF grain surface. They observed a grain size linearly decreasing with the time (in first 23 minutes, 8% reduction of a grain diameter was recorded). Since most experiments on dusty plasmas use argon, chemical etching is often neglected. Nevertheless, [16] observed the 6% size reduction during baking at 120 °C that is consistent with the results of [14] and about the 18% size reduction during applications of 4 h of operation of the RF discharge in argon [16]. Size changes were observed via evolving Mie scattering signal and also *ex situ* by the microscopy. These rates are much larger than those determined in UHV conditions and thus their enhancement would be probably attributed to the electron bombardment.

[23] studied the secondary electron emission from MF grains bombarded by high-energy electrons (5–10 keV) and observed a sudden change of the surface potential of the grain. Taken into account charging currents, the authors concluded that such instantaneous change cannot be caused by an increase of the grain charge and attributed it to a decrease of the grain effective radius due to a collapse. They speculated that the observed strange behavior can be caused by a grain deformation (changing shape and/or size) due to the inner electric field, resulting in a change of the electric capacitance. They observed up to about the 25% increase of the measured charge (Fig. 1, right in [23]), i.e., the capacitance (and thus a radius) should decrease by the same percentage if the surface potential and particle mass are expected to remain constant. These assumptions are well justified because the surface potential is given by a balance between incoming and outgoing electrons and ions that would not depend on the grain size or shape and the mass could not increase in the UHV conditions.

The size of small grains is usually exactly measured by electron microscope (EM) techniques. For example, Liu [12] reported transmission EM observations showing that the MF grains are smaller than specified by the manufacturer. However, the grains are bombarded by energetic electrons during EM measurements, and thus the results of such measurements should be taken with a care because the electron bombardment can change the grain diameter as we discussed above.

We have performed a series of SEM measurements in order to clarify an influence of energetic electrons on MF grain dimensions. Since the grain obtains a dose of electrons during measurements of its diameter, we have used two grains to separate effects caused by imaging from those resulting from an electron intensive bombardment. Fig. 4a shows these grains prior to the intensive electron bombardment. Their diameters are D_1 = 2207 nm and D_2 = 2168 nm, respectively, but the diameter would be 2350 nm ($\pm$ 40 nm) according to the manufacturer. The difference between measured and declared diameters cannot be caused by a decrease of the grain size in the vacuum mentioned above because the image was taken within first 20 minutes but we cannot exclude the influence of the electron beam.

After taking this image, the grain on the left-hand side was bombarded by the high-intensity 15-keV electron beam (its average current density was $\approx$ 71 A/m^2), the grain on the right-hand side was left unaffected for a comparison. Both grains obtained some electron dose during the SEM imaging but this dose was the same for both grains. SEM images were taken every 5 minutes of the electron bombardment. During 40 minutes of these operations, the left grain shrinks from 2207 nm to 1973 nm (11%), whereas the right grain shrinks from 2168 nm to 2139 nm (1.4%) only. The final image is shown in Fig. 4b.

Fig. 5 illustrates that the shrinking was approximately saturated after 30 minutes of the electron bombardment. Although the exact mechanism is unknown, it is evident that the electron bombardment affects the grain size. The black crosses show the results of measurements described above, other symbols stand for analogous measurements carried on different grains attached to Al and carbon substrates. The profiles in Fig. 5 confirm a decrease of the grain size under electron bombardments but the reduction rates are different.

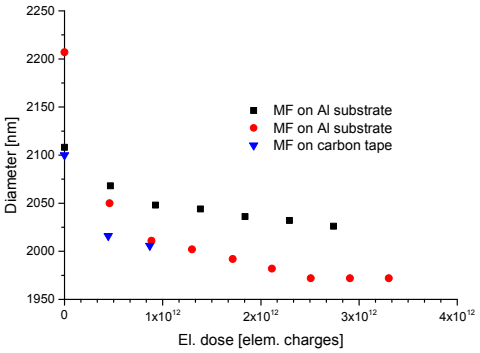
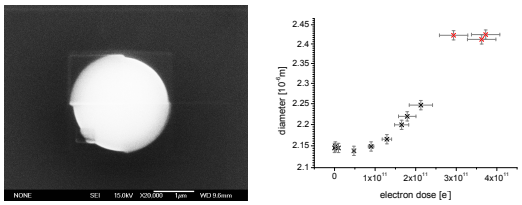


Fig. 5. A change of the MF grain diameter as a function of the electron dose (each data point was obtained after 5 minutes of the 15 keV electron bombardment). Two grains (red and black) were lying on the Al substrate and one grain (blue triangles) was attached to the carbon tape.



(a) (b)

Fig. 6. The MF grain bombarded by 15 keV electrons. (a) SEM image — upper left quarter of the grain was bombarded by electrons, upper right quarter is intact; (b) A diameter of the MF grain as a function of the electron dose (adopted from [24]).

In order to demonstrate a complex character of the interaction of MF grains with the electron beam, Fig. 6 shows the results of Pavlu et al. [24]. This experiment used another SEM facility allowing much higher beam intensities. The black points in Fig. 6b were obtained in a similar regime as the points in Fig. 5. We can see a small initial decrease of the grain diameter. The decreasing trend is consistent with Fig. 5 but this decrease is followed by a rapid increase for higher electron doses. Since this result was surprising, the authors have scanned only left upper quarter of the grain as it is shown in Fig. 6a and the corresponding red crosses in Fig. 6b belong to these scans. It can be seen that the increase of the grain size is strictly localized to the part that was affected by the electron beam.

D. Surface coating and its thickness

MF grains are offered in metal-coated versions (Au, Ni, Cu, Pt, ...) that would combine advantages of the low mass and metal surface. Two major problems concerning the metal layer were identified: (1) it is easily peeled off by energetic electrons (it can be caused by shrinking of the MF grain inside the metal crust as Fig. 7 illustrates using grains covered by the AU layer), and (2) the layer thickness does not meet expected values as it was shown by [25]. The authors adapted the secondary electron emission model to allow computations of the secondary emission from layered grains. They used MF spheres covered by a nickel layer as an example and a comparison with measured profiles of the secondary emission yield revealed that (unlike producer's expectations of the 100–200 nm thickness [26]), the thickness of the real Ni coating cannot exceed 20 nm. This result of computer simulations was confirmed by precise measurements of the mass distribution [25].

The experiments with Ni coated grains in SEM revealed another interesting peculiarity. Fig. 8 shows the grain fixed to a carbon tape prior to and after the bombardment by the 15-keV electron beam. The grain in the left panel obtained only a minimum dose of electrons needed for a creation of its image. The image demonstrates that the surface layer is not smooth and it is even not continuous. It is in an agreement with a small layer thickness discussed above. The middle panel presents a top view of the same grain after 30 minutes of the following electron bombardment. The grain radius is marked within the panel but one can note about a 50% particle increase even without such a tool. However, the grain is not only larger but its surface is very smooth. Moreover, the grain enlargement is not a simple inflation but it is connected with the change of the grain shape as a side view in the right panel shows.

An analysis of this and many other photos suggests that the grain is covered by a thick layer of a another material. To confirm this hypothesis, we used the FIB facility and cut the grain in half. The SEM photo of this cut is depicted in Fig. 9. Although the contrast of this image is not excellent, the important features can be identified. The dark core presents the MF grain with nearly unaffected size (in the horizontal direction) of $L1 = 2165$ nm. Its size in the vertical direction is probably smaller, $L1 = 1869$ nm. The grain core is bounded by a light thin layer of the original Ni coat; nevertheless, this coat seems to be removed at the top part of the grain. The whole grain is covered with a thick layer of unknown material but its outer boundary is rather diffusive in this photo.

A grow of a such layer was observed repeatedly for Ni covered MF grains attached to the carbon tape but we did not find this effect either for pure MF grains on carbon tape or for Ni covered grains fixed to an Al surface. Our interpretation of this observation is that the electron beam releases carbon atoms from the surface of the carbon tape and (probably) a volatile component of the MF resin. The catalytic properties of the Ni coat thus lead to synthesis of a new material that builds the layer on the grain surface.

E. Sputtering

Impacts of energetic ions lead to sputtering of a dust grain material. It is well known that the sputtering yield depends on the energy and mass of the ions and the direction of the ion velocity with respect to surface. Angular dependence of the sputtering yield leads to a modification of the shape of the originally spherical grain attached to a surface [27]. Also the surface morphology can change under the ion bombardment and surface ripples can be formed (e.g., [28], [29]).

We used 30 keV Ga ions from the focused ion beam (FIB) integrated into SEM to sputter MF grains. A sequence of photos of one grain sputtered with the beam intensity of

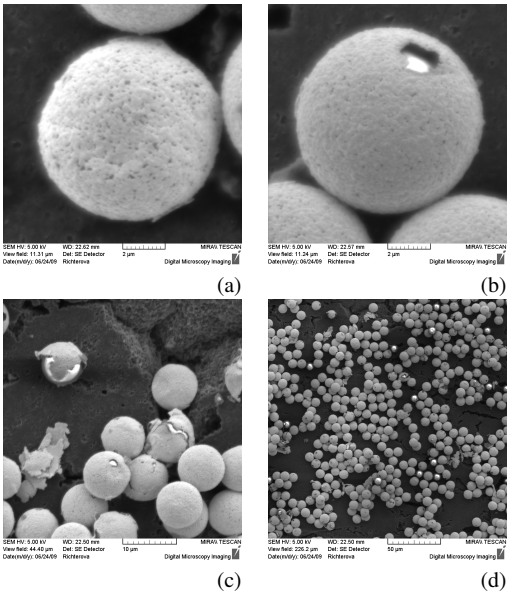


Fig. 7. SEM images of Au-coated MF grains: (a) a grain prior to the bombardment; (b) a detail of one grain after bombardment by 15-keV electrons (note that the Au layer is detached from the grain); (c) a destruction of the surface layer (it is rather common); and (d) a portion of grains is completely peeled off due to the electron bombardment.

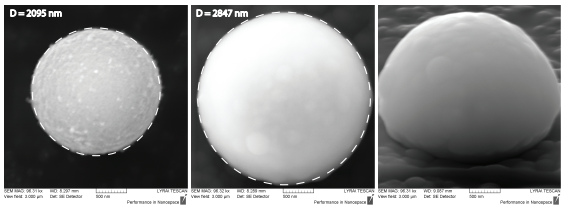


Fig. 8. An evolution of the grain size and shape during the bombardment by the 15-keV electron beam. The used sample: MF grain covered by Ni and fixed to a carbon tape for SEM diagnostics.

1 A/m^2 is shown in Fig. 10. A change of the grain overall shape seen in Fig. 10e is consistent with observations made on glass grains by Vysinka [27] and can be attributed to the angular dependence of the sputtering yield. However, this way of sputtering is not typical as Fig. 10f demonstrates. Moreover, the surface of the grain becomes rough with many shallow depressions even in early stages of sputtering (Fig. 10c).

Larger beam intensities amplify this effect as we show in Fig. 11 that presents the 2.4 μm MF grain prior to (a) and after (b) ion sputtering. The grain material is expected to be homogenous but holes through the grain are milled at some points. A creation of holes is probably connected with a strong angular dependence of the sputtering yield that can be inferred from the slope of the flanks of the sputtered particle in Fig. 11b. This effect seems to be more pronounced at larger intensities of the ion beam but we did not observe such behavior on other materials like SiO_2 (Fig. 11c) and glassy carbon (Fig. 11d).

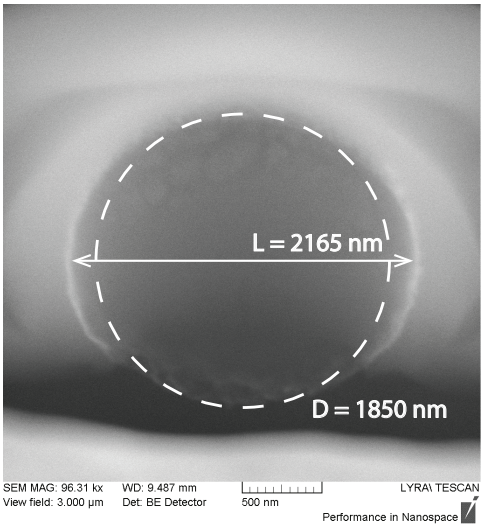


Fig. 9. The MF grain covered by Ni and fixed to a carbon tape after cutting in half by FIB. See the text for the detail explanation.

IV. Discussion

Despite many believes, the MF microspheres are not so stable as it is thought. They decrease their mass and diameter in UHV conditions, at raised temperatures, and under the influence of the electron beam with a very low intensity and energy, probably due to heating and evaporation of some water or other volatile components contained in the grain. The losses of the mass are as large as 1.2×10^{-18} kg/day for 2.4-micrometer grains. The spherical shape of the grain is probably not affected by these agents. On the other hand, larger energies of beam electrons result to notable, and sometimes abrupt changes of the grain dimensions. Its bombardment by energetic electrons usually leads to high surface potentials and it is not clear, whether the main cause of dimension changes is a destruction of the internal structure of the grains or the large electric field at the surface. We think that the small doses of electrons are probably sufficient to destroy the internal molecular structure and it results to the initial decrease of the grain diameter, whereas the large electric field causes a consecutive inflation of the grain.

However, in a view of new experiments (Figs. 8 and 9), we cannot exclude another interpretation of the observed grain growth that is related to the SEM experiments. The pressure in SEM facilities is usually rather moderate and a residual gas can contain different hydrocarbons from the pumping system. The growth of the grain (or its part, Fig. 6) could be thus caused by the synthesis of a layer of some material at the affected part of the grain surface. If this interpretation of the grain growth in Fig. 6 is correct, a role of energetic electrons in this synthesis is crucial because the growth is limited to the part of the grain surface that is affected by the electron beam.

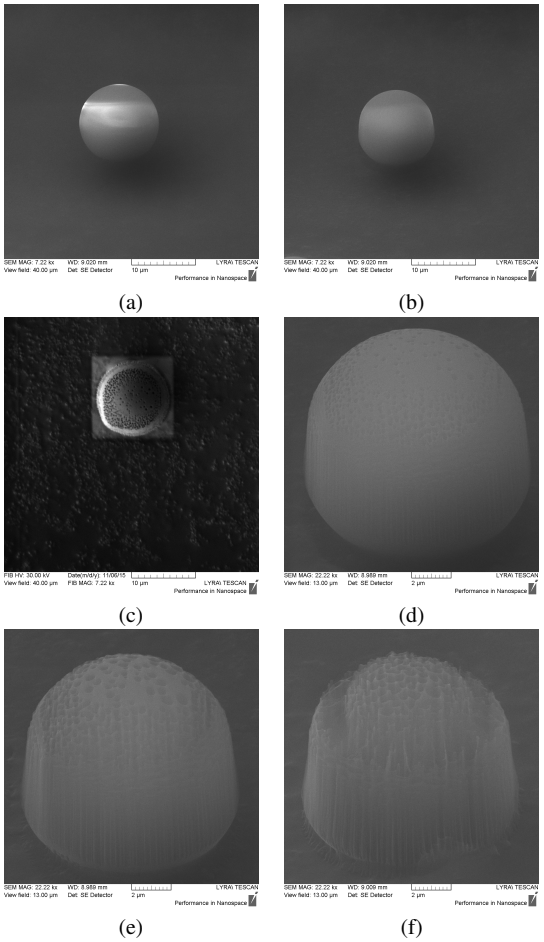


Fig. 10. Sputtering of a spherical MF grain by 30-keV Ga ions (beam intensity: 1.0 A/m^2): (a) prior to sputtering; (b) after 60 s of sputtering; (c) after 150 s — the view from top by FIB; (d) a detail of (c) by the SEM image; (e) after 300 s of sputtering; and (f) another grain sputtered for 540 s.

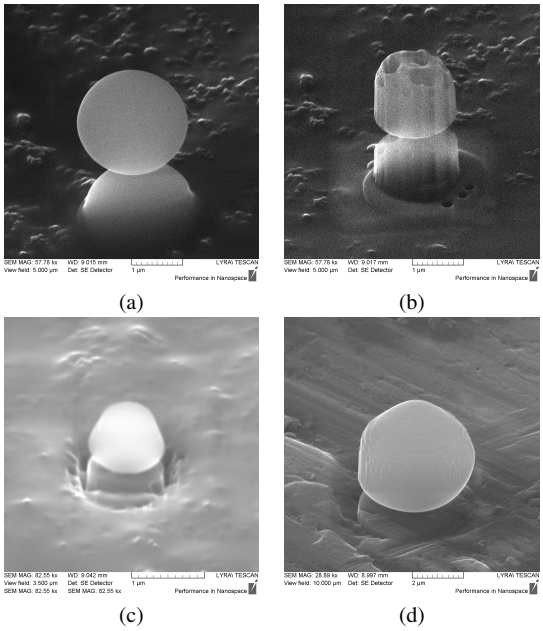


Fig. 11. Sputtering of spherical grains by 30-keV Ga ions: (a) the MF grain prior to; and (b) after 10 s of sputtering (ion beam intensity: 24.3 A/m^2); (c) the SiO_2 grain (ion beam intensity: 0.9 A/m^2, sputtering time: 90 s); and (d) the glassy carbon grain (8.8 A/m^2, 180 s).

We assume that the observed peeling off metallic surface layers that cover the MF grains is connected with the changes of dimensions of the grain inside the layer due to evaporation of volatile components in vacuum that can be amplified by energetic electrons that penetrated through the surface layer. This penetration is rather probable because the surface layers were found to be much thinner than the manufacturer declares.

We have determined the MF work function (4.5 eV) and its value was not affected by the bombardment with low-energy electrons (0.4 keV). The changes of the work function observed in experiments of Pavlu et al. [24] were most probably caused by the aforementioned effects of the large electric field at the grain surface and bombardment by energetic electrons.

We did not determine the sputtering yield but a comparison of photos of the MF grain and the grains from other materials shows that it would be comparable with the sputtering yield measured on SiO_2 spheres of similar diameter [27] but an overall shape of partially sputtered MF grains suggests that the angular dependence of the MF resin sputtering yield would be stronger. Sputtering is not homogenous; it forms grains to a cylindrical shape with milled holes throughout the entire volume. Such effect is observed even for large grains. Although it is hard to estimate the effect of the low-energy ion bombardment (e.g., in the discharge plasma), some peculiarities can be expected.

V. Conclusion

Our study and many already published reports have shown that the MF microspheres cannot to be recommended for applications where a stability of grain parameters is essential. SiO_2 grains that exhibit similar properties could be considered as a more suitable solution for dusty plasma experiments.

Acknowledgment

The authors appreciate help of J. Novakova and I. Khalakhan with SEM imaging and would like to to express their thanks to Prof. D. Vítek for fruitful discussions.

References

[1] G. Morfill, H. Thomas, B. Annaratone, A. Ivlev, R. Quinn, A. Nefedov, V. Fortov, and P.-N. Team, "Complex plasmas under microgravity conditions: First results from PKE-Nefedov," in *Dusty Plasmas in the New Millennium*, ser. AIP Conference Proceedings, R. Bharuthram, M. A. Hellberg, P. K. Shukla, and F. Verheest, Eds., vol. 649. Melville, New York: American Institute of Physics, 2002, pp. 91–109.

[2] A. Nefedov, G. Morfill, V. Fortov, H. Thomas, H. Rothermel, T. Hagl, A. Ivlev, M. Zuzic, B. Klumov, A. Lipaev, V. Molotkov, O. Petrov, Y. Gidzenko, S. Krikalev, W. Shepherd, A. Ivanov, M. Roth, H. Binnenbruck, J. Goree, and Y. Semenov, "PKE-Nefedov: plasma crystal experiments on the International Space Station," *New J. Phys.*, vol. 5, Apr. 2003.

[3] R. Seurig, G. Morfill, V. Fortov, and P. Hofmann, "Complex plasma research on ISS PKE-Nefedov, PK-3 Plus, PK-4, and impact laboratory," *Acta Astronaut.*, vol. 65, no. 5-6, pp. 651–656, 2009.

[4] H. Kersten, H. Deutsch, M. Otte, G. Swinkels, and G. Kroesen, "Microdisperse particles as probes for plasma surface interaction," *Thin Solid Films*, vol. 377-378, pp. 530–536, 2000.

[5] P. Hartmann, A. Z. Kovács, J. C. Reyes, L. S. Matthews, and T. W. Hyde, "Dust as probe for horizontal field distribution in low pressure gas discharges," *Plasma Sources Sci. T.*, vol. 23, no. 4, p. 045008, 2014. [Online]. Available: http://stacks.iop.org/0963-0252/23/i=4/a=045008

[6] M. Dropmann, R. Laufer, G. Herdrich, L. S. Matthews, and T. W. Hyde, "Analysis of magnetic field plasma interactions using microparticles as probes," *Phys. Rev. E*, vol. 92, p. 023107, Aug 2015.

[7] M. Puttscher and A. Melzer, "Dust particles under the influence of crossed electric and magnetic fields in the sheath of an rf discharge," *Phys. Plasmas*, vol. 21, no. 12, p. 123704, 2014.

[8] V. Land, A. Douglass, K. Qiao, L. Matthews, and T. Hyde, "The effect of dust charge variation, due to ion flow and electron depletion, on dust levitation," in *Dusty/Complex Plasmas: Basic and Interdisciplinary Research*, ser. AIP Conference Proceedings, V. Y. Nosenko, P. K. Shukla, M. H. Thoma, and H. M. Thomas, Eds., vol. 1397, no. 1. Melville, New York: American Institute of Physics, 2011, pp. 98–103.

[9] V. Land, A. Douglass, K. Qiao, Z. Zhang, L. S. Matthews, and T. Hyde, "Glow and dust in plasma boundaries," *IEEE Trans. Plasma Sci.*, vol. 41, no. 4, pp. 799–803, April 2013.

[10] A. Douglass, V. Land, K. Qiao, L. Matthews, and T. Hyde, "Determination of the levitation limits of dust particles within the sheath in complex plasma experiments," *Phys. Plasmas*, vol. 19, no. 1, p. 013707, 2012.

[11] M. Schwabe, S. Zhdanov, C. Räth, D. B. Graves, H. M. Thomas, and G. E. Morfill, "Collective effects in vortex movements in complex plasmas," *Phys. Rev. Lett.*, vol. 112, p. 115002, Mar 2014.

[12] B. Liu, J. Goree, V. Nosenko, and L. Boufendi, "Radiation pressure and gas drag forces on a melamine-formaldehyde microsphere in a dusty plasma," *Phys. Plasmas*, vol. 10, no. 1, pp. 9–20, 2003.

[13] X. Wang, M. Horányi, and S. Robertson, "Experiments on dust transport in plasma to investigate the origin of the lunar horizon glow," *J. Geophys. Res.*, vol. 114, no. A5, p. A05103, 2009.

[14] J. Pavlů, A. Velyhan, I. Richterová, Z. Němeček, J. Šafránková, I. Čermák, and P. Žilavý, "Mass-loss rate for MF resin microspheres," *IEEE Trans. Plasma Sci.*, vol. 32, no. 2, pp. 704–708, 2004.

[15] J. Carstensen, H. Jung, F. Greiner, and A. Piel, "Mass changes of microparticles in a plasma observed by a phase-resolved resonance method," *Phys. Plasmas*, vol. 18, no. 3, 2011.

[16] C. Killer, M. Mulsow, and A. Melzer, "Spatio-temporal evolution of the dust particle size distribution in dusty argon rf plasmas," *Plasma Sources Sci. T.*, vol. 24, no. 2, p. 025029, 2015.

[17] W. Paul and H. Steinwedel, "Apparatus for separating charged particles of different specific charges," German Patent, Patent 944,900, 1956.

[18] M. Beranek, I. Cermak, Z. Nemecek, J. Safrankova, M. Jerab, and J. Pavlu, "Linear trap with three orthogonal quadrupole fields for dust charging experiments," *Rev. Sci. Instrum.*, vol. 83, no. 11, p. 115109, 2012.

[19] J. Pavlů, I. Richterová, Z. Němeček, J. Šafránková, and I. Čermák, "Interaction between single dust grains and ions or electrons: laboratory measurements and their consequences for the dust dynamics," *Faraday Discuss.*, vol. 137, pp. 139–155, 2008.

[20] L. Nouzák, I. Richterová, J. Pavlů, Z. Němeček, and J. Šafránková, "Investigations of photoemission from lunar dust simulant," *IEEE Trans. Plasma Sci.*, vol. 44, no. 4, pp. 512–518, 2016.

[21] G. Swinkels, E. Stoffels, W. Stoffels, N. Simons, G. Kroesen, and F. de Hoog, "Treatment of dust particles in an RF plasma monitored by Mie scattering rotating compensator ellipsometry," *Pure Appl. Chem.*, vol. 70, no. 6, pp. 1151–1156, Jun. 1998.

[22] W. W. Stoffels, E. Stoffels, G. H. P. M. Swinkels, M. Boufnichel, and G. M. W. Kroesen, "Etching a single micrometer-size particle in a plasma," *Phys. Rev. E*, vol. 59, pp. 2302–2304, Feb 1999.

[23] I. Richterová, J. Pavlů, Z. Němeček, J. Šafránková, and M. Jeřáb, "Electric field influence on secondary emission," in *New Vistas in Physics of Dusty Plasmas*, ser. AIP Conference Proceedings, L. Boufendi, M. Mikikian, and P. K. Shukla, Eds., vol. 799. Melville, New York: American Institute of Physics, 2005, pp. 395–398.

[24] J. Pavlů, I. Richterová, D. Fujita, J. Šafránková, and Z. Němeček, "Changes of dust grain properties under particle bombardment," in *Multifacets of Dusty Plasmas*, ser. AIP Conference Proceedings, J. T. Mendonça, D. P. Resendesm, and P. K. Shukla, Eds., vol. 1041. Melville, New York: American Institute of Physics, 2008, pp. 299–300.

[25] I. Richterová, J. Pavlů, Z. Němeček, J. Šafránková, and P. Žilavý, "Secondary emission from dust grains with a surface layer: Comparison between experimental and model results," *Adv. Sp. Res.*, vol. 38, no. 11, pp. 2551–2557, 2006.

[26] H. Fiedler, private communication, Volmerstr. 9A, H.3.51, D-12489 Berlin, Germany, 2002/2003.

[27] M. Vyšinka, Z. Němeček, J. Šafránková, J. Pavlů, J. Vaverka, and J. Lavková, "Sputtering of spherical sio2 samples," *IEEE Trans. Plasma Sci.*, vol. 44, no. 6, pp. 1036–1044, 2016.

[28] G. M. McCracken, "The behaviour of surfaces under ion bombardment," *Rep. Prog. Phys.*, vol. 38, no. 2, p. 241, 1975.

[29] P. F. A. Alkemade, "Propulsion of ripples on glass by ion bombardment," *Phys. Rev. Lett.*, vol. 96, p. 107602, Mar 2006.

Nouzák et al. [2017]

ARTICLE IN PRESS

Planetary and Space Science xxx (2017) 1–7

Contents lists available at ScienceDirect

Planetary and Space Science

journal homepage: www.elsevier.com/locate/pss

Laboratory modeling of dust impact detection by the Cassini spacecraft

L. Nouzák [a], S. Hsu [b], D. Malaspina [b], F.M. Thayer [b], S.-Y. Ye [c], J. Pavlů [a], Z. Němeček [a,*], J. Šafránková [a], Z. Sternovsky [b,d]

[a] Department of Surface and Plasma Science, Charles University, Prague, 18000, Czech Republic
[b] Laboratory for Atmospheric and Space Physics, University of Colorado, Boulder, CO 80303, USA
[c] Physics and Astronomy Department, University of Iowa, Iowa City, IA 52242, USA
[d] Smead Aerospace Engineering Sciences Department, University of Colorado, Boulder, CO 80309, USA

ARTICLE INFO

Keywords:
Dust impacts
Monopole and dipole antennas
Plasma–surface interaction

ABSTRACT

The paper presents laboratory investigations of the response of a scaled down model of the Cassini spacecraft to impacts of submicron iron grains accelerated to velocities 5–25 km/s. The aim of the study is to help in a detailed analysis and interpretation of signals provided by the RPWS (Radio Wave Plasma Science) instrument that were attributed to dust impacts onto RPWS antennas or spacecraft body. The paper describes the experimental set-up, discusses its limitations, and presents the first results. Both monopole and dipole antenna configurations are investigated. We demonstrate that the amplitude and polarity of the impulse signals recorded by antenna amplifiers depend on the voltages applied onto the antennas or the spacecraft body and briefly introduce the mechanism leading to the signal generation. The experimental results support the recent suggestion by Ye et al. (2016) that antennas operated in a dipole mode are greatly insensitive to dust impacts on the spacecraft body. The pre-peak phenomenon, commonly observed in space, is also reproduced in the measurements and explained as the induced charge on the antenna from the impact plasma cloud that is becoming non-neutral due to the escape of the faster electrons.

1. Introduction

Voltage spikes associated with the impact of high velocity dust particles on a spacecraft have been observed by electric field sensors on several space missions. Voyager and Cassini observed such spikes in conjunction with passage through the rings of Saturn (Gurnett et al., 1983; Wang et al., 2006) and in connection with Jovian dust streams (Zook et al., 1996; Meyer-Vernet et al., 2009a). A survey of the Deep Space 1 and Vega spacecraft data revealed voltage spikes recorded in Borrelly and Halley comet dust tails (Tsurutani et al., 2003; Laakso et al., 1989) and these spikes were attributed to the dust impacts. STEREO and Wind electric field instruments observed dust impact signatures at 1 AU associated with interplanetary and interstellar dust (St Cyr et al., 2009; Meyer-Vernet et al., 2009a; Zaslavsky et al., 2012).

Hypervelocity impacts of dust particles on the antenna and/or spacecraft (SC) surfaces generate expanding plasma clouds that are (partially) recollected to generate transient voltage signals detectable by antenna instruments, such as RPWS (Radio Plasma Wave Science) onboard the Cassini spacecraft (Scarf et al., 1982; Aubier et al., 1983; Wang et al., 2006; Zaslavsky et al., 2012; Malaspina et al., 2014; Ye et al., 2014a, 2016; Andersson et al., 2015; Kellogg et al., 2016; Collette et al., 2016). Dust detection by RPWS is only very weakly limited by the spacecraft attitude, thus RPWS can provide continuous measurements with a good temporal/spatial coverage. The antennas are connected to a set of receivers, yielding two types of measurements: power spectra and waveforms (Gurnett et al., 2004). Individual dust impact pulses are best recognized in the waveforms, while the power spectrum has been used to estimate the average size/mass distribution in the regions with high dust impact rates.

The antenna signal is generated by a charge recollection from the impact plasma cloud and the polarity and the amplitude of the detected signal are determined by: (1) the total generated impact charge which depends on the dust mass and the impact speed, (2) the surface potential of the SC/antenna that controls the fraction of the recollected charge, (3) the measurement mode (dipole/monopole), and (4) the impact location (material properties, possible geometry effects). For example, an impact on a negatively charged spacecraft body (the usual case near the Enceladus orbit) results in a negative voltage spike in the monopole mode, since the SC charges temporarily more positively, and the monopole antenna measures the voltage difference relative to the SC. On the other

* Corresponding author. V Holesovickach 2, 180 00 Prague 8, Czech Republic.
E-mail address: zdenek.nemecek@mff.cuni.cz (Z. Němeček).

https://doi.org/10.1016/j.pss.2017.11.014
Received 1 August 2017; Received in revised form 14 November 2017; Accepted 16 November 2017
Available online xxxx
0032-0633/© 2017 Elsevier Ltd. All rights reserved.

Please cite this article in press as: Nouzák, L., et al., Laboratory modeling of dust impact detection by the Cassini spacecraft, Planetary and Space Science (2017), https://doi.org/10.1016/j.pss.2017.11.014

hand, the difference between potentials of two identical antenna booms is measured in the dipole mode and the impact on the spacecraft body would not generate a measurable signal in this configuration.

Recently, synergetic works have started to improve the understanding of the detection mechanism(s) as well as the RPWS data interpretation. Cassini measurements provide an ideal dataset for this purpose because they allow to a comparison of RPWS measurements in dust-rich environments with the dedicated and calibrated Cosmic Dust Analyzer (CDA) data (Ye et al., 2014b). Additionally, the involvement of the laboratory experiments serves for checking the existing data analysis procedures but also provides a mean to systematically understand the impact processes and to quantify the antenna dust detection (Collette et al., 2015, 2016). Previous works indicate that the RPWS measurements are semi-quantitatively consistent with CDA data during E ring-plane crossings and Enceladus flybys (Kurth et al., 2006; Ye et al., 2014a). However, studies of the RPWS data revealed tiny features of the detection mechanisms which, through careful examination, could significantly improve the accuracy and precision of the data interpretation and the usefulness of antenna dust detection at the Saturn's E ring and beyond.

The impact charge yield has been measured by recent laboratory experiments where iron projectiles were accelerated to tens of km/s before impacting on targets of common spacecraft surface materials in a vacuum chamber (Mocker et al., 2011; Collette et al., 2014). The response of a simulated spacecraft and monopole antenna to dust impacts has also been studied with the same accelerator facility (Collette et al., 2015) and we will return to this experimental setup in the next section. Tsintikidis et al. (1994) noted that the dust impact signals observed by Voyager dipole electric antennas are significantly lower than those observed by monopole antennas, and the difference has been attributed to a low sensitivity of dipole antennas to impacts on the spacecraft, yielding smaller pulses for numerous events. However, no dipole experiment has been carried out in a laboratory so far.

Meyer-Vernet et al. (2009b, 2014) compared the dust signals observed in monopole and dipole modes and concluded that the monopole antennas generally detect much greater signals than dipole antenna, because most of the impact charges are recollected by the spacecraft body. However, both these studies compared the frequency spectra of the signal and not the waveforms captured in these two antenna modes.

This paper is devoted to the experimental investigation of the differences between pulses registered in dipole and monopole antenna configurations that were induced by impacts of the dust grains onto different parts of the spacecraft including the antennas. The aim of the work is to confirm a working hypothesis that only impacts directly on the corresponding antennas are registered in the dipole mode. Elucidation of the differences between these two modes is important because, for example, Meyer-Vernet et al. (2014) attributed the disagreement of Wind and Stereo nanodust observations to the fact that Wind uses the dipole configuration of antennas. Our experiment uses iron dust projectiles from the 3 MV linear electrostatic dust accelerator at the University of Colorado, Institute for Modeling Plasma, Atmospheres, and Cosmic Dust (Shu et al., 2012) focused onto small tungsten plates mounted on the novel Cassini spacecraft model. The response of antenna amplifiers to each dust impact is recorded. It is important that the same dust impact is recorded by dipole and monopole antennas simultaneously, and thus the differences in the detection efficiency can be quantified. The results of the present study would be especially useful for an analysis of the last stages of Cassini operations because the spacecraft will operate in the ring regions and numerous dust impacts can be expected.

2. Experimental setup

The Cassini RPWS instrument consists of three nearly orthogonal, 10 m long, and 2.5 cm in diameter electric field antennas (Gurnett, 1998; Gurnett et al., 2004) marked as E_U, E_V, and E_W. The antenna elements are made of beryllium–copper and covered with silver. The E_U and E_V antennas are usually connected together in a dipole configuration, while E_W is typically operated in a monopole mode, measuring thus the antenna voltage relative to the SC body.

The first laboratory investigation of the response of antennas to dust impacts was performed by Collette et al. (2015). A simplified setup was used, consisting of aluminum plate to represent the spacecraft and an aluminum tube as the monopole antenna with independent bias voltages for each. Submicron-sized iron grains with velocities in the range of 8–12 km/s were shot onto a tungsten target mounted on the aluminum plate. The performed studies identified three distinct signal generation mechanisms: SC charging, antenna charging and induced signal generation from the space charge of the impact plasma. The study also clearly indicated that the absolute and relative bias potentials applied on the SC and the antennas affect polarities and amplitudes of the detected signals.

In order to eliminate potential effects caused by the spacecraft body geometry when comparing the simulated RPWS response to dust impacts onto monopole and dipole antennas, a new simplified and scaled down model (approximately 1:20) of the Cassini spacecraft was designed and fabricated. Fig. 1 (left) shows the main elements of the model that consists of the cylindrical spacecraft body, the High Gain Antenna (HGA) dish on the top and the protruding magnetometer boom. The antennas are electrically isolated from each other and from the SC body. They are mounted on a small block shown in the insert. The body is machined out of aluminum, while the antennas are made out of 1.6 mm diameter, 50 cm long stainless steel rods. The size of the model was chosen to fit without a mechanical interference into the available vacuum chamber that is about 1 m in diameter and 1.5 m long (Fig. 1, right). Both the body and the antennas are coated with graphite to ensure an electrically uniform surface (Robertson et al., 2004). There are ten designated impact locations represented by small 1×3 cm^2 tungsten foils attached conductively to the spacecraft body or antennas. The experiment uses three impact locations mounted approximately at the middle of the E_U and E_W antennas and on the top of the HGA. All measurements are performed using normal impact incidence. The benefits of using tungsten targets for the impact experiments include handling and cleaning, and a more direct comparability of measurements in different locations and with previous investigations (e.g., Collette et al., 2015). Moreover, tungsten offers a high impact yield, thus a better signal-to-noise ratio can be expected.

The model is equipped with the electronics shown in Fig. 2 for both the dipole (antennas E_U and E_V) and monopole (E_W) configurations. There are several features worth mentioning: First, all three antennas and the SC body can be independently biased through a large 10 MΩ resistor. Each element is connected to a voltage follower through AC-coupling. Differential amplifiers are then used to measure the voltage difference between the elements in both dipole and monopole configurations. The dashed lines schematically show the capacitances of the antennas (C_{ANT}) and spacecraft (C_{SC}) that are inseparable parts of the measuring circuitry.

In comparison to previous laboratory measurements used in Collette et al. (2015, 2016), this novel setup allows us to study a process of charge recollection in both monopole and dipole antenna geometries, thus more relevant to the real Cassini spacecraft. The signals from both antennas can be recorded simultaneously and, moreover, an influence of dust impact locations on produced signals can be studied. The circuits have a bandwidth of 50 Hz–400 kHz and a voltage gain of 100 and electronic boards are housed inside the cylindrical body of the Cassini model.

The interpretation of measurements is based on the present knowledge on a generation of the electric signals at the antennas. The charge collected on the antenna element and/or on the SC body is discharged through the parallel combination of two 10 MΩ resistors. The time constant of the discharge is then $\tau = RC_i$, where $R = 5$ MΩ and i stands for U, V, W or SC. There are two important implications of this concept. One is that the capacitances of the elements (that cannot be measured directly) can be determined from the time constant of the discharging. The second advantage is that the signal from charge collection can be clearly identified and separated from noise or induced spikes.

It is added for completeness that two similar sets of antennas along with their mounting blocks were manufactured. Guard cylinders were

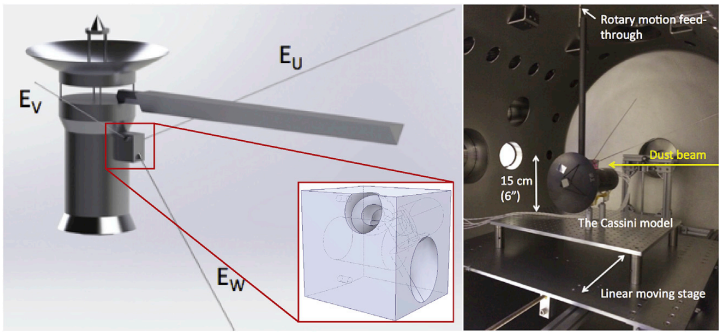


Fig. 1. (left) The CAD design of the Cassini spacecraft model, and (right) the photo of the fabricated model installed in the experimental vacuum chamber which is equipped with a linear moving stage and rotary motion feed-through for changing the impact position. The sensitive front-end electronics is housed inside the cylindrical SC body. The yellow arrow indicates the dust beam entering the chamber. In the left panel, the insert shows the holder of antennas. (For interpretation of the references to colour in this figure legend, the reader is referred to the web version of this article.)

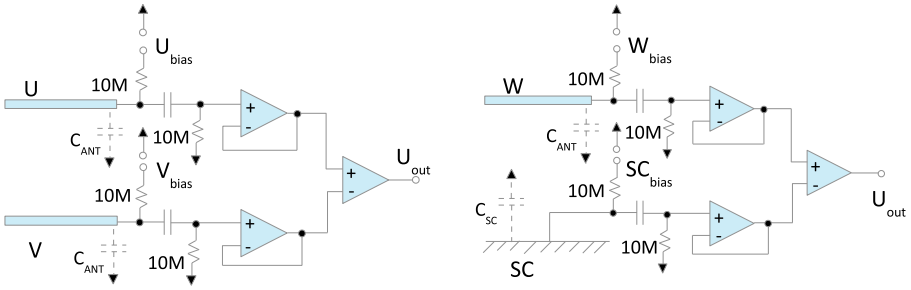


Fig. 2. The simplified schematics of the front-end electronics used for the laboratory measurements. See text for details.

inserted between the antennas and the mounting block in one of them to eliminate (or significantly reduce) any capacitive coupling between the antennas and spacecraft. However, the data taken by these two different antenna designs did not show qualitative differences.

The laboratory measurements were performed using the dust accelerator facility operated at the University of Colorado (Shu et al., 2012). The iron dust sample, loaded into a small reservoir, is electrostatically agitated and particles acquiring large positive charges from a contact with a highly biased sharp needle are subsequently accelerated by a 2.2 MV potential drop. The dust velocities 4–25 km/s were used for the experiments described here with the particles aimed onto one of the tungsten foils attached to the model. The Cassini model was mounted inside a large vacuum chamber evacuated by the turbo-molecular pump to about 10^{-6} Torr. A linear moving stage and a rotary motion feed-through are used to reposition the model without braking vacuum. The power supplies, including those providing the electric bias voltages and the data acquisition electronics are located outside the chamber. A fast digital storage scope is used for data acquisition. The accelerator diagnostics provide the velocity, charge, and energy of the accelerated dust grains; their mass is computed from the velocity and energy of a grain.

Fig. 3 shows the masses (corresponding diameters, *d*) and velocities of the dust grains used in the present analysis. The red and blue colors denote grains used in the first and second measuring campaigns, respectively. The difference is in the design of antenna holders – the antennas were double shielded in the holder used in the second campaign in order to reduce a possible capacitive coupling between antennas. It should be kept in mind that the dust grains gain the energy given by the accelerator voltage and the grain charge. Since the charges of the grains are similar (typically units to tens of fC), there is about a power law dependence between the velocities and their masses, and smaller particles can be accelerated to higher velocities.

In Fig. 3, the black vertical lines show the approximate limits that were set for the accelerator velocity filters. The green line stands for the noise floor of the charge sensitive amplifier (CSA) that provides triggering impulses. The orange line depicts the limit determined under an assumption of the spherical grains and ion field emission threshold of 10^9 V/m (Pavlů et al., 2008) and the magenta line shows the expected relation of the dust grain mass and velocity if all grains will be charged to

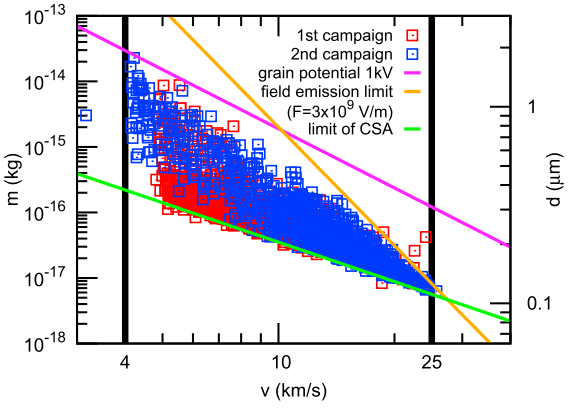


Fig. 3. The mass-velocity distribution of the iron particles used for the measurements.

1 kV at the accelerator input. As it can be seen, the dust grain parameters fit into the area given by aforementioned limits.

3. Experimental results

This section describes the details of the measurements performed in two experimental campaigns taking data sets with similar goals. Although we tried to simulate real conditions, there are several differences between Cassini observations of the dust impacts and our laboratory experiment. Whereas the whole RPWS antenna surface acts as a sensor element and any part of it can be hit by the dust, only a small target is bombarded in the experiment. Moreover, the spacecraft is immersed into a plasma and different parts (spacecraft body and antennas) are charged due to the interaction with plasma particles and UV radiation. We can simulate this charging by an application of DC bias voltages onto different parts of the Cassini model with respect to the grounded vacuum chamber.

The collection of charge from the impact generated plasma cloud depends on the applied bias voltages. To decrease a possible degree of freedom, we kept the antennas and spacecraft on the same potential and a bias voltage was applied between the spacecraft and vacuum chamber. In the first run, one dipole antenna boom with constant bias voltages of $-25, -10, -5, 0, +5, +10$, and $+25$ V was bombarded. The changes of the amplifier response to the dust impacts can be seen in Fig. 4 for positive bias voltages. The measured signals for negative biases resemble those recorded for the unbiased spacecraft.

Two distinct features can be observed for the data taken for positive applied voltages ($+5$ V and above). One is the sharp positive-going peak that is followed by a slower negative-going signal. The latter is from the net collection of electrons from the impact plasma by the applied positive bias voltage. The fact that the exponential decay of this signal corresponds to the characteristic RC time constant of the electronics (Fig. 2) supports this interpretation. On the other hand, the short positive spike cannot be caused by the charge collection because it is much shorter than the time constant of the measuring circuits. Instead, it is the induced (or image) charge of the impact plasma cloud. The thermal speed of the electrons in the impact plasma is much higher than that of the ions. The electrons that have a sufficient energy to overcome the attractive potential of the antenna quickly escape and leave behind a net positive space charge (ions) that induces a positive signal on the antenna. Such feature is commonly observed in data from space missions and is known as a pre-peak. The duration of the pre-peak signal is determined by a number of parameters, including space-charge effects, the expansion speed of the impact plasma ions, and the geometry, or a characteristic size of the impacted element. Following the work by Meyer-Vernet et al. (2009a), the expanding plasma cloud remains quasi-neutral only till it grows larger than the Debye length, after which charge decoupling can occur. For the conditions in the presented laboratory experiments, the impact plasma remains quasi-neutral only till it expands to a size that is a fraction of a millimeter, thus it is not a limiting factor neither for the onset, nor the duration of the pre-peak signal. Note that dust impacts in space generate considerably more impact charge and thus quasi-neutrality can hold till the plasma cloud expends to centimeter or tens of centimeters in a size. Nevertheless, it is still small compared to a characteristic size of a spacecraft for typical conditions.

The expansion speed, v_E of ions generated by high-velocity dust impacts is in the range of $v_E = 10 - 20$ km/s that was determined from both laboratory experiments and analysis of data collected in space (see, for example, Collette et al. (2016) or Kellogg et al. (2016)). The duration of the induced pre-peak signal thus can be estimated to be L/v_E, i.e., the time that the ions need to disperse from the vicinity of the impacted element with a characteristic size, L.

The left top panel in Fig. 4 is the case with zero applied bias potential. The pre-peak is created by the same mechanism, and it is clearly visible during the first several microseconds. When the ions disperse, a rest of the image charge and a net collected positive charge from the impact plasma discharge slowly through the amplifier circuits (Fig. 2).

Pre-peaks can be observed for both the dipole and monopole antenna

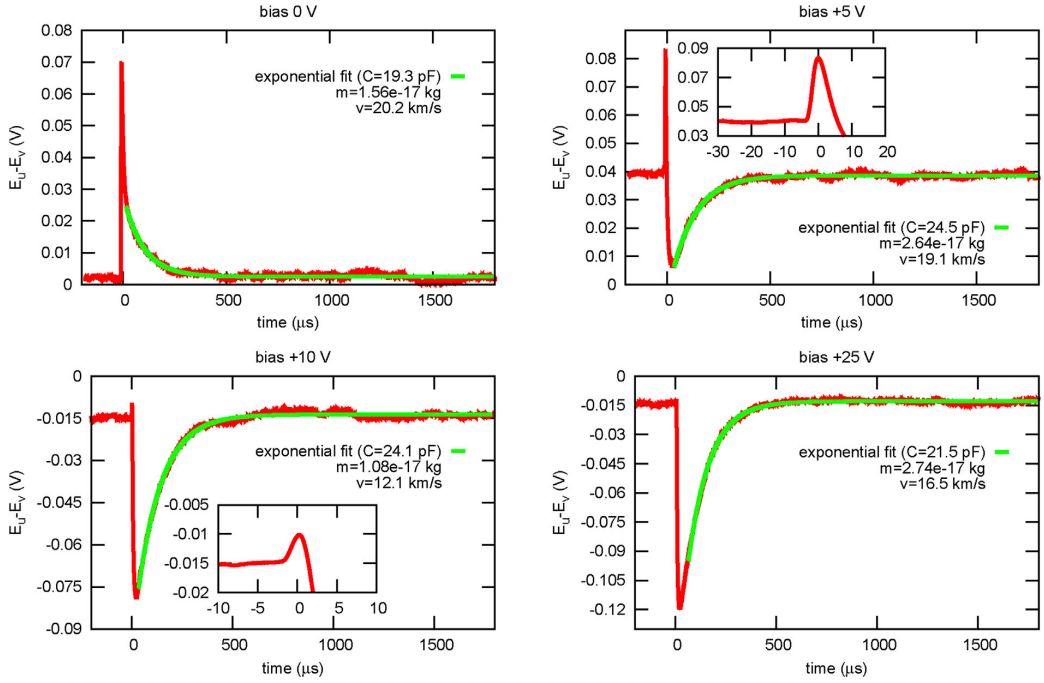


Fig. 4. The example of the impact signal detected by the antenna (E_U boom was bombarded) in a dipole configuration and an illustration of a determination of the time constant of the antenna. The inserts show details of the positive spikes.

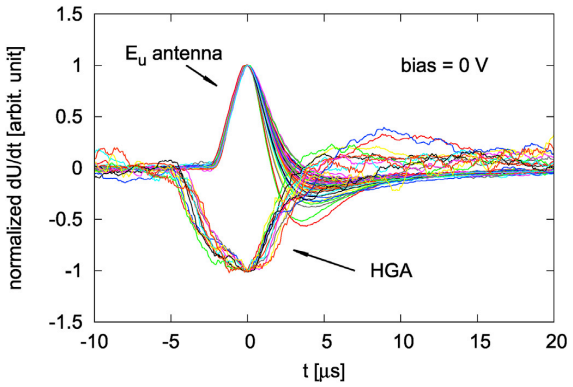


Fig. 5. A comparison of the derivatives of the pre-peaks measured from dust impacts on the E_U antenna boom and the HGA. See the text for details.

configurations. In the latter case, the polarity of the pre-peaks is negative for dust impacts occurring on the SC body because of the way the electronics is set up (Fig. 2). Note that the HGA is a part of the SC body in our simplified model. In the model, the characteristic size of the HGA antenna is $L = 15$ cm and the duration of the pre-peak is of the order of 10 μs, thus the resulting ≈ 15 km/s velocity is in a good agreement with the velocity of expected ion expansion. Fig. 5 presents a further indication supporting the suggested mechanism for the generation of the pre-peak signals. The figure shows the derivatives of the pre-peak signals for the 0 V bias potential; the maxima in Fig. 5 correspond to the pre-peak rising edge. The data are normalized for a direct comparison and present the impacts on both the E_U antenna boom (positive spikes) and the HGA (negative spikes). For the former case, the uniform signal shapes are due to the limited bandwidth of the amplifiers used. On the other hand, for the case of a dust impact on the HGA, the signal duration is clearly longer because the HGA is much larger than both monopole and dipole antennas. The diminishing of the image charge is thus much slower and can be recorded by our amplifier.

3.1. Capacitance measurements

The scaling constant between the collected charge and the voltage registered by the amplifier is the capacitance of the antenna (C_{ANT}) or spacecraft (C_{SC}). As discussed in Sec. 2, these capacitances are difficult to measure directly, but they can be calculated from the time constants of detected signals. The leading edges of the impulses or a shape of the voltage spikes preceding the impulses shown in Fig. 4 are determined by the amplifier bandwidth, whereas the following exponential decay is given by the discharging of the antenna capacitance. The time constant can be determined from the exponential fit to the discharging profile and calculation of the capacitance is based on the assumption that it is discharged through the 5 MΩ resistor (see Section 2). The fits are shown in Fig. 4 by the green lines and the corresponding capacitances are given in figure captions.

The capacitances determined by this way from about 1600 impacts (collected in two data sets) on each antenna and spacecraft are shown in histograms in Fig. 6. One can see that the fits provide capacitances in relatively large ranges. A spread of capacitance values is mainly due to a noise in the signal. For this reason, we made the Gaussian fits to each distribution and we use the capacitances determined by this way in further processing. The capacitances of the antennas for dipole and monopole configurations were determined as 20.9 pF and 20.4 pF, respectively (see Fig. 6 left and middle). The capacitance of the spacecraft was determined from impacts on the HGA dish as 118.6 pF (Fig. 6 right).

3.2. Dipole–monopole relations

The experimental set-up provides a large variety of possible configurations. There are several possible impact locations, different bias voltages can be applied on various parts of the spacecraft model and the signals from monopole and dipole antennas can be recorded. The following analysis will be limited to the signals recorded by the dipole antenna and to a possible reaction of the monopole antenna on the dust impacts onto dipole antenna.

The general observation through the entire data set collected is that dust impacts on the HGA or the monopole antenna do not produce measurable signals on the dipole antenna. The explanation of this observation is that the symmetric dipole antenna remains insensitive to transient variation in the SC potential and also that the recollection of impact charge on the dipole antennas is negligible. The latter seems valid as the impact locations investigated were the HGA and the middle of the monopole antenna that are both relatively far from the dipole antennas. Moreover, the dipole antenna booms are placed symmetrically with respect to the used impact locations. It may be, however, possible that dust impacts to other locations on the SC surface, closer to the dipole antennas, or those with very large impact charges, could be picked up by the dipole antenna as well. An extended experimental campaign is planned in the future to follow up on this effect and to determine how important it can be in the space.

On the other hand, impacts on the dipole antenna often result in a detectable response on the monopole antenna. Fig. 7 illustrates one such event. The records shown in this figure belong to the impact of a 3.2×10^{-17} kg grain with the velocity of 17.1 km/s. A relatively large impulse registered by the dipole antenna is shown in the left panel and its much smaller counterpart recorded simultaneously by the monopole antenna is depicted in the right panel. The opposite polarity of the signals is consistent with the scheme in Fig. 2 and capacitive coupling between the dipole and spacecraft body. However, we cannot exclude that a partial recollection of the charge generated at the dipole antenna contributes to the monopole signal. It should be noted that such a clear response is not too frequent because the signals on the monopole antenna are close to the noise level.

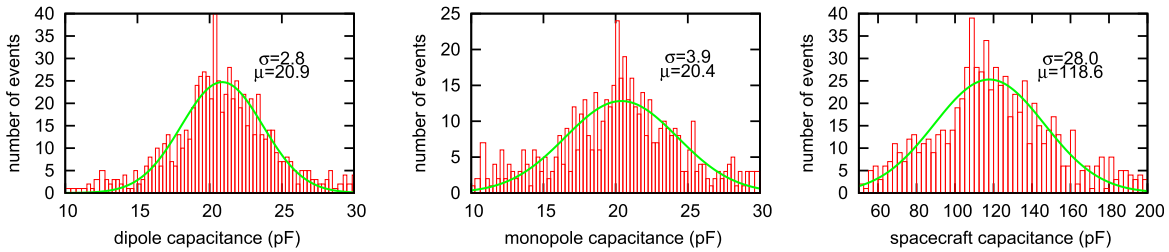


Fig. 6. Specific capacitance of antennas, C_{ANT} established from dipole (left) and monopole (middle) configurations and capacitance of the spacecraft, C_{SC} (right).

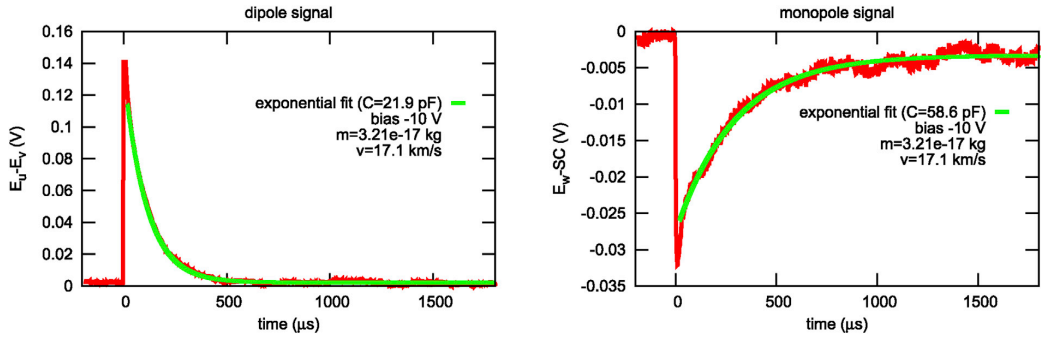


Fig. 7. Demonstration of a response of the monopole antenna on the impacts onto the dipole antenna. See the text for more details.

4. Conclusion

The first experimental study has been carried out to investigate the dust impact signal generation mechanisms on monopole and dipole antennas. The setup used was a scaled down model of the Cassini spacecraft, nevertheless, the findings are likely useful for a broader range of missions.

The presented preliminary analysis of the performed experiments appears to confirm the previous findings by Collette et al. (2015) that the three main mechanisms for the dust impacts generating measurable signals on the antennas are the recollection of charge on the spacecraft, the antenna, and induced (or image) charges from non-neutral plasma clouds. It is clear that the polarity and the magnitude of the SC and antenna potentials have a determining effect on the shape and magnitude of the recorded signals. The qualitative analysis of the data offers an explanation for the pre-peak phenomena that are often observed in space as well. This explanation is that the antennas are detecting the induced charge from an impact plasma cloud that is becoming non-neutral due to the escape of the faster electrons.

One of the results of our laboratory studies is a confirmation of the fact that dipole antennas are greatly insensitive to dust impacts on the spacecraft body or the monopole antenna. It is in agreement with Ye et al. (2016) that suggested that dust detections by dipole antennas need to be analyzed as impacts directly on these antennas. The experiments also revealed a surprising feature that dust impacts on the dipole antenna, on the other hand, often generate a detectable signal on the monopole antenna. No physical explanation exists yet for this observation, which may also be due to the crosstalk between the two analog channels. The further investigation of this effect, as well as a more details analysis of the impact signal will be followed up in a future study.

Acknowledgements

The authors thank Jessy Lopes Barreto for designing and building the scaled down Cassini model used in the experiments, and David James and John Fontanese for help with measurements at the dust accelerator. This study was made possible by past funding from NASAs Heliospheric Science program under grant NNX13AG24G and current funding from the Planetary Science program under grant NNX17AF99G. The dust accelerator was made available for the measurements by the SSERVI IMPACT project under grant number NNA14AB06A. The contributions of authors L. N., J. P., Z. N., and J. Š. were supported by the Czech Science Foundation (project 16-057625), by the Grant Agency of Charles University (project 728616), and by the Department of Education, Youth, and Sport (project LTAUSA17066).

Appendix A. Supplementary data

Supplementary data related to this article can be found at https://doi.org/10.1016/j.pss.2017.11.014.

References

Andersson, L., Weber, T.D., Malaspina, D., Crary, F., Ergun, R.E., Delory, G.T., Fowler, C.M., Morooka, M.W., McEnulty, T., Eriksson, A.I., Andrews, D.J., Horanyi, M., Collette, A., Yelle, R., Jakosky, B.M., 2015. Dust observations at orbital altitudes surrounding Mars. Science 350, 6261.

Aubier, M.G., Meyer-Vernet, N., Pedersen, B.M., 1983. Shot noise from grain and particle impacts in Saturn's ring plane. Geophys. Res. Lett. 10 (1), 5–8.

Collette, A., Grün, E., Malaspina, D., Sternovsky, Z., 2014. Micrometeoroid impact charge yield for common spacecraft materials. J. Geophys. Res. Space Phys. 119, 6019–6026. https://doi.org/10.1002/2014JA020042.

Collette, A., Meyer, G., Malaspina, D., Sternovsky, Z., 2015. Laboratory investigation of antenna signals from dust impacts on spacecraft. J. Geophys. Res. 120 (7), 5298–5305. https://doi.org/10.1002/2015JA021198.

Collette, A., Malaspina, D.M., Sternovsky, Z., 2016. Characteristic temperatures of hypervelocity dust impact plasmas. J. Geophys. Res. Space Phys. 121, 2169–9402. https://doi.org/10.1002/2015JA022220.

Gurnett, D.A., Grün, E., Gallagher, D., Kurth, W.S., Scarf, F.L., 1983. Micron-sized particles detected near Saturn by the Voyager plasma wave instrument. Saturn Conf. 53 (2), 236–254.

Gurnett, D.A., 1998. Principles of space plasma wave instrument design. In: Pfaff, R., Borovsky, J., Young, D. (Eds.), Measurement Techniques for Space Plasmas, AGU Monogr, vol. 103. AGU, Washington, D. C, pp. 121–136.

Gurnett, D.A., et al., 2004. The Cassini radio and plasma wave science investigation. Space Sci. Rev. 114, 395–463.

Kellogg, P.J., Goetz, K., Monson, S.J., 2016. Dust impact signals on the Wind spacecraft. J. Geophys. Res. 121 (2), 966–991. https://doi.org/10.1002/2015JA021124.

Kurth, W.S., Averkamp, T.F., Gurnett, D.A., Wang, Z., 2006. Cassini RPWS observations of dust in Saturn's E ring. Planet. Space Sci. 54, 988–998.

Laakso, H., Grard, R., Pedersen, A., Schwehm, G., 1989. Impacts of large dust particles on the VEGA spacecraft. Adv. Space Res. 9, 269–272. https://doi.org/10.1016/0273-1177(89)90273-1.

Malaspina, D.M., Horanyi, M., Zaslavsky, A., Goetz, K., Wilson, L.B., Kersten, K., 2014. Interplanetary and interstellar dust observed by the Wind WAVES electric field instrument. Geophys. Res. Lett. 41, 266–272. https://doi.org/10.1002/2013GL058786.

Meyer-Vernet, N., Lecacheux, A., Kaiser, M.L., Gurnett, D.A., 2009a. Detecting nanoparticles at radio frequencies: Jovian dust stream impacts on Cassini/RPWS. Geophys. Res. Lett. 36, L03103 https://doi.org/10.1029/2008GL036752.

Meyer-Vernet, N., Maksimovic, M., Czechowski, A., Mann, I., Zouganelis, I., Goetz, K., Kaiser, M.L., St Cyr, O.C., Bougeret, J.L., Bale, S.D., 2009b. Dust detection by the wave instrument on STEREO: nanoparticles picked up by the solar wind? Sol. Phys. 256 (1), 463–474.

Meyer-Vernet, N., Moncuquet, M., Issautier, K., Lecacheux, A., 2014. The importance of monopole antennas for dust observations: why Wind/WAVES does not detect nanodust. Geophys. Res. Lett. 41, 2716–2720. https://doi.org/10.1002/2014GL059988.

Mocker, A., Bugiel, S., Auer, S., Baust, G., Collette, A., Drake, K., Fiege, K., Grn, E., Heckmann, F., Helfert, S., Hillier, J., Kempf, S., Matt, G., Mellert, T., Munsat, T., Otto, K., Postberg, F., Rser, H.-P., Shu, A., Sternovsky, Z., Srama, R., 2011. A 2 MV Van de Graaff accelerator as a tool for planetary and impact physics research. Rev. Sci. Instrum. 82 (9), 095111.

Pavlů, J., Richterová, I., Němeček, Z., Šafránková, J., 2008. Field emission characteristics of gold dust grains. Adv. Space Res. 42 (1), 129–135.

Robertson, S., Sternovsky, Z., Walch, B., 2004. Reduction of asymmetry transport in the annular penning trap. Phys. Plasmas 11 (5), 1753–1756.

Scarf, F.L., Gurnett, D.A., Kurth, W.S., Poynter, R.L., 1982. Voyager 2 plasma wave observations at Saturn. Science 215 (4532), 587–594.

Shu, A., Collette, A., Drake, K., Grün, E., Horanyi, M., Kempf, S., Mocker, A., Munsat, T., Northway, P., Srama, R., Sternovsky, Z., Thomas, E., 2012. 3 MV hypervelocity dust

accelerator at the Colorado center for lunar dust and atmospheric studies. Rev. Sci. Instrum. 83 (7), 5108,. https://doi.org/10.1063/1.4732820.

St Cyr, O.C., et al., 2009. STEREO SECCHI and S/WAVES observations of spacecraft debris caused by micron-size interplanetary dust impacts. Sol. Phys. 256 (1), 475–488.

Tsintikidis, D., Gurnett, D., Granroth, L.J., Allendorf, S.C., Kurth, W.S., 1994. A revised analysis of micron-sized particles detected near Saturn by the Voyager 2 plasma-wave instrument. J. Geophys. Res. Space Phys. 99 (2), 2261–2270.

Tsurutani, B.T., Clay, D.R., Zhang, L.D., Dasgupta, B., Brinza, D., Henry, M., Mendis, A., Moses, S., Glassmeier, K.-H., Musmann, G., Richter, I., 2003. Dust impacts at comet P/Borrelly. Geophys. Res. Lett. 30 (22), 2134,. https://doi.org/10.1029/2003GL017580.

Wang, Z., Gurnett, D.A., Averkamp, T.F., Persoon, A.M., Kurth, W.S., 2006. Characteristics of dust particles detected near Saturn's ring plane with the Cassini Radio and Plasma Wave instrument. Planet. Space Sci. 54 (9), 957–966.

Ye, S.-Y., Gurnett, D.A., Kurth, W.S., Averkamp, T.F., Morooka, M., Sakai, S., Wahlund, J.-E., 2014a. Electron density inside Enceladus plume inferred from plasma oscillations excited by dust impacts. J. Geophys. Res. Space Phys. 119, 2169–9402. https://doi.org/10.1002/2014JA019861.

Ye, S.-Y., Gurnett, D.A., Kurth, W.S., Averkamp, T.F., Kempf, S., Hsu, H.W., Srama, R., Grün, E., 2014b. Properties of dust particles near Saturn inferred from voltage pulses induced by dust impacts on Cassini spacecraft. J. Geophys. Res. Space Phys. 119 (8), 6294–6312. https://doi.org/10.1002/2014ja020024.

Ye, S.-Y., Kurth, W.S., Hospodarsky, G.B., Averkamp, T.F., Gurnett, D.A., 2016. Dust detection in space using the monopole and dipole electric field antennas. J. Geophys. Res. Space Phys. 121 (12), 11964–11972.

Zaslavsky, A., Meyer-Vernet, N., Mann, I., Czechowski, A., Issautier, K., Le Chat, G., Pantellini, F., Goetz, K., Maksimovic, M., Bale, S.D., Kasper, J.C., 2012. Interplanetary dust detection by radio antennas: mass calibration and fluxes measured by STEREO/WAVES. J. Geophys. Res. 117, A05102.

Zook, H.A., Grün, E., Baguhl, M., Hamilton, D.P., Linkert, G., Liou, J.C., Forsyth, R., Phillips, J.L., 1996. Solar wind magnetic field bending of Jovian dust trajectories. Science 274 (5), 1501–1503.